LATTICE BOLTZMANN COMPUTATION OF MICRO AND MACRO FLUID FLOWS AND HEAT TRANSFER

A Thesis

Submitted in Partial Fulfilment of the Requirements

for the Degree of

DOCTOR OF PHILOSOPHY

By

D. ARUMUGA PERUMAL

DEPARTMENT OF MECHANICAL ENGINEERING
INDIAN INSTITUTE OF TECHNOLOGY GUWAHATI
GUWAHATI, INDIA
May 2010

LATTICE BOLTZMANN COMPUTATION OF MICRO AND MACRO FLUID FLOWS AND HEAT TRANSFER

A Thesis

Submitted in Partial Fulfilment of the Requirements

for the Degree of

DOCTOR OF PHILOSOPHY

By

D. ARUMUGA PERUMAL

(Roll No. 05610311)

DEPARTMENT OF MECHANICAL ENGINEERING
INDIAN INSTITUTE OF TECHNOLOGY GUWAHATI
GUWAHATI, INDIA
May 2010

DECLARATION

It is certified that the work contained in the thesis entitled "**Lattice Boltzmann Computation of Micro and Macro Fluid Flows and Heat Transfer**" has been done by me, a student in the Department of Mechanical Engineering, Indian Institute of Technolgy Guwahati under the guidance of Prof. Anoop K. Dass for the award of Doctor of Philosophy and that this work has not been submitted elsewhere for a degree.

Date:

_____

D. Arumuga Perumal

Department of Mechanical Engineering

Indian Institute of Technology Guwahati

CERTIFICATE

It is certified that the work contained in the thesis entitled "**Lattice Boltzmann Computation of Micro and Macro Fluid Flows and Heat Transfer**" by **D. Arumuga Perumal**, has been carried out under my supervision and that this work has not been submitted elsewhere for a degree.

Date:

_____

Dr. Anoop K. Dass

Professor

Department of Mechanical Engineering

Indian Institute of Technology Guwahati

Dedicated
to
My Parents &
to
My Chithra

ACKNOWLEDGEMENT

This is the space in my dissertation to pay tribute to those individuals who stood by me, encouraged me, believed in me and contributed in many ways to help overcome one of the toughest challenges. First, I thank my supervisor Prof. Anoop K. Dass for his guidance and constant encouragement. I am highly indebted to him for providing me ample freedom to work my way and simultaneously giving me a taste of research work. I learnt a lot many things from him, which will be an asset for my future life.

I would like to thank Prof. Subash C. Mishra, Prof. Anupam Dewan (now in the Department of Applied Mechanics, IIT Delhi), Dr. Anugrah Singh, Chemical Engineering, IIT Guwahati, Dr. Manmohan Pandey (now in the Department of Mechanical Engineering, IIT Gandhinagar), Dr. Manab K. Das (now in the Department of Mechanical Engineering, IIT Kharagpur), Dr. U.K. Saha, Mechanical Engineering for reviewing my work regularly and for their valuable suggestions for my doctoral research. My special thanks to Dr. C. Somayaji and Dr. Amaresh Dalal for giving valuable suggestions in the final phase of my research work. I specially acknowledge Prof. S.K. Dwivedy and Dr. Jiten C. Kalita for their suggestions and encouragement throughout my research period. I am sincerely thankful to Prof. P.S. Robi, Prof. U.S. Dixit and Prof. D. Chakraborty (Head, Mechanical Engineering) for providing me sufficient funds to do my research work successfully. I am thankful to other faculty members who directly or indirectly motivated me to complete my research work.

I express my thanks to the Department staff members D.K. Saikia, L. Saikia and R. Patowari for their help in official matters. I am thankful to Mr. Amal Kalita and Mr. Nip Borah for providing good facilities in the CAD lab. I would like to express my gratitude to my parents whose blessings and neverending support is the real impetus that continuously motivates me to produce my best. I am deeply indebted to my Ph.D.-, M.Tech-, and B.Tech friends for their moral support, constant encouragement and immense love throughout my research period. Finally, I express my sincere thanks to all my friends who helped me during my stay at Siang Hostel, IIT Guwahati.

(D. Arumuga Perumal)

List of Publications

Book Chapter

1. **D. Arumuga Perumal** and Anoop K. Dass, Simulation of Incompressible thermal flows by Lattice Boltzmann Method, Chapter 4, *Modelling and Simulation in Computational Mechanics: Engineering Applications*, Lambert Academic Publishers, Germany, 2009.

International Journals

1. **D. Arumuga Perumal** and Anoop K. Dass, Multiplicity of Steady Solutions in Two-Dimensional Lid-Driven Cavity Flows by the Lattice Boltzmann Method, *Computers & Mathematics with Applications*, doi:10.1016/j.camwa.2010.03.053, 2010. (In Press)
2. **D. Arumuga Perumal** and Anoop K. Dass, Simulation of Incompressible Flows in Two-Sided Lid-Driven Square Cavities. Part II - LBM, *CFD Letters*, Vol. 2, No.1, pp. 25-38, 2010.
3. **D. Arumuga Perumal** and Anoop K. Dass, Simulation of Incompressible Flows in Two-Sided Lid-Driven Square Cavities. Part I - FDM, *CFD Letters*, Vol. 2, No.1, pp. 13-24, 2010.
4. **D. Arumuga Perumal**, Gundavarapu V.S. Kumar, Anoop K. Dass, Application of Lattice Boltzmann Method to flows in Microgeometries, *CFD Letters*, Vol. 2, No.2, pp. 75-84, 2010.
5. **D. Arumuga Perumal**, V. Krishna, G. Sarvesh and Anoop K. Dass, Numerical Simulation of Gaseous Microflows by Lattice Boltzmann Method, *International Journal of Recent Trends in Engineering*, Vol. 1, No. 5, pp. 15-20, 2009.

International Conferences

1. **D. Arumuga Perumal** and Anoop K. Dass, Multiplicity of Steady Solutions in Two-Dimensional Lid-Driven Square Cavity Flows by the Lattice Boltzmann

Method, *Sixth International Conference for Mesoscopic Methods in Engineering and Science (ICMMES-09)*, Guangzhou, China, July 13-17, 2009.

2. **D. Arumuga Perumal**, Gundavarapu V.S. Kumar and Anoop K. Dass, Application of Lattice Boltzmann Method to Micro-Cavities, *International Conference on Advanced Nanomaterials and Nanotechnology (ICANN-09)*, IIT Guwahati, India, Dec 9-11, 2009.
3. **D. Arumuga Perumal** and Anoop K. Dass, Lattice Boltzmann Simulation of Two and Three dimensional Flow in a Lid-driven Cavity, *International Conference on Advances in Mechanical Engineering, (IC-ICAME-08)*, IISc Bangalore, India, July 21-24, 2008.
4. **D. Arumuga Perumal** and Anoop K. Dass, Simulation of Flow in Two-sided Lid-driven Square Cavities by Lattice Boltzmann Method, *Advances in Fluid Mechanics VII, WIT Transactions on Engineering Sciences, (AFM VII)*, 45-54, The New Forest, United Kingdom, May 21-23, 2008.
5. **D. Arumuga Perumal** and Anoop K. Dass, Incompressible Viscous Flow Simulation in the Lid-Driven Cavity by LBM, *Second International Congress on Computational Mechanics and Simulation (ICCMS-06)*, IIT Guwahati, India, Dec 8-10, 2006.

National Conferences

1. Anoop K. Dass and **D. Arumuga Perumal**, Investigation of Fluid-flow and Heat Transfer Problems through Lattice Boltzmann Method, *National Conference on Recent Advances in Mechanical Engineering (NCRAME-2008)*, NIT Silchar, India, Dec 20-21, 2008. (Keynote Paper).

Abstract

This thesis is concerned with the application of Lattice Boltzmann Method (LBM) to various steady incompressible fluid-flow and heat-transfer problems in the macro- and micro-flow regimes. The Lattice Boltzmann Method is a means of flow computation based on simplified kinetic models using discrete particle velocities, which exploits the fact that the collective behaviour of the molecules does not explicitly depend on their individual dynamics. Being a relatively new and an alternative method of flow computation, it is still being experimented with to realize its full scope of application and to test its ability to capture untested physics. The present thesis can be considered an attempt in that direction. Several computer programs based on the programming language 'C' have been developed to carry out computations to solve a host of problems, some of which are hitherto unexamined. To provide a means of comparison of the LBM results for untested flow configurations, a Finite-Difference-Method (FDM) code has been developed and its results are shown to be highly accurate through a careful code-validation exercise. In the applications, first a number of two-dimensional (2D) single-lid-driven cavity flow problems are computed through the LBM Single-Relaxation-Time (SRT) and Multi-Relaxation-Time (MRT) methods and the LBM-MRT method is shown to overcome some of the problems faced by the LBM-SRT method - especially in resolving the corner singularities at high-Reynolds number situations. Then a new test problem, namely, 'two-sided lid-driven square cavity flow' is proposed and many carefully established qualitative and quantitative results are given for algorithm validation by other workers. It is shown that for parallel motion of the walls there is a 'free-shear'

layer midway between the moving plates and that near-trailing-edge corner vortices form at a much lower Reynolds number compared with the single-lid-driven cavity flow. Computing flows in two-sided non-facing and four-sided lid-driven square cavities and in a two-sided rectangular cavity with parallel wall motion, it is demonstrated that not only continuum-based methods like the Finite Difference Method and Finite Volume Method (FVM) but also LBM has the ability to capture multiple-steady solutions. It may be noted that the traditional mathematical concept of well-posedness does not apply here and for the first time the ability and accuracy of the Lattice Boltzmann Method to obtain solutions to this peculiar class of problems is demonstrated. LBM computations are also carried out for the single- and two-sided lid-driven cubic and prism cavity flows. For the single-lid-driven case, two-dimensional and three-dimensional (3D) velocity profiles in the symmetry plane are compared to study the end-wall effects. For 3D computations the *D3Q19* lattice model is shown to be the most convenient to use. Also LBM in conjunction with the IEDDF approach is used to compute thermally-driven flows in the square and cubic cavities. Comparing the 2D and 3D velocity profiles in the symmetry plane, effect of the end walls with increasing Rayleigh numbers is brought out - probably for the first time. LBM is then applied to compute flows in various micro-geometries. The study reveals many interesting features of micro-couette, micro-channel (pressure-driven) and micro-lid-driven cavity flows and demonstrates the ability of LBM to capture those flow features. The main concern of this thesis is the computation of steady flows. In keeping with this theme, highly accurate LBM computations are also carried out for the flow past a circular cylinder at low Reynolds numbers when the flow is steady and symmetric. To demonstrate the ability of the present method to compute time-varying

flows, computations are also carried out for a higher Reynolds number at which the symmetry breaks and the flow becomes time-periodic. All the results presented in the thesis are independent of the lattice size and they are substantiated carefully. Though all the computed flows fall in the laminar regime, difficult flow configurations exemplified by large values of the Reynolds and Rayleigh numbers are also computed. The work successfully demonstrates that LBM has come of age and is now an important alternative solution procedure in computational fluid dynamics.

Contents

List of Figures

List of Tables

Nomenclature

Symbol	**Description**
Ma	Mach Number
Re	Reynolds number
$\boldsymbol{F}$	body force
$Q(f)$	collision integral
$f_i(\mathbf{x},t)$	particle distribution function
$f_i^{(0)}(\mathbf{x},t)$	equilibrium distribution function
$\tilde{f}_i(\mathbf{x},t)$	post-collision state of the distribution function
$g_i(\mathbf{x},t)$	internal energy distribution function
$g_i^{eq}(\mathbf{x},t)$	equilibrium internal energy distribution function
$\boldsymbol{c}_i$	discrete velocity
w_i	lattice weights
υ	kinematic viscosity
τ	relaxation time
$\underline{R}$	vector space
$\underline{S}$	diagonal matrix
M	transformation matrix
ρ	fluid density
e	energy
δx	lattice spacing
u_0	reference velocity
c_s	lattice speed of sound
p	pressure
$\boldsymbol{u}$	macroscopic velocity

D_1Q_2	one-dimensional two-velocity model
D_1Q_3	one-dimensional three-velocity model
D_1Q_5	one-dimensional five-velocity model
D2Q7	two-dimensional seven-velocity model
D2Q9	two-dimensional nine-velocity model
D3Q15	three-dimensional fifteen-velocity model
D3Q19	three-dimensional nineteen-velocity model
D3Q27	three-dimensional twenty seven-velocity model
$\boldsymbol{e}_i$	molecular velocities of the incident particles
$\boldsymbol{e}_i'$	molecular velocities of the reflected particles
A_N	normalization coefficient
σ	tangential momentum accommodation coefficient
M	tangential momentum of the molecules
i, j, k	indices along the *x*-, *y*- and *z*- directions respectively
g	Acceleration due to gravity
K	aspect ratio
L	characteristic length
Ra	Rayleigh number
Pr	Prandtl number
T	temperature
T_C, T_H	cold and hot wall temperatures
T_0	reference temperature
x, y	cartesian horizontal and vertical co-ordinates
t	time
Nu	Nusselt number
ψ	stream function
ω	vorticity
D	depth of the cavity
W	width of the cavity

$\boldsymbol{U}$	maximum velocity
F	external force
$t_s^{(1)}$	symmetric solution of the two-sided lid-driven cavity flow
$t_a^{(1)}$	asymmetric solution of the two-sided lid-driven cavity flow
$t_a^{(2)}$	asymmetric solution of the two-sided lid-driven counterpart
$f_S^{(1)}$	symmetric solution of the four-sided lid-driven cavity flow
$f_a^{(1)}$	asymmetric solution of the four-sided lid-driven cavity flow
$f_a^{(2)}$	asymmetric solution of the four-sided lid-driven cavity counterpart
τ_v	relaxation time for the density distribution function
τ_c	relaxation time for the internal energy distribution function
α	thermal diffusivity
R	gas constant
β	coefficient of thermal expansion
ΔT	temperature difference
T_m	mean temperature of the fluid
$q_x(x, y)$	local heat flux
$\overline{Nu}$	average Nusselt number
$Nu_{1/2}$	average Nusselt number along the vertical centreline
Nu_0	average Nusselt number at the hot wall
$U_{\max}$	maximum horizontal velocity on the vertical mid-plane
$V_{\max}$	maximum vertical velocity on the horizontal mid-plane
Kn	Knudsen number
λ	mean free path of the gas molecules
N_y	number of lattice nodes in y-direction
P^*	nonlinear pressure variation
P_{out}	pressure at the exit of the channel

B	Blockage ratio
C_D	Coefficient of Drag
D	cylinder diameter
U_∞	velocity at the channel entry
H	cylinder channel width

Abbreviations

CFD	Computational Fluid Dynamics
FDM	Finite Difference Method
FVM	Finite Volume Method
ODE	Ordinary Differential Equation
PDE	Partial Differential Equation
FEM	Finite Element Method
LBM	Lattice Boltzmann Method
BGK	Bhatnagar-Gross-Krook
LBM-SRT	Lattice Boltzmann Method with Single-Relaxation-Time
LBM-MRT	Lattice Boltzmann Method with Multi-Relaxation-Time
LGA	Lattice Gas Automata
LBE	Lattice Boltzmann Equation
ADI	Alternate Direction Implicit
3D-TSNFL	Three-dimensional two-sided non-facing lid-driven square cavity
TLBM	Thermal Lattice Boltzmann Method
IEDDF	internal energy density distribution function
FTCS	Forward Time Centered Space
3D	Three-dimensional
2D	Two-dimensional
MEMS	Micro-electro-mechanical systems
NEMS	Nano-electro-mechanical systems
MD	Molecular Dynamics
DSMC	Direct Simulation Monte Carlo
TMAC	Tangential Momentum Accommodation Coefficient
BSBC	Bounce-back and specular boundary condition
SBC	Specular boundary condition
DSBC	Diffuse scattering boundary condition

Chapter 1

Introduction

1.1. General Background

Numerical simulation of fluid flow has been a major topic of research for the past few decades [1, 2]. The continuous growth of computer power has motivated the scientific community to use Computational fluid dynamics (CFD) for numerical solution of the governing equations of fluid dynamics. Generally the mathematical models used in CFD include convective and diffusive transport of some variables. These mathematical models consist of governing equations in the form of ordinary or partial differential equations (ODEs or PDEs). As a great number of such model equations like the Navier-Stokes equations do not possess analytical solutions, one has to resort to numerical methods. The difficulty in solving the Navier-Stokes equations is due to their nonlinear terms. In conventional numerical methods, the macroscopic variables of interest such as velocity and pressure are usually obtained by solving the Navier-Stokes equations.

Over the years, the finite difference method (FDM) and finite volume method (FVM) are frequently being used in CFD [3]. FDM consists in essentially setting up a uniform rectangular grid in the problem domain, discretizing the governing equations with respect to the grid by replacing the derivatives with their finite-difference approximations and solving the resulting algebraic equations numerically. For nonuniform grids FDM requires a transformation of the physical space onto a computational space with an

uniform grid. FVM requires no such transformation as it solves the integral form of the governing equations that are integrated over (generally) irregularly-shaped finite volumes. The finite element method (FEM) has not gained as much popularity in fluid mechanics as it has in structural mechanics.

In the last two decades, a different kind of numerical method for applications in CFD, namely, the Lattice Boltzmann Method (LBM) has gained popularity [4]. LBM has emerged as a new effective and alternative approach of CFD and it has achieved considerable success in simulating fluid flows and heat transfer problems [5]. In the LBM approach, one solves the kinetic equation for the particle distribution function. The macroscopic variables such as velocity and pressure are obtained by evaluating the hydrodynamic moments of the particle distribution function [6]. One of the most popular and simple approaches in the LBM is lattice Boltzmann equation with linearized collision operator based on the Bhatnagar-Gross-Krook (LBM-SRT) collision model [7].

1.2. Literature Review

The basic of the LB method is discussed in sufficient details in the books by Succi [1] and Chang *et al.* [4]. Chen and Doolen [5] have written an excellent review paper on the subject. In the past few years, researchers have been using lattice Boltzmann method for simulating and modeling in physical, chemical, social systems including flows in magnetohydrodynamics [8], immiscible fluids [9], multiphase flows [10], heat transfer problems [11-13], porous media [14] and isotropic turbulence [15]. Historically, LBM originated from the method of Lattice gas automata (LGA), which was first introduced in 1973 by Hardy, Pomeau and de Pazzis (HPP) [16]. In LGA, the term Lattice implies that

one is working on a lattice which is d-dimensional and usually regular. Gas suggests that a gas is moving on the lattice. The gas is usually represented by boolean particles (0 or 1). Automata indicate that the gas evolves according to a set of rules. In the LGA model, the space, time and particle velocities are all discrete. The iteration of an LGA consists of a collision and propagation step. But, the major drawbacks of the LGA were intrinsic noise, non-Galilean invariance, an unphysical velocity dependent pressure and large numerical viscosities. In 1986, Frisch, Hasslacher and Pomeau (FHP) obtained the correct Navier-Stokes equations using a hexagonal lattice. Lattice Boltzmann Equations has been used at the cradle of Lattice Gas Automata (LGA) by Frisch *et al.* [17] to calculate viscosity. To eliminate statistical noise, in 1988 McNamara and Zanetti [18] did away with the Boolean operation of LGA involving the particle occupation variables by neglecting particle correlations and introducing averaged distribution functions giving rise to the LBM.

Higuera and Jimenez [19] brought about an important simplification in LBM by presenting a lattice Boltzmann Equation (LBE) with a linearized collision operator that assumes that the distribution is close to the local equilibrium state. A particularly simple version of linearized collision operator based on the Bhatnagar-Gross-Krook (BGK) [20] collision model was independently introduced by several authors including Koelman [21] and Chen *et al.* [22]. The lattice BGK (LBGK) model [23, 24] utilizes the local equilibrium distribution function to recover the macroscopic Navier-Stokes equations.

The fluid motion inside a closed, square container with rigid walls induced by the tangential motion of a lid constitutes a classical paradigm for internal vortex flows [25-

33]. The lid-driven cavity flow problem is not only technically important but also of great scientific interest because it displays almost all fluid mechanical phenomena in the simplest geometrical settings [25]. Miller [26] presented two-dimensional lid-driven cavity flow LBM results with Dirichlet and Neumann boundary conditions and results were compared with analytical solutions. Hou *et al.* [27] extensively studied viscous flow in a square cavity for a wide range of Reynolds number using LBM-SRT model with bounce-back boundary condition. He found some ripples in the streamline, vorticity and pressure contour plots for high Reynolds number. Some of the notable works in cavity flow by the LBM include those of Shi *et al.* [28], De *et al.* [29], Patil *et al.* [30] and Shu *et al.* [31]. There appears to be very little work done on deep cavities by LBM, although they are of more theoretical interest [32, 33].

Boundary condition plays a crucial role in Lattice Boltzmann simulations [34-41]. The bounce-back boundary condition is a popular boundary condition in LBM. It is derived from LGA and has been extensively applied in LBM simulations. In this scheme, the particle distribution function at the wall lattice node is assigned to be the particle distribution function of its opposite direction. The easy implementation of this no-slip velocity condition supports the LBM is ideal for simulating fluid flows. Noble *et al.* [34] proposed hydrodynamic boundary condition on no-slip walls by enforcing a pressure constraint to replace the bounce-back boundary condition. They simulated steady flow of an incompressible fluid between two infinite parallel plates and demonstrated accurate results by LBM. Inamuro *et al.* [35] suggested that a slip velocity near wall nodes could be induced by the bounce-back scheme and proposed to use a counter-slip velocity to cancel that effect. Filippova and Hanel [38] proposed curved boundary treatment using

Taylor series expansion in both space and time for particle distribution function. In addition, curved boundary treatment was independently introduced by Mei *et al.* [39] and Bouzidi *et al.* [40]. A unified scheme for second order accurate curved wall treatment was proposed by Yu *et al.* [41].

The problem of buoyancy driven square cavity with adiabatic top and bottom walls and differentially heated vertical walls has been the topic of extensive study in the past few decades. McNamara *et al.* [42] were among the first to investigate two-dimensional enclosures using LBM isothermal models. They used only density distribution function in terms of multi-speed approach. The main disadvantage of this approach is its numerical instability. Eggels and Somers [43] proposed passive-scalar LBM approach, in which the temperature is simulated using a separate distribution function which is independent of the density distribution function. This approach enhances the numerical stability, but the disadvantage of this approach is that viscous heat dissipation and compression work done by the pressure cannot be incorporated. He *et al.* [44] developed internal energy density distribution function (IEDDF) approach and it shows greater stability. This model is numerically more stable, and it can incorporate viscous heat dissipation and compression work done by the pressure. Some of the notable works by the LBM include those of Shan [45], Peng *et al.* [46], Onishi *et al.* [47], Shu *et al.* [48] and Dixit and Babu [49].

Tolke *et al.* [50] introduced nonlinear multigrid solution approach for the discrete Boltzmann equation. Marviplis [51] presented efficient solution strategies for the steady state lattice Boltzmann equation. He checked the ability of the multigrid LBM for the driven cavity. Multigrid techniques applied to LBM are promising but, as occurred in

traditional CFD techniques, problems in the prolongation and restriction steps near complex walls have not yet been fully addressed. To increase the numerical accuracy in LBM non-uniform grid has been introduced. He *et al.* [52] described lattice Boltzmann method to simulate the Navier-Stokes equation on arbitrary non-uniform grids. They presented results of flow in a two-dimensional symmetric channel with sudden expansion. Kuznik *et al.* [53] simulated natural convection in a square cavity using double population lattice Boltzmann method with non-uniform mesh. To maintain the inherent advantage of the LBM, such as simplicity in coding and computational efficiency one prefers to employ the uniform lattice [54].

The majority of the LBM works so far dealt with two-dimensional flows. Limited number of reliable numerical results for steady state three-dimensional results has been obtained by LBM in the past few years. In 2000, Mei *et al.* [55] employed Lattice Boltzmann method for 3D lid-driven cubic cavity flow with second-order accurate curved boundary treatment in the range of Reynolds number from Re = 100 to 2000. They found that the three-dimensional fifteen-velocity (*D3Q15*) model was more prone to numerical instability, the three-dimensional twenty seven-velocity (*D3Q27*) model was more computationally intensive and the three-dimensional nineteen-velocity (*D3Q19*) model provided balance between computational reliability and efficiency. In 2003, Shu *et al.* [56] simulated 3D lid-driven cubical cavity flow by Taylor series expansion and least squares-based Lattice Boltzmann method (TSLBM) using the fifteen-velocity model (D3Q15) at three different Reynolds numbers Re = 100, 400 and 1000. Peng *et al.* [57] extended the solutions of IEDDF model for three-dimensional cubical thermal cavity in the range of Rayleigh numbers 10^3 to 10^5.

Alexander *et al.* [58] formulated an isothermal LBM models for which can include shocks. It has a selectable sound speed. This feature allows one to simulate compressible fluid flows with high Mach numbers. Qian and Orszag [59] studied the nonlinear deviation of the LBGK model in compressible regimes and presented the numerical simulation of a shock profile. Sun [60, 61] formulated adaptive lattice Boltzmann model in which a particle possesses two different kinds of velocity, one the migrating velocity, relating to the transport of a particle and the other phase velocity, relating to the momentum of a particle. Yu and Zhao [62] applied LBM to simulate compressible flows with high Mach number up to 5 introducing an attractive force.

The Lattice Boltzmann method is a relatively novel technique of flow computation, there is some scope for speculation as to the accuracy of the present LBM computations. Therefore the existing LBM results always has been compared favourably with finite difference methods [63], finite volume methods [64], finite element methods [65], spectral methods [66] and artificial compressibility methods [67].

Currently LBM is mainly applied to the continuum flow regime only. First, Nie *et al.* [68] used the LBM with bounce-back boundary condition to simulate two-dimensional micro-channel and micro lid-driven cavity flow. They employed the LBM in the no-slip and slip regime, but it is known that the no-slip boundary conditions are generally unrealistic for slip and transition flows and it cannot capture the real microflow characteristics. Tang *et al.* [69, 70] applied kinetic theory based boundary condition to study gaseous slip flow in micro-scale geometries. Zhang *et al.* [71] used the tangential momentum accommodation coefficient (TMAC) to describe the gas-surface interactions. Shirani and Jafari [72]

applied a combination of bounce-back and specular boundary conditions and their results are in good agreement with the experimental data and analytical solutions. Niu *et al.* [73] used diffuse scattering boundary condition to simulate isothermal two-dimensional microchannel flows.

The uniqueness of steady flows is almost an article of faith for a given geometry and boundary conditions. But some nonlinear systems in fluid mechanics display multiple-steady solutions for the same set of governing equations and boundary conditions. So far conventional methods like FVM, FDM are being used to capture these multiple solutions. Aidun *et al.* [74] studied single-sided lid-driven cavity with spanwise aspect ratio of 3.0 for $100 \leq Re \leq 2000$. They presented flow visualizations from the downstream side wall of two-cell, three-cell and four-cell stable steady states. Albensoeder *et al.* [75] were among the first to investigate the nonlinear regime and found multiple two-dimensional states in rectangular lid-driven cavities. They have found seven and five flow states in antiparallel and parallel motion respectively. More recently, the multiplicity of flow states induced by the motion of two-sided non-facing lid-driven square cavity flow and four-sided lid-driven cavity flow have been investigated by Wabha [76].

1.3. Motivation

Many of the works published so far reveals a plethora of issues concerning Lattice Boltzmann with single-relaxation-time (LBM-SRT) model and its applicability to incompressible viscous flows in particular. Furthermore, in contrast to the fairly large number of studies conducted for single-sided lid-driven cavities, only a few investigations have been carried out for flows in two-sided lid-driven cavities by

continuum-based methods and no attempt has been made to compute the flow in a two-sided lid-driven square cavity with various Reynolds number by LBM. The multiplicity of steady flows is also a very topical research field in fluid dynamics. Very interestingly, however, to the author's knowledge, there is no literature to discuss multiple steady solutions by LBM. The realistic three-dimensional flows possess features which are fundamentally different from those of two-dimensional flows. These three-dimensional flows offer tough challenges to any computational algorithm especially at high Reynolds numbers and Rayleigh numbers, and not many LBM computations for such flows are seen. In this context, it seems important to examine how the LBM scheme performs when computing such flows. The vast majority of the LBM works so far deals with two-dimensional flows and it is mainly applied to the continuum flow regime only. Application of LBM to compute gaseous microflows is still an emerging area with some unanswered questions. Very few attempts using LBM have been made to compute gaseous flows in micro-geometries. Application of LBM for these problems has challenges and is replete with many interesting possibilities. These are the major motivating factors behind this work, which is concerned with addressing these issues.

1.4. Objectives

In the context described above, the main aims of the present work are as follows:

- The primary objective of this work is to get acquainted with various aspects of the Lattice Boltzmann Method and develop efficient codes that can numerically compute micro and macro fluid flows and heat transfer involving various levels of complexities.

- To examine the possibility of broadening the scope of applicability of LBM to hitherto unexplored problems.
- To demonstrate the ability of lattice Boltzmann Method to capture multiple steady solutions that exist for certain flow configurations.
- To examine the effect of three-dimensionality at certain planes using different three-dimensional Lattice Boltzmann models at high Reynolds and Rayleigh numbers.
- To compute gaseous microflows in micro-geometries in the slip and threshold of transition regime.
- To stimulate further studies using the Lattice Boltzmann approach.

1.5. The Work

The present dissertation is concerned with the application of LBM to incompressible viscous flows with or without heat transfer and microflows so as to examine its behaviour in some unexamined situations and extend its range of applicability to such areas like capturing multiple steady-state solutions.

First, we compute the two-dimensional single-lid-driven cavity flow by the single-relaxation-time (LBM-SRT) model. Besides the LBM-SRT model, the multi-relaxation-time LBM-MRT model, which has certain advantages is also used. In the LBM-SRT model formulation, the bulk and shear viscosities are both determined by the same relaxation time. The LBM-MRT model attempts to relax different modes with different relaxation times so that bulk and shear viscosities can be determined by different relaxation times and adjusted independently. The Reynolds number effect on the flow structure is clearly manifested by the streamlines, velocity profiles, vorticity and pressure

contours. For high Reynolds number flows using LBM-SRT model produces spatial oscillations near singular points in the pressure and vorticity flow fields. We use LBM-MRT model to obtain pressure and vorticity fields for high Reynolds numbers that are free from spurious oscillations. In each case our computed LBM solutions agree very well, both qualitatively and quantitatively, with established results. Also, using LBM-SRT method on a 375×375 lattice size for Re = 3200 we capture a quaternary corner vortex, hitherto unreported through LBM. Then for Re = 100-1500 the LBM simulation is extended to deep cavity flows using LBM-SRT model and the results are validated with conventional-method results. Accurate implementation of the LBM algorithm in the present codes is thus ascertained. Then, the LBM-SRT computation is carried out for the flow past a circular cylinder at low Reynolds numbers when the flow is steady and periodic. All the results computed with LBM compares well with existing results.

After having thus gained confidence in the present code, we carry out LBM computations for a hitherto unexplored problem, namely, two-sided lid-driven- square-cavity flow. In this problem, top and bottom walls move in the same (parallel motion) or opposite (antiparallel motion) direction with a uniform velocity. It is found that for parallel motion of the walls, there appears a pair of counter-rotating secondary vortices of equal size near the centre of a wall. Because of symmetry, this pair of counter-rotating vortices has similar shapes and their detailed study as to how they grow with increasing Reynolds number has been carried out in this chapter through both the LBM-SRT and LBM-MRT models. The results for the antiparallel motion of the walls are also presented in some detail. As the flow configuration is new and the Lattice Boltzmann method is a relatively novel technique of flow computation, there is some scope for speculation as to the

accuracy of the present LBM computations. Therefore, to create a basis for substantiating the results another FDM code using the stream function-vorticity form of the Navier-Stokes equations based on central differencing and ADI time integration is developed. This code has second order spatio-temporal accuracy and it is used to produce steady results in a time-marching fashion. The close agreement of the LBM results with FDM results produced on sufficiently fine grids lends physical legitimacy to the computations.

In LBM the nonlinearity of the Navier-Stokes equations is hidden in the quadratic velocity terms of the equilibrium distribution function. Therefore, multiple solutions appear to be a possible to be captured through LBM. However, so far no investigation is seen that uses LBM to capture multiple solutions. Conventional numerical solutions show that the symmetric solutions exist for all Reynolds numbers whereas multiplicity of states of one symmetric and two asymmetric solutions for two-sided and four-sided square-cavity flows are identified above a critical Reynolds number. We demonstrate that Lattice Boltzmann method also has the ability to capture multiple steady solutions at post-critical Reynolds numbers for both the two-sided non-facing and four-sided square cavity flows. The computation for multiple-steady flows is also carried out for the two-sided parallel-wall-motion rectangular cavity flows. In this case we find up to five different steady-flow states amply demonstrating the ability of the LBM to capture multiple-steady solutions.

Owing to the boundary layer effect of the side walls, in cubical cavities, the 3D results at mid-plane will deviate from the 2D results. Three-dimensional Lattice Boltzmann models including the fifteen-velocity model (*D3Q15*), the nineteen-velocity model (*D3Q19*), the twenty seven-velocity model (*D3Q27*) are used to compute the flow in a cubical cavity and the 3D mid-span results are compared with 2D LBM results using the nine-velocity

model (*D2Q9*) to study the effect of three-dimensionality. Next, the LBM simulation is extended to three-dimensional prism cavity flow carried out at Re = 100 to 1000. Then we compute 3D two-sided non-facing lid-driven cavity flow. Overall the computations have been carried out for low to high Reynolds numbers and they are validated by comparison with established results wherever possible.

One chapter of this thesis work is concerned with the application of LBM to two-dimensional and three-dimensional incompressible thermal flows with heat transfer. Computations are carried out for laminar flows in a differentially heated square cavity ($Ra = 10^3$ to 10^6) and a cubical cavity ($Ra = 10^3$ to 10^5). The boundary conditions used are stable and of good accuracy. To lend credibility to the thermal LBM model, square-cavity results are further compared with those obtained from a finite- difference-based code developed for this purpose. The Internal Energy Density Distribution Function (IEDDF) approach with two 3D particle velocity models, namely, the *D3Q15* and the *D3Q19* models, and a 2D model, namely, the *D2Q9* model are used to compute the fluid flow and heat transfer in the cubic and square cavities. Very close resemblance of the streamlines, isotherm patterns and vorticity contours of the present LBM and FDM results lends credibility to the computations. Comparisons are also carried out with other established results.

Towards the end of this dissertation a chapter is devoted to the application of the Lattice Boltzmann Method (LBM) compute gaseous flows in micro-geometries. LBM is used to simulate the pressure-driven micro-channel flow, micro lid-driven-cavity flow with various aspect ratios and micro-couette flows. Simulation of microflows not only requires an appropriate method, it also requires suitable boundary conditions to provide a well-

posed problem and unique solution. The Knudsen number is used to measure the degree of rarefaction in the microflows. In this chapter LBM and three slip boundary conditions, namely, diffuse scattering, specular reflection and a combination of bounce-back and specular reflection boundary conditions are used to predict the flow fields. The results are substantiated through comparison with existing results and it is felt that the present methodology is good enough to be employed in analyzing the flows in micro-systems.

1.6. Organization of the Thesis

The present dissertation is arranged in nine chapters. Chapter 2 gives an overview of the Lattice Boltzmann Method with boundary conditions. In Chapter 3, Part I, computations are carried out for the single lid-driven cavity flows using LBM-SRT and LBM-MRT methods. In Part II of the same chapter LBM computation is carried out for the flow past a circular cylinder confined in a channel. Various two-sided facing-lid-driven cavity flows (parallel and antiparallel wall motion) are studied in Chapter 4. Chapter 5 is focuses on LBM computation of two- and four-sided lid-driven square cavity flows and two-sided rectangular cavity flows to capture multiple steady solutions. In Chapter 6 we carry out LBM computation of flows in three-dimensional cavities with various types of wall motion. Chapter 7 focuses on the application of LBM to two- and three-dimensional incompressible thermal flows. Chapter 8 is concerned with application of LBM to compute gaseous flows in micro-geometries. Finally, concluding remarks made in Chapter 9. To clarify certain points and to make the dissertation self-contained to a certain extent, a number of appendices are added at the end.

Chapter 2

Lattice Boltzmann Method

2.1. General Background

In the past few decades, the relation between the Boltzmann Equation and Navier-Stokes equation for the study of fluid dynamics has been an active and popular topic of research [1, 77]. The Boltzmann equation relates the time evolution and spatial variation of a collection of molecules to a collision operator that describes the interaction of the molecules. It is known that, the Boltzmann equation provides a more efficient representation of gaseous flows for a whole range of flow regimes than the Navier-Stokes equation. But researchers generally prefer to use the conventional numerical methods (finite difference method, finite volume method, finite element method..etc.) based on the discretization of partial differential equations (Navier-Stokes equations) in continuum regime than solving the Boltzmann equations. This is because solution of the Boltzmann equation is a non-trivial task owing to the complexity of the collision term.

The development of Lattice Gas Automata (LGA) and Lattice Boltzmann Method (LBM) are the promising methods that use different kind of nonconventional techniques for applications in CFD. The LGA, however, suffered from drawbacks such as the lack of Galilean invariance, statistical noise and nonphysical solution (e.g., pressure depending on velocity). LBM overcame the difficulties of LGA using the simple model of linearized

collision operator based on the Bhatnagar-Gross-Krook (LBGK) collision model [20]. The justification for the LBM approach is the fact that the collective behaviour of many microscopic particles is behind the macroscopic dynamics of a fluid and this dynamics is not particularly dependent on the details of the microscopic phenomena exhibited by the individual molecules. It is the solution of a minimal Boltzmann kinetic equation, rather than the discretization of the Navier-Stokes equations of continuum mechanics. It provides stable and efficient numerical computations for the macroscopic behaviour of fluids, although describing the fluid in a microscopic way.

The lattice model in LBM notation follows a D_mQ_n reference, where m is the number of dimensions and n denotes the number of particle velocities. As an example popular one-dimensional (1-D) model is referred to as the one-dimensional two-velocity (D_1Q_2) model. Other 1-D models are the one-dimensional three-velocity (D_1Q_3) and one-dimensional five-velocity (D_1Q_5) models. Two-dimensional lattice models are two-dimensional seven-velocity (D_2Q_7) and two-dimensional nine-velocity (D_2Q_9) models. The three-dimensional counterparts are the three-dimensional fifteen-velocity (D_3Q_{15}), three-dimensional nineteen-velocity (D_3Q_{19}) and three-dimensional twenty seven-velocity (D_3Q_{27}) models. In all the above models, the particles move according to a finite, discrete set of velocities. It is known that, through a Chapman-Enskog analysis, one can recover the governing continuity and momentum equations in the low Mach number limit.

The kinetic nature of the LBM introduces three important aspects. First, the convection operator of the LBM in phase space (or velocity space) is linear. Therefore the computational efforts are greatly reduced compared with conventional methods. Second, the pressure of the LBM is calculated using an equation of state. In contrast, in the numerical simulation of the unsteady incompressible Navier-Stokes equations, the pressure satisfies a Poisson equation with velocity strains acting as sources. Conventional methods solving this Poisson equation for the pressure often encounters numerical difficulties requiring special treatment, such as iteration or relaxation methods. Third, the LBM utilizes a minimal set of velocities in phase space. In contrast, the phase space of the traditional Boltzmann equation with Maxwell equilibrium distribution is a complete functional space and the average process involves getting information from the whole velocity phase space. In LBM, one or two speeds and a few directions are used, and therefore, the transformation relating the microscopic distribution function and macroscopic quantities is extremely simple.

It is now observed that an increasing number of researchers simply use the LBM as an alternative to conventional numerical methods for the Navier-Stokes equation. As a computational tool, the lattice Boltzmann method differs from incompressible Navier-Stokes equations-based methods as follows [54]:

1. Navier-Stokes equations are second-order partial differential equations (PDEs); the discrete velocity model from which LBM is derived consists of a set of first-order PDEs (kinetic equations).
2. Navier-Stokes equations have nonlinear convection terms; the convection terms in LBM are linear.

3. Lattice Boltzmann Equation (LBE) is a discretized kinetic equation; Navier-Stokes equations can take integral or differential forms.
4. LBM depends on lattice structure; Navier-Stokes equations are in vector form that is independent on the coordinate and grids.
5. The Navier-Stokes solver usually employs iterative procedures to obtain a converged solution; the LBM is explicit in form and do not need iterative procedures.
6. Boundary conditions involving complicated geometries require careful treatments in both Navier-Stokes equations-based and LBM solvers. In LBM, the boundary condition is in the form of particle distribution functions.
7. Due to the kinetic nature of the Boltzmann equation, the physics associated with the molecular level interaction can be incorporated more easily in the LBE model.

Also it is known that there is no continuum assumption involved in the LBM; therefore, its prospect in simulating microflows is quite evident and the choice of using LBM for microflow simulation is a good one owing to the fact that it is based on the Boltzmann equation which is valid for the whole range of the Knudsen number (which is the ratio of the mean free path of molecules to the characteristic length).

The dimensionless Mach number is defined by

$$Ma = \frac{u_0}{c_s} \tag{2.1}$$

which must fulfill $Ma < 0.3$ to be within incompressible limit. Here, c_s is the speed of sound. The Reynolds number is defined as

$$Re = \frac{u_0 L}{\upsilon} \tag{2.2}$$

$L = N\delta x$ being the characteristic length, N the number of lattice nodes in the characteristic length, δx the lattice spacing and u_0 the reference velocity of the flow. The lattice spacing δx and lattice timing δt determine the lattice dimensions.

2.2. Boltzmann Equation

Historically the Lattice Boltzmann Method evolved from Lattice Gas Automata (LGA); an alternative interpretation of LBM is obtained by considering the Boltzmann equation directly. The Boltzmann equation, also known as the Boltzmann transport equation describes the statistical distribution of particles in a fluid. It is an equation for the time evolution of $f(\boldsymbol{r}, \boldsymbol{c}, t)$, the particle distribution function in the phase space. Phase space can be viewed as a space in which coordinates are given by the position and momentum vectors at the time. The distribution function $f(\boldsymbol{r}, \boldsymbol{c}, t)$ gives the probability of finding a particular molecule with a given position and momentum.

The classic continuum Boltzmann equation is an integro-differential equation for a single particle distribution function $f(\boldsymbol{r}, \boldsymbol{c}, t)$ and written as [77]

$$\frac{\partial f}{\partial t} + \boldsymbol{c}.\frac{\partial f}{\partial \boldsymbol{r}} + \boldsymbol{F}.\frac{\partial f}{\partial \boldsymbol{c}} = Q(f) \tag{2.3}$$

where $\boldsymbol{c}$ is the particle velocity, $\boldsymbol{F}$ is the body force and $Q(f)$ is the collision integral. For the two-particle collision one may write

$$Q(f(f_1, f_2)) = \int d\boldsymbol{c}_2 \int \sigma(\Omega)|c_1 - c_2|\left[f_1' f_2' - f_1 f_2\right] d\Omega \tag{2.4}$$

where $\sigma(\Omega)$ is the differential collision cross section for the two particle collision which transforms the velocities from $\{\mathbf{c}_1, \mathbf{c}_2\}$ (incoming) into $\{\boldsymbol{c_1'}, \boldsymbol{c_2'}\}$ (outgoing). One of the major problems when dealing with the Boltzmann equation is the complicated nature of the collision integral $Q(f)$. To facilitate numerical and analytical solutions of the

Boltzmann equation, this collision integral is replaced by a simpler expression proposed by Bhatnagar, Gross and Krook [20]. This widely used replacement is called the lattice Boltzmann with BGK approximation or single-relaxation-time model and is given by

$$Q_{BGK}(f) = -\frac{f - f^{eq}}{\tau} \tag{2.5}$$

where τ is a typical single-relaxation-time associated with collision relaxation to the local equilibrium. It may be noted that alternative formulations based on lattice Boltzmann with multi-relaxation-time [78] is also available (two-dimensional formulation is used in this thesis).

2.3. Lattice Boltzmann Single-Relaxation-Time (LBM-SRT) Model

The LBGK model with single-relaxation-time (LBM-SRT), which is a commonly used lattice Boltzmann method, is given by [27]

$$f_i(\mathbf{x}+\boldsymbol{c_i}\Delta t, t+\Delta t) - f_i(\mathbf{x},t) = -\frac{1}{\tau}\left(f_i(\mathbf{x},t) - f_i^{(0)}(\mathbf{x},t) \right) \tag{2.6}$$

where $f_i(\mathbf{x},t)$ and $f_i^{(0)}(\mathbf{x},t)$ are the particle and equilibrium distribution functions at $(\mathbf{x},t)$, $\boldsymbol{c_i}$ is the particle velocity along the i^{th} direction and τ is the single-relaxation-time parameter that controls the rate of approach to equilibrium. The above Equation 2.6 is updated in the following two steps:

Collision step: $$f_i^{\%}(\mathbf{x},t) = f_i(\mathbf{x},t) - \frac{1}{\tau}\left[f_i(\mathbf{x},t) - f_i^{eq}(\mathbf{x},t) \right] \tag{2.7}$$

Streaming step: $$f_i(\mathbf{x}+\boldsymbol{c_i}\Delta t, t+\Delta t) = f_i^{\%}(\mathbf{x},t) \tag{2.8}$$

where f_i and $f_i^{\%}$ denote the pre- and post-collision states of the distribution function, respectively. For simulating two-dimensional flows, the two-dimensional nine-velocity

model (*D2Q9*) with nine discrete velocities $\boldsymbol{c}_i$ ($i = 0,1..,8$) is commonly used. In a *D2Q9* square lattice each node has eight neighbours connected by eight links as shown in Figure 2.1. Particles residing on a node move to their nearest neighbours along these links in unit time step. The occupation of the rest particle is designated as f_0. The occupation of the particles moving along the *x*- and *y*-axes are designated as f_1, f_2, f_3 and f_4, while the occupation of diagonally moving particles are designated as f_5, f_6, f_7 and f_8.

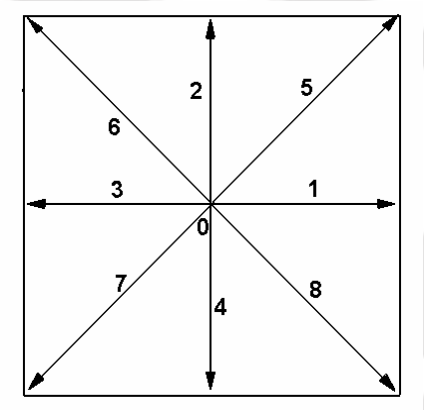

Figure 2.1: Two-Dimensional nine-velocity square lattice model.

The macroscopic quantities such as density ρ and momentum density $\rho\boldsymbol{u}$ are obtained as velocity moments of the distribution function f_i as follows:

$$\rho = \sum_{i=0}^{N} f_i, \tag{2.9}$$

$$\rho\boldsymbol{u} = \sum_{i=0}^{N} f_i \boldsymbol{c_i} \tag{2.10}$$

where $N = 8$. The density is determined from the particle distribution function. The density and the velocities satisfy the Navier-Stokes equations in the low-Mach number

limit. This can be demonstrated by using the Chapman-Enskog expansion. In the *D2Q9* square lattice, a suitable equilibrium distribution function that has been proposed is [27]

$$\begin{aligned} f_i^{(0)} &= \rho w_i\left[1-\frac{3}{2}\boldsymbol{u}^2\right], \ i=0 \\ f_i^{(0)} &= \rho w_i\left[1+3(\boldsymbol{c_i}.\boldsymbol{u}) + 4.5\ (\boldsymbol{c_i}.\boldsymbol{u})^2 - 1.5\ \boldsymbol{u}^2\right], \ i=1,2,3,4 \\ f_i^{(0)} &= \rho w_i\left[1+3(\boldsymbol{c_i}.\boldsymbol{u}) + 4.5\ (\boldsymbol{c_i}.\boldsymbol{u})^2 - 1.5\ \boldsymbol{u}^2\right], \ i=5,6,7,8 \end{aligned} \tag{2.11}$$

where the lattice weights are given by $w_0 = 4/9$, $w_1 = w_2 = w_3 = w_4 = 1/9$ and $w_5 = w_6 = w_7 = w_8 = 1/36$. The relaxation time that fixes the rate of approach to equilibrium is related to the viscosity by [27]

$$\tau = \frac{6\upsilon+1}{2} \tag{2.12}$$

where υ is the kinematic viscosity measured in lattice units. It is seen that $\tau = 0.5$ is the critical value for ensuring a non-negative kinematic viscosity. Numerical instability can occur for a τ value of close to this critical one. This situation takes place at high Reynolds numbers. For simulating three-dimensional flows, the fifteen-velocity model (*D3Q15*, $i=0,1..,14$) the nineteen-velocity model (*D3Q19*, $i=0,1..,18$) and the twenty seven-velocity model (*D3Q27*, $i=0,1..,26$) are used. Figure 2.2 shows the *D3Q15, D3Q19 and D3Q27* cubic lattice models. All the above 3D LBM models incorporate a rest particle in the discrete velocity set $\{\boldsymbol{c}_i\}$, because the LBM models with a rest particle have better computational stability and reliability. We now give the discrete particle velocities and weights associated with the commonly used models.

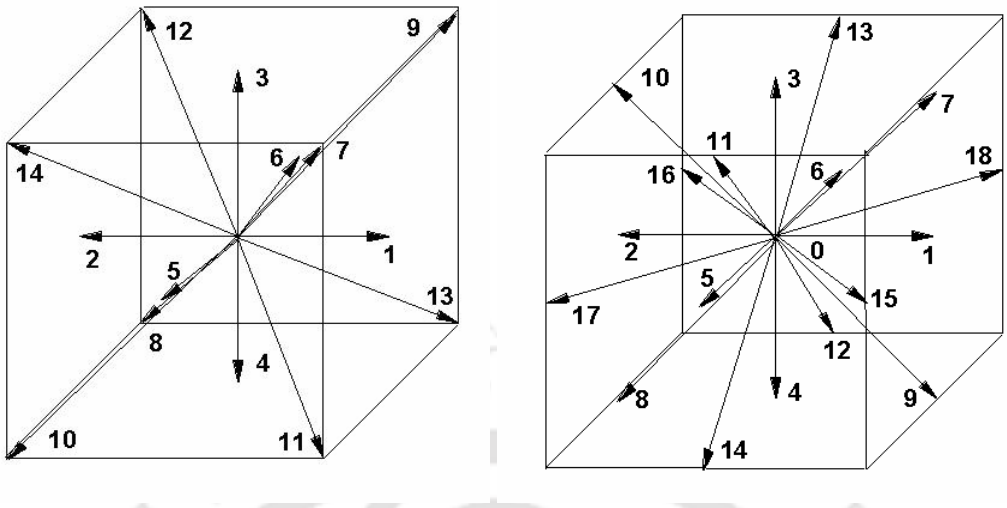

(a) (b)

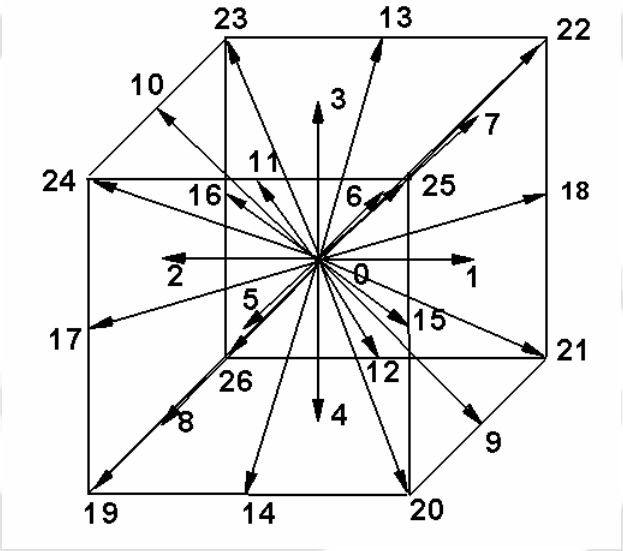

(c)

Figure 2.2: Three-Dimensional lattice models: (a) *D3Q15* (b) *D3Q19* and (c) *D3Q27*.

For the *D2Q9* model the discrete velocity set $\{\boldsymbol{c}_i\}$ is written as [27]

$$\mathbf{c}_{\boldsymbol{i}} = \begin{cases} 0, & i = 0 \\ c(\cos((i-1)\pi/4), \sin((i-1)\pi/4), & i = 1, 2, 3, 4, \\ \sqrt{2}c(\cos((i-1)\pi/4), \sin((i-1)\pi/4), & i = 5, 6, 7, 8. \end{cases} \tag{2.13}$$

and the lattice weights are

$$w_i = \begin{cases} 4/9, & i = 0; \\ 1/9, & i = 1,2,3,4; \\ 1/36, & i = 5,6,7,8; \end{cases} \tag{2.14}$$

For the *D3Q15* model the discrete velocity set $\{\boldsymbol{c}_i\}$ can be expressed as [55]

$$\boldsymbol{c_i} = \begin{cases} (0,0,0), & i = 0; \\ c(\pm 1,0,0), c(0,\pm 1,0), c(0,0,\pm 1), & i = 1,2,\ldots,6; \\ c(\pm 1,\pm 1,\pm 1), & i = 7,8,\ldots..,14; \end{cases} \tag{2.15}$$

and the lattice weights are

$$w_i = \begin{cases} 2/9, & i = 0; \\ 1/9, & i = 1,2,\ldots,6; \\ 1/72, & i = 7,8,\ldots..,14; \end{cases} \tag{2.16}$$

For the *D3Q19* model the discrete velocity set $\{\boldsymbol{c}_i\}$ can be expressed as [55]

$$\boldsymbol{c_i} = \begin{cases} (0,0,0), & i = 0; \\ c(\pm 1,0,0), c(0,\pm 1,0), c(0,0,\pm 1), & i = 1,2,\ldots,6; \\ c(\pm 1,\pm 1,0), c(\pm 1,0,\pm 1), c(0,\pm 1,\pm 1), & i = 7,8,\ldots..,18; \end{cases} \tag{2.17}$$

and the lattice weights are

$$w_i = \begin{cases} 2/9, & i = 0; \\ 1/18, & i = 1,2,\ldots,6; \\ 1/36, & i = 7,8,\ldots..,18; \end{cases} \tag{2.18}$$

For the *D3Q27* model the discrete velocity set $\{\boldsymbol{c}_i\}$ can be expressed as [55]

$$\boldsymbol{c}_i = \begin{cases} (0,0,0), & i=0; \\ c(\pm 1,0,0), c(0,\pm 1,0), c(0,0,\pm 1), & i=1,2,...,6; \\ c(\pm 1,\pm 1,0), c(\pm 1,0,\pm 1), c(0,\pm 1,\pm 1), & i=7,8,.....,18; \\ c(\pm 1,\pm 1,\pm 1), & i=19,20,...,26; \end{cases} \tag{2.19}$$

and the lattice weights are

$$w_i = \begin{cases} 8/27, & i=0; \\ 2/27, & i=1,2,...,6; \\ 1/54, & i=7,8,.....,18; \\ 1/216, & i=19,20,...,26; \end{cases} \tag{2.20}$$

2.4. Lattice Boltzmann Multi-Relaxation-Time (LBM-MRT) Model

Lallemand and Luo [78] showed the robustness of the Lattice Boltzmann Method with multi-relaxation-time (LBM-MRT) model and presented high accuracy results and numerical stability of high Reynolds numbers. They have performed the detailed theoretical analysis on the dispersion, dissipation and stability characteristics of a generalized Lattice Boltzmann Equation model proposed by d'Humieres [79]. The two-dimensional Multi-relaxation-time collision model [78, 79] is also used in the present work (Chapter 3 and Chapter 4). For simulating 2D flows a *D2Q9* model is used and the discrete particle velocities are represented as $\left\{\boldsymbol{c}_{\boldsymbol{i}} \middle| i = 0, 1,.....,N\right\}$ and the particle distribution function is represented as $\left\{f_i(\mathbf{x},t) \middle| \ i = 0, 1,...., N\right\}$. The discretized particle distribution function in a vector space $\underline{R}$ can be written as

$$\left| f_i(\mathbf{x}_i, t_n) \right\rangle = \left\{ f_0(\mathbf{x}_i, t_n),\, f_1(\mathbf{x}_i, t_n), \ldots\ldots, f_N(\mathbf{x}_i, t_n) \right\}^T \tag{2.21}$$

The lattice Boltzmann multi-relaxation-time (LBM-MRT) model evolution equation can be written in discretized form [80]

$$\left| f_i(\mathbf{x}_i + \boldsymbol{c}_i \Delta t, t_n + \Delta t) \right\rangle - \left| f_i(\mathbf{x}_i, t_n) \right\rangle = -M^{-1} \underline{S} \left(\left| m_i(\mathbf{x}_i, t_n) \right\rangle - \left| m_i^{eq}(\mathbf{x}_i, t_n) \right\rangle \right) \tag{2.22}$$

where $\underline{S}$ is the diagonal matrix, M for the *D2Q9* model is a 9×9 transformation matrix that linearly transforms the velocity distribution functions f_i to the macroscopic moments. The transformation matrix M can be written as

$$M = \begin{pmatrix} 1 & 1 & 1 & 1 & 1 & 1 & 1 & 1 & 1 \\ -4 & -1 & 2 & -1 & 2 & -1 & 2 & -1 & 2 \\ 4 & -2 & 1 & -2 & 1 & -2 & 1 & -2 & 1 \\ 0 & 1 & 1 & 0 & -1 & -1 & -1 & 0 & 1 \\ 0 & -2 & 1 & 0 & -1 & 2 & -1 & 0 & 1 \\ 0 & 0 & 1 & 1 & 1 & 0 & -1 & -1 & -1 \\ 0 & 0 & 1 & -2 & 1 & 0 & -1 & 2 & -1 \\ 0 & 1 & 0 & -1 & 0 & 1 & 0 & -1 & 0 \\ 0 & 0 & 1 & 0 & -1 & 0 & 1 & 0 & -1 \end{pmatrix} \tag{2.23}$$

The moments for the D2Q9 model are $\left| m_i \right\rangle = (\rho, e, \varepsilon, j_x, q_x, j_y, q_y, p_{xx}, p_{xy})^T$. Here ρ is the fluid density, e is the energy, ε is related to square of energy, j_x and j_y are the momentum density (mass flux), q_x and q_y are the energy flux, p_{xx} and p_{xy} correspond to the diagonal and off-diagonal component of the viscous stress tensor. Diagonal matrix ($\underline{S}$) can be written as $\underline{S} = (0, s_2, s_3, 0, s_5, 0, s_7, s_8, s_9)$. It is known that for the LBM-

MRT model if we set $s_8 = s_9 = \frac{1}{\tau}$ then we can get same viscosity formula for the LBM-SRT model. In LBM-MRT model it is more flexible to chose the rest of the relaxation parameters s_2, s_3, s_5, s_7. In general these parameters can be chosen to be slightly larger than 1.0. Another important point, is to recover LBM-SRT model results we can set LBM-MRT parameters s_2, s_3, s_5, s_7, s_8, $s_9 = \frac{1}{\tau}$.

2.5. Boundary Conditions

Boundary Conditions and initial conditions are essential for any computational fluid dynamic methods. In LBM several boundary conditions have been proposed [34-41]. Implementation of boundary conditions in LBM is an important task owing to the fact that one has to translate given information from macroscopic variables to particle distribution function (f_i), since it is the only variable to be evaluated in LBM.

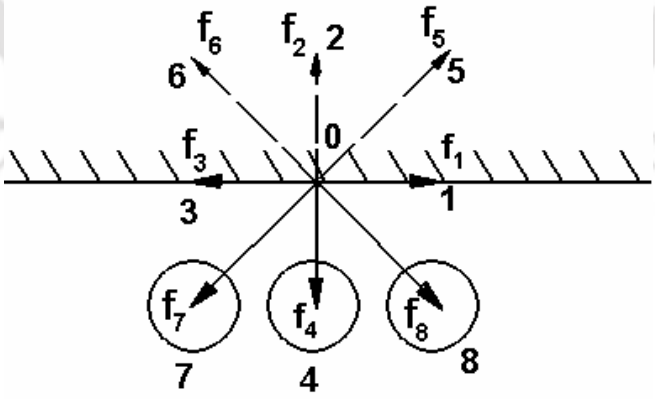

Figure 2.3: Solid-fluid surface interaction at the top wall.

2.5.1. Periodic Boundary Conditions

Periodic boundary conditions are the simplest instance of boundary conditions. To illustrate the idea, let us take the *D2Q9* model (Figure 2.3) as an example and consider only the direction along the *x*-axis. After streaming the unknown distribution functions for inlet are f_1, f_5, f_8 and also for outlet are f_3, f_7, f_6 .

Inlet (Left boundary)

$$\begin{aligned} f_1(1, y, t) &= f_2(L, y, t) \\ f_5(1, y, t) &= f_5(L, y, t) \\ f_8(1, y, t) &= f_8(L, y, t) \end{aligned} \tag{2.24}$$

Outlet (Right boundary)

$$\begin{aligned} f_3(L, y, t) &= f_3(1, y, t) \\ f_7(L, y, t) &= f_7(1, y, t) \\ f_6(L, y, t) &= f_6(1, y, t) \end{aligned} \tag{2.25}$$

2.5.2. Bounce-back Boundary Conditions

The so-called 'no-slip' boundary condition physically means that there is no flow motion at the boundaries. An implementation of this boundary condition is the so-called bounce-back scheme of the distribution function. The bounce-back boundary condition means that when a particle reaches a wall node, the particle will scatter back to the fluid nodes along its incoming direction. For the *D2Q9* model (Figure 2.3) and considering the bottom wall, after streaming unknown distribution functions f_2 , f_5, f_6 are given by

$$\begin{aligned} f_5(x, y, t) &= f_7(x, y, t) \\ f_2(x, y, t) &= f_4(x, y, t) \\ f_6(x, y, t) &= f_8(x, y, t) \end{aligned} \tag{2.26}$$

This complete reflection guarantees that both tangential and normal components of the wall fluid speed vanish identically.

2.5.2.1. Improved Bounce-Back Boundary Condition

To ensure the no-slip boundary condition ($\boldsymbol{U} = 0$) on the wall, Yu *et al.* [41] suggested a improved bounce-back boundary condition using a linear interpolation formula

$$f_{\bar{i}}(\mathbf{x}_w) = f_{i}(\mathbf{x}_w) + \frac{\Delta}{1+\Delta}\left(f_{\bar{i}}(\mathbf{x}_f + \boldsymbol{c}_i) - f_{\bar{i}}(\mathbf{x}_w)\right) \tag{2.27}$$

The above boundary condition is valid for both $\Delta < 0.5$ and $\Delta \geq 0.5$. For a moving wall they added additional momentum

$$f_{\bar{i}}(\mathbf{x}_w, t+\Delta t) = f_i(\mathbf{x}_\mathbf{w}, t+\Delta t) + 2w_i\rho\frac{3}{c^2}\boldsymbol{c}_i.\boldsymbol{u}_\mathbf{w} \tag{2.28}$$

where $f_{\bar{i}}$ indicates post-collision state.

2.5.3. Temperature Boundary Conditions

For the temperature distribution function, adiabatic walls are simulated by putting the temperature at the sites of the walls equal to the temperature at the nearest sites inside the flow domain. In this thesis, second-order finite difference approximation is used for temperature. As an example, for the top wall in a square cavity *D2Q9* model

$$g_{i,NY} = \frac{4}{3}\,g_{i,NY-1} - \frac{1}{3}\,g_{i,NY-2} \tag{2.29}$$

where $g_{i,NY}$ is the temperature on the wall; $g_{i,NY-1}$ and $g_{i,NY-2}$ are the temperatures inside the flow domain near the wall.

2.5.4. Slip Boundary Conditions

Case I: Specular Reflection Boundary condition (SBC)

The specular reflection means the particle will reflect in the specular direction like a ray of light. For the *D2Q9* model (Figure 2.3) and considering the bottom wall, after streaming the unknown distribution functions f_2, f_5, f_6 are given by

$$\begin{aligned} f_5(x, y, t) &= f_8(x, y, t) \\ f_2(x, y, t) &= f_4(x, y, t) \\ f_6(x, y, t) &= f_7(x, y, t) \end{aligned} \tag{2.30}$$

2.5.5. Partial-Slip Boundary Conditions

Case I: Bounceback and Specular Boundary condition (BSBC)

For gas flow in microgeometries, neither pure no-slip (bounce-back in LBM) nor pure free-slip (specular reflection in LBM) boundary condition can accurately capture the real flow phenomena. For such geometries, combination of bounce-back and specular boundary condition using the tangential momentum accommodation coefficient (TMAC) σ is used to simulate the partial-slip boundary condition on the walls. For gaseous flow in micro-devices the TMAC can be expressed as

$$\sigma = \frac{M_i - M_r}{M_i - M_w} \tag{2.34}$$

where M is the tangential momentum of the molecules and the subscripts *i, r, w* refer to the incident, reflected and wall molecules respectively. With reference to Figure 2.3 the boundary conditions at the top wall using TMAC are as follows:

$$f_7 = \sigma \times f_5 + (1-\sigma) \times f_6$$
$$f_4 = f_2 \qquad (2.35)$$
$$f_8 = \sigma \times f_6 + (1-\sigma) \times f_5$$

The value of σ lies between 0 and 1. Physically, σ = 0 represents the case in which the tangential momentum of all the incident molecules equals to the same of the reflected molecules (specular reflection). As a result, the gas molecules do not exchange any net tangential momentum with the wall on collision. Then, σ = 1 denotes the case in which the incipient gas molecules the same tangential momentum as that of the wall (diffuse reflection).

Case II: Diffuse Scattering Boundary Condition (DSBC)

DSBC is derived from the gas surface interaction law of the kinetic theory. The main theme of the DSBC is that the particles in the LBM arriving at the wall lose their information and are redistributed with respect to the mass-balance and normal-flux conditions. The DSBC of the LBM is as follows

$$\left|\left(\boldsymbol{e}_i - \boldsymbol{u}_w\right).\boldsymbol{n}\right| f_i = \sum_{\left(\boldsymbol{e}_{i'} - \boldsymbol{u}_w\right).\boldsymbol{n} < 0} \left|\left(\boldsymbol{e}_{i'} - \boldsymbol{u}_w\right).\boldsymbol{n}\right| \Re_f \left(\boldsymbol{e}_{i'} \rightarrow \boldsymbol{e}_i\right) f_{i'} \qquad (2.31)$$

where $\boldsymbol{e}_i$ and $\boldsymbol{e}_{i'}$ are the molecular velocities of the incident and reflected particles, respectively, $\boldsymbol{n}$ is the inward unit normal vector of the wall and w indicates the wall boundary. The scattering kernel, which is given by

$$\Re_f \left(\boldsymbol{e}_{i'} \rightarrow \boldsymbol{e}_i\right) = \frac{A_N}{\rho_w}\left(\left(\boldsymbol{e}_i - \boldsymbol{u}_w\right).\boldsymbol{n}\right) f_i^{eq}\Big|_{\boldsymbol{u}=\boldsymbol{u}_w} \qquad (2.32)$$

A_N is a normalization coefficient and can be obtained by satisfying zero normal flux conditions on the walls. This coefficient is also dependent on the velocity model used in the LBM. For the *D2Q9* model, A_N is 6.

To illustrate the DSBC choose a straight solid wall with velocity u_w. Figure 2.3 shows the solid arrow lines (i = 1, 3, 7, 4, 8) represent the particles streaming from the flow domain with the known distribution functions while the dashed arrow lines (i= 5, 2, 6) are the particles reflected from the wall boundary with the unknown distribution functions, which are to be determined by the DSBC and we have

$$\begin{aligned} f_5 &= \frac{A_N}{\rho_w} f_5^{eq}(\rho_w, \mathbf{u}_w)(f_7 + f_4 + f_8) \\ f_2 &= \frac{A_N}{\rho_w} f_2^{eq}(\rho_w, \mathbf{u}_w)(f_7 + f_4 + f_8) \\ f_6 &= \frac{A_N}{\rho_w} f_6^{eq}(\rho_w, \mathbf{u}_w)(f_7 + f_4 + f_8) \end{aligned} \tag{2.33}$$

2.6. Conclusion

In this chapter an overview of the Lattice Boltzmann Method is given. The formulation of Lattice Boltzmann model with single-relaxation-time and multi-relaxation-time is also presented. Boundary conditions which are suitable for LBM simulation is also discussed in some detail.

Chapter 3

Simulation of Some Two-Dimensional Incompressible Isothermal Flows

Part I: Single Lid-Driven Cavity Flows

3.1. Introduction

The classical lid-driven cavity flow problem consisting in an incompressible viscous flow in a cavity whose top wall moves with a uniform velocity in its own plane has long been used for evaluating numerical techniques for the solution of incompressible viscous flows. This problem is not only technically important but also of great scientific interest because it displays almost all fluid mechanical phenomena such as corner vortices, longitudinal vortices, Taylor-Gortler vortices that occur in the simplest of geometrical settings. It retains all the difficult flow physics and is characterized by a large primary eddy at the centre and secondary eddies located near the cavity corners. Because of its popularity, a plethora of experimental and numerical results are readily available for this problem in the literature [25-33, 51, 54, 74-76, 81-85].

This lid-driven cavity problem is also attractive because of its importance in industrial applications such as coating & drying technologies, melt spinning processes and many others [25]. It is also known that, the rectangular lid-driven cavity flow is an idealized

representation of several engineering situations, such as the flow over cutouts, designs and repeated slots on the walls of heat exchangers or on the surface of aircraft bodies [74].

A number of experimental and numerical studies have been conducted to investigate the flow field of a lid-driven cavity flow in the last several decades. The first major studies of the steady two-dimensional single lid-driven cavity flow are due to Burggraf [81] for the square cavity and Pan and Acrivos [82] for other geometrical aspect ratios. A review on computational and also experimental studies on two- and three-dimensional lid-driven cavity flow can be found in Shankar & Deshpande [25]. They have studied and analyzed corner eddies, nonuniqueness, transition and turbulence in the lid-driven cavity. Ghia *et al.* [83] have applied a multi-grid strategy and presented solutions for Reynolds numbers starting from Re = 100 to as high as Re = 10000. In most of the available literature, the cavity flow field calculation is based on solving the Navier-Stokes equation using a finite difference method (FDM), finite volume method (FVM) (or) finite element method (FEM) [25, 81-85]. In fact, as hundreds of papers attest, the lid-driven cavity flow problem is one of the standard benchmark problems used to test new computational schemes.

It is known that, the lattice Boltzmann method has recently become a useful and alternative approach for computational fluid dynamics. Many researchers carried out simulations of single lid-driven cavity flow by lattice Boltzmann method [26-33]. From the literature, it is found that most of the work deals with lattice Boltzmann with single-relaxation-time (LBM-SRT) and bounce-back boundary condition to study the cavity

flow field. There appears to be very little work done on rectangular cavities (deep and shallow cavity) by continuum based methods and LBM, although they are of theoretical interest [32, 33]. Therefore the main objective of the present chapter, part I, is to simulate the single lid-driven cavity flows using LBM.

3.2. Lattice Boltzmann Models with Boundary Conditions

In this chapter, part I, two lattice Boltzmann relaxation models, namely, computationally convenient LBM-SRT and LBM-MRT are used to study the well known square cavity problem (Figure 3.1) for a wide range of Reynolds numbers. A *D2Q9* square lattice incompressible LB model in two-dimensional space has been used since it is known to give more accurate results compared with *D2Q7* hexagonal lattice.

3.2.1. Boundary Conditions

In this chapter, part I, the second order accurate linear interpolation (improved bounce-back scheme, discussed in chapter 2, section 2.5.2) boundary condition given by Yu *et al.* [41] is enforced on all the stationary walls. However for the moving wall, the equilibrium boundary condition [27] is applied. At the lattice nodes on the moving walls, flow-variables are re-set to their pre-assumed values at the end of every streaming-step. The top lid-velocity of $\boldsymbol{U} = 0.01$ for $Re = 1$ and $\boldsymbol{U} = 0.1$ for $100 \leq Re \leq 7500$ is considered to maintain for which the present algorithm is designed.

3.2.2. LBM Simulation Procedure

The velocity components u and v are in the x- and y-directions. Initially the velocities at all lattice nodes, except at the top nodes, are set to zero. The x-velocity of the top plate is fixed at a value of $\boldsymbol{U}$ and the y-velocity is zero. Uniform fluid density $\rho = 1.0$ is imposed initially. The equilibrium distribution function $f_i^{eq}(\mathbf{x},t)$ is calculated and particle distribution function $f_i(\mathbf{x},t)$ is set to equal to $f_i^{eq}(\mathbf{x},t)$ for all node at t = 0. The distribution function can be found by a succession of propagation and collision processes. At the end of each process distribution function is set to the equilibrium state. The solution procedure of the LBM at each time step comprise of streaming and collision step, application of boundary conditions, calculation of particle distribution function followed by calculation of macroscopic variables. All of our computations are carried out on a Pentium 4-based PC with 512 MB RAM.

3.3. Finite Difference (FD) Stream Function-Vorticity Based Solver

As the LBM method is intended to be used to compute the flow in an unexplored geometry, need was felt to develop a finite difference (FD) code to attack the same problem thus providing a basis for comparison. The alternate direction implicit (ADI) method is used for time integration [97]. The FD code numerically solves the 2D Navier-Stokes equations in the stream function-vorticity form given by

$$\frac{\partial^2 \psi}{\partial x^2} + \frac{\partial^2 \psi}{\partial y^2} = -\omega \tag{3.1}$$

$$\frac{\partial \omega}{\partial \mathrm{t}} + u\frac{\partial \omega}{\partial x} + v\frac{\partial \omega}{\partial y} = \frac{1}{Re}\left(\frac{\partial^2 \omega}{\partial x^2} + \frac{\partial^2 \omega}{\partial y^2}\right). \tag{3.2}$$

It is intended to obtain the steady state solution from the discretized equations in a time marching fashion. It is well known that if an explicit technique that uses a forward time-stepping of first order accuracy and a central spatial discretization, the stability limit restricts the time-step to a very small value and the convergence to the steady state is painfully slow. This is especially true for larger Reynolds numbers at which it is extremely difficult to obtain the steady state solution when central space-differencing is used. To overcome this problem a first order accurate one sided space-differencing can be used in the convective term. This however, limits accuracy of the results and is no solution to the problem encountered. Maintaining a good spatial accuracy of second order by using central space-differencing and adopting an implicit time stepping through alternate direction implicit (ADI) technique that improves the stability behaviour of the computation remarkably, we circumvent this problem and obtain accurate solutions at higher Reynolds numbers as well. This code will provide a legitimate basis for comparison only after it has been validated and this exercise is presented in the next sub-section.

3.4. Code Validation

The geometry and boundary conditions of the single lid-driven cavity flow is shown in Figure 3.1. First, the developed LBM code is used to compute the flow on a 129×129 lattice arrangement shown in Figure 3.2. Figure 3.3 shows the steady-state u-velocity profile along a vertical line passing through the geometric centre of the square cavity at Re = 1000. Here the top lid moves from left to right and it is observed that the agreement between our LBM-SRT results and those of FDM is excellent. The same figure also

displays our LBM-MRT results which again are in excellent agreement with the two earlier results.

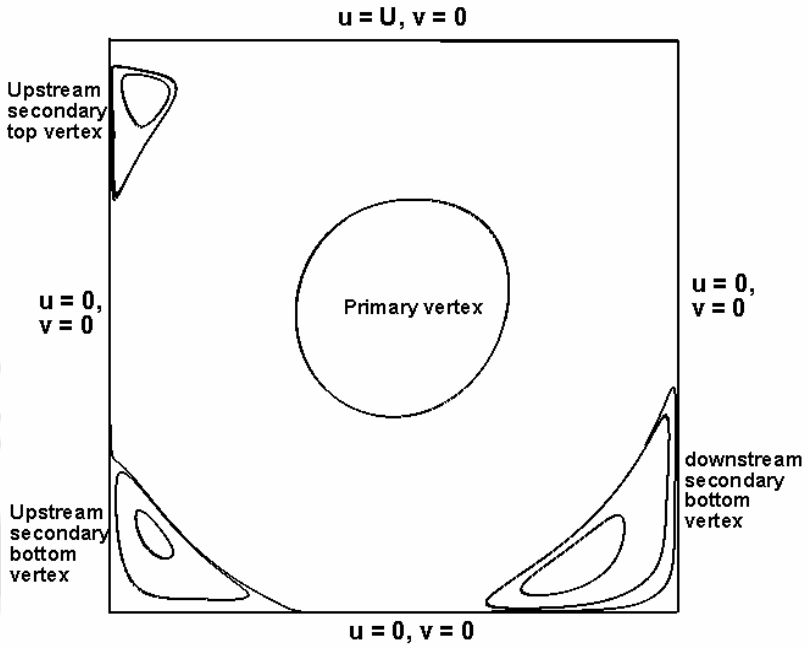

Figure 3.1: Geometry of a single lid-driven cavity flow with boundary conditions.

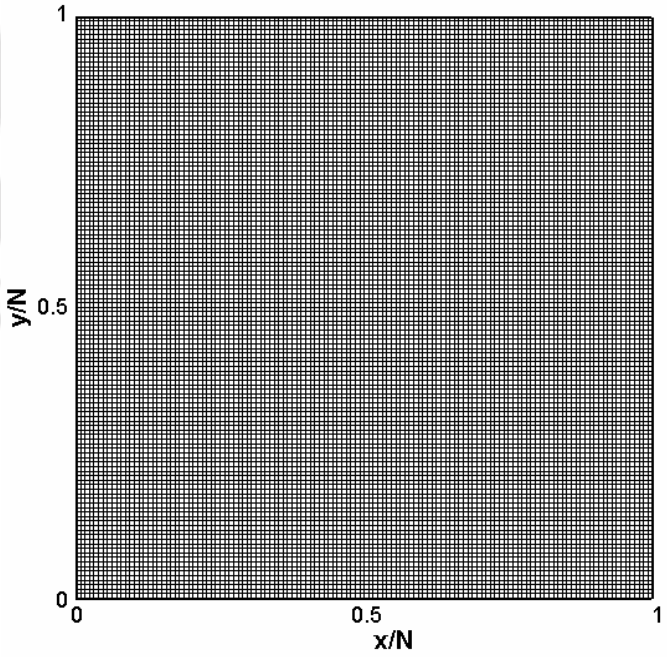

Figure 3.2: Schematic diagram of a 129×129 uniform lattice arrangement.

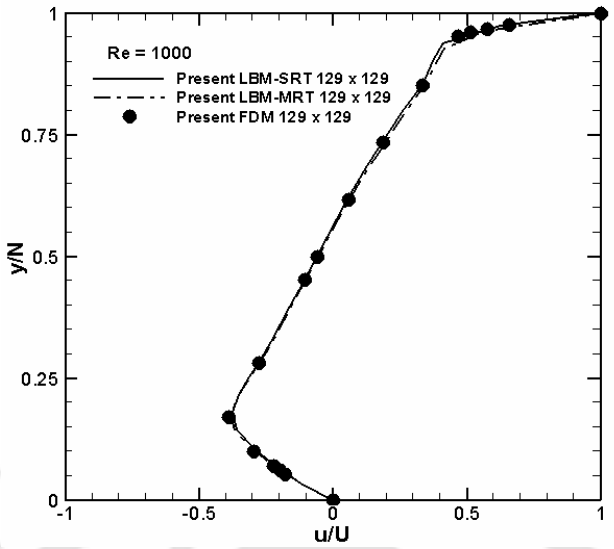

Figure 3.3: *u*-velocity profile along the vertical centreline for single lid-driven square cavity flow.

3.5. Numerical Experiments

In order to study the validity and effectiveness of the lattice Boltzmann method, it is applied to three problems. These are (i) square cavity flow (ii) deep cavity flow and (iii) shallow cavity flow. In this chapter, the aspect ratio (K) of the cavity is defined as a formula $K = D/W$, where D and W are the depth and width of the cavity respectively.

3.5.1. Test Problem 1: Square Cavity Flow ($K = 1$)

The considered problem consists of a two-dimensional square cavity whose top plate moves from left to right with a uniform velocity, while the other three walls are fixed. In this problem, the moving wall generates vorticity which diffuses inside and this diffusion is the driving mechanism of the flow. The streamline patterns for the square cavity flow

with Reynolds number increasing from Re = 1 to 7500 using LBM-SRT model on a 201×201 lattice arrangement are shown in Figures 3.4 and 3.5. Our results agree well with existing results [27, 30, 31, 83-85]. As the Reynolds number increases, the following observations are made. For Re = 1, flow is symmetric about the vertical centreline. For $Re \geq 100$ the flow structure inside the cavity is characterized by a large primary vortex filling almost the whole cavity. With the increase of Reynolds number from 100, the primary vortex centre shifts from the top right corner towards the geometric centre of the cavity, which virtually becomes invariant for $Re \geq 5000$ (Figure 3.5). With Reynolds number there is an expansion of the recirculation zone for the secondary vortices with a tendency of their centres to shift towards the geometric centre. The appearance of the top-left secondary vortex can be seen for Re = 2000 and more.

As expected, better scale resolution is obtained by increasing the number of lattices. The bottom right corner vortices are resolved up to the tertiary level for Re = 3200 on a 201×201 lattice size. Figure 3.6 (magnified view) shows that use of an LBM-SRT model on a 375×375 lattice arrangement for Re = 3200 allows us to capture a quaternary corner vortex that has not probably been captured through LBM so far. In Figure 3.7 we present the horizontal velocities on the vertical centreline and the vertical velocities on the horizontal centreline of the square cavity for Reynolds numbers ranging from 100 to 7500 and compare our data with those of Ghia *et al.* [83]. In each case, our velocity profiles exhibit a close match with those given by Ghia *et al.* [83].

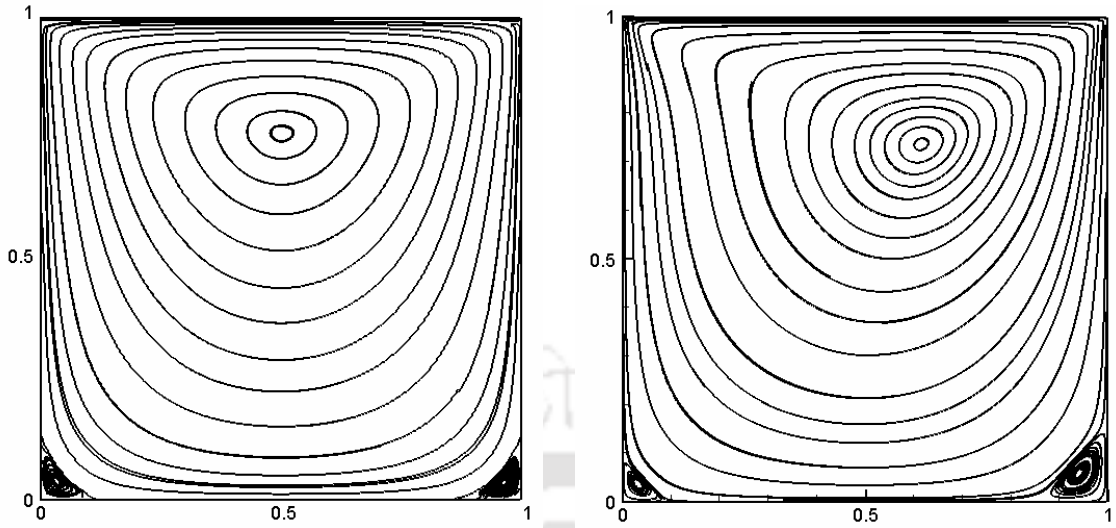

(a) Re = 1 (b) Re = 100

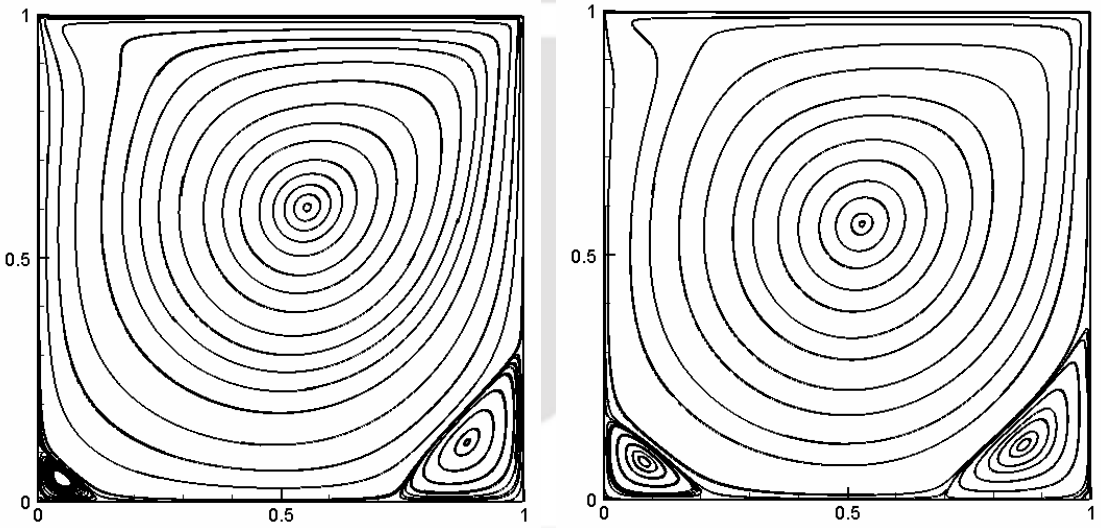

(c) Re = 400 (d) Re = 1000

Figure 3.4: Streamline pattern for the single lid-driven square cavity flow for (a) Re = 1, (b) Re = 100, (c) Re = 400 and (d) Re = 1000 by LBM–SRT method. Simulations were carried out on a 201×201 lattice arrangement.

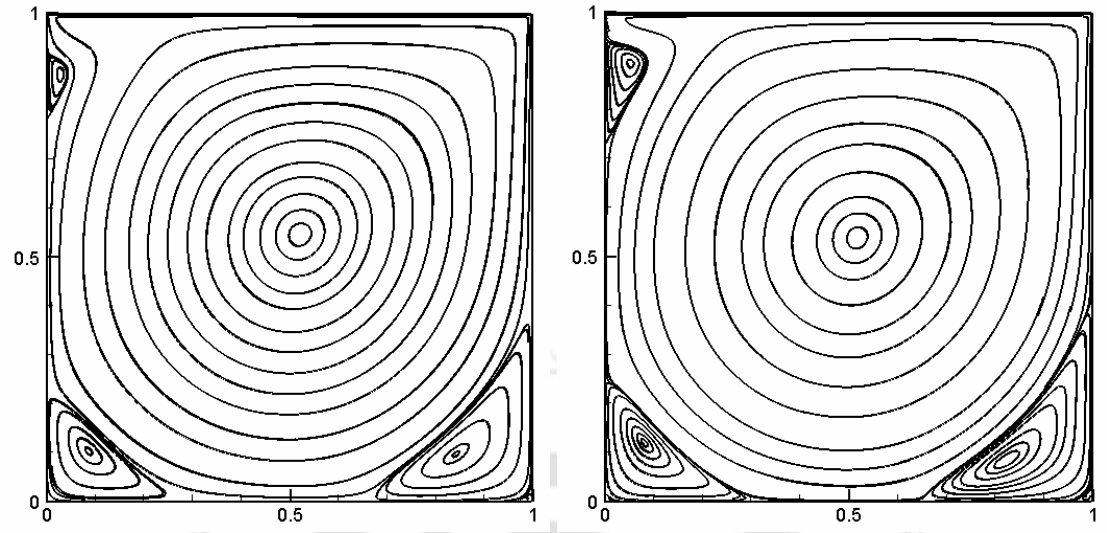

(a) *Re* = 2000 (b) *Re* = 3200

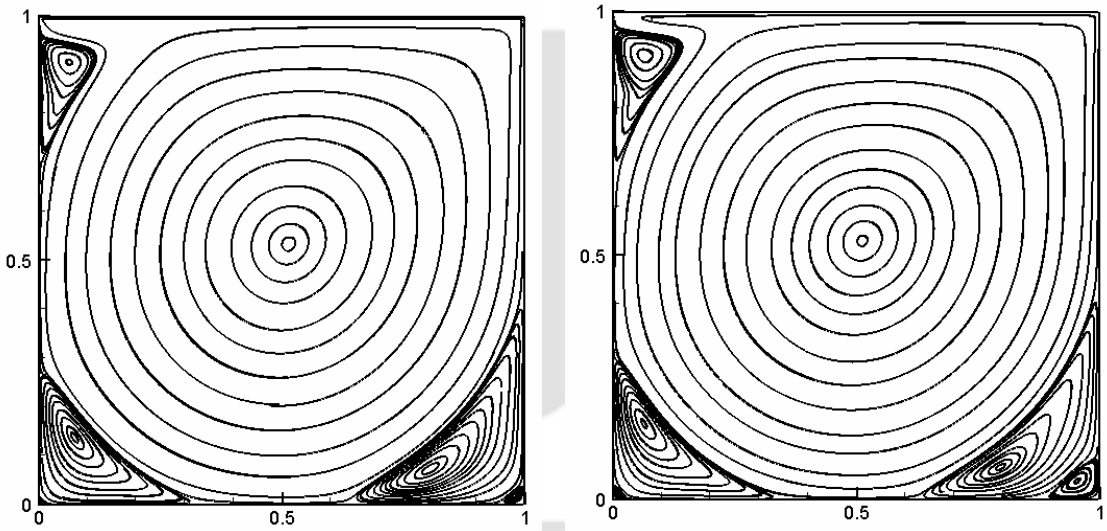

(c) *Re* = 5000 (d) *Re* = 7500

Figure 3.5: Streamline pattern for the single lid-driven square cavity flow for (a) *Re* = 2000, (b) *Re* = 3200, (c) *Re* = 5000 and (d) *Re* = 7500 by LBM–SRT method. Simulations were carried out on a 201×201 lattice arrangement.

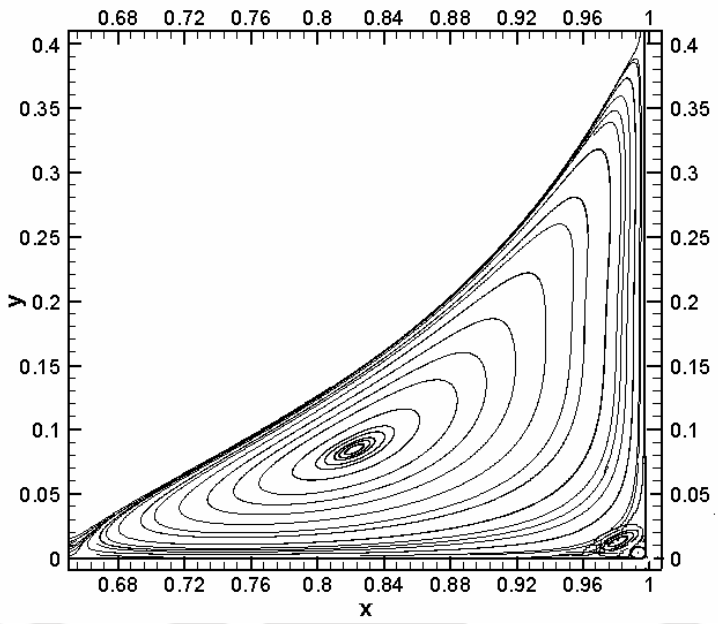

Figure 3.6: Flow pattern at the bottom right corner for the single lid-driven square cavity flow at *Re* = 3200 on a 375×375 lattice arrangement: secondary, tertiary and quaternary vortices.

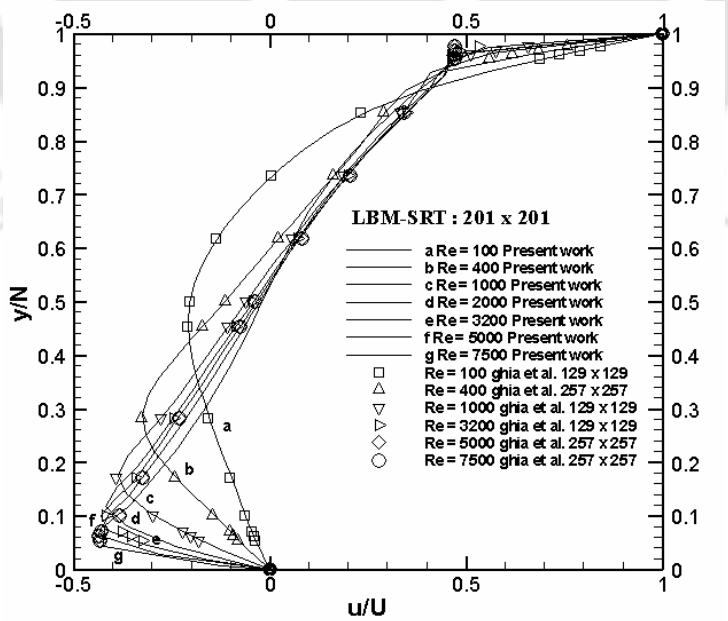

(a)

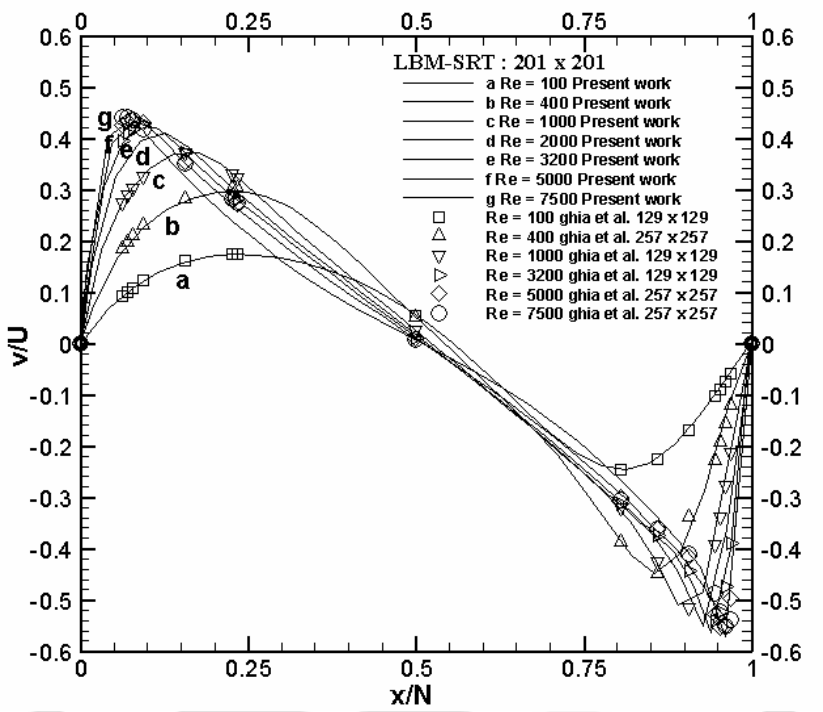

(b)

Figure 3.7: Comparison of LBM-SRT square cavity results: (a) *u*-velocity along the vertical centreline and (b) *v*-velocity along the horizontal centreline.

In Figures 3.8 and 3.9 we present the vorticity and pressure contours for the range of Reynolds numbers 1 to 1000 obtained by LBM-SRT method. Though results are not presented in this section, we have observed that the presented velocity profile results are agree well with other researchers [31, 32, 54, 80, 85].

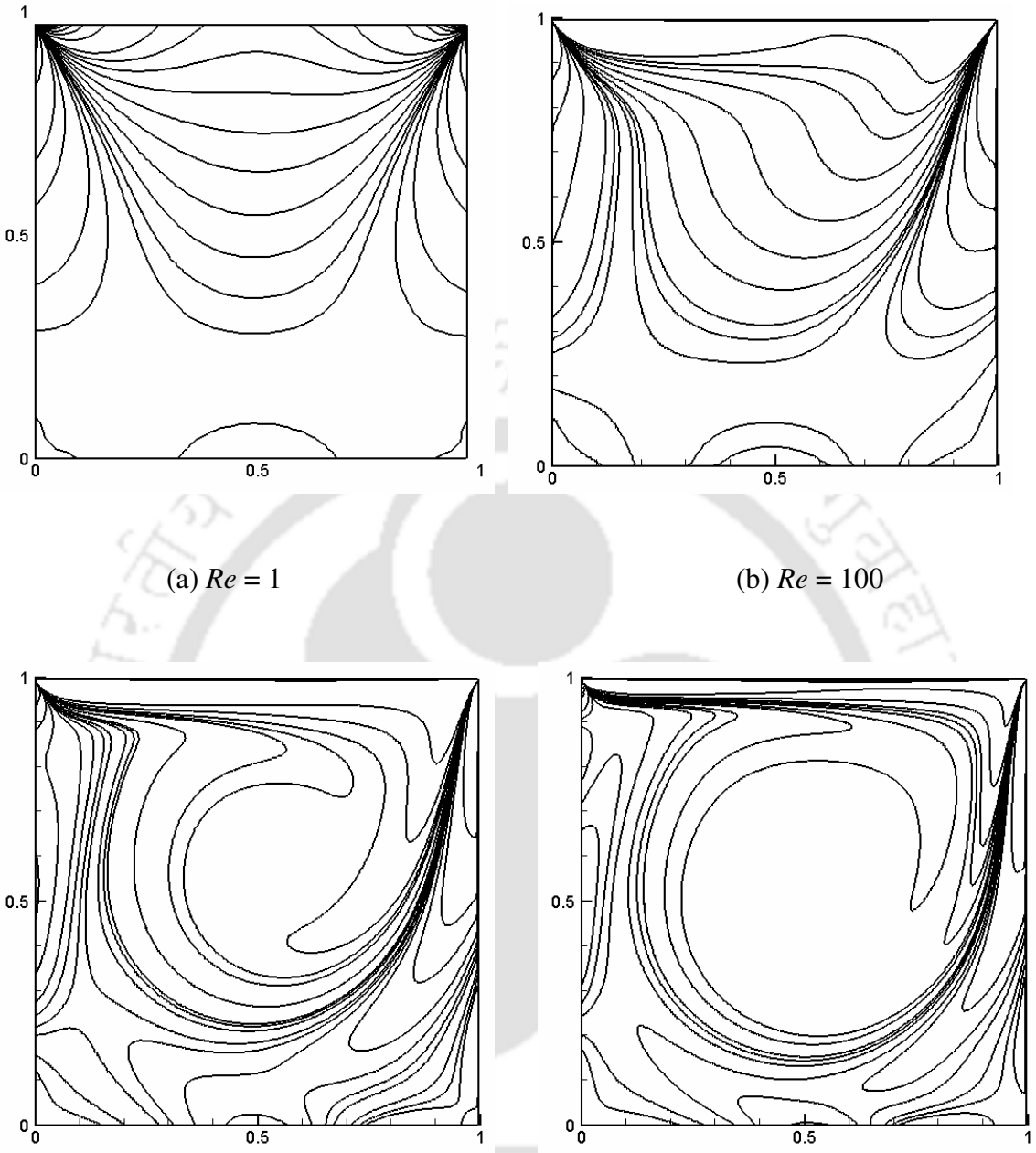

(a) $Re = 1$ (b) $Re = 100$

(c) $Re = 400$ (d) $Re = 1000$

Figure 3.8: Vorticity contours for the single lid-driven square cavity flow for (a) $Re = 1$, (b) $Re = 100$, (c) $Re = 400$ and (d) $Re = 1000$ by LBM – SRT model. Simulations are carried out on a 201×201 lattice arrangement.

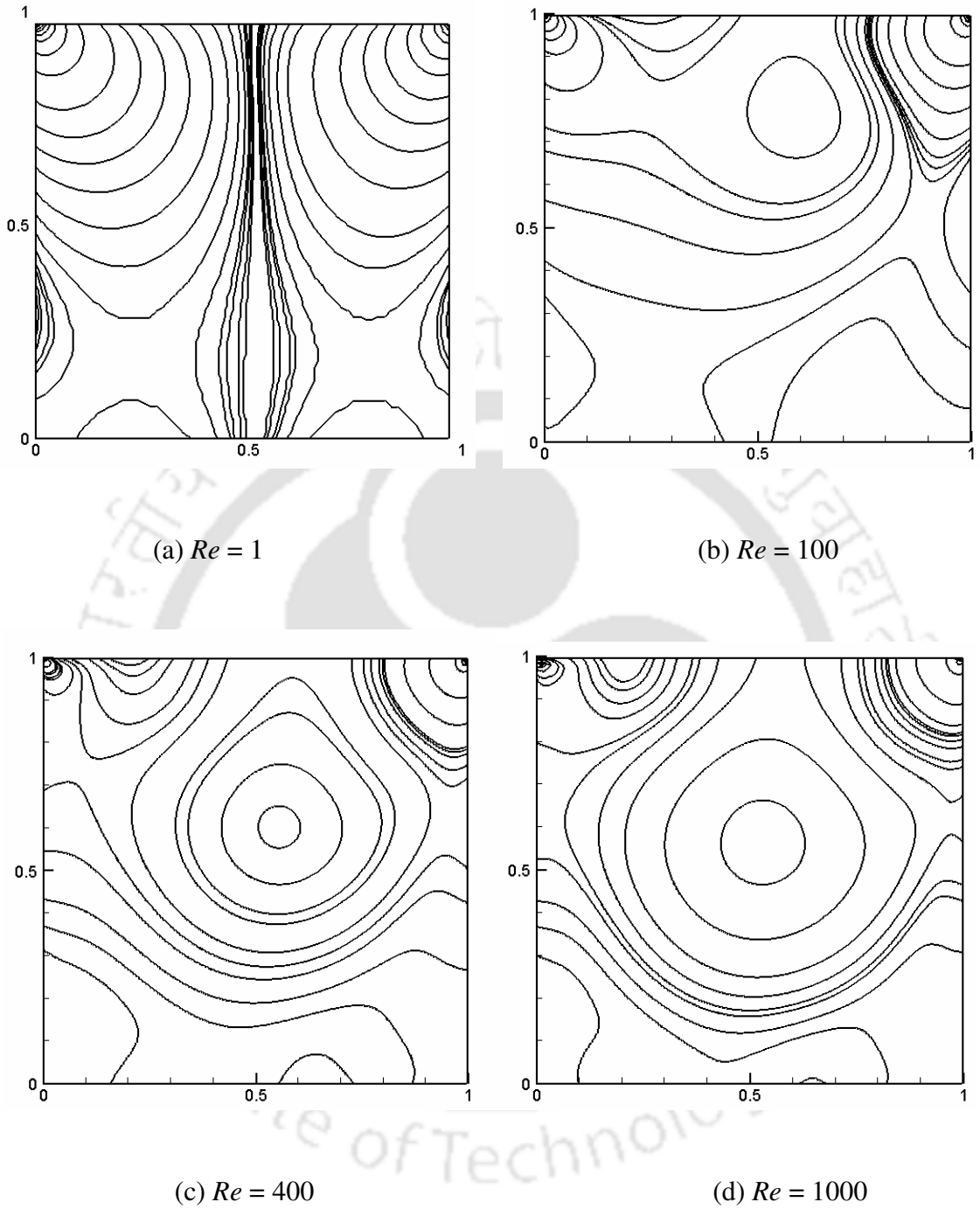

(a) $Re = 1$ (b) $Re = 100$

(c) $Re = 400$ (d) $Re = 1000$

Figure 3.9: Pressure contours for the single lid-driven cavity flow for (a) $Re = 1$, (b) $Re = 100$, (c) $Re = 400$ and (d) $Re = 1000$ by LBM – SRT model. Simulations are carried out on a 201×201 lattice arrangement.

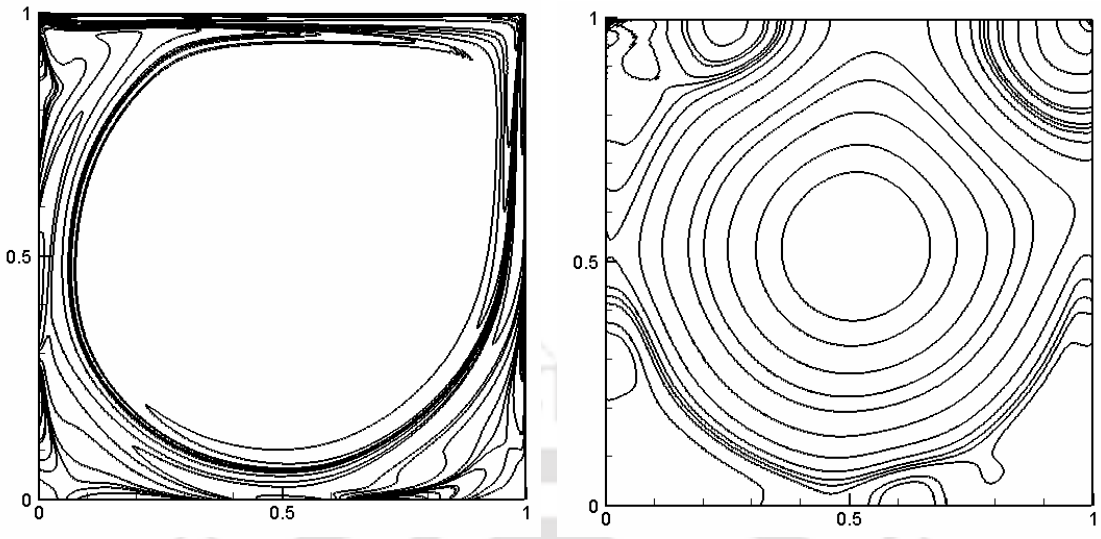

Figure 3.10: (a) Vorticity contour and (b) Pressure contour for the single lid-driven square cavity flow obtained by LBM–SRT method at Re = 7500 on a 201×201 lattice arrangement.

Figure 3.10 shows the vorticity and pressure contours for the square cavity flow obtained by LBM–SRT model at Re = 7500. Here we observe some wiggles or ripples in the vorticity and pressure contour plot near the upper corners, where singularities exist. Lallemand and Luo [78] concluded that LBM-MRT model can reduce the oscillations near singular points. Therefore, we also use the LBM-MRT model to compute the square cavity flow field to find its effects. Figure 3.11 shows the vorticity contour for higher Reynolds number ranging from 2000 to 7500. It is seen that several regions of high vorticity gradients indicated by the concentration of the vorticity contours appears within the cavity. The thinning of the wall boundary layers with increasing Reynolds number is evident from these plots. Comparing Figure 3.10 (a) and Figure 3.11 (d) it is seen that LBM-MRT technique captures the vorticity pattern better near the points of singularity at the top corners.

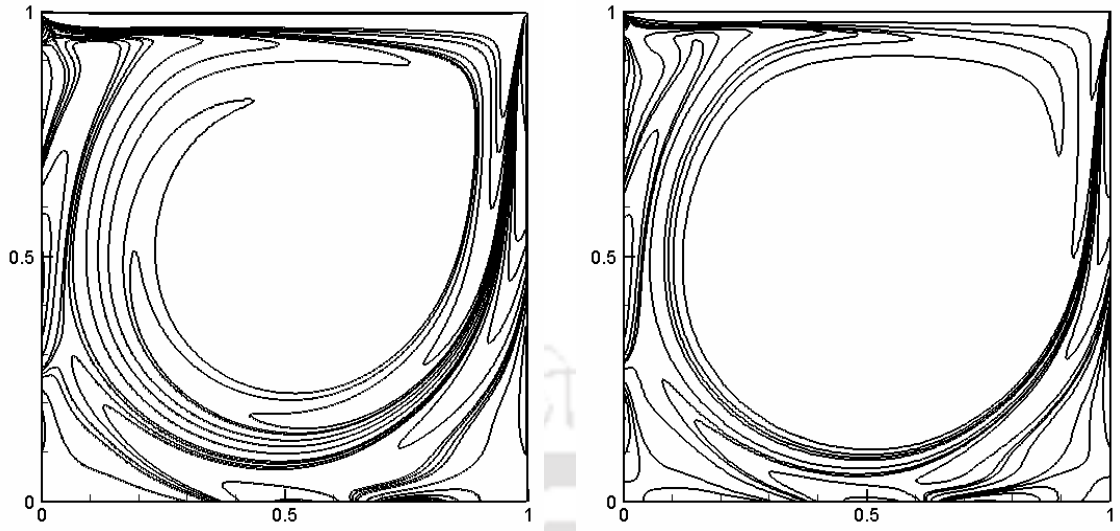

(a) *Re* = 2000 (b) *Re* = 3200

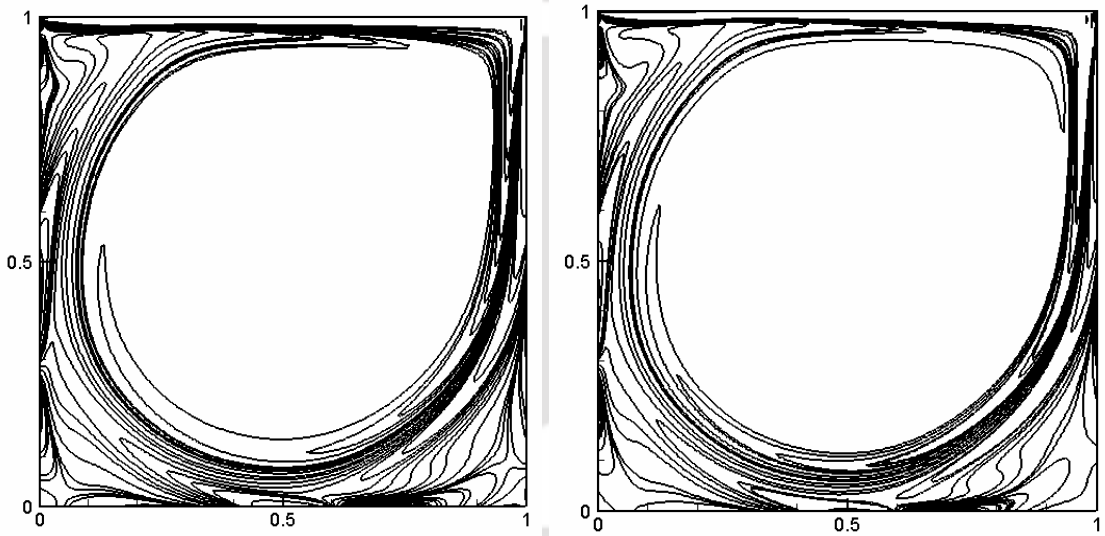

(c) *Re* = 5000 (d) *Re* = 7500

Figure 3.11: Vorticity contours for the single lid-driven square cavity flow for (a) *Re* = 2000, (b) *Re* = 3200, (c) *Re* = 5000 and (d) *Re* = 7500 obtained by LBM–MRT method. Simulations are carried out on 201×201 lattice arrangement.

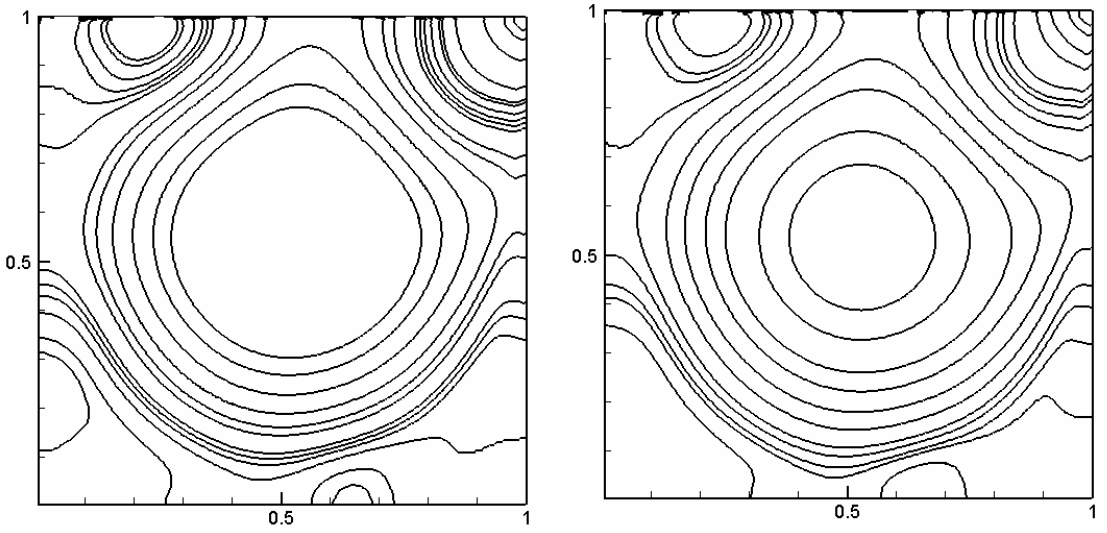

(a) Re = 2000 (b) Re = 3200

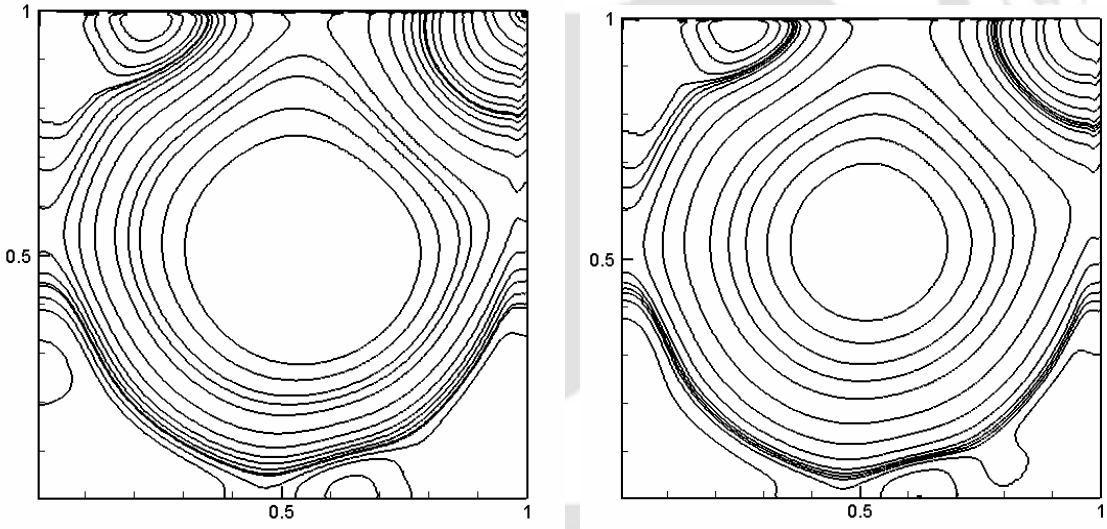

(c) Re = 5000 (d) Re = 7500

Figure 3.12: Pressure contours for the single lid-driven square cavity flow for (a) Re = 2000, (b) Re = 3200, (c) Re = 5000 and (d) Re = 7500 obtained by LBM–MRT method. Simulations are carried out on a 201×201 lattice arrangement.

Figure 3.12 presents the LBM-MRT isobars at higher Reynolds number ranging from 2000 to 7500. By examining the closed contours it is seen that the inviscid core grows with increasing values of Reynolds number. These results are well known in the literature and exhibit no surprises thereby confirming the fact that our LBM-MRT results yield qualitatively accurate solutions. As expected, at higher Reynolds number flows, LBM-MRT model gives much less spatial oscillations near geometrical singular points (compare Figure 3.10 (b) and 3.12 (d)). In Figure 3.13 we present comparisons of the horizontal velocities on the vertical centreline and the vertical velocities on the horizontal centreline of the square cavity for Reynolds numbers ranging from 100 to 7500. To lend credibility to the LBM-MRT results they are further compared with those obtained through the finite difference-based code described earlier. Overall, the Reynolds number effect on the flow structure is clearly manifested by the streamlines, velocity profiles, vorticity and pressure contours.

In Table 3.1-3.4 we present the quantitative data for our square cavity solutions. In Table 3.1, we present the location of the centre of the primary vortex for $1 \le Re \le 7500$. In each case our LBM and FDM solutions exhibit an excellent match with the best and accurate solutions available in the literature. In Table 3.2, we present the vortex-centre data of the secondary vortices for $1 \le Re \le 7500$ in the bottom-left and bottom-right corners of the square cavity. In Table 3.3, we present the vortex-centre data of the secondary vortex in the top-left corner (or near the trailing edge of the moving wall) of the lid-driven square cavity for $2000 \le Re \le 7500$. Our LBM and FDM results again exhibit an excellent match with the published results. In Table 3.4 we present data on the tertiary vortices for $3200 \le Re \le 7500$ and our results match very well with those in the literature [83, 84].

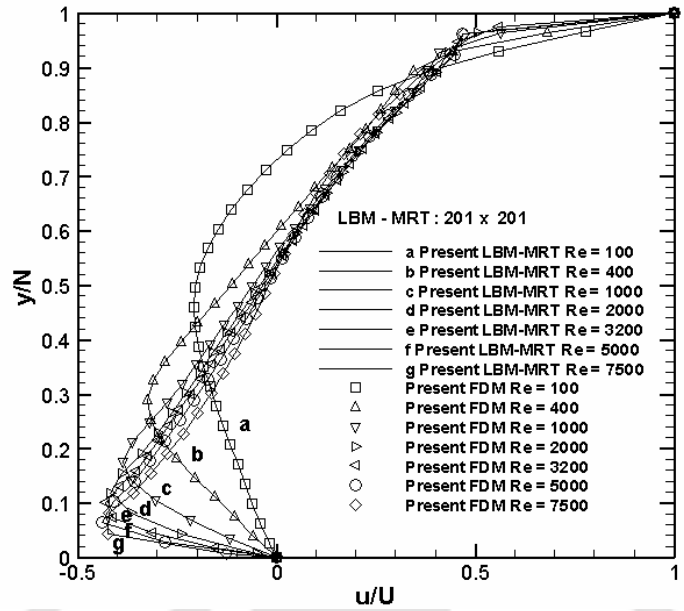

(a)

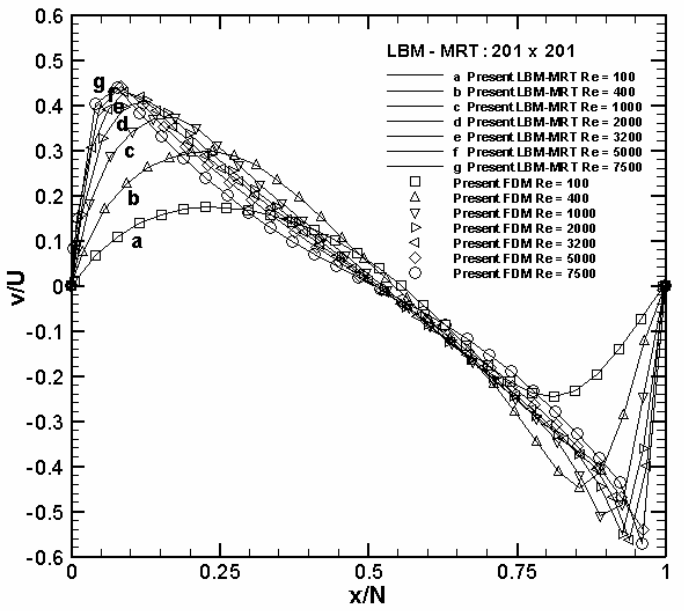

(b)

Figure 3.13: Comparison of LBM-MRT square cavity results: (a) *u*-velocity along the vertical centreline and (b) *v*-velocity along the horizontal centreline.

Table 3.1: Location of the centre of primary vortex for the single lid-driven square cavity flow.

Re	Authors	*x*	*y*
1	Present LBM – SRT Method	0.4994	0.7546
	Present LBM – MRT Method	0.4993	0.7528
	Present FDM	0.4991	0.7519
100	Ghia *et al*. [83]	0.6172	0.7344
	Hou *et al*. [27]	0.6196	0.7373
	Gupta & Kalita [84]	0.6125	0.7375
	Patil and Lakshmisha [30]	0.6161	0.7296
	Present LBM – SRT Method	0.6152	0.7361
	Present LBM – MRT Method	0.6156	0.7366
	Present FDM	0.6188	0.7375
400	Ghia *et al*. [83]	0.5547	0.6055
	Hou *et al*. [27]	0.5608	0.6078
	Gupta & Kalita [84]	0.5500	0.6125
	Patil and Lakshmisha [30]	0.5506	0.5972
	Present LBM – SRT Method	0.5537	0.6041
	Present LBM – MRT Method	0.5534	0.6039
	Present FDM	0.5512	0.6136
1000	Ghia *et al*. [83]	0.5313	0.5625
	Hou *et al*. [27]	0.5333	0.5647
	Gupta & Kalita [84]	0.5250	0.5625
	Patil and Lakshmisha [30]	0.5259	0.5777
	Present FDM	0.5268	0.5637
	Present LBM – SRT Method	0.5304	0.5616
	Present LBM – MRT Method	0.5302	0.5635
2000	Hou *et al*. [27]	0.5255	0.5490
	Gupta & Kalita [84]	0.5250	0.5500
	Present LBM – SRT Method	0.5238	0.5469
	Present LBM – MRT Method	0.5218	0.5462
	Present FDM	0.5236	0.5448
3200	Ghia *et al*. [83]	0.5165	0.5469
	Gupta & Kalita [84]	0.5188	0.5438
	Patil and Lakshmisha [30]	0.5189	0.5441

	Present LBM – SRT Method	0.5169	0.5458
	Present LBM – MRT Method	0.5162	0.5455
	Present FDM	0.5160	0.5421
5000	Ghia *et al*. [83]	0.5117	0.5352
	Hou *et al*. [27]	0.5176	0.5373
	Gupta & Kalita [84]	0.5125	0.5375
	Present LBM – SRT Method	0.5143	0.5362
	Present LBM – MRT Method	0.5147	0.5331
	Present FDM	0.5131	0.5367
7500	Ghia *et al*. [83]	0.5117	0.5322
	Hou *et al*. [27]	0.5176	0.5333
	Gupta & Kalita [84]	0.5125	0.5313
	Present LBM – SRT Method	0.5111	0.5302
	Present LBM – MRT Method	0.5107	0.5308
	Present FDM	0.5104	0.5301

Table 3.2: Location of the centres of secondary corner vortices at the bottom of the single lid-driven square cavity flow.

Re	Authors	Bottom-left vortex		Bottom-right vortex	
		x	*y*	*x*	*y*
1	Present LBM – SRT Method	0.0343	0.0364	0.9508	0.0362
	Present LBM – MRT Method	0.0339	0.0358	0.9502	0.0354
	Present FDM	0.0332	0.0352	0.9510	0.0365
100	Ghia *et al*. [83]	0.0313	0.0391	0.9453	0.0625
	Hou *et al*. [27]	0.0392	0.0353	0.9451	0.0627
	Gupta & Kalita [84]	0.0375	0.0375	0.9375	0.0625
	Patil and Lakshmisha [30]	0.0345	0.0324	0.9451	0.0574
	Present LBM – SRT Method	0.0321	0.0365	0.9432	0.0648
	Present LBM – MRT Method	0.0320	0.0371	0.9405	0.0681
	Present FDM	0.0318	0.0341	0.9423	0.0667
400	Ghia *et al*. [83]	0.0508	0.0469	0.8906	0.1250
	Hou *et al*. [27]	0.0549	0.0510	0.8902	0.1255
	Gupta & Kalita [84]	0.0500	0.0500	0.8875	0.1250

	Patil and Lakshmisha [30]	0.0526	0.0471	0.8862	0.1258
	Present LBM – SRT Method	0.0503	0.0502	0.8899	0.1259
	Present LBM – MRT Method	0.0501	0.0500	0.8896	0.1247
	Present FDM	0.0499	0.0477	0.8891	0.1248
1000	Ghia *et al*. [83]	0.0859	0.0781	0.8594	0.1094
	Hou *et al*. [27]	0.0902	0.0784	0.8667	0.1137
	Gupta & Kalita [84]	0.0875	0.0750	0.8625	0.1125
	Patil and Lakshmisha [30]	0.0904	0.0989	0.8778	0.1261
	Present LBM – SRT Method	0.0830	0.0777	0.8616	0.1114
	Present LBM – MRT Method	0.0826	0.0776	0.8612	0.1112
	Present FDM	0.0817	0.0761	0.8604	0.1108
2000	Hou *et al*. [27]	0.0902	0.1059	0.8471	0.0980
	Gupta & Kalita [84]	0.0785	0.1000	0.8375	0.1000
	Present LBM – SRT Method	0.0889	0.1041	0.8452	0.0986
	Present LBM – MRT Method	0.0878	0.1074	0.8448	0.0997
	Present FDM	0.0861	0.1026	0.8427	0.0962
3200	Ghia *et al*. [83]	0.0859	0.1094	0.8125	0.0859
	Gupta & Kalita [84]	0.0813	0.1188	0.8125	0.0875
	Patil and Lakshmisha [30]	0.0993	0.0963	0.8619	0.0971
	Present LBM – SRT Method	0.0854	0.1192	0.8119	0.0842
	Present LBM – MRT Method	0.0849	0.1187	0.8108	0.0835
	Present FDM	0.0845	0.1179	0.8115	0.0829
5000	Ghia *et al*. [83]	0.0703	0.1367	0.8086	0.0742
	Hou *et al*. [39]	0.0784	0.1373	0.8078	0.0745
	Gupta & Kalita [84]	0.0750	0.1313	0.8000	0.0750
	Present LBM – SRT Method	0.0737	0.1367	0.8059	0.0736
	Present LBM – MRT Method	0.0733	0.1367	0.8051	0.0733
	Present FDM	0.0732	0.1342	0.8048	0.0727
7500	Ghia *et al*. [83]	0.0645	0.1504	0.7813	0.0625
	Hou *et al*. [27]	0.0706	0.1529	0.7922	0.0667
	Gupta & Kalita [84]	0.0688	0.1500	0.7813	0.0625
	Present LBM – SRT Method	0.0648	0.1535	0.7820	0.0634
	Present LBM – MRT Method	0.0638	0.1542	0.7898	0.0646
	Present FDM	0.0635	0.1532	0.7804	0.0612

Table 3.3: Location of the centre of the secondary vortex at the top-left side wall of the single lid-driven square cavity.

Re	Authors	*x*	*y*
2000	Gupta and Kalita [84]	0.0375	0.8875
	Present LBM – SRT Method	0.0358	0.8845
	Present LBM – MRT Method	0.0352	0.8841
	Present FDM	0.0352	0.8827
3200	Ghia *et al*. [83]	0.0547	0.8984
	Gupta & Kalita [84]	0.0563	0.9000
	Patil and Lakshmisha [30]	0.0316	0.8689
	Present LBM – SRT Method	0.0559	0.8991
	Present LBM – MRT Method	0.0554	0.8995
	Present FDM	0.0552	0.8996
5000	Ghia *et al*. [83]	0.0625	0.9102
	Hou *et al*. [27]	0.0667	0.9059
	Gupta & Kalita [84]	0.0688	0.9125
	Present LBM – SRT Method	0.0630	0.9089
	Present LBM – MRT Method	0.0615	0.9071
	Present FDM	0.0612	0.9092
7500	Ghia *et al*. [83]	0.0664	0.9141
	Hou *et al*. [27]	0.0706	0.9098
	Gupta & Kalita [84]	0.0688	0.9125
	Present LBM – SRT Method	0.0661	0.9098
	Present LBM – MRT Method	0.0652	0.9071
	Present FDM	0.0659	0.9069

Table 3.4: Location of the centres of the tertiary vortices at the bottom corners of the single lid-driven square cavity.

Re	Authors	Bottom left vortex		Bottom right vortex	
		x	*y*	*x*	*y*
3200	Ghia *et al*. [83]	0.0078	0.0078	0.9844	0.0078
	Gupta & Kalita [84]	0.0063	0.0063	0.9875	0.0125
	Present LBM – SRT Method	0.0074	0.0073	0.9861	0.0132
	Present LBM – MRT Method	0.0071	0.0071	0.9852	0.0143
	Present FDM	0.0067	0.0067	0.9890	0.0091
5000	Ghia *et al*. [83]	0.0177	0.0078	0.9805	0.0195
	Gupta & Kalita [84]	0.0063	0.0063	0.9750	0.0188
	Present LBM – SRT Method	0.0082	0.0089	0.9808	0.0190
	Present LBM – MRT Method	0.0075	0.0069	0.9801	0.0194
	Present FDM	0.0091	0.0099	0.9724	0.0269
7500	Ghia *et al*. [83]	0.0177	0.0177	0.9492	0.0430
	Gupta & Kalita [84]	0.0063	0.0125	0.9500	0.0375
	Present LBM – SRT Method	0.0147	0.0145	0.9463	0.0489
	Present LBM – MRT Method	0.0129	0.0134	0.9474	0.0475
	Present FDM	0.0112	0.0109	0.9489	0.0459

3.5.2. Test Problem 2: Deep Cavity Flow ($K > 1$)

We now consider the problem of a lid-driven flow in a deep cavity with aspect ratio of 2.0. The range of Reynolds numbers 100 to 1500 is considered here. Boundary condition for velocity on the top wall is given by $\boldsymbol{U} = 0.1$, $v = 0$. On all other walls of the cavity the velocities are zero ($u = v = 0$). The LBM-SRT model square cavity solution procedure is now extended to this problem. Figure 3.14 shows the streamline pattern for this problem for Reynolds number ranging from $Re = 100$ to 1500. In each of these cases, we observe two rotating primary vortices as well as secondary vortices in the bottom corners of the deep cavity.

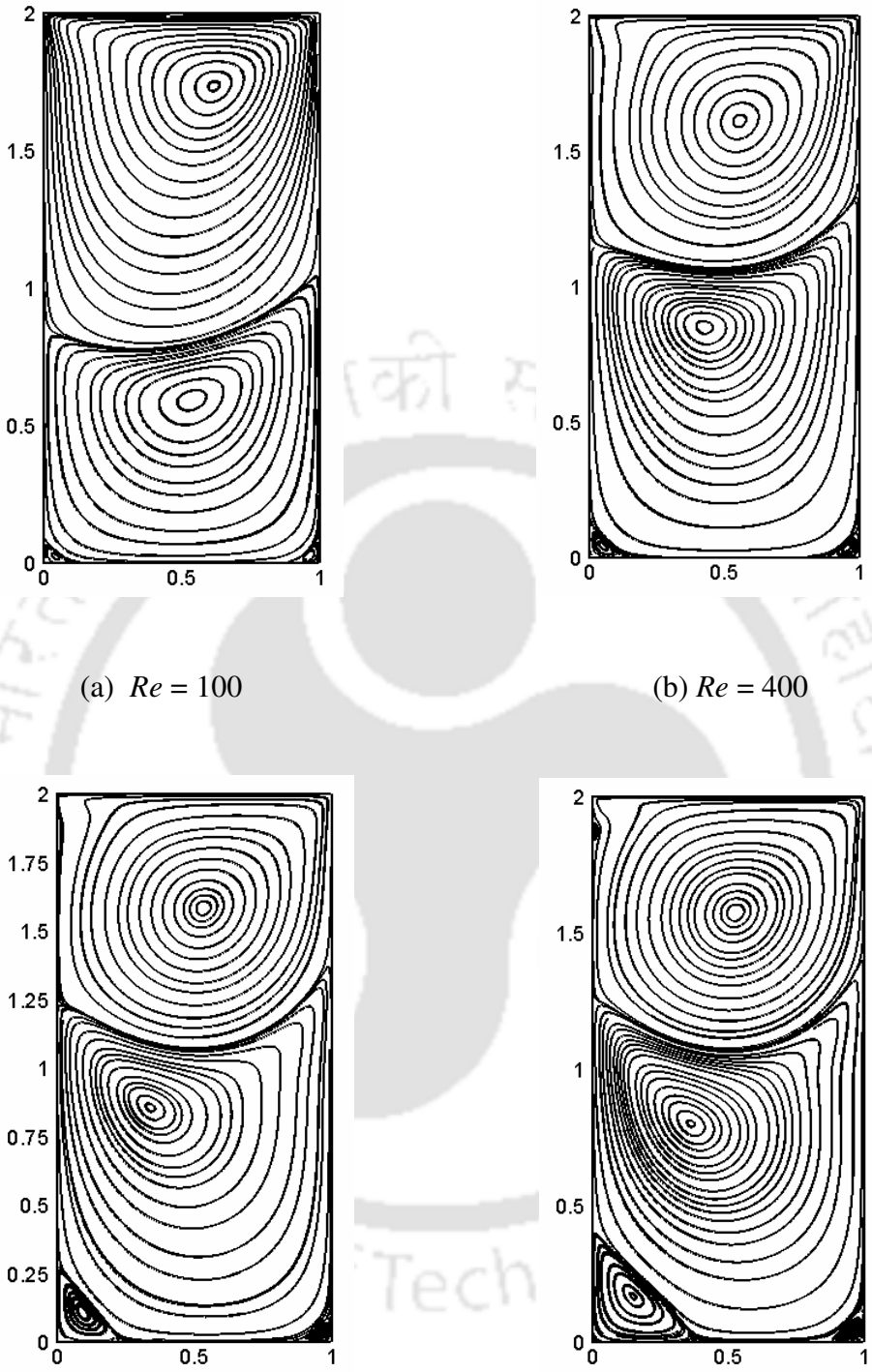

(a) Re = 100 (b) Re = 400

(c) Re = 1000 (d) Re = 1500

Figure 3.14: Streamline patterns for the single lid-driven deep cavity flow with aspect ratio 2.0 for (a) Re = 100, (b) Re = 400, (c) Re = 1000 and (d) Re = 1500 by LBM – SRT.

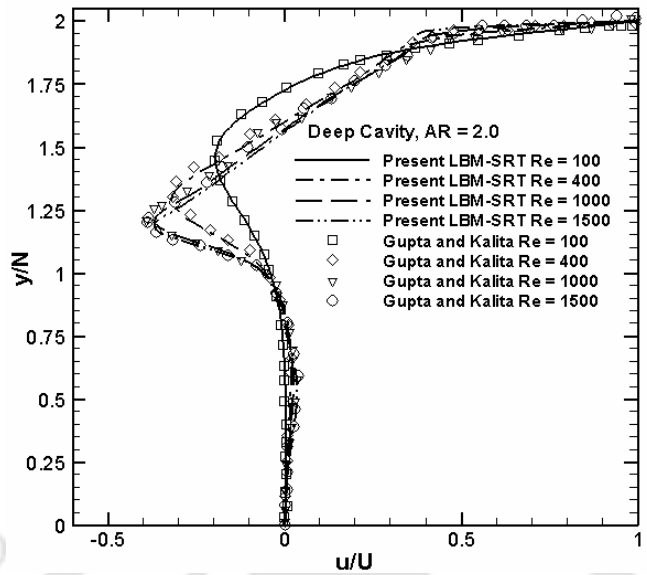

(a)

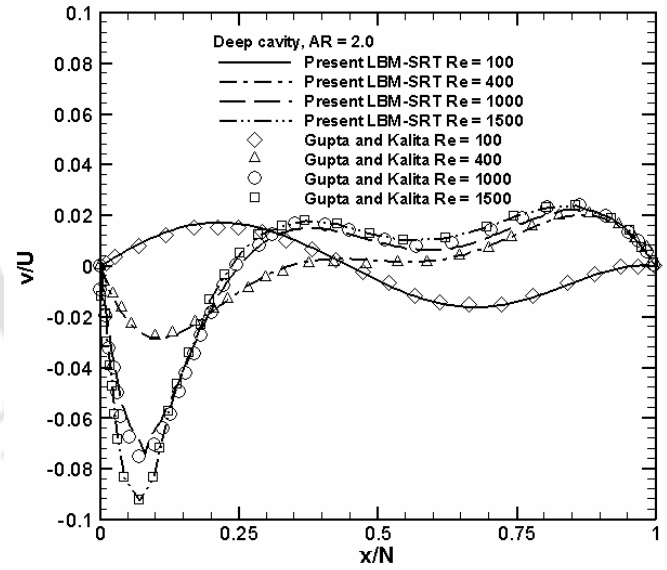

(b)

Figure 3.15: Comparisons of (a) *u*-velocity along the vertical centreline and (b) *v*-velocity along the horizontal centreline for the deep lid-driven cavity flow with aspect ratio = 2.0 from *Re* = 100 to *Re* = 1500. Simulations are carried out on 120×240 lattice arrangement.

In Figure 3.15 we present comparisons of the horizontal velocities on the vertical centreline and the vertical velocities on the horizontal centreline of the deep cavity for Reynolds numbers ranging from 100 to 1500. In each case our velocity profiles exhibit a perfect match with the higher order accurate scheme results given by Gupta and Kalita [84]. In Table 3.5, we present quantitative data on the vortex centre locations of the primary, secondary and tertiary vortices for $100 \le Re \le 1500$ and our results match very well with those in the literature. We have observed that as the aspect ratio increases, the number of primary vortices also increases and will now try to give a physical reason for that. Before doing that we intend to mention that even in the lid-driven square cavity, at the corner, there is an infinite series of vortices [25]. The secondary corner vortex induces a tertiary vortex, which in turn produces a quaternary vortex, which again produces post-quaternary vortex and so on.

The generation of these vortices is due to the shearing effect of the vortex that is generated first. In the backdrop of this, we may reason that the moving lid causes the attached liquid to move with the same velocity and this momentum diffuses into the interior because of viscosity, with the result that it generates one primary vortex. The direct effect of the lid does not percolate too much when the aspect ratio is high. The vortex which is generated first then acts on the body of fluid that remains below and gives rise to a circulating mass of fluid which constitutes another (weaker primary) vortex. If the aspect ratio is large, there is a larger expanse of fluid that allows this chain of events to continue. This is the reason why an aspect ratio increases, so does the number of vortices.

Table 3.5: Location of the vortex centres for the single lid-driven deep cavity flow with aspect ratio 2.0.

Re	Authors	100		400		1000		1500	
		x	*y*	*x*	*y*	*x*	*y*	*x*	*y*
Primary (top)	Bruneau & Jouron [86]	0.6172	1.7344	0.5547	1.5938	0.5273	1.5625	-	-
	Gupta & Kalita [84]	0.6125	1.7375	0.5500	1.6125	0.5250	1.5875	0.5250	1.5750
	Present LBM-SRT	0.6138	1.7326	0.5509	1.6123	0.5265	1.5788	0.5282	1.5712
	Present FDM	0.6117	1.7357	0.5504	1.6129	0.5281	1.5865	0.5291	1.5737
Primary (bottom)	Bruneau & Jouron [86]	0.5391	0.5859	0.4297	0.8125	0.3516	0.7891	-	-
	Gupta & Kalita [84]	0.5625	0.6000	0.4375	0.8625	0.3250	0.8750	0.3498	0.8250
	Present LBM-SRT	0.5405	0.5888	0.4317	0.8568	0.3242	0.8698	0.3507	0.8095
	Present FDM	0.5384	0.5901	0.4268	0.8532	0.3330	0.8674	0.3586	0.8020
Secondary (bottom left)	Bruneau & Jouron [86]	0.0313	0.0313	0.0391	0.0469	0.0977	0.1094	-	-
	Gupta & Kalita [84]	0.0250	0.0375	0.0500	0.0500	0.1000	0.1250	0.1750	0.2000
	Present LBM-SRT	0.0302	0.0297	0.0508	0.0502	0.0996	0.1241	0.1685	0.1901
	Present FDM	0.0341	0.0318	0.0516	0.0489	0.0973	0.1208	0.1597	0.1868
Secondary (bottom right)	Bruneau & Jouron [86]	1.000	0.3750	0.9688	0.0391	1.0000	0.3750	-	-
	Gupta & Kalita [84]	0.9750	0.0375	0.9500	0.0375	0.9600	0.0420	0.9375	0.0625
	Present LBM-SRT	0.9728	0.0347	0.9567	0.0354	0.9645	0.0389	0.9398	0.0575
	Present FDM	0.9755	0.0361	0.9512	0.0346	0.9697	0.0366	0.9409	0.0519
Tertiary (bottom left)	Gupta & Kalita [84]	-	-	-	-	-	-	0.0125	0.0125
	Present LBM-SRT	-	-	-	-	-	-	0.0130	0.0109
	Present FDM	-	-	-	-	-	-	0.0133	0.0102

3.5.3. Test Problem 3: Shallow Cavity Flow ($K < 1$)

Next, we consider the problem of a lid-driven flow in a shallow cavity with the aspect ratio of 0.5. Figure 3.16 shows the streamline pattern and vorticity contour for this problem for Reynolds number ranging from Re = 100 to 1000. As the Reynolds number increases, the primary circulation is driven towards the upper-right corner, with the secondary vortex cores moving up and across the cavity. At Re = 1000 a strong primary circulation forms with a nearly circular shape at the right side of the cavity. For this Reynolds number the recirculation region on the left side of the cavity is approximately half the size of the primary circulation while the circulation zone at the lower right corner is much smaller. In each case, our LBM-SRT method streamline patterns exhibit an excellent match with the solutions available in the literature [29, 32].

In Figure 3.17, we present comparisons of the horizontal velocities on the vertical centreline and the vertical velocities on the horizontal centreline of the shallow cavity for Reynolds numbers ranging from 100 to 1000. In Table 3.6, we present our quantitative data on the vortex centre locations of primary, secondary and tertiary vortices for $100 \leq Re \leq 1500$. We conclude that vertical stretching of the cavity is not found to alter the flow patterns significantly whereas horizontal stretching creates a large recirculation region for example at a Reynolds number of 1000 as seen from Figure 3.16 (c).

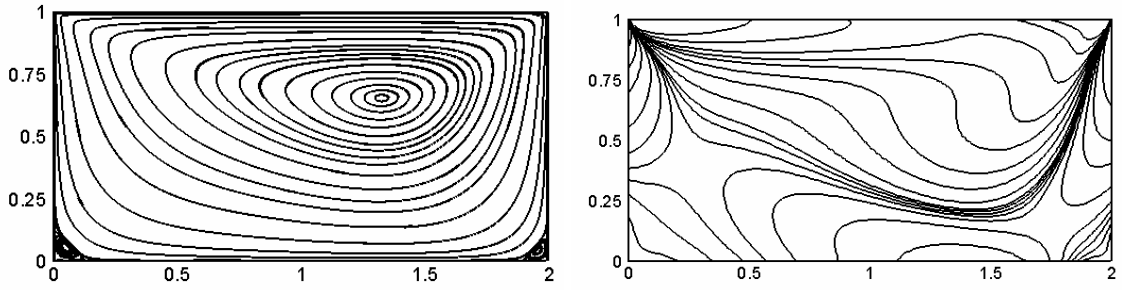

(a) *Re* = 100

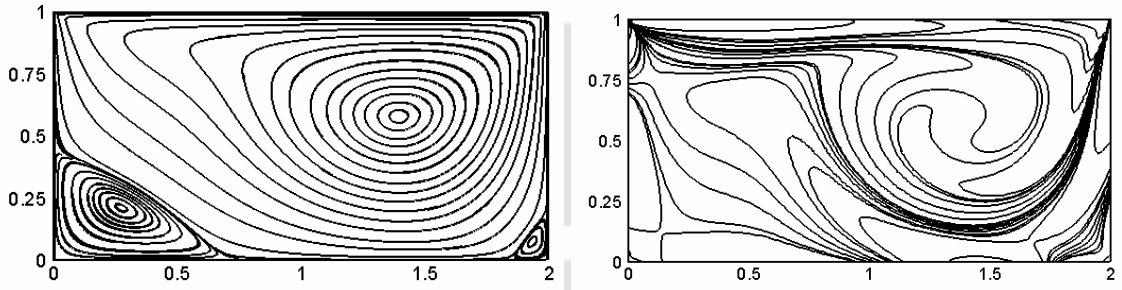

(b) *Re* = 400

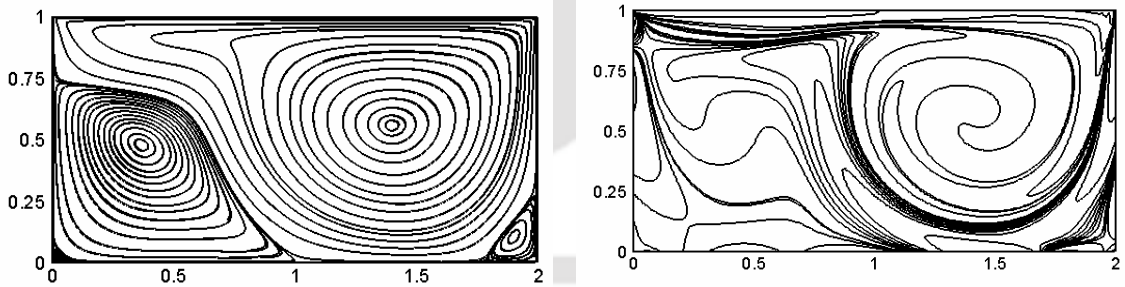

(c) *Re* = 1000

Figure 3.16: Streamline pattern for the single lid-driven shallow cavity flow with aspect ratio 0.5 for (a) *Re* = 100, (b) *Re* = 400 and (c) *Re* = 1000 by LBM–SRT model. Simulations were carried out on a 240×120 lattice arrangement.

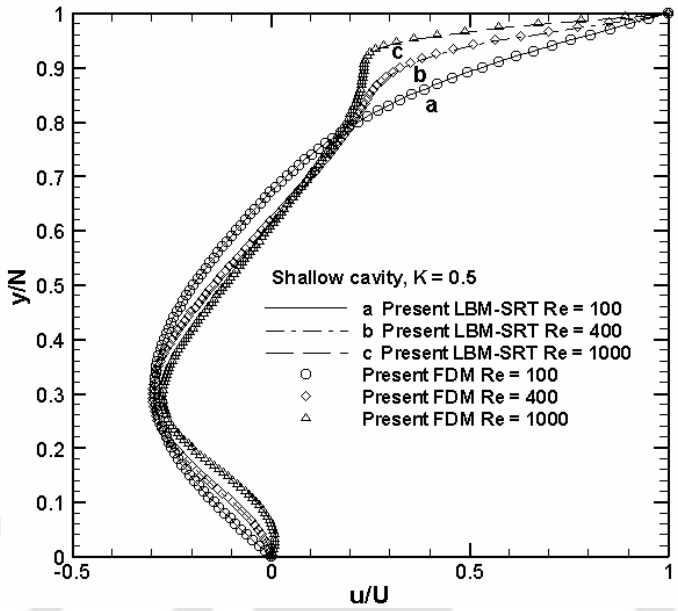

(a)

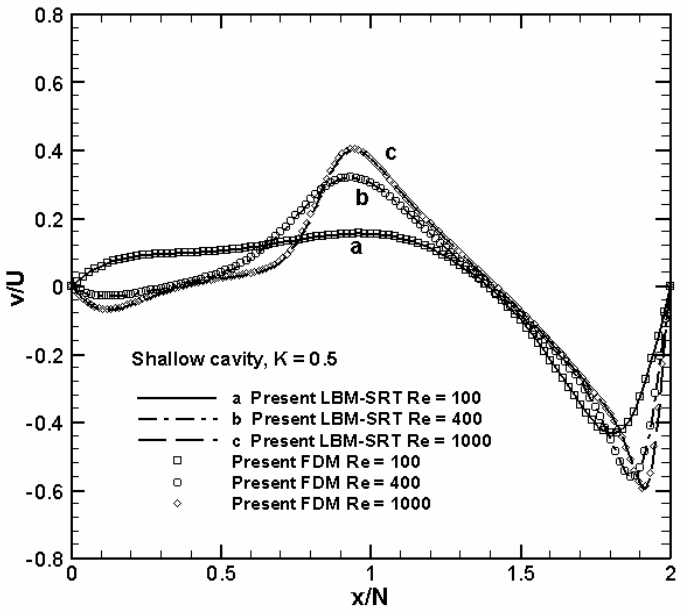

(b)

Figure 3.17: Comparisons of (a) *u*-velocity along the vertical centreline and (b) *v*-velocity along the horizontal centreline for the shallow lid-driven cavity with aspect ratio = 0.5.

Table 3.6: Location of the vortex centres for the single lid-driven shallow cavity flow with aspect ratio 0.5.

Re		100		400		1000	
		x	*y*	*x*	*y*	*x*	*y*
Primary eddy	Present LBM-SRT	1.3577	0.6401	1.3932	0.5771	1.3985	0.5561
	Present FDM	1.3605	0.6374	1.3914	0.5716	1.4019	0.5529
Secondary eddy (bottom left)	Present LBM-SRT	0.0674	0.0717	0.2730	0.2098	0.3670	0.4782
	Present FDM	0.0710	0.0798	0.2736	0.2096	0.3619	0.4811
Secondary eddy (bottom right)	Present LBM-SRT	1.9529	0.0474	1.9214	0.0821	1.8989	0.1093
	Present FDM	1.9558	0.0536	1.9239	0.0839	1.8898	0.1076
Tertiary (bottom left)	Present LBM-SRT	-	-	-	-	0.0315	0.0327
	Present FDM	-	-	-	-	0.0381	0.0415
Tertiary (bottom right)	Present LBM-SRT	-	-	-	-	1.9910	0.0041
	Present FDM	-	-	-	-	1.9950	00050

Part II: Flow over a Circular Cylinder

3.6. Introduction

The classical problem of viscous incompressible flow over a circular cylinder [87] is one of the most widely studied problems in CFD. This type of flow problems frequently arise in various engineering fields which offer tough challenges particularly at high Reynolds numbers. Experiments reveal that at a Reynolds number of 43 flow past a circular

cylinder becomes unsteady and periodic [88]. For $Re < 43$ the flow is steady and symmetric. Because of its popularity, a plethora of numerical, theoretical and experimental results are available for this problem in the literature [54, 87-90]. A large number of attempts have been made to study flow over a circular cylinder using continuum-based methods and a very few attempts have been made using LBM. This section is mainly concerned with LBM computation of flow over a circular cylinder at low Reynolds numbers when the flow is steady and symmetric. We also show just the vorticity contours at $Re = 60$, when the flow is periodic, to demonstrate the present code has the ability to compute the unsteady vortex-shedding flow behind a circular cylinder. We, however, retrain from analyzing the unsteady flow in details as the main thrust of the present thesis is LBM computation of 'steady' flows.

3.7. LBM Computation

The schematic diagram of the flow past a circular cylinder confined in a channel configuration is shown in Figure 3.18. For a blockage ratio $B = H / D = 8$ computations are carried out at $Re = 5$, 20 and 40 with the help of single-relaxation-time LBM method based on the *D2Q9* model. Here we compute the flow about a cylinder of diameter D placed in a channel of width H at low Reynolds numbers. An upstream length of $l = L/4$ or 12.5 D has been chosen. The lattice size of 500×80 is used for the present configuration. In this problem, Reynolds number is defined as $Re = U_\infty D/\upsilon$, where U_∞ is the velocity at the channel entry and D is the cylinder diameter (10 lattice units in the present work). Bounce-back boundary condition (described in chapter 2, section 2.5.2) is enforced on the top and bottom walls. A simple extrapolation boundary condition is

employed at the exit kept at a large distance (37.5*D*) from the cylinder. Bounce-back boundary condition with momentum is enforced (section 2.5.2.1) at the inlet [54]. A curved boundary treatment proposed by Bouzidi *et al.* [40], which is used on the cylinder surface is written as

$$f_{\bar{i}}(\mathbf{x}_f, t+\Delta t) = \frac{1}{2\Delta} f_i^{*}(\mathbf{x}_f, t) + \frac{2\Delta - 1}{2\Delta} f_{\bar{i}}^{*}(\mathbf{x}_f, t) \quad \text{for } \Delta > 1/2 \tag{3.3}$$

where $f_{\bar{i}}(\mathbf{x}_f, t+\Delta t)$ equivalent to $f_{\bar{i}}^{o}(\mathbf{x}, t)$. This boundary condition satisfies the no-slip condition to the second-order in Δx and preserves the geometrical integrity of the wall boundary. The drag coefficient over a circular cylinder of radius *r* is defined as [54]

$$C_D = \frac{|F_x|}{\rho U^2 r} \tag{3.4}$$

Some details of simulation of this flow configuration can be found in Mei *et al.* [39].

3.8. Results and Discussion

The schematic diagram of the flow past a circular cylinder confined in a channel configuration is shown in Figure 3.18. It may be mentioned that the results shown in the Figures 3.19 – 3.26 and Table 3.7 are lattice size independent. Steady-state streamline patterns and vorticity contours for this flow for Reynolds numbers *Re* = 5, 20 and *Re* = 40 are shown in Figures 3.19 – 3.24. In Figure 3.19 we show the streamline pattern for *Re* = 5. In this case, two stationary eddies symmetric about the channel centreline develop behind the cylinder. Figure 3.20 and 3.21 show the streamlines for *Re* = 20 and 40. It is again seen that two vortices downstream of the cylinder, symmetrically placed about the

channel centreline, develop and remain attached to the cylinder. It is also observed that for steady flows the sizes of the vortices increase with Reynolds number. Figures 3.22 – 3.24 show the vorticity contours at Re = 5, 20 and 40. Interestingly, on the line of symmetry downstream of the cylinder flow is irrotational. In Table 3.7, we present the coefficient of drag for Reynolds numbers 20 and 40. All the results computed with LBM compares well with existing results [88-90]. As we have seen, the flow at lower Reynolds numbers is steady whereas at higher Reynolds numbers unsteadiness develops and the flow becomes periodic. The periodic flow is characterized by the so called von Karman vortex street generated by alternate and periodic shedding of vortices from the top and bottom.

Table 3.7: Coefficient of Drag C_D for Reynolds numbers 20 and 40.

Authors	Re = 20	Re = 40
Tritton (Experimental) [88]	2.22	1.48
Dennis and Chang (Numerical) [89]	2.05	1.52
Present LBM	2.25	1.50

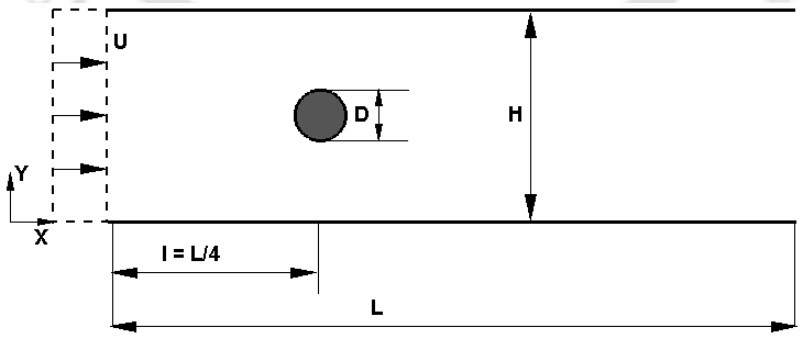

Figure 3.18: Schematic diagram of the flow past a circular cylinder confined in a channel.

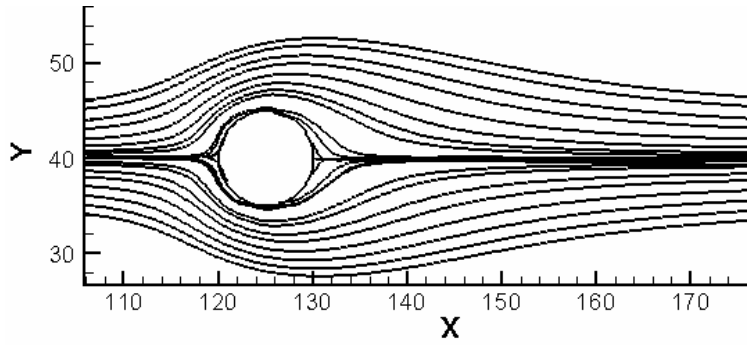

Figure 3.19: Streamline pattern for *Re* = 5 for the flow over a circular cylinder; Lattice size: 500×80.

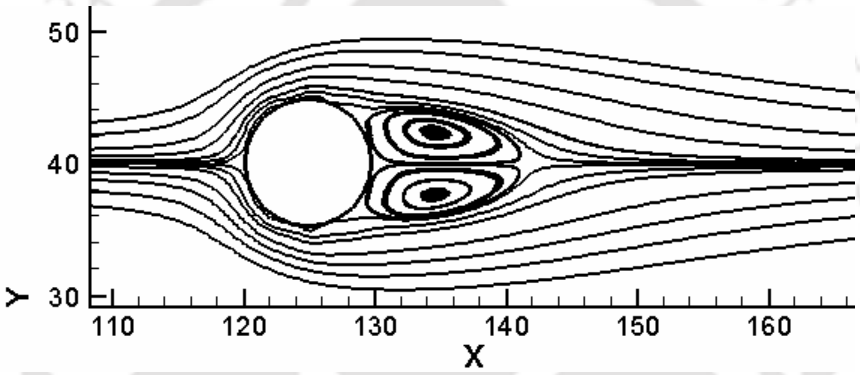

Figure 3.20: Streamline pattern for *Re* = 20 for the flow over a circular cylinder; Lattice size: 500×80.

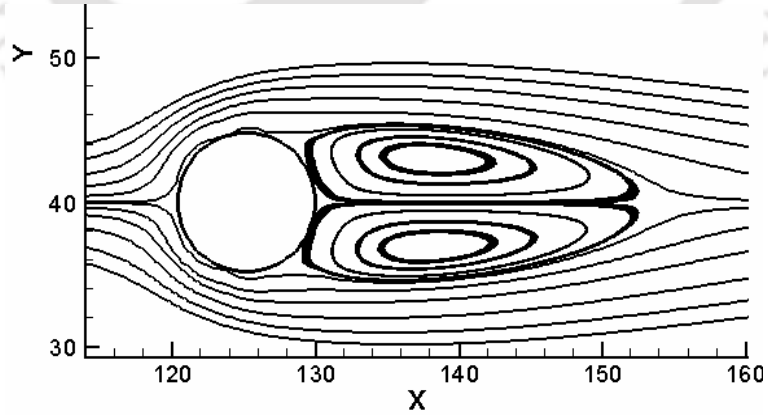

Figure 3.21: Streamline pattern for *Re* = 40 for the flow over a circular cylinder; Lattice size: 500×80.

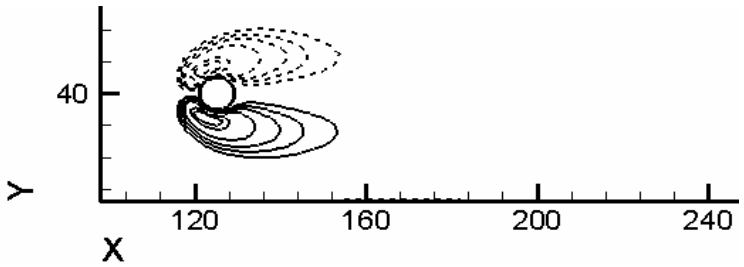

Figure 3.22: Vorticity contours for *Re* = 5 for the flow over a circular cylinder.

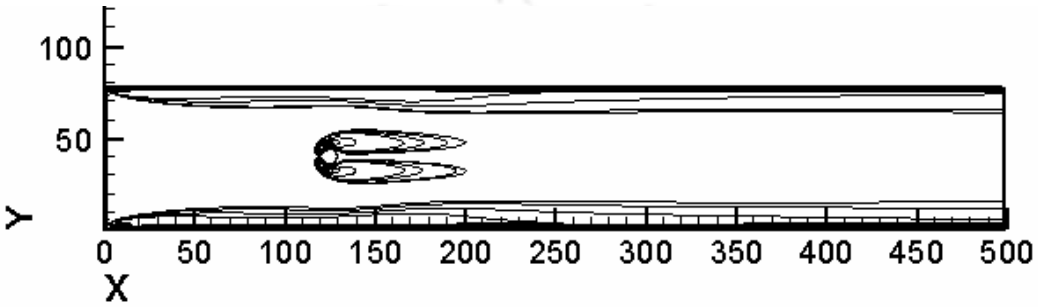

Figure 3.23: Vorticity contours for *Re* = 20 for the flow over a circular cylinder.

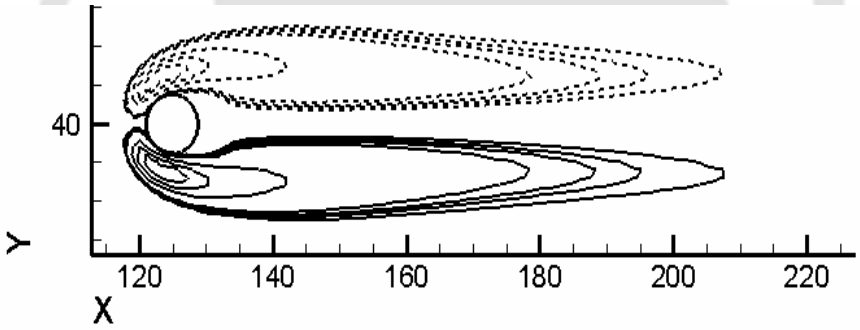

Figure 3.24: Vorticity contours for *Re* = 40 for the flow over a circular cylinder.

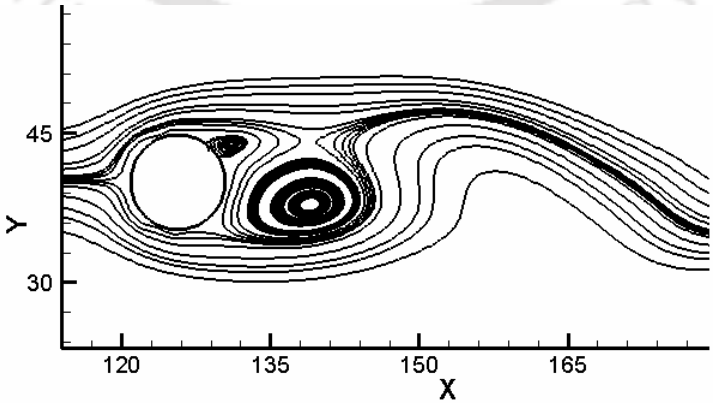

Figure 3.25: Streamline pattern for *Re* = 60 for the flow over a circular cylinder.

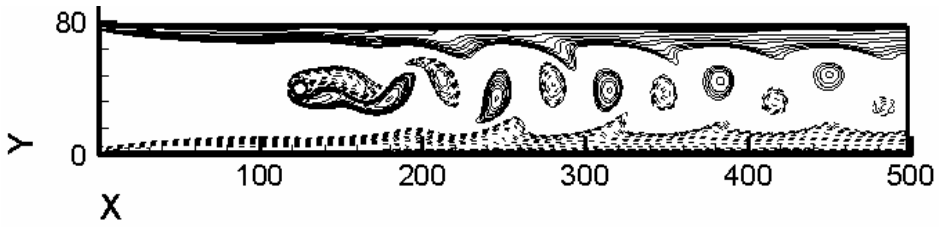

Figure 3.26: Vorticity contours for *Re* = 60 for the flow over a circular cylinder; Lattice size: 500×80.

As the main intent of the present thesis is to compute various steady flows, to show the ability of the present LBM code to capture unsteadiness we also give the instantaneous streamline and vorticity contour of the time-periodic flow for *Re* = 60 in Figures 3.25 – 3.26.

3.9. Conclusion

In Part I, simulation of incompressible viscous flow in a two-dimensional single lid-driven cavity is presented. Whenever comparison is possible, the present lid-driven cavity flow results are found to be in good agreement with the results reported by other researchers. The Lattice Boltzmann Method with single-relaxation-time (LBM-SRT) and multi-relaxation-time (LBM-MRT) models is able to reproduce the simulation of lid-driven square cavity flows by conventional methods and is a convenient way of computing flows governed by the incompressible Navier-Stokes equations. For all the Reynolds numbers, detailed discussion on the flow structure and comparison with numerical results are provided. In this chapter, results of the square (K=1) cavity is presented along with those for the deep (K>1) and shallow (K<1) cavities. The effects of the aspect ratio and Reynolds number on the size, centre position and number of vortices are studied in detail together with the flow pattern in the cavity. In each case, our

computed LBM and FDM solutions agrees very well, both qualitatively and quantitatively with established results. The present LBM computations not only confirms the flow features by previous researchers, but also reveals the effects of Reynolds number and the aspect ratio on the flow structure in the cavity in a systematic way.

The accuracy and physical fidelity of the LBM-SRT and LBM-MRT methods are clearly seen in this chapter. The robustness and effectiveness of the LBM-SRT is illustrated by its applicability to three problems of varying physical complexities, represented among others, by Reynolds numbers ranging from 1 to 7500 in the square cavity problem, 100 to 1500 in the deep cavity problem and 100 to 1000 in the shallow cavity problem. This verification gives confidence to apply the present method to other complex systems. Simplicity appears to be the major virtue of the LBM-SRT method. Due to the extreme simplicity of the popular LBM-SRT method, it is recommended for simulating lid-driven cavity flow at low and moderate Reynolds numbers. Another merit of the present LBM-SRT model is that it can be easily extended to three-dimensional problems. However LBM-MRT method is seen to remove the difficulties faces by the LBM-SRT method at higher Reynolds numbers. In Part II LBM computation is carried out for the flow past a circular cylinder confined in a channel. This problem serves two purposes: it demonstrates that (i) LBM can be used to handle curved boundaries without much difficulty (ii) LBM has the ability to capture the unsteady flow states characterized by the circular cylinder at relatively higher Reynolds number.

Chapter 4

Simulation of Two-Sided Lid-Driven Square Cavities

4.1. Introduction

Flow in an enclosure driven by moving boundaries is a fundamental and interesting problem in basic fluid mechanics. It has already been mentioned that single lid-driven square and rectangular cavity flow was studied extensively in the literature [25-33, 51, 54, 74-76, 81-85]. Another classic example is the case where a flow is induced by the tangential movement of two facing cavity boundaries with constant velocities. If the facing walls move in the same direction, it is termed parallel wall motion and if in the opposite direction, it is termed antiparallel wall motion. Kuhlmann and other investigators [91-94] extended the single lid-driven cavity flow to the two-sided rectangular cavity flow. They have done several experiments on two-sided lid-driven rectangular cavity with various aspect ratios. Blohm and Kuhlmann [91] were among the first to experimentally investigate the incompressible fluid flow in a rectangular container driven by two facing sidewalls which move steadily in an anti-parallel direction up to *Re* = 1200. Kalita *et al.* [95] developed a higher order compact (HOC) algorithm for the Stream-function vorticity formulation of the two-dimensional Navier-Stokes equations on graded Cartesian meshes. Kumar *et al.* [96] used the algorithm to compute the flow in a two-sided lid-driven cavity (*Re* = 400) where, besides wall shear, a 'free-shear' flow is

also encountered. The two-sided lid-driven cavity problem has multiple steady solutions for some aspect ratios. However, for the aspect ratio of unity no multiplicity of solutions has been observed. Also it is found that for parallel motion of the walls, there appears a pair of counter-rotating secondary vortices of equal size near the centre of a wall. Because of symmetry, this pair of counter-rotating vortices has similar shapes and their detailed study as to how they grow with increasing Reynolds number has not yet been made. Such a study is attempted in this chapter through the Lattice Boltzmann Method, as the results of the problem have the potential of being used for testing various solution methods for incompressible viscous flows. The results for the antiparallel motion of the walls are also presented in some detail.

4.2. Two-Sided Lid-Driven Square Cavity Flow

An incompressible viscous flow in a square cavity whose top and bottom walls move in the same (parallel motion) or opposite (antiparallel motion) direction with a uniform velocity is the problem investigated in the present chapter. In the case of parallel wall motion, a 'free-shear' layer exists midway between the top and bottom walls apart from the wall bounded shear layers, whereas in the case of antiparallel wall motion, only wall bounded shear layers exist.

4.3. Numerical Method

4.3.1. LBM Procedure and Boundary Conditions

Here we use Lattice Boltzmann method with single-time-relaxation (LBM-SRT) and multi-time-relaxation (LBM-MRT) models to investigate the flow driven by the parallel and antiparallel motion of two facing walls in a square cavity for Reynolds number up to 2000. The D2Q9 model, described in chapter 2, is used. In LBM-SRT model, the improved boundary condition based on the bounce-back scheme proposed by Bouzidi *et al.* [40] was used to copy the velocity no-slip condition on walls. They showed that their results have second-order accuracy for curved boundary. For this reason, this boundary condition has been employed here on the two stationary walls. However for the moving walls, the equilibrium boundary condition [27] is applied. At the lattice nodes on the moving walls, flow-variables are re-set to their pre-assumed values at the end of every streaming-step. A lid-velocity of $U = 0.1$ has been considered in this work. Since Mach number is U/c_s, where c_s equals $1/\sqrt{3}$ a Mach number of 0.1732, well within the incompressible limit, is obtained. The velocities are assumed to be zero at the time of starting the simulations for all nodes.

Initially, the equilibrium particle distribution function that corresponds to the flow-variables is assumed as the unknown distribution function for all node at $t = 0$. Also a uniform fluid density $\rho = 1.0$ is imposed initially. The boundary conditions for parallel and antiparallel wall motion cases are shown in the Figure 4.1 (a) and 4.1 (b). The solution procedure of the LBM models at each time step comprise streaming and collision step, application of boundary conditions, calculation of particle distribution function followed by calculation of macroscopic variables. As the problem (for the square cavity with aspect ratio of unity) has not been investigated before, to lend

credibility to the results they are further compared with those obtained from a finite difference method (FDM) code developed for this purpose.

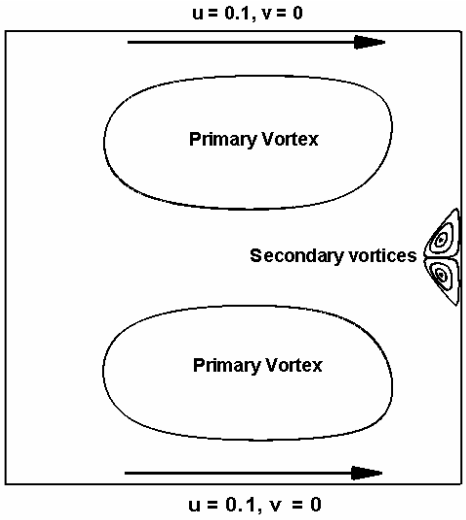

(a)

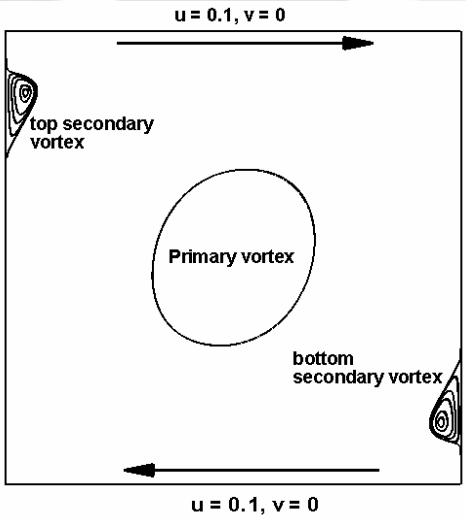

(b)

Figure 4.1: Two-Sided Lid-Driven Square Cavity for (a) parallel wall motion (b) antiparallel wall motion with LBM boundary conditions for the moving walls.

4.3.2. Stream Function-Vorticity Based Finite Difference Solver

The FD code the results of which provides a basis for comparison, numerically solves the 2D Navier-Stokes equations in the stream function-vorticity form given by

$$\frac{\partial^2 \psi}{\partial x^2} + \frac{\partial^2 \psi}{\partial y^2} = -\omega \tag{4.1}$$

$$\frac{\partial \omega}{\partial t} + u\frac{\partial \omega}{\partial x} + v\frac{\partial \omega}{\partial y} = \frac{1}{Re}\left(\frac{\partial^2 \omega}{\partial x^2} + \frac{\partial^2 \omega}{\partial y^2}\right). \tag{4.2}$$

More details of this code has already been given in chapter 3.

4.4. Parallel Wall Motion

Streamline patterns on a lattice size of 513 × 513 for the parallel wall motion using LBM-SRT model are shown in Figure 4.2. Here the upper and lower walls move in the same direction along the *x*-axis with the same velocity. The streamlines are found to be symmetrical with respect to a line parallel to these walls and passing through the cavity centre. Figure 4.2 (a) shows the streamline pattern for the parallel wall motion at *Re* = 100 with the top and bottom walls moving from the left to right. Two counter-rotating primary vortices symmetrical to each other are seen to form with a 'free-shear' layer in between. At this Reynolds number the primary vortex cores are seen to be somewhat away from the centres of the top and the bottom halves of the cavity towards the righthand top and righthand bottom corners respectively.

At *Re* = 400 (Figure 4.2 (b)), apart from the primary vortices a pair of counter-rotating secondary vortices symmetrically placed about the horizontal centreline are seen to

appear near the centre of the right wall. Figures 4.2 (c) and 4.2 (d) show the streamline patterns at Re = 1000 and Re = 2000 respectively. From Figure 4.2 it is observed that as the Reynolds number increases the cores of the primary vortices move from near the top right and bottom right corners towards the centres of the top and bottom halves of the cavity respectively. As the Reynolds number increases the secondary vortices near the centre of the right wall grow in size. The counter-rotating pairs of primary and secondary vortices maintain their symmetry at all the Reynolds numbers investigated here.

Figure 4.3 shows the vorticity contours for all the Reynolds numbers computed by the LBM-SRT model. As mentioned earlier the streamline patterns are now authenticated by comparison with the results given by the validated FDM code. Figure 4.4 shows the FDM streamline patterns on a 257 × 257 grid for Re = 100, 400, 1000 and 2000. Comparison with Figure 4.2 shows that LBM-SRT streamline patterns compare very well with those of the FDM. Figure 4.5 shows the vorticity contours for the various Reynolds numbers by the FDM. The present LBM code has second-order accuracy boundary conditions and it has been adequately validated, the flow details for this untested configuration should be accurate. A magnified view of the secondary vortices at Re = 1000 and obtained by the LBM-SRT and FDM for the parallel wall motion is shown in Figure 4.6. An extremely close agreement between the LBM-SRT and FDM results once again lends credibility to the LBM results.

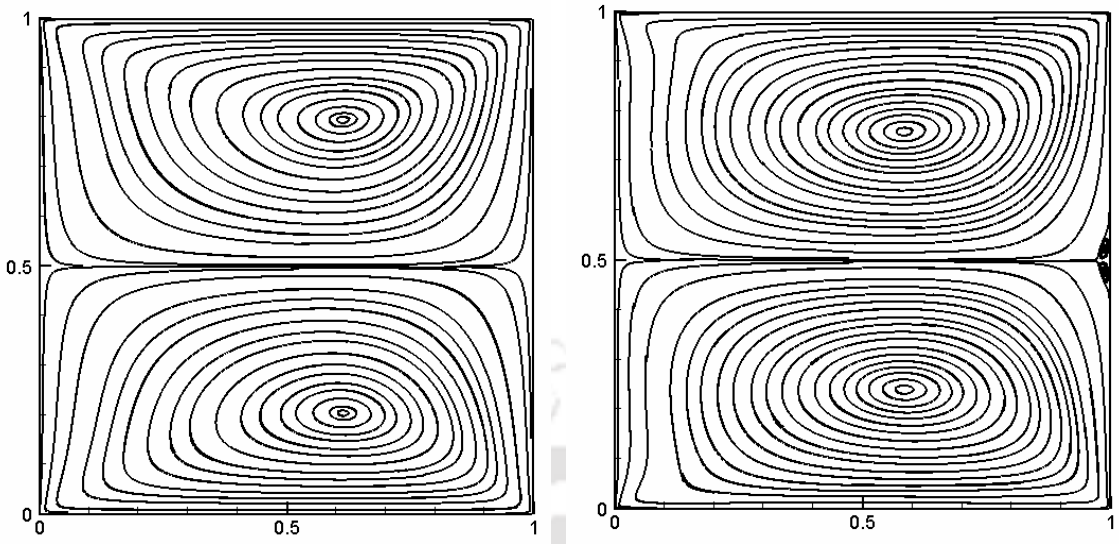

(a) Re = 100 (b) Re = 400

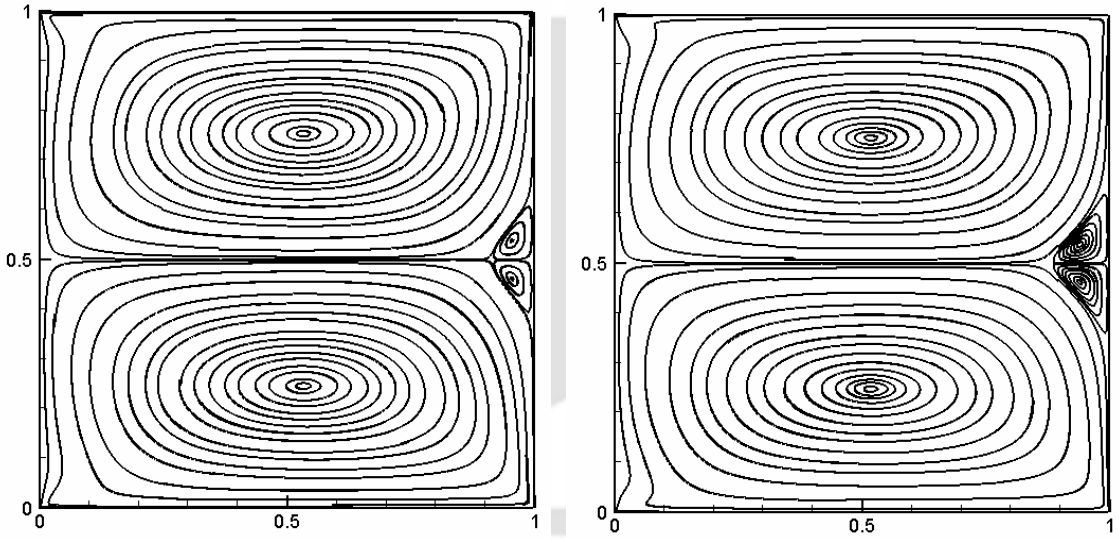

(a) Re = 1000 (b) Re = 2000

Figure 4.2: Streamline pattern for parallel wall motion at (a) Re = 100 (b) Re = 400 (c) Re = 1000 and (d) Re = 2000 by LBM-SRT model on a 513 × 513 lattice arrangement.

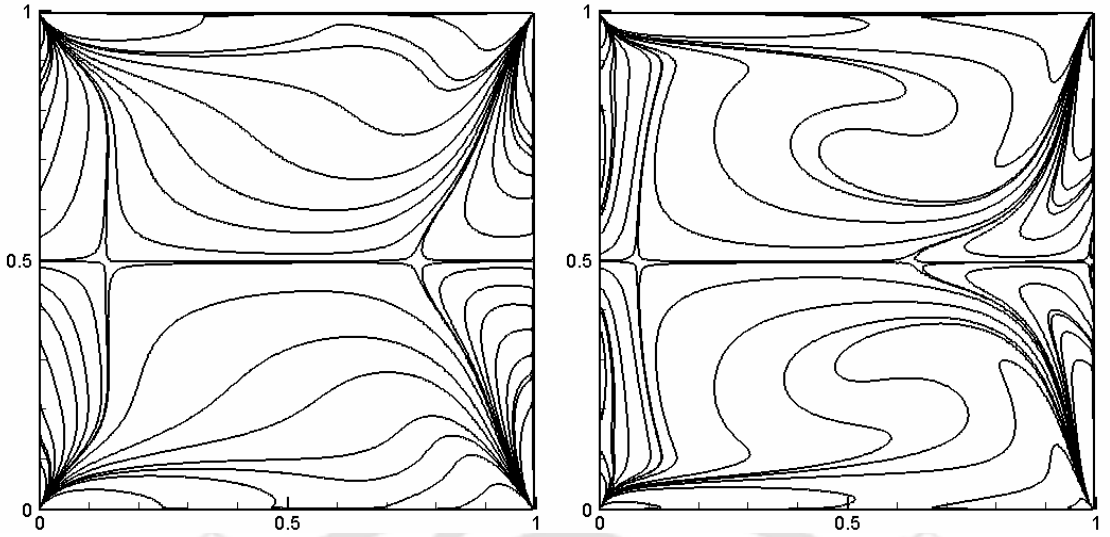

(a) Re = 100 (b) Re = 400

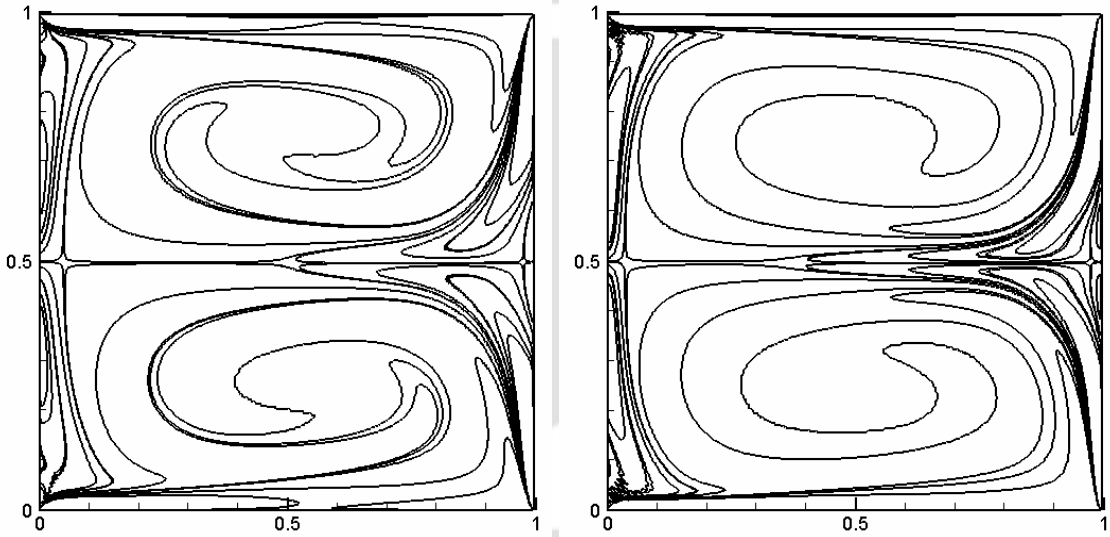

(a) Re = 1000 (b) Re = 2000

Figure 4.3: Vorticity contours for parallel wall motion at (a) Re = 100 (b) Re = 400 (c) Re = 1000 and (d) Re = 2000 by LBM-SRT model on a 513 × 513 lattice arrangement.

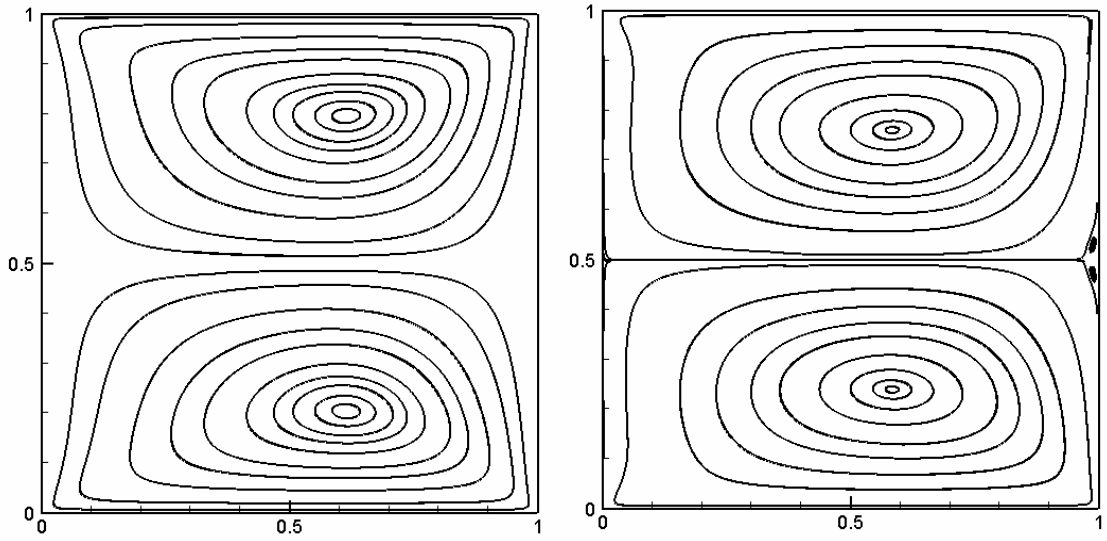

(a) *Re* = 100 (b) *Re* = 400

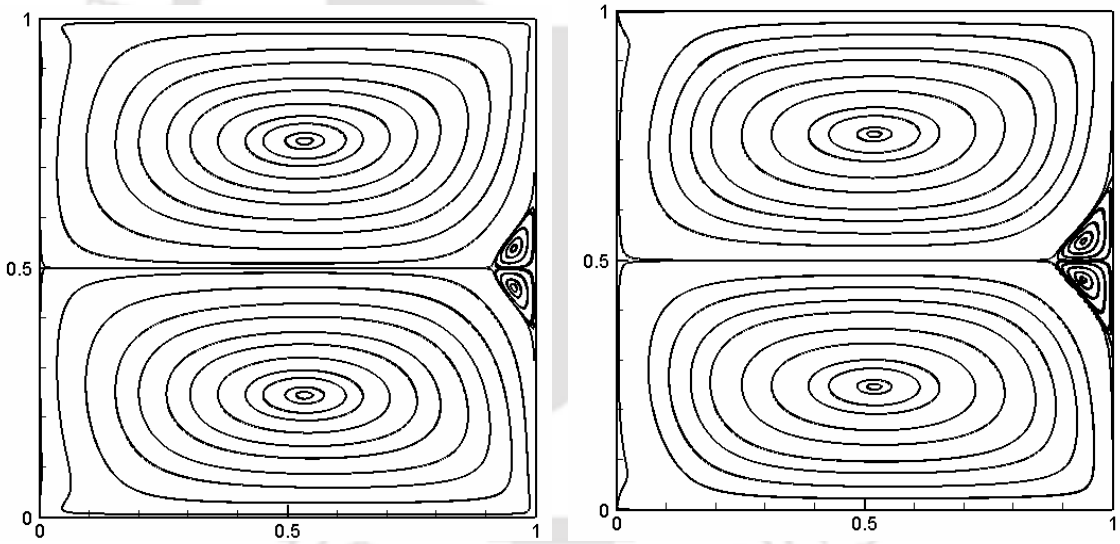

(a) *Re* = 1000 (b) *Re* = 2000

Figure 4.4: Streamline pattern for parallel wall motion at (a) *Re* = 100 (b) *Re* = 400 (c) *Re* = 1000 and (d) *Re* = 2000 by FDM on a 257 × 257 grid.

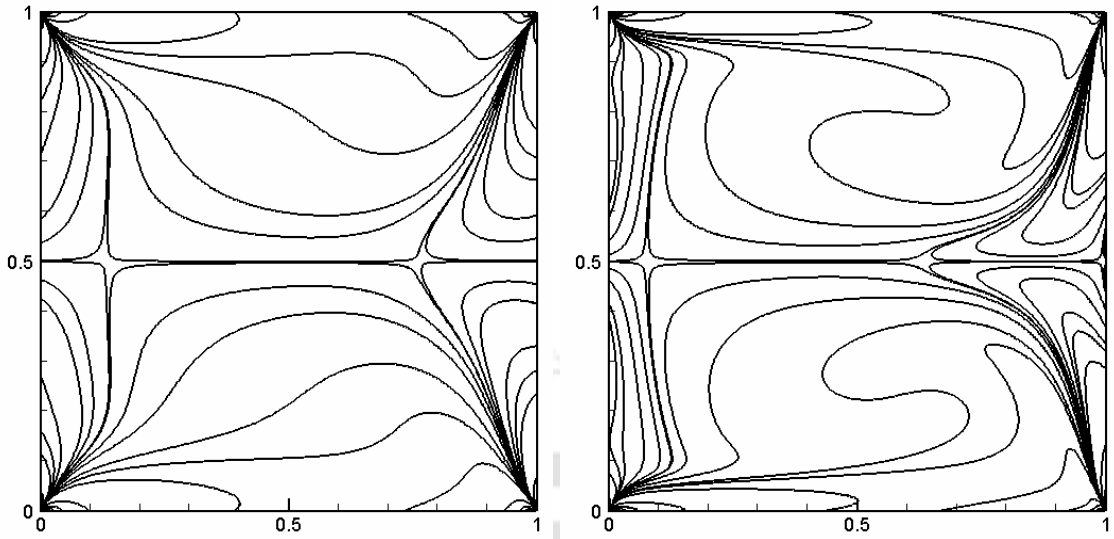

(a) $Re = 100$ (b) $Re = 400$

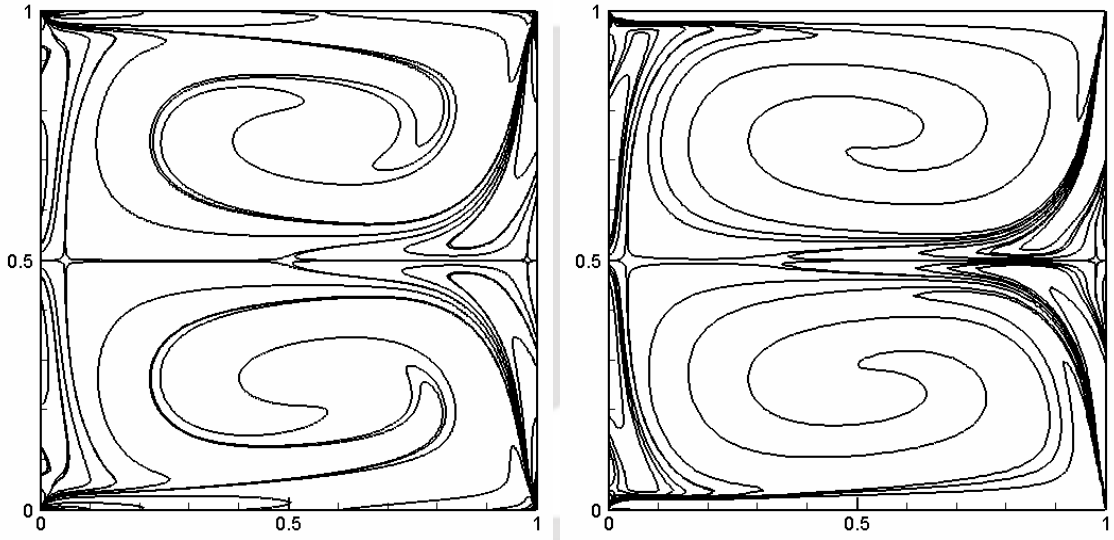

(a) $Re = 1000$ (b) $Re = 2000$

Figure 4.5: Vorticity contours for parallel wall motion at (a) $Re = 100$ (b) $Re = 400$ (c) $Re = 1000$ and (d) $Re = 2000$ by FDM on a 257×257 grid.

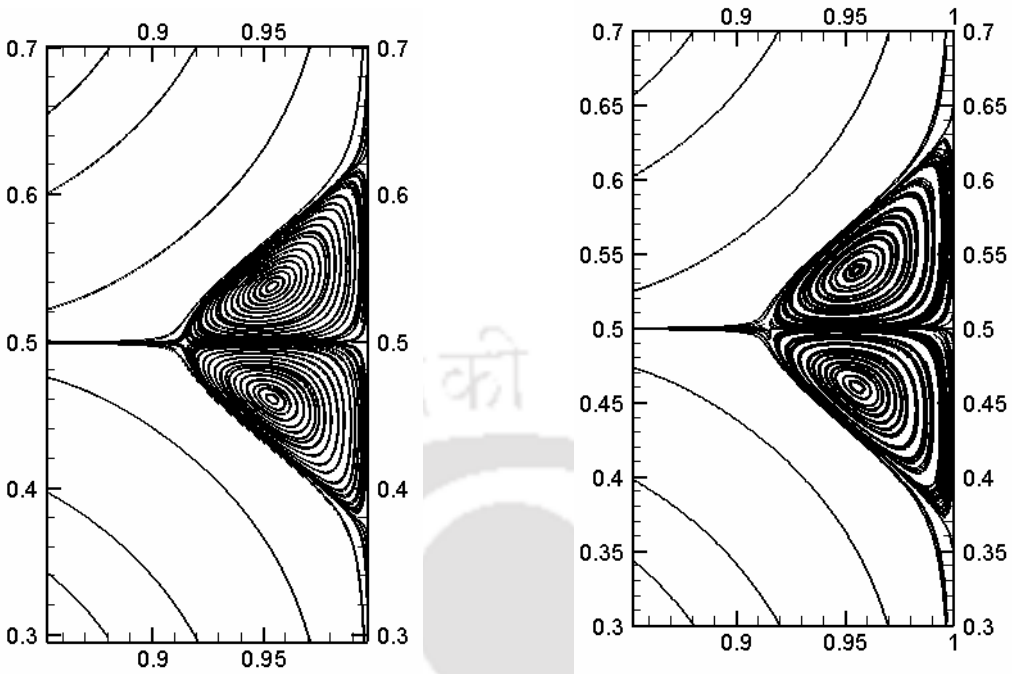

Figure 4.6: A magnified view of secondary vortices (a) Parallel wall motion LBM-SRT model (Re = 1000) (b) Parallel wall motion FDM (Re = 1000).

Figures 4.7-4.10 show the comparison of the LBM-SRT, LBM-MRT and FDM for horizontal velocity profiles along vertical lines and vertical velocity profiles along horizontal lines passing through different points of the cavity for various Reynolds numbers. Agreement of the velocity profiles given by both the methods is once again excellent. LBM-MRT model is also used to compute the flow. Table 4.1 gives the locations of the vortices given by the LBM-SRT, LBM-MRT and FDM for Re = 100, 400, 1000, 1500 and 2000. Considering the fact that the present FDM code has second-order spatio-temporal accuracy and it has been adequately validated, the listings of various flow details for this untested configuration should be accurate. All these results show that the agreement is very good, which further substantiates the accuracy of the

LBM computations. We thus accurately list various flow details for this unexplored configuration.

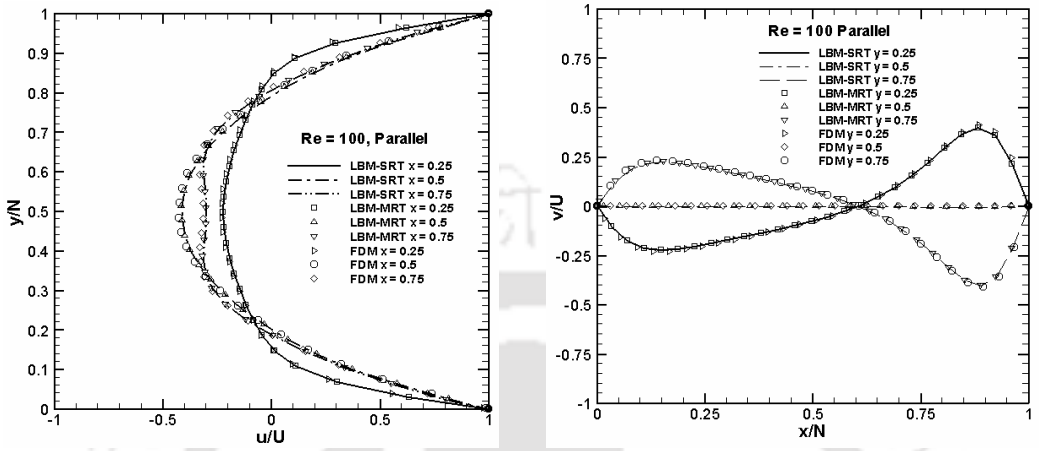

Figure 4.7: Parallel wall motion, *Re* = 100: (a) horizontal velocity *u* along vertical lines (b) vertical velocity *v* along horizontal lines passing through *y* = 0.25, 0.50 and 0.75.

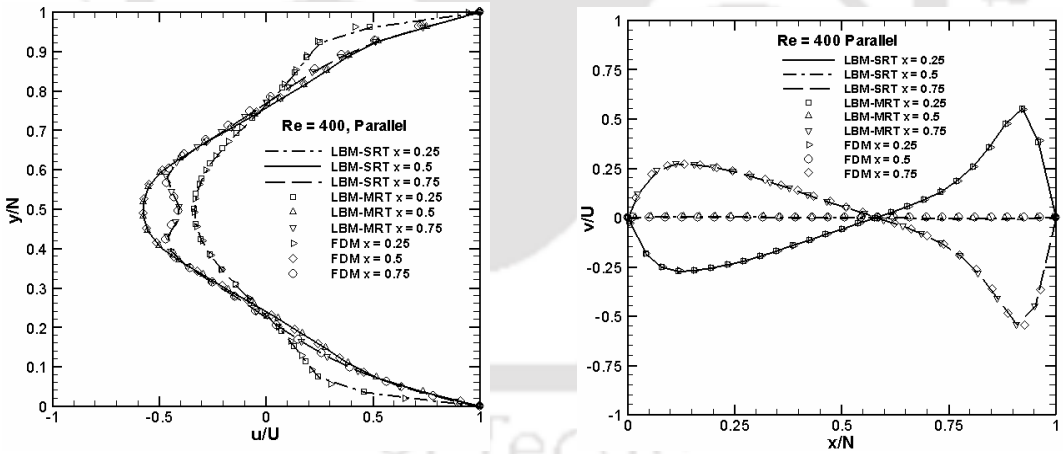

Figure 4.8: Parallel wall motion, *Re* = 400: (a) horizontal velocity *u* along vertical lines (b) vertical velocity *v* along horizontal lines passing through *y* = 0.25, 0.50 and 0.75.

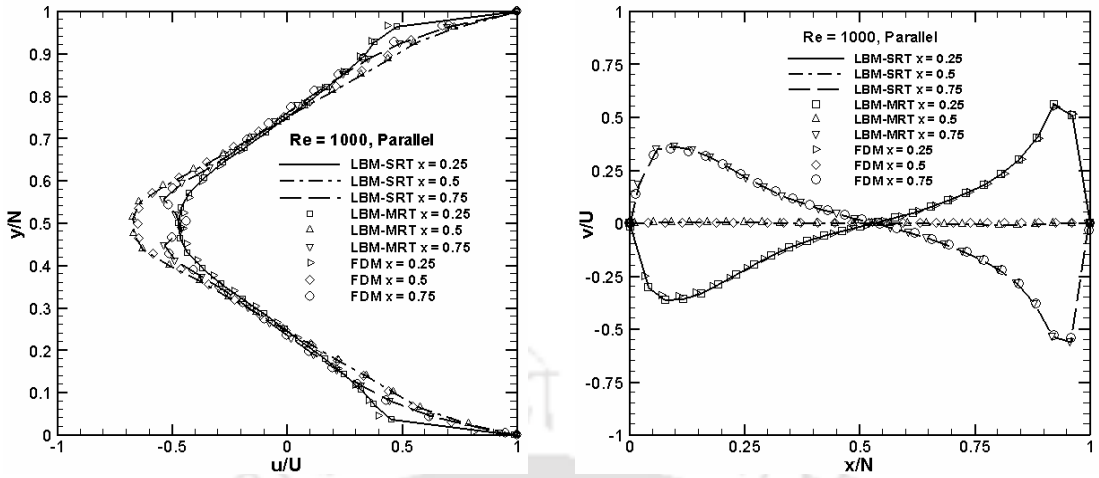

Figure 4.9: Parallel wall motion, *Re* = 1000: (a) horizontal velocity *u* along vertical lines (b) vertical velocity *v* along horizontal lines passing through *y* = 0.25, 0.50 and 0.75.

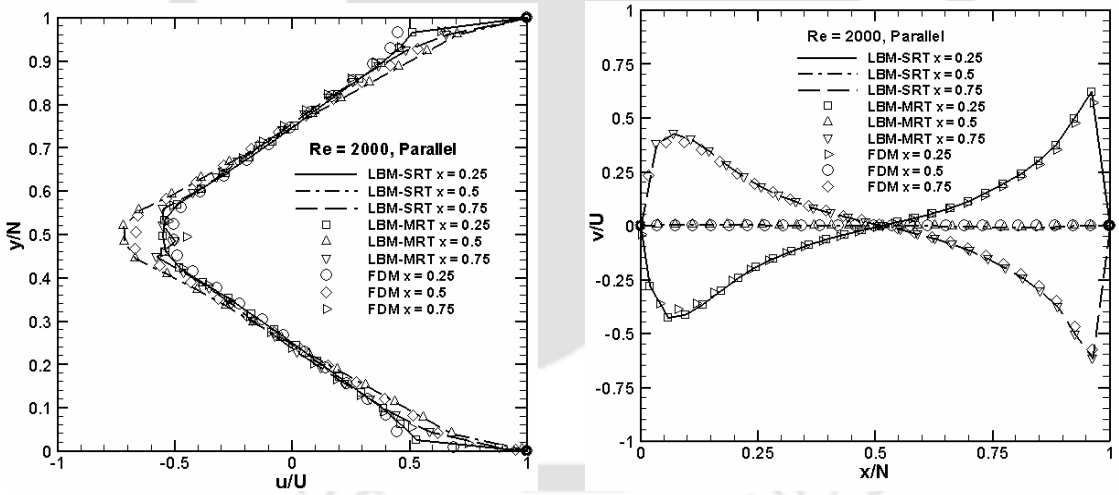

Figure 4.10: Parallel wall motion, *Re* = 2000: (a) horizontal velocity *u* along vertical lines (b) vertical velocity *v* along horizontal lines passing through *y* = 0.25, 0.50 and 0.75.

Table 4.1: Locations of the vortices for parallel wall motion: **a.** FDM, **b.** LBM-SRT Model and **c.** LBM-MRT Model.

Re	Primary vortex centres				Secondary vortex centres			
	Bottom		Top		Bottom		Top	
	x	*y*	*x*	*y*	*x*	*y*	*x*	*y*
100	**a.** 0.6145 **b.** 0.6146 **c.** 0.6146	0.2026 0.2027 0.2025	0.6145 0.6146 0.6145	0.7959 0.7957 0.7951	---- ---- ----	---- ---- ----	---- ---- ----	---- ---- ----
400	**a.** 0.5845 **b.** 0.5846 **c.** 0.5844	0.2388 0.2389 0.2386	0.5845 0.5846 0.5844	0.7553 0.7552 0.7550	0.9873 0.9874 0.9875	0.4638 0.4653 0.4658	0.9873 0.9874 0.9871	0.5264 0.5273 0.5273
1000	**a.** 0.5354 **b.** 0.5342 **c.** 0.5324	0.2452 0.2438 0.2432	0.5354 0.5342 0.5328	0.7547 0.7552 0.7556	0.9551 0.9542 0.9531	0.4570 0.4697 0.4678	0.9551 0.9542 0.9538	0.5409 0.5391 0.5389
1500	**a.** 0.5246 **b.** 0.5239 **c.** 0.5241	0.2452 0.2438 0.2435	0.5251 0.5239 0.5241	0.7527 0.7521 0.7517	0.9443 0.9439 0.9441	0.4569 0.4571 0.4564	0.9444 0.9439 0.9432	0.5429 0.5342 0.5328
2000	**a.** 0.5132 **b.** 0.5108 **c.** 0.5121	0.2474 0.2489 0.2469	0.5132 0.5108 0.5115	0.7528 0.7497 0.7465	0.9400 0.9378 0.9385	0.4573 0.4598 0.4562	0.9400 0.9377 0.9367	0.5478 0.5389 0.5374

4.5. Antiparallel Wall Motion

Streamline patterns on a lattice size of 513×513 for the antiparallel wall motion using LBM-SRT model are shown in Figure 4.11. Here the upper and lower walls move in opposite directions along the *x*-axis with the same velocity. A single primary vortex centred at the geometric centre of the cavity is formed at low Reynolds numbers (Figures 4.11 (a) and 4.11 (b)). These two figures show the streamline patterns for *Re* = 100 and 400 respectively.

Figures 4.11 (c) and 4.11 (d) depict the streamline patterns for Re = 1000 and 2000 showing the appearance of two secondary vortices near the top left and the bottom right corners of the cavity and a very small shift of the primary vortex centre from the geometric centre of the cavity. It may be noted that the corresponding secondary vortex for a single lid-driven cavity flow does not appear at a Reynolds number as low as 1000 but much beyond that (at some value higher than 1000). It has also been observed that the primary vortex centre remains very close to the geometric centre of the cavity even for these higher values of Re = 1000 and 2000. However the size of the secondary vortices are seen to increase between Re = 1000 and 2000. Similar increase in the size of the secondary vortices with Reynolds numbers was also observed for the parallel wall motion. Figure 4.12 shows the vorticity contours for the various Reynolds numbers computed by the LBM-SRT model.

Figure 4.13 gives for the same configuration the FDM streamline patterns on a 257 × 257 grid for Re = 100, 400, 1000 and 2000. Comparison with Figure 4.11 shows that LBM-SRT streamline patterns compare very well with those of the FDM. Figure 4.14 shows the vorticity contours for the Reynolds numbers computed by the FDM. Once again a close resemblance of these contours is observed with those of the LBM-SRT given in Figure 4.12. A magnified view of the secondary vortices (the ones at the top left corner) at Re = 1000 given by the LBM-SRT and FDM is shown in Figure 4.15. The results include figures and tables that record the details of several flow features like position of the vortex centres and their sizes. The agreement is found to be very good.

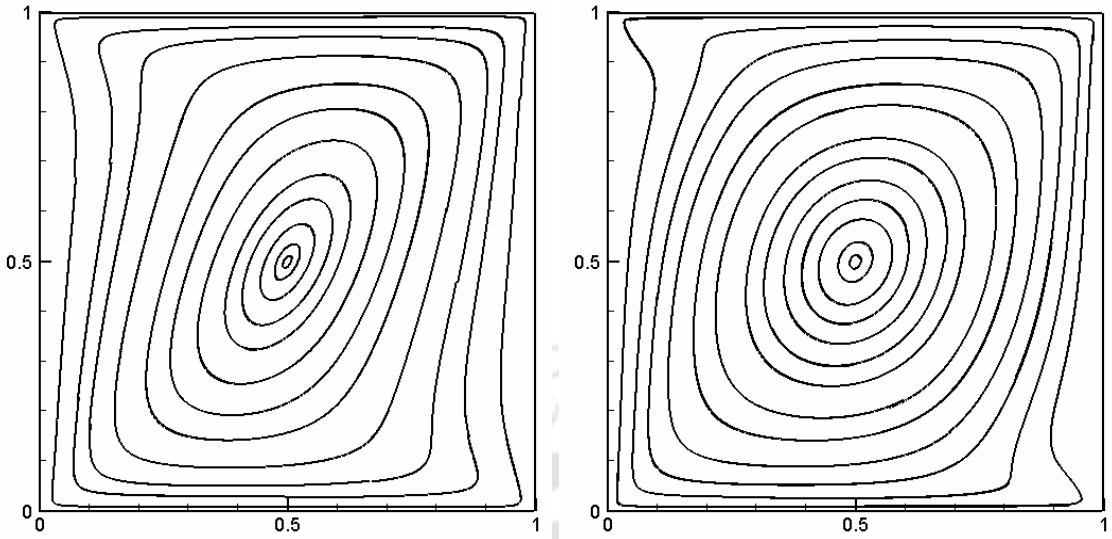

(a) Re = 100 (b) Re = 400

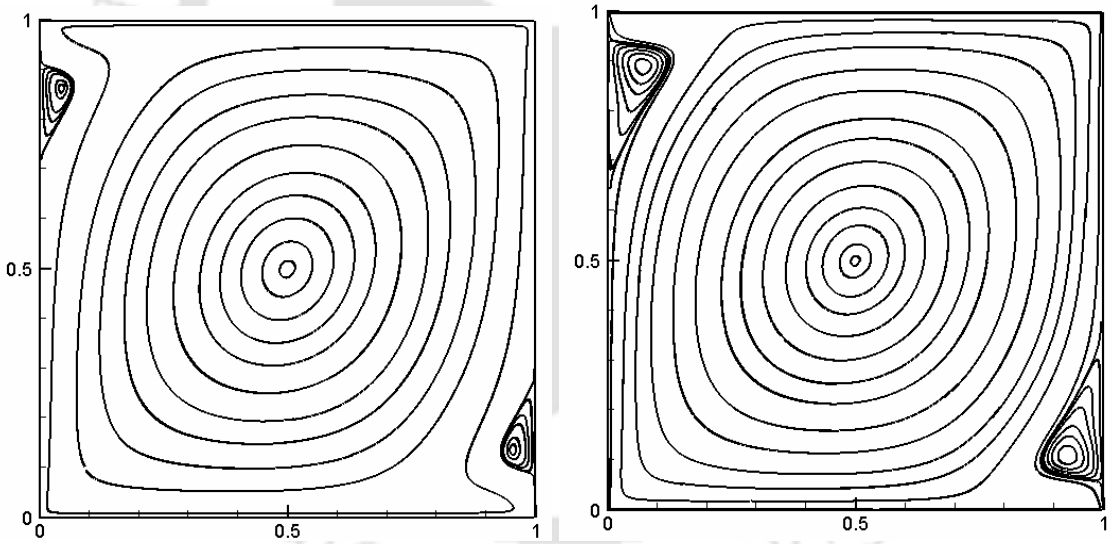

(a) Re = 1000 (b) Re = 2000

Figure 4.11: Streamline pattern for antiparallel wall motion at (a) Re = 100 (b) Re = 400 (c) Re = 1000 and (d) Re = 2000 by LBM-SRT model on a 513 × 513 lattice arrangement.

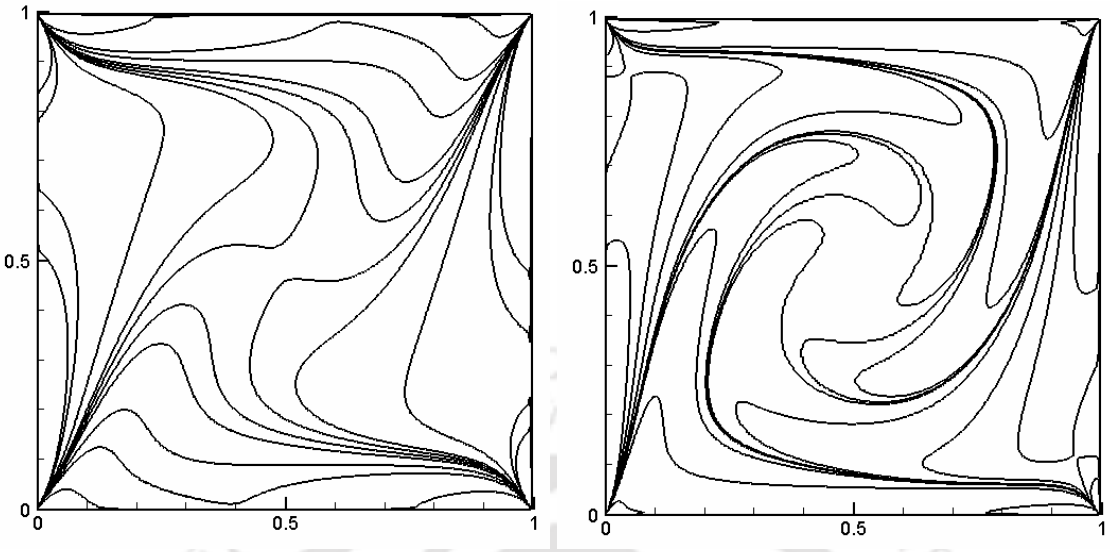

(a) Re = 100 (b) Re = 400

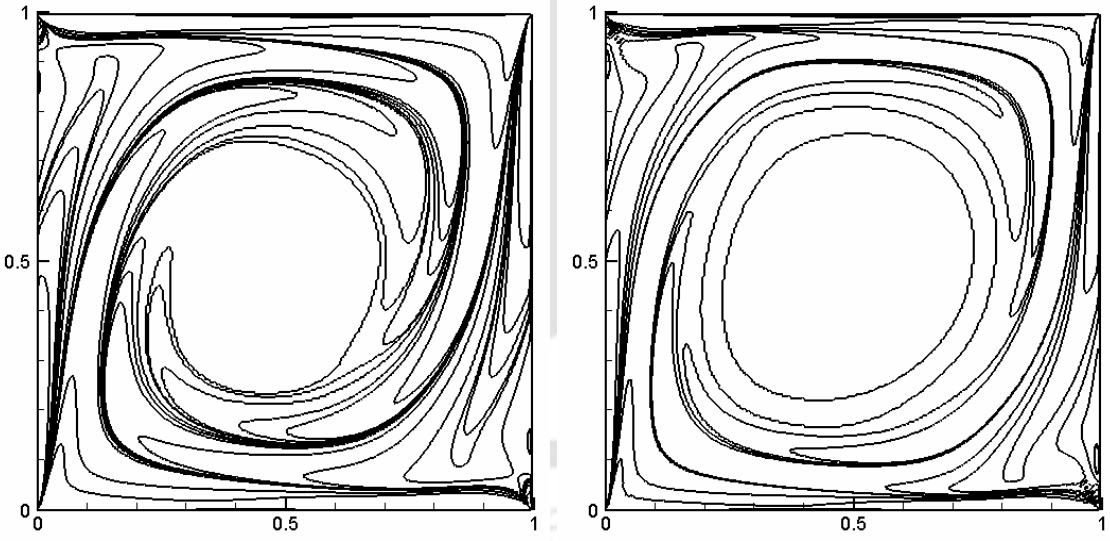

(a) Re = 1000 (b) Re = 2000

Figure 4.12: Vorticity contours for antiparallel wall motion at (a) Re = 100 (b) Re = 400 (c) Re = 1000 and (d) Re = 2000 by LBM-SRT model on a 513 × 513 lattice arrangement.

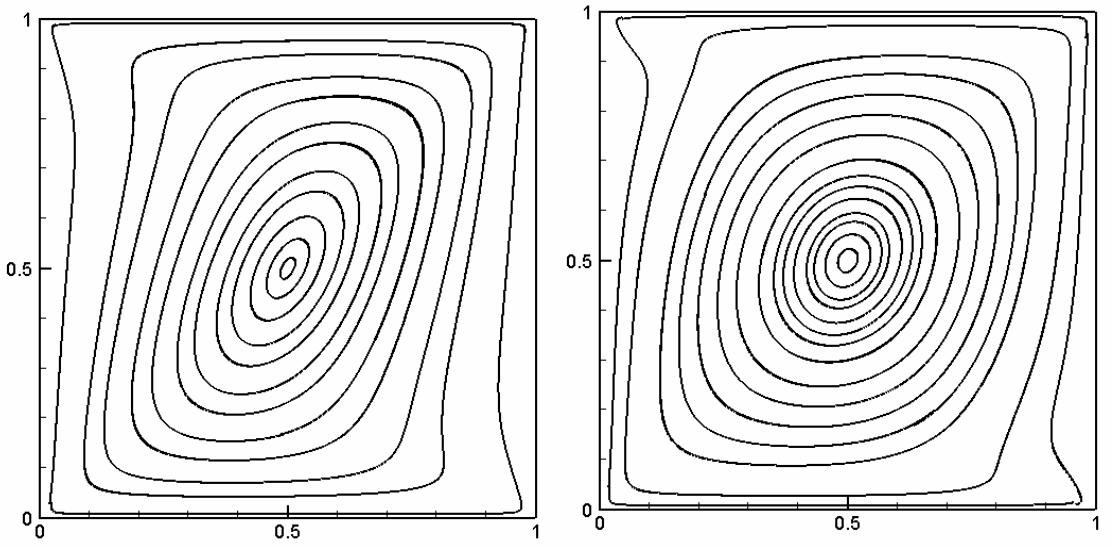

(a) Re = 100 (b) Re = 400

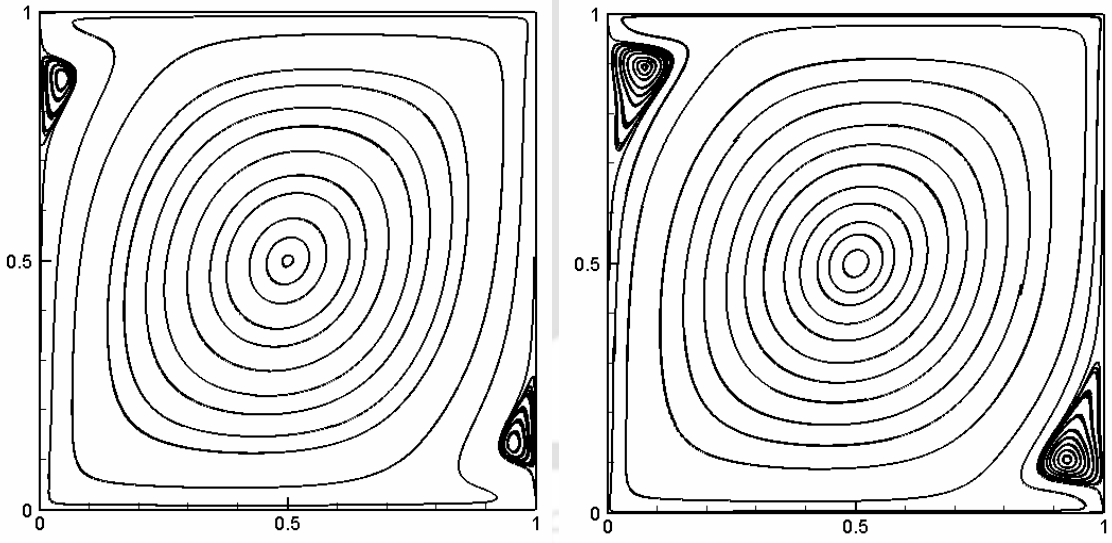

(a) Re = 1000 (b) Re = 2000

Figure 4.13: Streamline pattern for antiparallel wall motion at (a) Re = 100 (b) Re = 400 (c) Re = 1000 and (d) Re = 2000 by FDM on a 257 × 257 grid.

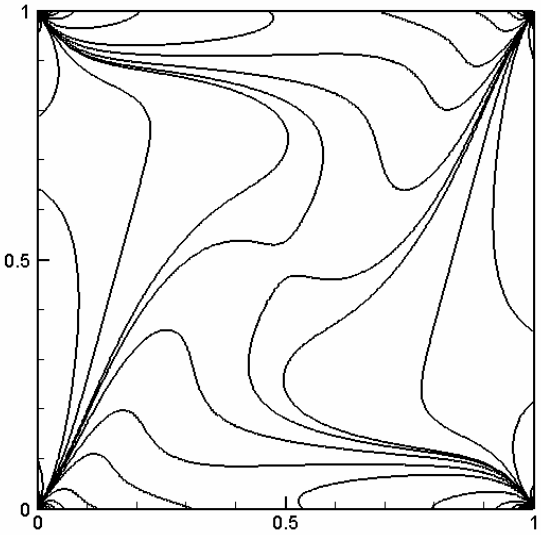

(a) Re = 100

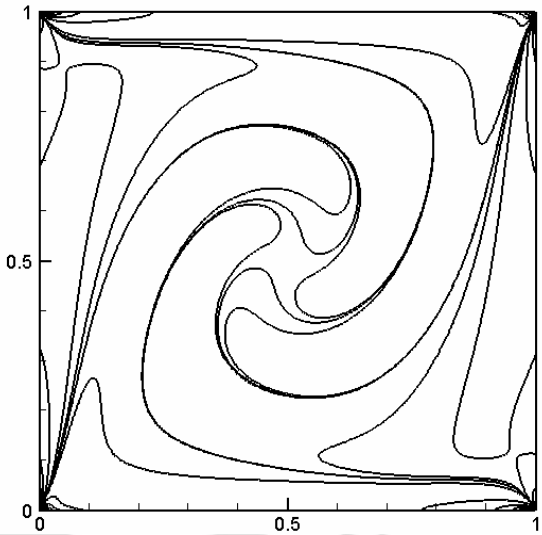

(b) Re = 400

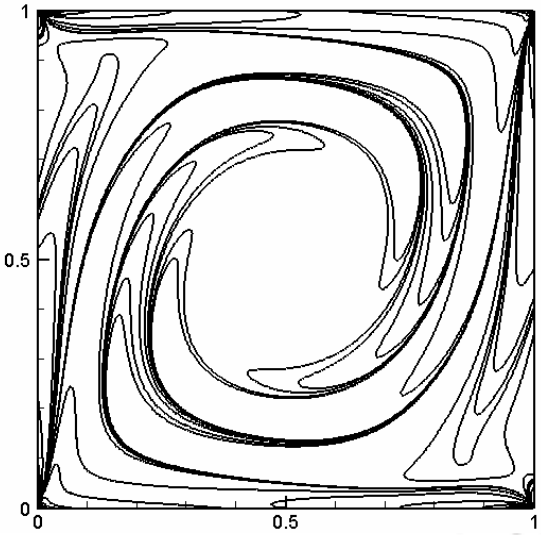

(a) Re = 1000

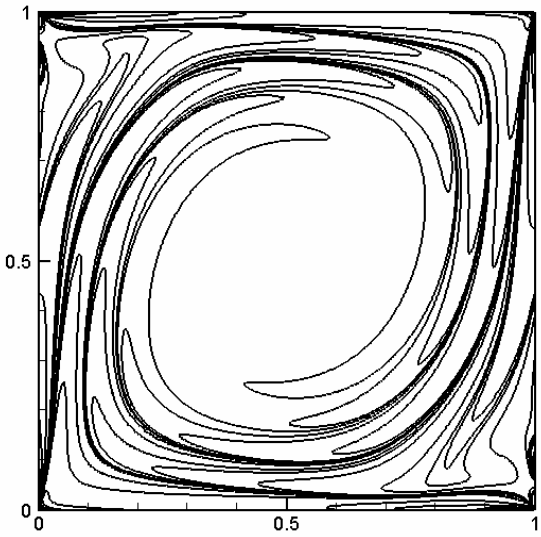

(b) Re = 2000

Figure 4.14: Vorticity contours for antiparallel wall motion at (a) Re = 100 (b) Re = 400 (c) Re = 1000 and (d) Re = 2000 by FDM on a 257 × 257 grid.

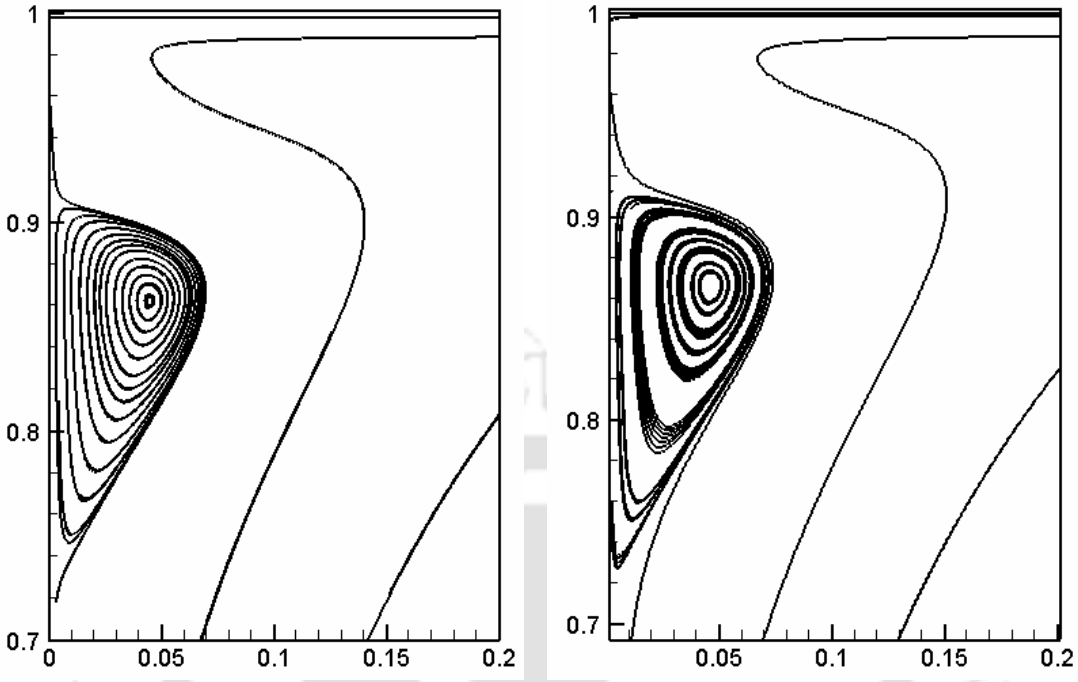

Figure 4.15: A magnified view of secondary vortices (a) antiparallel wall motion LBM-SRT model (*Re* = 1000) (b) antiparallel wall motion FDM (*Re* = 1000).

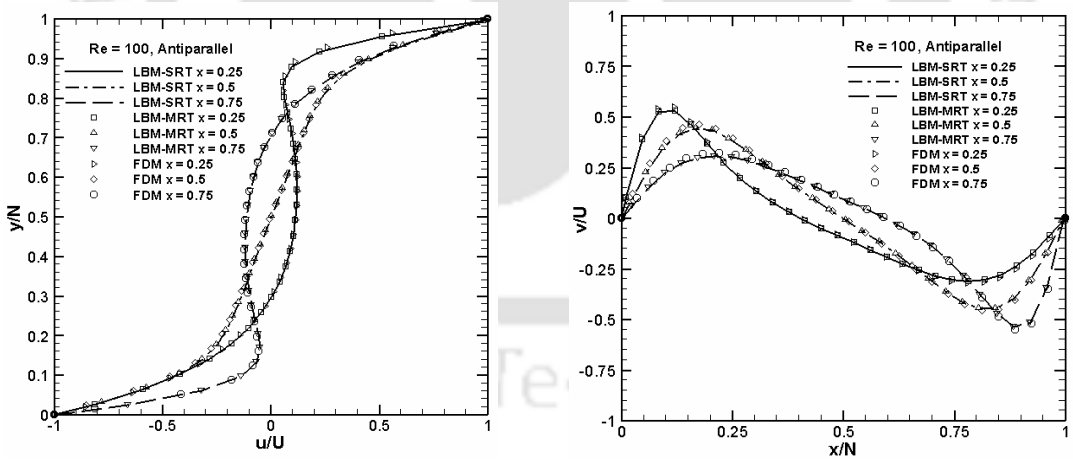

Figure 4.16: Antiparallel wall motion, *Re* = 100: (a) horizontal velocity *u* along vertical lines (b) vertical velocity *v* along horizontal lines passing through *y* = 0.25, 0.50 and 0.75.

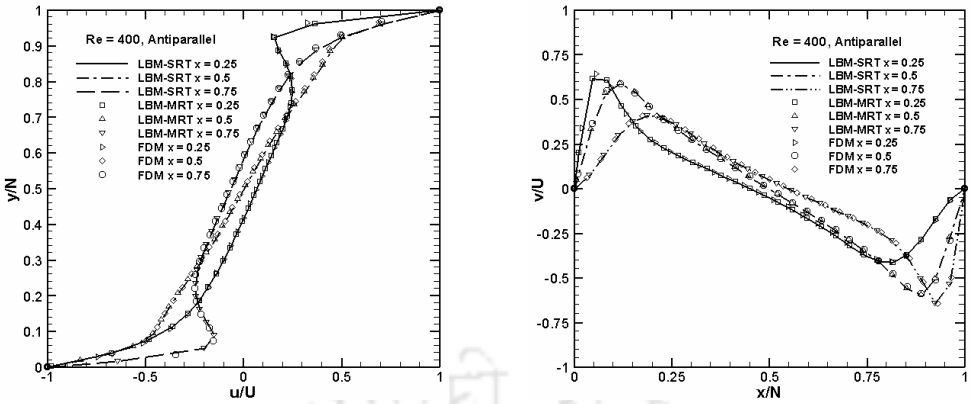

Figure 4.17: Antiparallel wall motion, *Re* = 400: (a) horizontal velocity *u* along vertical lines (b) vertical velocity *v* along horizontal lines passing through *y* = 0.25, 0.50 and 0.75.

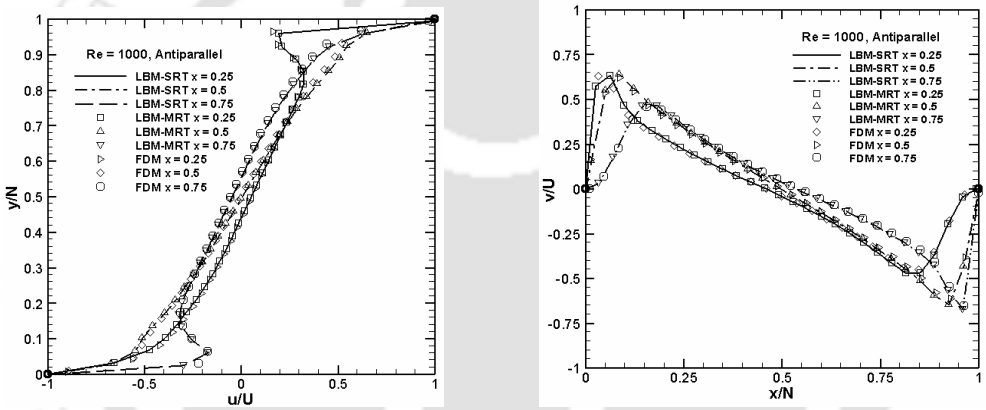

Figure 4.18: Antiparallel wall motion, *Re* = 1000: (a) horizontal velocity *u* along vertical lines (b) vertical velocity *v* along horizontal lines passing through *y* = 0.25, 0.50 and 0.75.

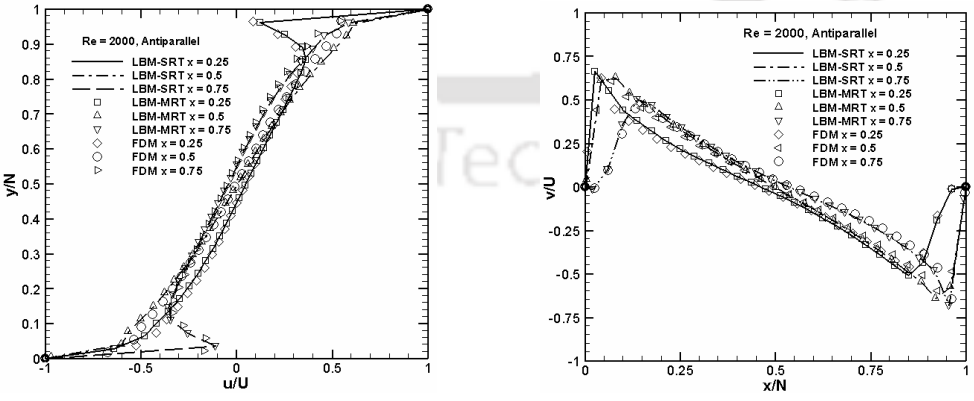

Figure 4.19: Antiparallel wall motion, *Re* = 2000: (a) horizontal velocity *u* along vertical lines (b) vertical velocity *v* along horizontal lines passing through *y* = 0.25, 0.50 and 0.75.

Figures 4.16-4.19 show the comparisons the LBM-SRT, LBM-MRT and FDM for horizontal velocity profiles along vertical lines and vertical velocity profiles along horizontal lines passing through different points of the cavity for the various Reynolds numbers. It is seen that, the quantitative comparison of the velocity profiles obtained by the present LBM models and those obtained through the other FDM model excellent. Table 4.2 gives the locations of the vortices given by the LBM-SRT, LBM-MRT and FDM for *Re* = 100, 400, 1000, 1500 and 2000. Clearly the results given by the LBM agree very well with those of the FDM. We thus see that the LBM results presented in all the figures and tables are in excellent agreement with the FDM results produced through the validated code. This lends credibility to the current LBM results for this hitherto unexplored problem.

Table 4.2: Locations of the vortices for parallel wall motion: **a.** FDM, **b.** LBM-SRT Model and **c.** LBM-MRT Model.

Re	Primary Vortex (PV)		Secondary Vortices (SV)			
	x	*y*	Bottom Right		Top Left	
			x	*y*	*x*	*y*
100	**a.** 0.5001 **b.** 0.5002 **c.** 0.5002	0.5002 0.5001 0.5001	… …	… …	… …	… …
400	**a.** 0.5002 **b.** 0.5001 **c.** 0.5003	0.4981 0.4982 0.4979	… … …	… … …	… … …	… … …
1000	**a.** 0.5009 **b.** 0.5011 **c.** 0.5010	0.4980 0.4981 0.4979	0.9507 0.9499 0.9495	0.1319 0.1324 0.1327	0.0492 0.0478 0.0471	0.8663 0.8637 0.8639
1500	**a.** 0.5007 **b.** 0.5009 **c.** 0.5008	0.4982 0.4981 0.4979	0.9308 0.9317 0.9312	0.1156 0.1169 0.1162	0.0692 0.0681 0.0676	0.8856 0.8841 0.8847
2000	**a.** 0.5002 **b.** 0.5003 **c.** 0.5002	0.5001 0.4996 0.4998	0.9227 0.9238 0.9232	0.1082 0.1081 0.1079	0.0771 0.0761 0.0762	0.8920 0.8875 0.8899

4.6. Two-Sided Lid-Driven Rectangular Cavity Flow

4.6.1. Parallel Wall Motion

An incompressible viscous flow in a rectangular cavity (Aspect ratio K=2) whose top and bottom walls move in the same (parallel motion) direction with a uniform velocity is now investigated. This is similar to the previous problem (Figure 4.1 (a)) except for the aspect ratio. Figure 4.20 shows the flow patterns of for a Reynolds number of 700 with an aspect ratio of 2. It is seen that, the induced primary and secondary vortices and the streamlines are symmetric with respect to the horizontal centreline of the cavity. Though FDM results are not presented here, we have observed that the flow patterns obtained by the present LBM-SRT model and by FDM agree very well with each other.

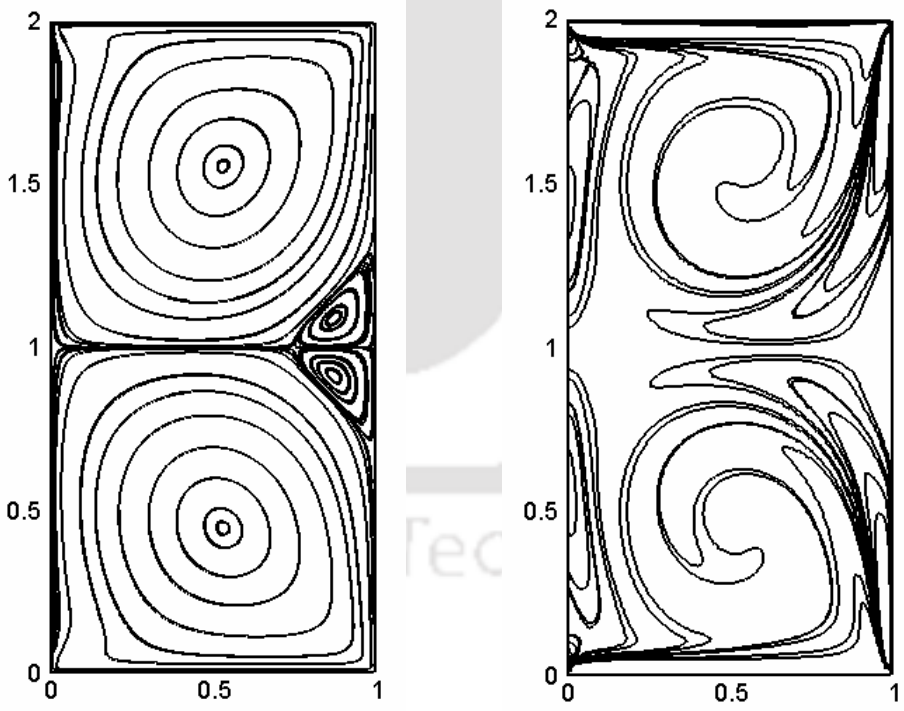

Figure 4.20: (a) Streamline pattern (b) Vorticity contour for parallel wall motion at Re = 700 with aspect ratio 2.0.

4.6.2. Antiparallel Wall Motion

An incompressible viscous flow in a rectangular cavity, whose top wall moves to the right and bottom wall moves to the left with a uniform velocity is now computed through LBM. This configuration is similar to the one given by Figure 4.1(b) except for the aspect ratio. Figure 4.21 shows the flow patterns for a Reynolds number of 700 with an aspect ratio of 2. Here, the near-wall primary vortices have the same sense of rotation and are well-separated as the aspect ratio is large. It is also seen that, the vortices and the streamlines are point symmetric with respect to the geometric centre of the cavity. We also observe that the flow patterns obtained by the present LBM-SRT model agree well with those given by Khulmann and other investigators [91, 92, 94].

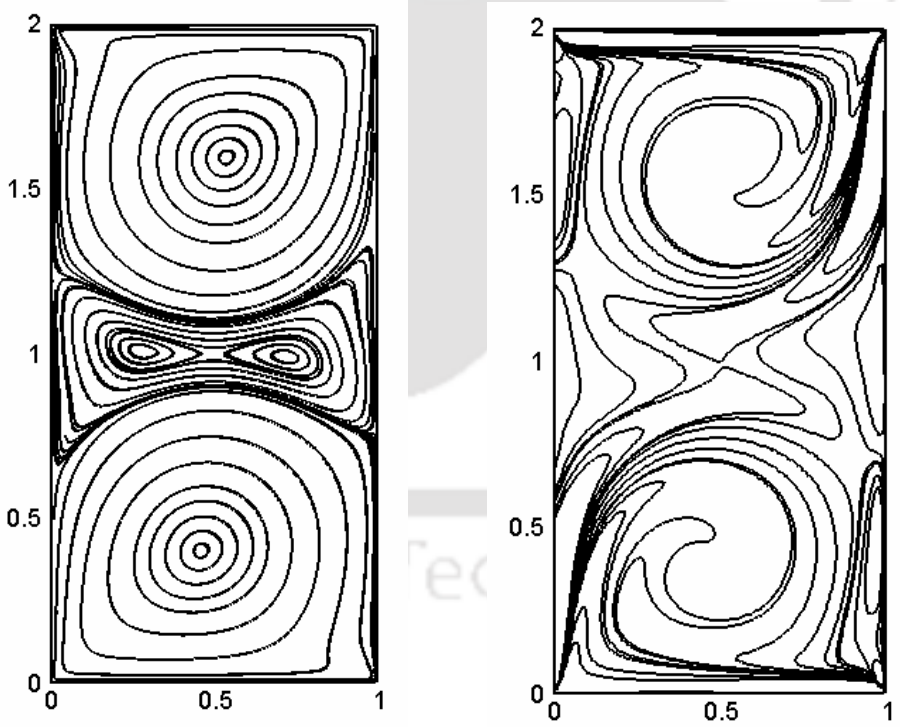

Figure 4.21: (a) Streamline pattern (b) Vorticity contours, for antiparallel wall motion at *Re* = 700 with aspect ratio 2.0.

4.7. Conclusion

In this chapter the flow in an unexplored configuration, the two-sided lid-driven square cavity for the parallel and anti-parallel wall motion is computed with the LBM-SRT and LBM-MRT models. This flow configuration is fraught with many interesting issues in that in the case of parallel wall motion it involves development of a pair of off-corner vortices and a 'free-shear' layer and in the case of anti-parallel wall motion it exhibits corner vortices that appear at a lower Reynolds number compared with the single sided lid-driven square cavity. As the flow configuration is new and the Lattice Boltzmann method is a relatively novel technique of flow computation, there is some scope for speculation as to the accuracy of the present LBM computations. Therefore, to create a basis for substantiating the results another FDM code for the stream function-vorticity form of the Navier-Stokes equations based on central differencing and ADI time integration is developed. This code has second order spatio-temporal accuracy and it is used to produce steady results in a time-marching fashion. The close agreement of the LBM results with FDM results produced on sufficiently fine grids lends physical legitimacy to the computations. Finer lattices and grids are used in the computations, because it would resolve the corner vortices better. As the present computations for the flow situations explored have no predecessor, these results provide an important basis to future investigators to compare their results with. Consequently, the present flow configuration and results, like those of the single lid-driven cavity flow, may be used for validating the algorithms for computing steady flows governed by the two-dimensional incompressible Navier-Stokes equations. Towards the end, we also briefly give the results for a deep cavity for both parallel and antiparallel wall motion at $Re = 700$.

Chapter 5

Simulation of Two-Dimensional Cavity Flows with Multiple Steady Solutions

5.1. Introduction

The uniqueness of steady flows is almost an article of faith for all researchers. For a given geometry and boundary conditions the flow field should generally be unique. But lid-driven cavity flows provide interesting counter examples to shake this believe. It is already mentioned that cavity flows arise in applications such as short-dwell coating, drag-reducing riblets in aerodynamics, removal of species from structured surfaces, mixing and flow in drying devices. Aidun *et al.* [74] pointed out in the coating industry the processes do not always behave the same way under identical operating conditions. They concluded that this may be caused by the multiplicity of permissible flow states [74]. Conventional numerical solutions reveal that in a single-sided lid-driven cavity flow beyond a critical Reynolds number Hopf bifurcation takes place with the steady-flow solution becoming unstable. The single-sided lid-driven cavity flow problem was extended to two-sided lid-driven cavity by Kuhlmann and other investigators [75, 91-94] and they have done several experiments on the two-sided lid-driven cavity with various aspect ratios. They numerically simulated the rectangular cavity flow for parallel and antiparallel motion of two of the walls and showed that a plethora of vortex patterns can

be generated with different aspect ratios and directions of motion of the walls. Many nonlinear systems give multiple steady solutions even though governing equations and boundary conditions are the same. The concept of uniqueness of numerical solution associated with the so called well-posed nature of the problem is not applicable here as nonuniqueness of solution is an inherent property of these types of problems. An analogy can be drawn with the algebraic quadratic equation that has two solutions. As the governing equations for fluid flow are nonlinear in nature, the possibility of their multiple solutions exists. In the case of lid-driven cavity flows multiple solutions are generally observed only if the walls move in pairs. In case of parallel motion of two facing walls, multiple solutions are seen to exist only in cavities with aspect ratios other than one, i.e. in rectangular cavities. Albensoeder *et al.* [75] were among the first to investigate the nonlinear regime and find multiple two-dimensional steady states in rectangular two-sided lid-driven cavities. They have found five and seven flow states in parallel and antiparallel motion respectively. However, if the nonfacing walls of the cavity move, multiple steady solutions are observed even in square cavities [76].

Luo and Yang [98] numerically investigated flow bifurcation with and without heat transfer in a two-sided lid-driven rectangular cavity. More recently, the multiplicity of flow states induced by the motion of two-sided non-facing lid-driven square cavity flow and four-sided lid-driven cavity flow have been investigated by Wabha [76]. He found the critical Reynolds numbers of 1073 for the two-sided non-facing lid-driven square cavity and 129 for the four-sided lid-driven square cavity, beyond which it is possible for multiple steady states to exist.

So far conventional methods like Finite Volume Method (FVM), Finite Difference Method (FDM) etc. are being used to capture the multiple solutions for cavity flows. It is known that the Lattice Boltzmann Method is an alternative way of fluid simulation to conventional numerical methods for the Navier-Stokes equation [99]. In LBM the nonlinearity of the Navier-Stokes equations is hidden in the quadratic velocity terms of the equilibrium distribution function. Therefore, LBM appears to have the ability to capture multiple solutions. However, so far no investigation is seen that uses LBM to capture multiple solutions. The present work is an attempt in that direction. The present work is concerned with the computation of two-sided, four-sided lid-driven square cavity and two-sided lid-driven rectangular cavity flows by Lattice Boltzmann Method (LBM) and obtaining multiple steady solutions. In the two-sided square cavity two of the adjacent walls move with equal velocity and in the four-sided square cavity all the four walls move in such a way that parallel walls move in opposite directions with the same velocity. Conventional numerical solutions show that the symmetric solutions exist for all Reynolds numbers whereas multiplicity of states of one symmetric and two asymmetric solutions for two-sided and four-sided cavity flows are identified above the critical Reynolds number. Generally, to obtain multiple steady solutions through conventional techniques one uses an iterative solution procedure with different initial conditions. Here we demonstrate that Lattice Boltzmann method also has the ability to capture multiple steady solutions at post-critical Reynolds numbers for both the two-sided and four-sided cavity flows. The strategy employed to obtain these solutions is also described.

This chapter is organized in five sections. In section 5.2 the credibility of the present LBM-SRT code is established through a comparison exercise with the results of two

other works. Section 5.3 gives the strategy employed to capture the multiple-steady solutions and the results and discussion. Concluding remarks are made in section 5.4.

5.2. Establishing the Credibility of the LBM-SRT Code

It may be noted that for the single lid-driven square cavity some experimental, numerical and theoretical results exist, by reproducing which with LBM an insight about the appropriateness of the present boundary conditions can be gained. Lai *et al.* [99] compared the lattice Boltzmann method and the finite volume Navier-Stokes solver and concluded that bounce-back boundary condition has better than first order accuracy. In this work bounce-back and equilibrium boundary condition [27] are applied on the stationary and moving walls respectively. This knowledge is then utilized when applying the LBM-SRT to compute the two-sided, four-sided square cavity flows. To lend credibility to the present LBM-SRT code its results for the single lid-driven square cavity flow is first compared with those of two other works.

To validate the present numerical method, the LBM-SRT code is used to compute the single lid-driven flow in a square cavity on a 161×161 lattice. A lid-velocity of $U = 0.1$ is considered in this work. Figure 5.1 depicts the streamline pattern at $Re = 1000$ obtained through LBM, which closely resembles those given by Ghia *et al.* [83]. Figure 5.2 shows the comparison of steady-state u-velocity profile along a vertical line and v-velocity profile along a horizontal line passing through the geometric centre of the cavity at $Re = 1000$. It is observed that the agreement between the present LBM-SRT results and those of the two works used for comparison is excellent. Thus the present LBM-SRT code stands validated.

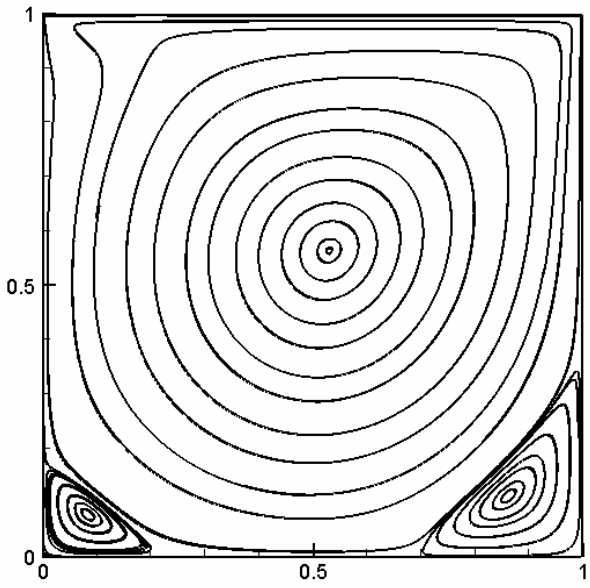

Figure 5.1: Streamline pattern for the single sided lid-driven cavity flow at *Re* = 1000.

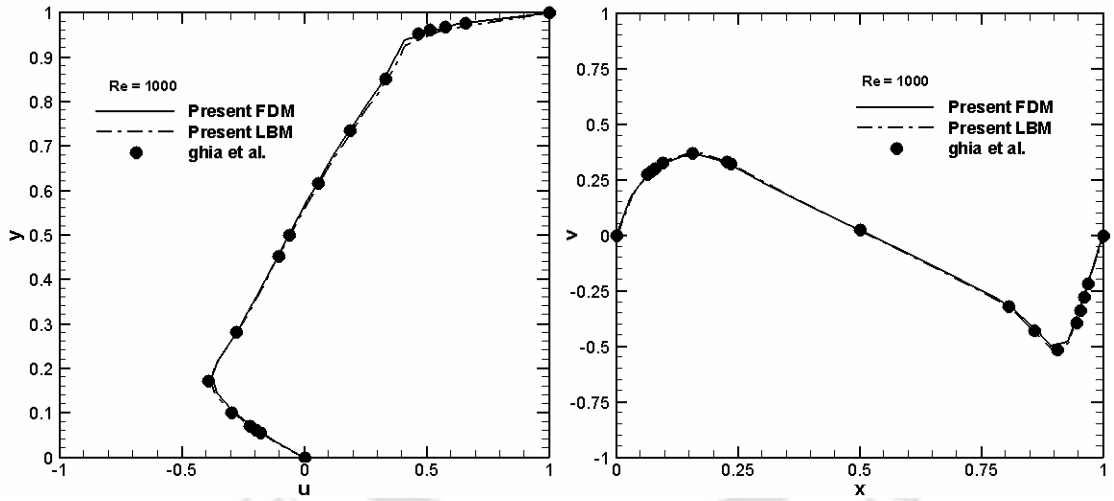

Figure 5.2: Code validation: *u*-velocity along vertical centreline and *v*-velocity along horizontal centreline for single lid-driven square-cavity (*Re* = 1000).

5.3. Results and Discussions

As already mentioned, in this chapter the multiple steady-flow states in two-sided non-facing lid-driven square cavity and four-sided lid-driven square cavity are first

numerically captured using the Lattice Boltzmann Method. Unlike non-facing lid-driven cavities, for the parallel motion of two facing walls, the square cavity always gives a unique solution. However, for rectangular cavities with parallel motion of two walls multiple stable solutions exist [75]. Thus the present study is extended to two-dimensional rectangular cavity with parallel wall motion as well to capture multiple-steady solutions. The method used to obtain multiple steady solutions in the LBM framework is also described in this section.

5.3.1. Strategy used to obtain Multiple Steady Solutions through LBM

In the conventional techniques like finite volume method one uses time-marching or other iterative procedures to obtain steady-flow solutions. Multiple solutions are obtained starting with different initial conditions that may be cleverly chosen to suit a certain type of final solution. Sometimes the choice of the sweeping direction for line-implicit iterative solver also determines the type of solution captured. In the Lattice Boltzmann Method, however, one deals with the time-evolution of the particle distribution functions and their relation with the macroscopic flow parameters is not immediately apparent.

It is also known that, the relaxation time that fixes the rate of approach to equilibrium is related to the viscosity by

$$\tau = \frac{6\upsilon+1}{2} \tag{5.1}$$

where υ is the kinematic viscosity measured in lattice units. To capture multiple solutions in the cavity flow for a certain Reynolds number by Lattice Boltzmann Method,

lid velocity U may be changed remaining within the incompressible Mach number limit. For the same Reynolds number, altering the value of the lid velocity U, results in a change in the value of kinematic viscosity (see Equation (5.1)) and hence a change in the relaxation time. All the multiple solutions given in the next subsections for several Reynolds numbers are obtained using various lid velocities, and hence various relaxation times. Excellent agreement is obtained between the LBM and previous studies based on continuum approach.

5.3.2. Two-Sided Non-Facing Lid-Driven Square Cavity Flow

The geometry and boundary conditions of the two-sided non-facing lid-driven square cavity flow is shown in Figure 5.3. In this problem, while the upper cavity wall moves towards the right, the left cavity wall moves in the downward direction with an equal velocity. Figure 5.4 depicts the streamlines of predicted flow patterns on a lattice size of 201×201 at Reynolds numbers 100, 500, 1000 and 1071 for the two-sided non-facing lid-driven square cavity. The solution demonstrates that symmetric solutions exist at all Reynolds numbers. The streamlines are diagonally symmetric for all the Reynolds numbers. The symmetric state is denoted by $t_S^{(1)}$, where two separate primary vortices are formed apparently adjacent to each of the moving walls. It is evident that for these relatively low Reynolds numbers two primary and two secondary vortices are formed.

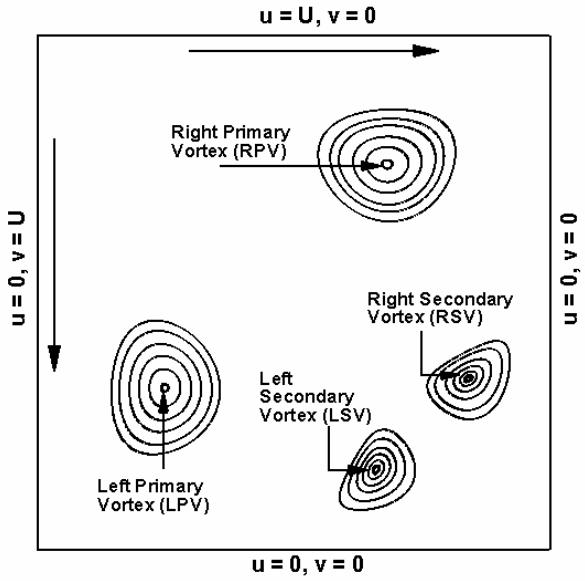

Figure 5.3: Geometry and boundary conditions of the two-sided lid-driven square cavity flow.

As the Reynolds number increases the secondary vortices grow bigger. Additional asymmetric flow patterns can be obtained above the critical Reynolds number of 1073 [76]. Here we choose a post-critical Reynolds number of 2000 to demonstrate the existence of multiple steady solutions. Figure 5.5 depicts the streamline patterns for the two-sided non-facing lid-driven square cavity flow at Re = 2000. It is known that when the inertial effects become important at higher Reynolds numbers additional flow states arise in pairs that break the respective symmetry spontaneously. One symmetric state and two asymmetric states are identified in this problem. Beyond the critical Reynolds number at least one solution satisfies the symmetry geometry. One symmetric state $t_s^{(1)}$ and two asymmetric states denoted by $t_a^{(1)}$, $t_a^{(2)}$ are identified. These symmetric and asymmetric flow patterns agree well with those given by Wabha [76].

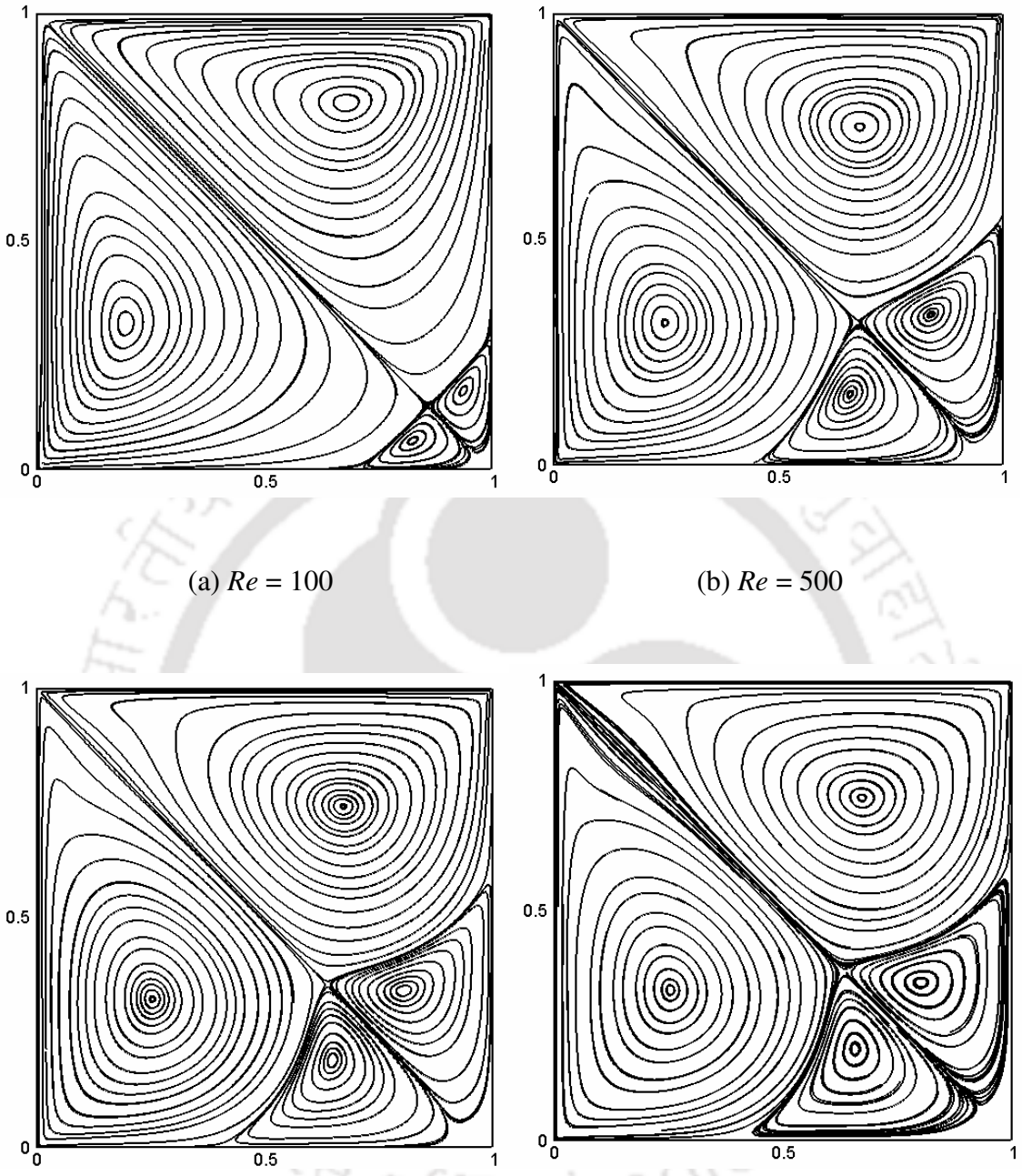

(a) *Re* = 100 (b) *Re* = 500

(c) *Re* = 1000 (d) *Re* = 1071

Figure 5.4: Streamline pattern for two-sided lid-driven cavity flow at (a) *Re* = 100 (b) *Re* = 500 (c) *Re* = 1000 and (d) *Re* = 1071 by LBM on a 201× 201 lattice arrangement.

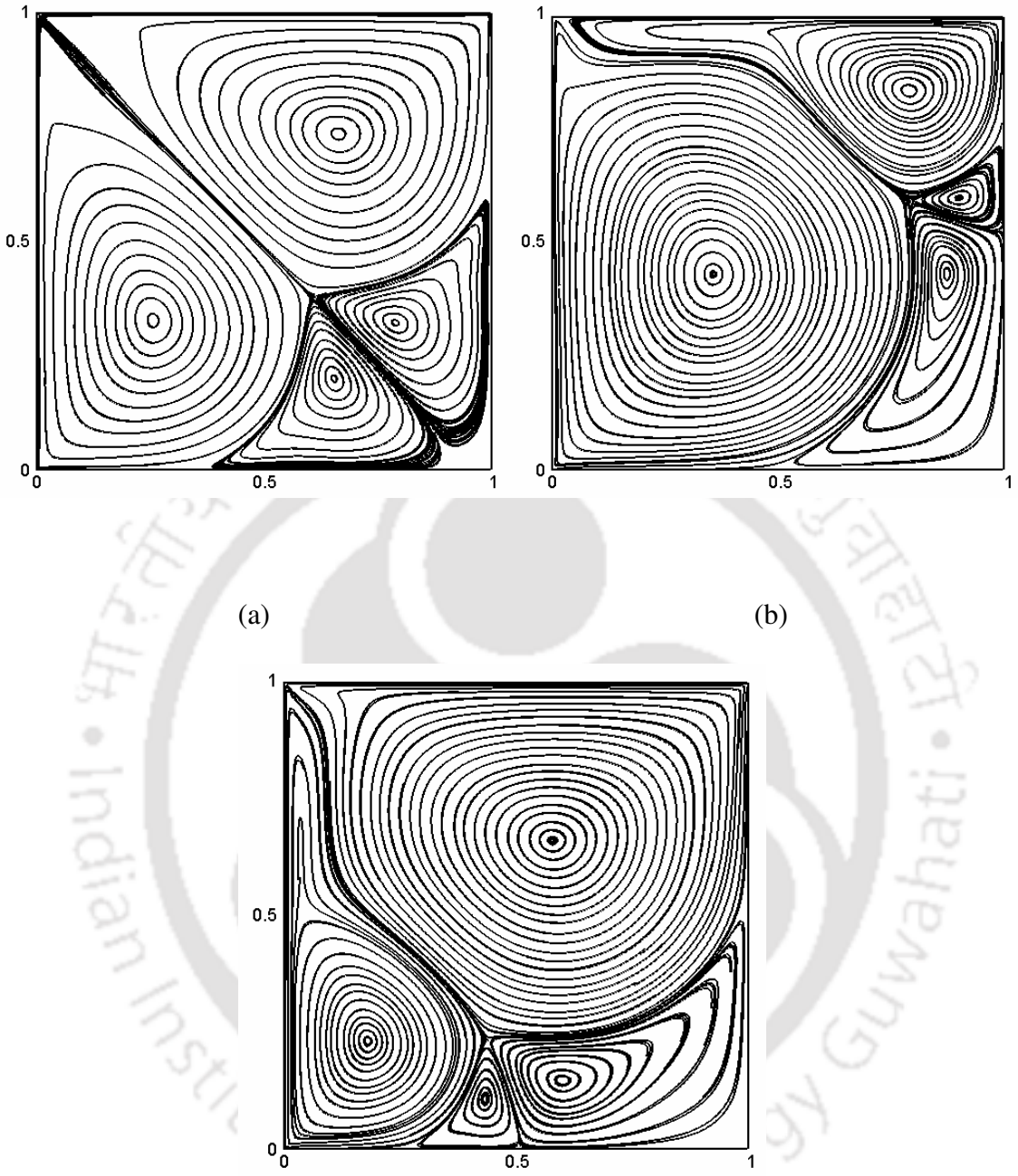

Figure 5.5: Multiplicity of flow states for two-sided non-facing lid-driven cavity flow at *Re* = 2000. Shown are streamline patterns of the (a) symmetric solution $t_s^{(1)}$, (b) asymmetric solution $t_a^{(1)}$ and (c) asymmetric solution counterpart $t_a^{(2)}$.

In Table 5.1 we present the locations of the left-primary, right-primary, left-secondary and right-secondary vortex centres for the pre-critical *Re* = 100, 500, 1000 and 1071. From this table and also from Figure 5.4 all the vortex centres are seen to move towards the symmetry diagonal as Reynolds number increases. In Table 5.2 is presented the locations of the vortex centres for the symmetric and asymmetric solutions for the post-critical Re = 2000.

Table 5.1: Locations of the vortex centres for two-sided lid-driven square cavity flow. The letters LPV, RPV, LSV and RSV denote Left Primary Vortex, Right Primary Vortex, Left Secondary Vortex and Right Secondary Vortex respectively.

Re	Left Primary Vortex (LPV)		Right Primary Vortex (RPV)		Left Secondary Vortex (LSV)		Right Secondary Vortex (RSV)	
	x	*y*	*x*	*y*	*x*	*y*	*x*	*y*
100	0.190	0.321	0.680	0.810	0.813	0.066	0.934	0.186
500	0.250	0.320	0.680	0.750	0.657	0.160	0.840	0.335
1000	0.252	0.321	0.675	0.744	0.658	0.199	0.780	0.343
1071	0.253	0.326	0.675	0.744	0.655	0.199	0.800	0.343

Table 5.2: Locations of the vortex centres for two-sided square cavity flow at *Re* = 2000.

Re	LPV		RPV		LSV		RSV	
	x	*y*	*x*	*y*	*x*	*y*	*x*	*y*
symmetry $t_s^{(1)}$	0.254	0.326	0.675	0.746	0.655	0.199	0.799	0.344
asymmetric ($t_a^{(1)}$)	0.353	0.426	0.781	0.827	0.862	0.421	0.895	0.583
asymmetric ($t_a^{(2)}$)	0.178	0.226	0.575	0.653	0.421	0.106	0.583	0.143

5.3.3. Four-Sided Lid-Driven Square Cavity Flow

The geometry and boundary conditions of the four-sided lid-driven square cavity flow is shown in Figure 5.6. In this problem, the upper cavity wall moves towards the right, the lower wall moves towards the left, while the right wall moves upwards, the left wall moves downwards with an equal velocity. Figure 5.7 shows the streamlines of the predicted flow patterns on a lattice size of 161×161 for various Reynolds numbers ranging from low to critical (*Re* =10, 100 and 127). The streamlines are diagonally symmetric with respect to both the cavity diagonals for all these pre-critical Reynolds numbers. The symmetric state is denoted by $f_S^{(1)}$. Additional asymmetric flow patterns can be obtained above the critical Reynolds number of 129 [76]. To demonstrate the existence of multiple steady solutions a post-critical Reynolds number of 300 is chosen. Figure 5.8 shows the streamline patterns for the four-sided lid-driven cavity flow at *Re* = 300.

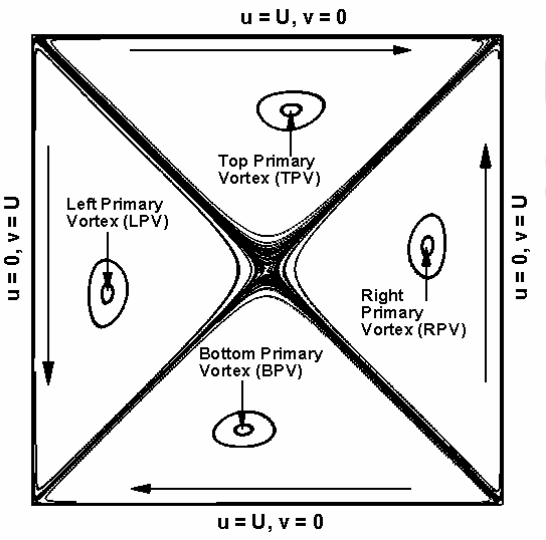

Figure 5.6: Geometry and boundary conditions of the two-sided lid-driven cavity flow.

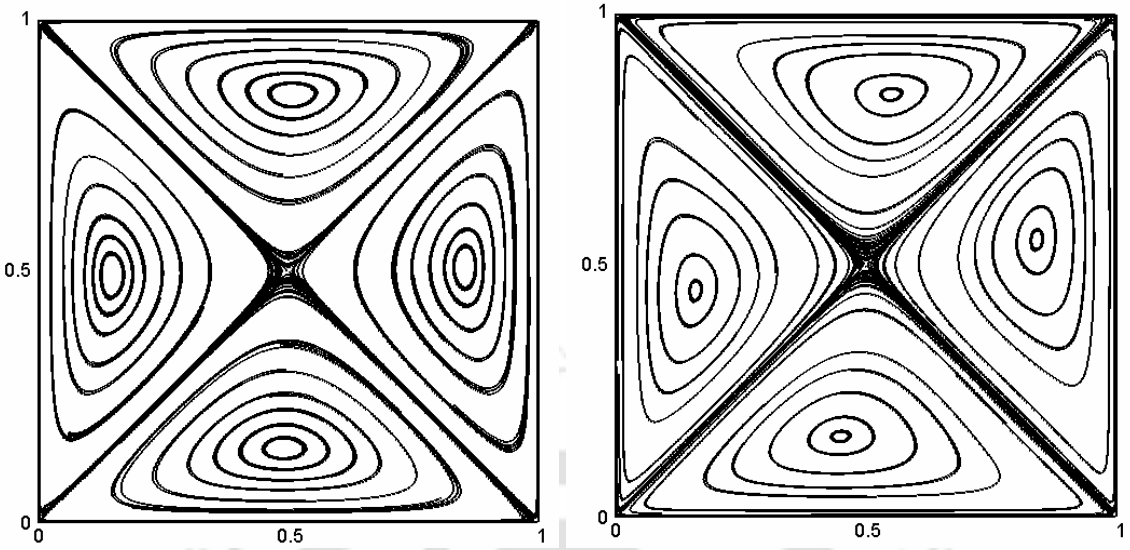

(a) Re = 10 (b) Re = 100

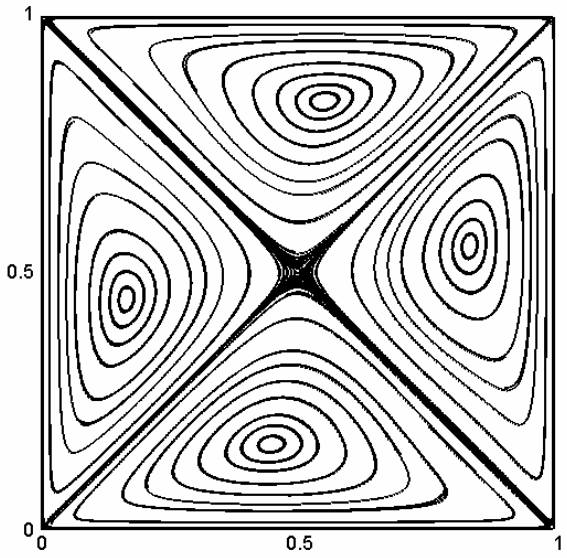

(c) Re = 127.

Figure 5.7: Streamline pattern for four-sided lid-driven cavity flow at (a) Re = 10 (b) Re = 100 and (c) Re = 127 by LBM on a 161× 161 lattice arrangement.

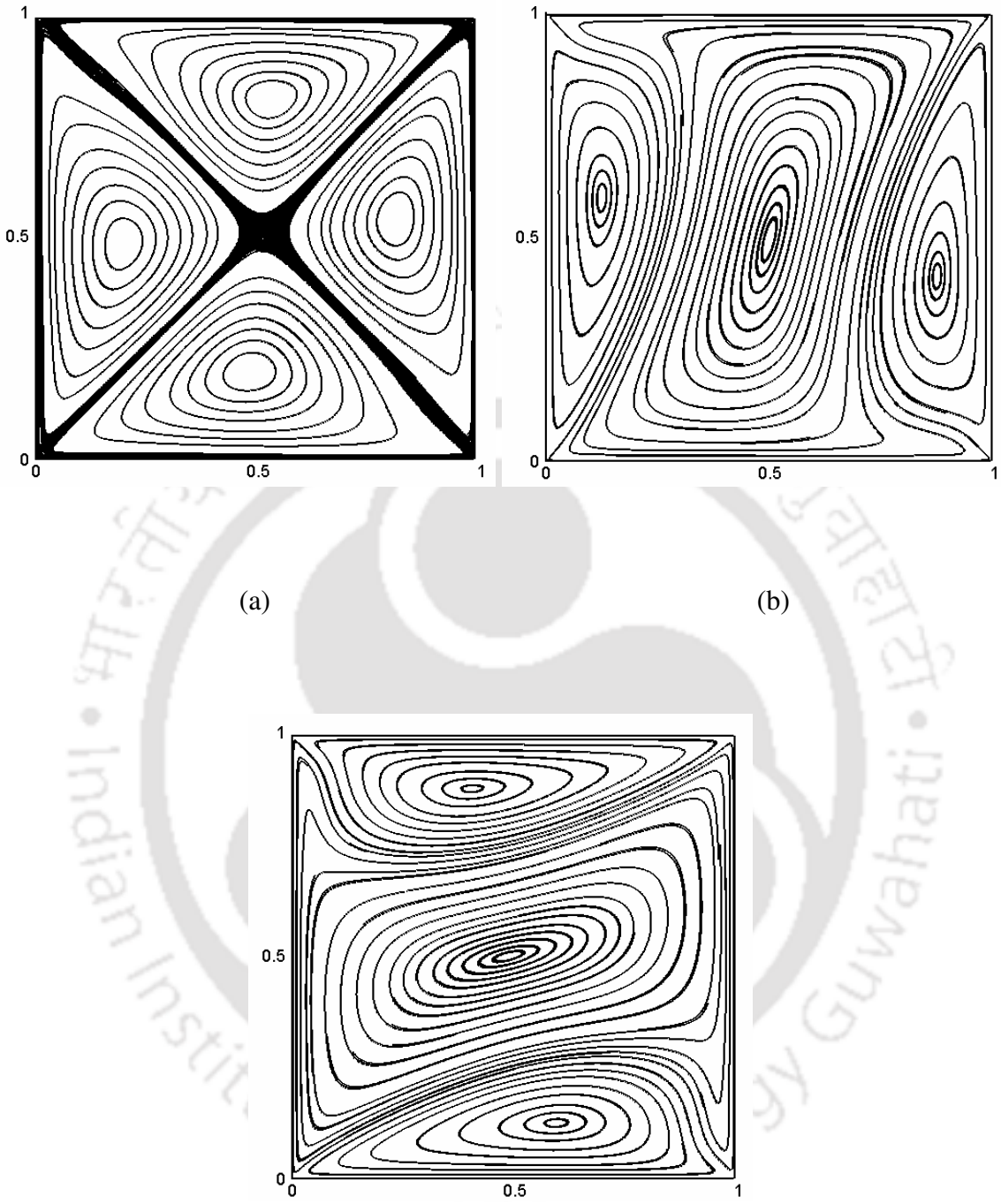

Figure 5.8: Multiplicity of flow states for four-sided non-facing lid-driven cavity flow at *Re* = 300. Shown are streamline patterns of the (a) symmetric solution $f_S^{(1)}$, (b) asymmetric solution $f_a^{(1)}$ and (c) asymmetric solution counterpart $f_a^{(2)}$.

Table 5.3: Locations of the vortex centres for four-sided lid-driven square cavity flow. The letters LPV, RPV, TPV and BPV denote Left Primary Vortex, Right Primary Vortex, Top Primary Vortex and Bottom Primary Vortex respectively.

Re	Left Primary Vortex (LPV)		Right Primary Vortex (RPV)		Top Primary Vortex (TPV)		Bottom Primary Vortex (BPV)	
	x	*y*	*x*	*y*	*x*	*y*	*x*	*y*
10	0.150	0.490	0.849	0.510	0.510	0.850	0.490	0.149
100	0.160	0.450	0.840	0.550	0.550	0.840	0.450	0.160
127	0.170	0.450	0.830	0.550	0.548	0.830	0.449	0.168

It is seen that when the inertial effects become important additional flow states arise in pairs that break the respective symmetry spontaneously. One symmetric state $f_s^{(1)}$ and two asymmetric states denoted by $f_a^{(1)}$, $f_a^{(2)}$ are identified for the four-sided lid-driven cavity flow at this Reynolds number. Beyond the critical Reynolds number at least one solution satisfies the symmetry geometry. Our symmetric and asymmetric flow patterns compare well with those given for the same problem by Wabha [76]. In Table 5.3, we present the locations of the left, right, top and bottom vortex centres (Figure 5.8) for Reynolds numbers 10, 100 and 127. As the Reynolds number increases the vortex centres are seen coming closer to the diagonal joining the leading edges of the moving plates. The locations of the vortex centres for the symmetry solution at the post-critical Re = 300 (Figure 5.8(a)) for the left, right, top and bottom vortices are (0.196, 0.481), (0.807, 0.532), (0.527, 0.806) and (0.481, 0.196) respectively. For one of the asymmetric solutions (Figure 5.8(b)) the locations for the left, centre and right vortices are (0.123, 0.589), (0.498, 0.497) and (0.876, 0.409) respectively.

5.3.4. Two-Sided Lid-Driven Rectangular Cavity Flow

The geometry and boundary conditions of the two-sided rectangular cavity with parallel wall motion is shown in Figure 5.9. In this problem, both the left and right walls moves in the upward direction with an equal velocity. The flow geometry suggests that there is a flow pattern symmetric about the vertical centreline. This symmetric state exists for all Reynolds numbers. Multiple stable solutions, however, exist only for the higher values of Reynolds number. For the present flow configuration we demonstrate the existence of multiple solutions for a cavity aspect ratio of 0.75 and a Reynolds number of 600. Figure 5.10 shows the multiple streamline patterns obtained by LBM using a 224×256 lattice structure. For this flow geometry five multiple stable solutions are obtained. Figure 5.10 (a) shows the weakly-stable symmetric solution, Figure 5.10 (b) shows one of the two weakly-stable asymmetric solutions and Figure 5.10 (c) shows one of the two strongly-stable asymmetric solutions.

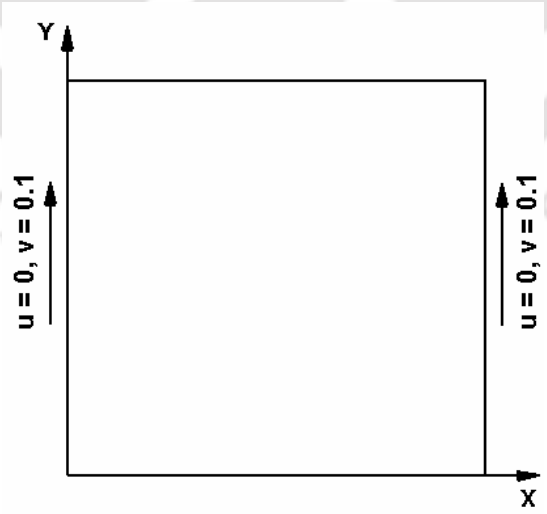

Figure 5.9: Geometry and boundary conditions of the two-sided rectangular cavity parallel wall motion.

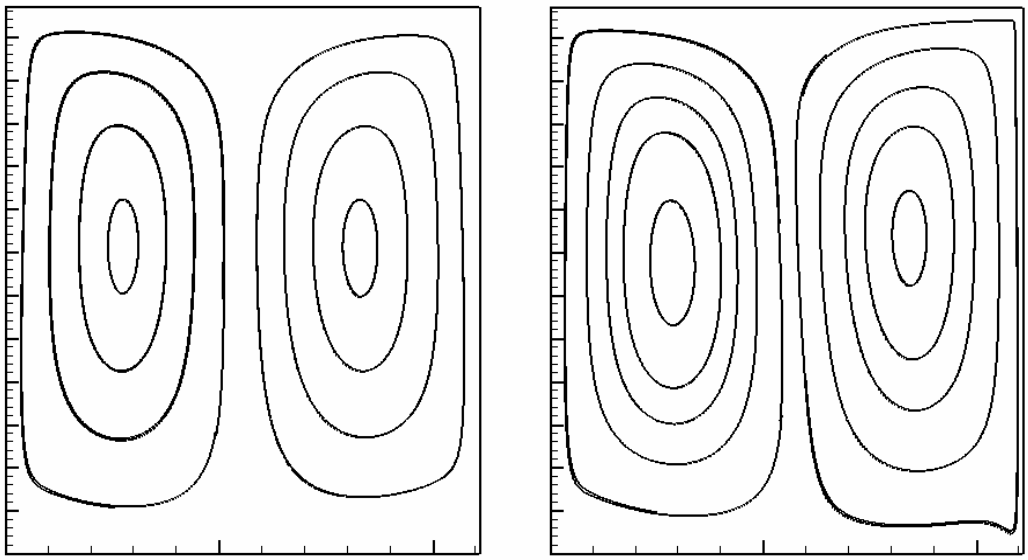

(a) (b)

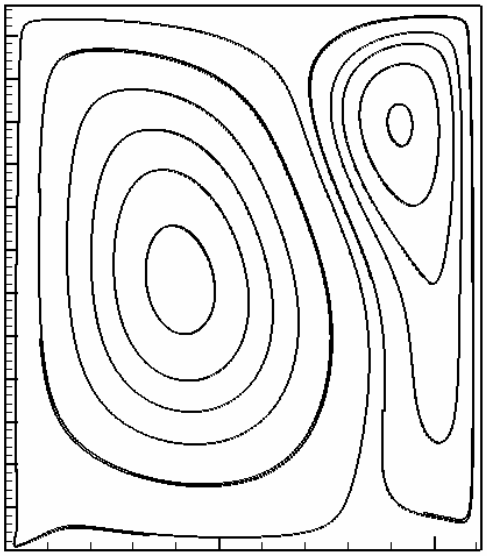

(c)

Figure 5.10: Multiplicity of flow states for the two-sided rectangular cavity flow with parallel wall motion at Re = 600 (based on the shorter side) and aspect ratio of 0.875 on a 224×256 lattice. Shown are the streamline patterns of (a) symmetric solution, (b) weakly-stable asymmetric solution and (c) strongly-stable asymmetric solution.

What is meant by weakly stable is that if a relatively milder 'perturbation' is given to the state, there is likely to be a change of state to one of the other solution. For the strongly-stable asymmetric state, such disturbance will not be strong enough to cause a change of steady state. These results compare very well with those given for the same problem by Albensoeder *et al.* [75]. The locations of the vortex centres are not mentioned here as they keep changing with the cavity aspect ratio.

5.4. Conclusion

A single-relaxation-time model using *D2Q9* lattices is used to carry out LBM computations to obtain multiple steady solutions for two- and four-sided lid-driven square cavities and two-sided rectangular cavities. To establish the credibility of the developed code it is first used to compute the flow in a standard 2D single-lid-driven square cavity to demonstrate that the results closely agree with the results generated with a finite-difference-based code. So far various works have demonstrated the ability of continuum-based approaches to capture multiple steady-flow solutions exhibited by some nonlinear situations. Though LBM has the ability to solve the nonlinear equations that govern the dynamics of fluid flow, it was not known how it will perform when employed to capture multiple steady solutions, which are specifically nonlinear phenomena.

The present chapter shows that LBM has the ability to obtain multiple steady solutions; however, the strategy to obtain these solutions are somewhat different. The problems chosen to demonstrate this ability are the two-sided non-facing lid-driven cavity (Re = 2000) and the four-sided lid-driven cavity (Re = 300) flow, for which continuum-approach results exist. These three flow configurations are fraught with interesting flow

features in that they exhibit multiple steady solutions. As the present LBM results compare very well with these results, it may be concluded that LBM has sufficient accuracy and ability to capture multiple steady solutions in the configurations studied. Though results are not presented here, we have observed that for each of several Reynolds numbers beyond critical (Re = 1073 for the two-sided problem and Re = 129 for the four-sided problem) LBM has the ability to produce one weakly-stable-symmetric and two stable-asymmetric solutions. With this added ability it can be concluded that LBM, as an alternative to the continuum based methods, holds very good promise in computational fluid dynamics.

Chapter 6

Computation of Flows in Cubic and Prism Cavities

6.1. Introduction

Three-dimensional cavity flows, which are more complex, realistic and global became an interesting research topic in the last three decades [55, 56, 100-107]. Owing to the boundary layer effect of the side walls the three-dimensional results at mid-plane will deviate from the two-dimensional results. It may be recalled that, in steady two-dimensional flows all streamlines are closed except for streamlines that separate eddies by starting and ending on walls. It is known that, the three-dimensional streamlines do not close, not even in mid-plane even at low *Re*. There have been few reliable attempts to understand the three-dimensional flow field in cubic and prism cavities. It is also known that, limited number of available reliable results exists that study the three-dimensional boundary layer effect. Therefore, in the present chapter, the LBM-SRT method is used to study the effect of three-dimensionality in the 3D cubic and prism cavities with various type of wall motion.

Three-dimensional Lattice Boltzmann models including the fifteen-velocity model (*D3Q15*), the nineteen-velocity model (*D3Q19*), the twenty seven-velocity model (*D3Q27*) and a two-dimensional model namely, the nine-velocity model (*D2Q9*) are used in the present chapter to compute the flow in a cubic and square cavity and the mid-span

3-D LBM results are compared with appropriate 2-D LBM results to study the effect of three-dimensionality. Computations have been carried out for low to high Reynolds numbers and they are validated by comparison with established results.

The main objective of this chapter is to demonstrate the validity of the Lattice Boltzmann Method with single-relaxation-time scheme for three-dimensional problems. Another objective of this chapter is to have an idea about the relative performances of various three-dimensional models like *D3Q15*, *D3Q19* and *D3Q27*. Therefore, the three-dimensional lid-driven cubic and prism cavities with various types of wall motion are studied in an effort to evaluate the performance of the LBM and to produce accurate steady state solutions for various Reynolds number.

6.2. LBM Numerical Procedure

Initially a constant density $\rho =$ 1.0 is imposed for the whole cavity field and the velocities at all lattice nodes, except at the nodes on the moving top wall, are set to zero. The x-velocity of the top plate is fixed at a value of $\boldsymbol{U}$ = 0.1 and the y- and z-velocity are set to zero. The equilibrium distribution function $f_i^{eq}(\mathbf{x},t)$ is calculated and particle distribution function $f_i(\mathbf{x},t)$ is set equal to $f_i^{eq}(\mathbf{x},t)$ for all nodes at t = 0. The bounce-back boundary conditions are used on the stationary solid walls. The convergence criterion for all computations was set as

$$\frac{\sum\left(u_{i,j,k}^{n+1}-u_{i,j,k}^{n}\right)^2}{\sum\left(u_{i,j,k}^{n+1}\right)^2} \leq 10^{-6} \tag{6.1}$$

All the present results obtained in this chapter are normalized by the top velocity ***U.***

6.3. Numerical Experiments

Three-dimensional transport momentum differs from the two-dimensional cases under similar boundary conditions due to the three-dimensional effect which is more realistic. Therefore, we now apply LBM to compute flows in three 3D configurations. These are (i) single lid-driven cubic cavity flow (ii) single lid-driven prism cavity flow and (iii) two-sided non-facing lid-driven cubic cavity flow.

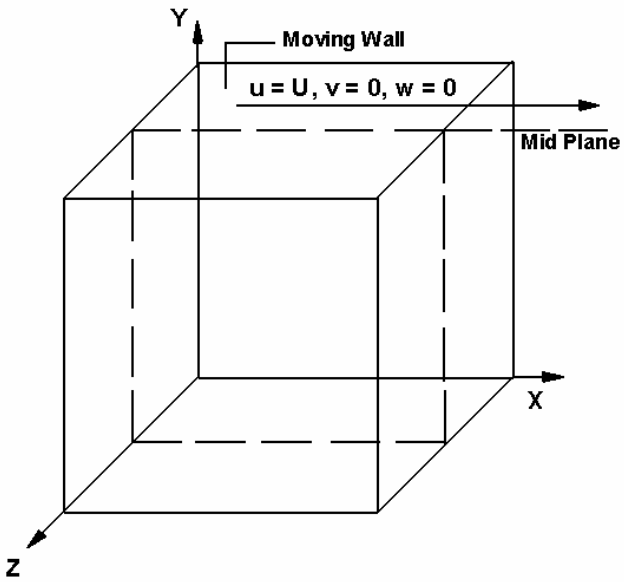

Figure 6.1: Geometry of the three-dimensional single lid-driven cubic cavity flow.

6.3.1. Test Problem 1 - Single lid-driven cubic cavity flow

First, the three-dimensional single lid-driven cubic cavity flow is considered. The geometry and the moving-wall boundary condition of a single lid-driven cubic cavity

flow is shown in Figure 6.1. The cubic cavity has both the depth-to-width aspect ratio and a span-to-width aspect ratio of unity.

It is known that, the cubic cavity is the three-dimensional analogue of the square cavity problem. Computational results for a 3-D lid driven cubic cavity flow at *Re* = 100, 400, 1000 and 2000 using three-dimensional LBM models like *D3Q15*, *D3Q19* and *D3Q27* are presented in this section. The velocity profiles of the u-component on the vertical centreline and the v-component on the horizontal centreline on the plane $z = 0.5$ (i.e. at mid-span) at *Re* = 100, 400, 1000 and 2000 are shown in Figures 6.2-6.5. The present computations are carried out on a modest $71\times71\times71$ lattice arrangement for *Re* = 100, 400, 1000 and a $91\times91\times91$ lattice arrangement for *Re* = 2000. To show the three-dimensional effect, the two-dimensional results obtained by the *D2Q9* model are also included in Figures 6.2-6.5. All the results of the square cavity problem presented here are obtained on a lattice with a resolution of 201×201.

Figure 6.2 (a) and 6.2 (b) shows the variation of u–velocity along the vertical centreline and v–velocity along the horizontal centreline on the $z = 0.5$ plane (i.e. mid-span) at *Re* = 100. To validate the present results, centreline velocity profiles have been compared with the LBM results of Mei *et al.* [55] and the pseudo-spectral-method results of Ku *et al.* [104]. The present results compare well with those of both these works, however, agreement with [104] is better. It is seen that, at *Re* = 100, the effects of end walls are small and is more prominent on the *x*-velocity. At this Reynolds number the differences among the three 3-D LBM model results are not significant.

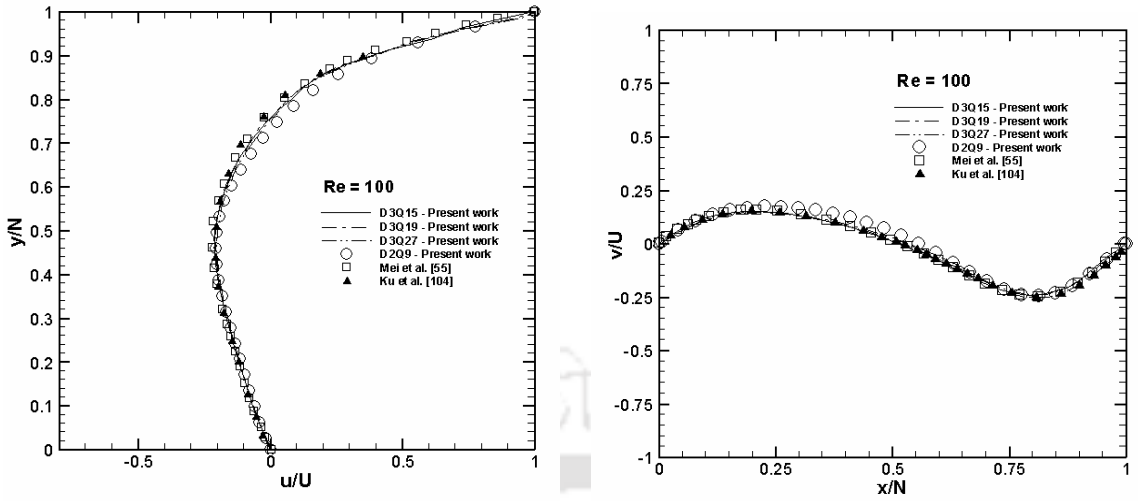

(a) Centreline u – velocity (b) Centreline v-velocity

Figure 6.2: Comparison of centreline velocities of cubic (mid-span) and square cavity at Re = 100.

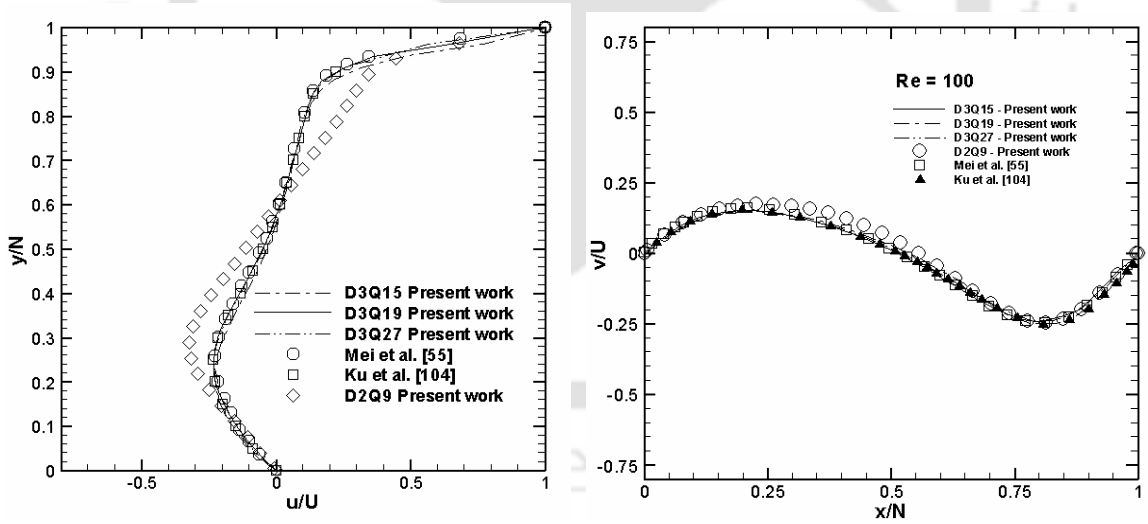

(a) Centreline u – velocity (b) Centreline v-velocity

Figure 6.3: Comparison of centreline velocities of cubic (mid-span) and square cavity at Re = 400.

Figure 6.3 (a) and 6.3 (b) shows the variation of u–velocity along the vertical centreline and v–velocity along the horizontal centreline on the $z = 0.5$ plane (i.e. mid-span) at *Re* = 400. A satisfactory agreement is found once again between calculated velocity profiles and those reported by Mei *et al.* [55] and Ku *et al.* [104]. The discrepancy between the two- and three-dimensional velocity profiles is a proof of the end-wall effect even at low *Re*. It is also observed that the *D3Q15* model result slightly differs from the *D3Q19* and *D3Q27* results. The reason behind is that the *D3Q15* model is the least 3-D isotropic model and it is prone to numerical instability at higher Reynolds number [55].

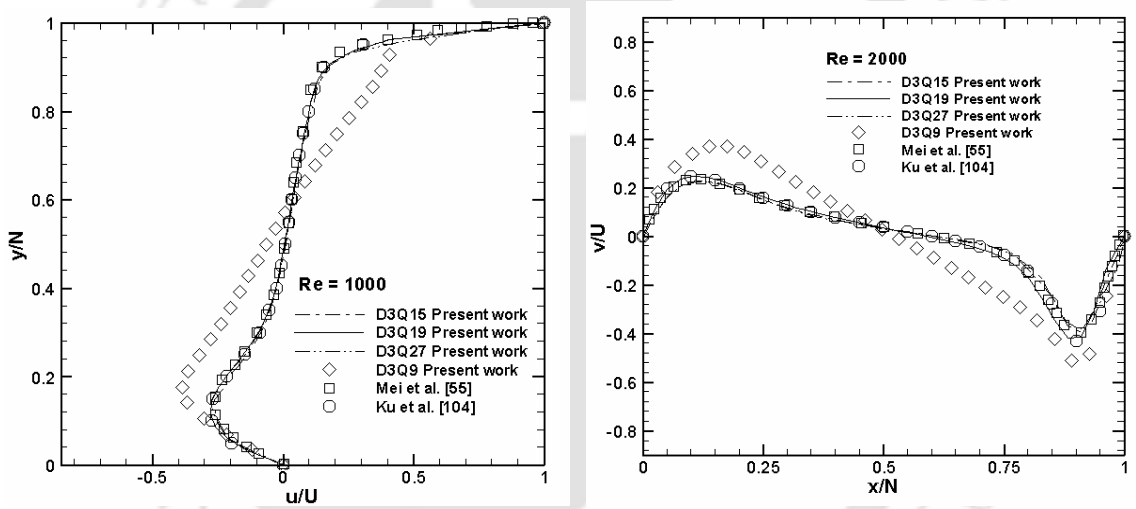

(a) Centreline u – velocity (b) Centreline v – velocity

Figure 6.4: Comparison of centreline velocities of cubic (mid-span) and square cavity at *Re* = 1000.

Figure 6.4 (a) and 6.4 (b) shows the variation of u–velocity along the vertical centreline and v–velocity along the horizontal centreline on the $z = 0.5$ plane (i.e. mid-span) at *Re*

= 1000. It is seen that, the centerline velocity profile results of *D3Q19* and *D3Q27* models are agrees very well with those reported by Mei *et al.* [55] and Ku *et al.* [104].

It is already mentioned that the *D3Q15* model is more prone to numerical instability. It is known that, if the number of lattice nodes increases the numerical solution becomes more stable. Therefore, to get improved solution obtained by *D3Q15* model 81×81×81 lattice nodes are used for *Re* = 1000. It is also seen that, as the Reynolds number increases the discrepancy between two- and three-dimensional velocity profiles (at mid-plane) also increases. Another point is that, the results of the centreline velocity profiles obtained by the *D3Q19* and *D3Q27* models are almost identical at all Reynolds numbers.

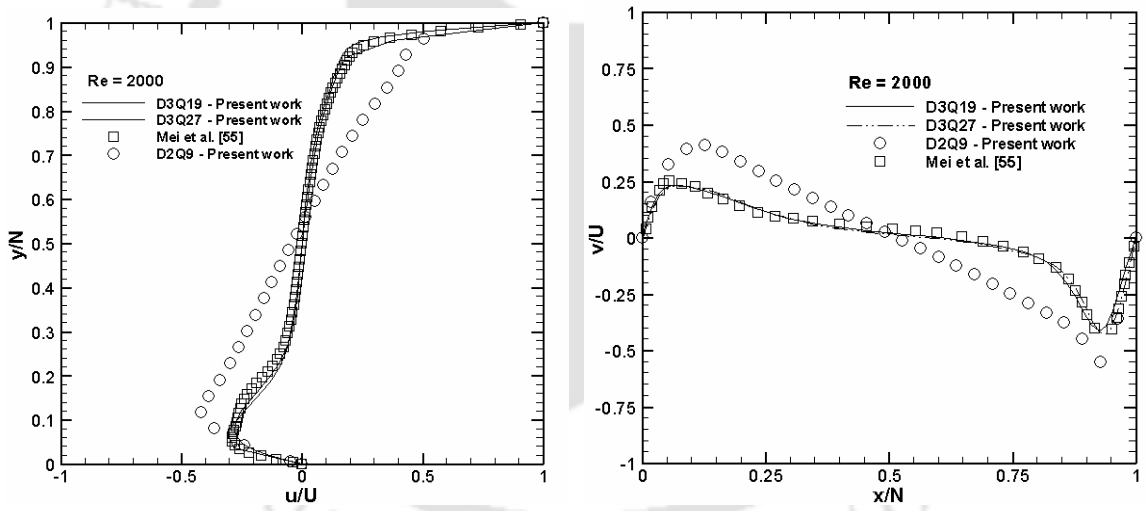

(a) Centreline u – velocity (b) Centreline v – velocity

Figure 6.5: Comparison of centreline velocities of cubic (mid-span) and square cavity at *Re* = 2000.

Figure 6.5 (a) and 6.5 (b) shows the variation of u–velocity along the vertical centreline and v-velocity along the horizontal centreline on the $z = 0.5$ plane (i.e. mid-span) at *Re* = 2000. In this case, the computations have been carried out on a modest 91×91×91 lattice nodes using the *D3Q19* and *D3Q27* models only. It is seen that, the centreline velocity profile results of *D3Q19* and *D3Q27* models agree very well with those reported by Mei *et al.* [55]. Though results are not presented in this chapter, we have observed that the presented velocity profile results agree well with those of Shu et al. [56], Albensoeder and Kuhlmann [100], Cortes and Miller [102], Shew and Tsai [103] and Iwatsu et al. [106]. The presented 3D mid-span velocity profiles plotted alongside corresponding 2D profiles reveal the fact that as Reynolds number increases the influence of the sidewalls also increases. Another observation that can be made is that all along the centrelines the magnitude of the *x*- and *y*-components of the 3D velocity are smaller than that of the corresponding 2D velocities, the discrepancy increasing with the Reynolds number. This is along expected lines, as with the increase in Reynolds number the velocity component normal to the *z*-plane also increases. Also observed is the fact that the *D3Q19* results are more accurate compared with the *D3Q15* results.

Figures 6.6-6.9 show the streamtraces projected onto three mid-planes of (a) *x*-*y* (b) z-*x* and (c) z-*y* for *Re* = 100, 400, 1000 and 2000. To plot streamtraces, the *D3Q19* model is used in the present section as it consumes less memory and computational time compared with *D3Q27*. Our 3-D results once again are in excellent match with existing results [56, 105]. Owing to the boundary layer effect of the side walls the mid-span (z = 0.5) flow in the cubic cavity is different from that in the square cavity case (presented in chapter 3).

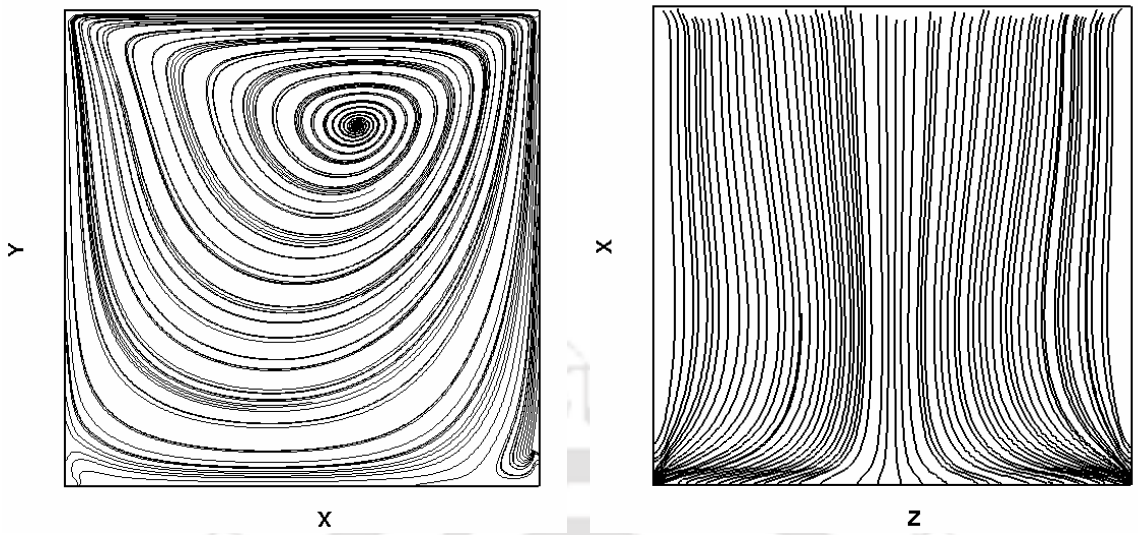

(a) $z = 0.5$ (b) $y = 0.5$

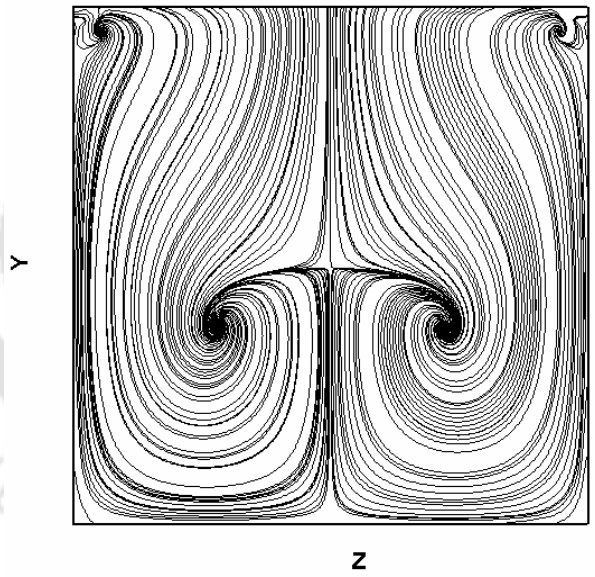

(c) $x = 0.5$

Figure 6.6: Streamtraces on three mid-planes for $Re = 100$.

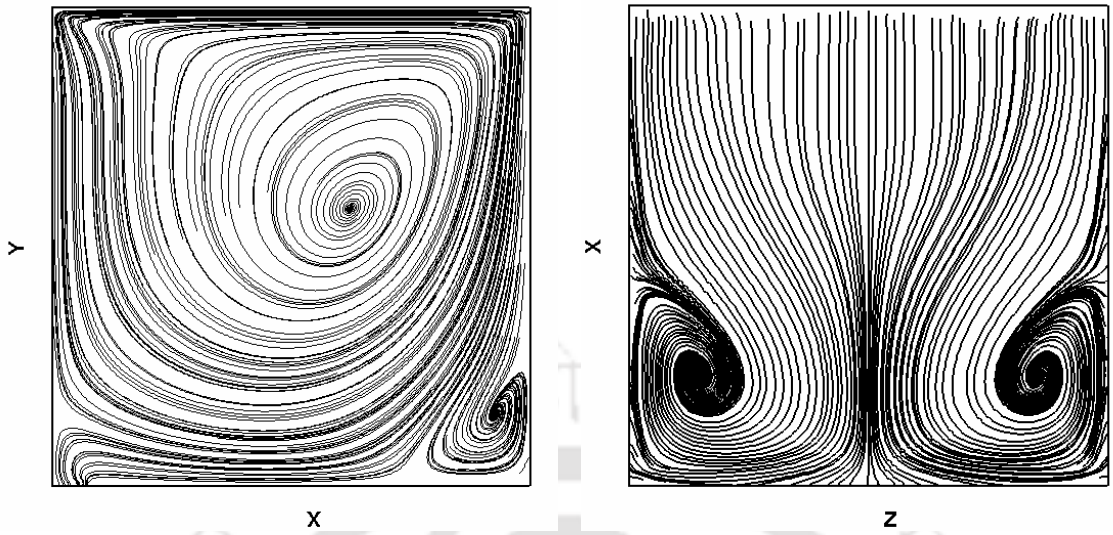

(a) $z = 0.5$ (b) $y = 0.5$

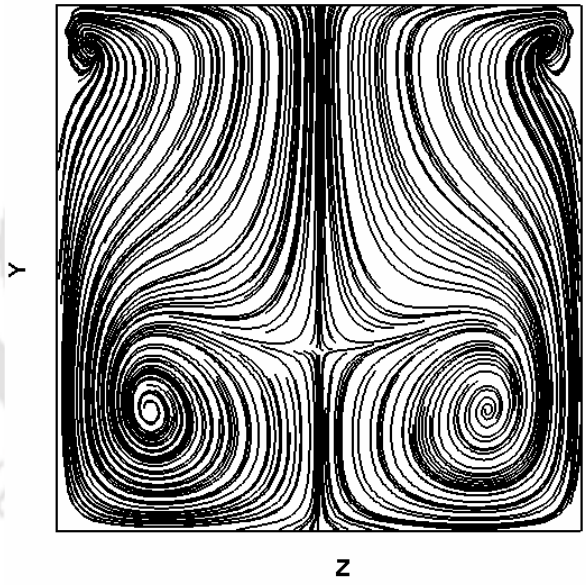

(c) $x = 0.5$

Figure 6.7: Streamtraces on three mid-planes for $Re = 400$.

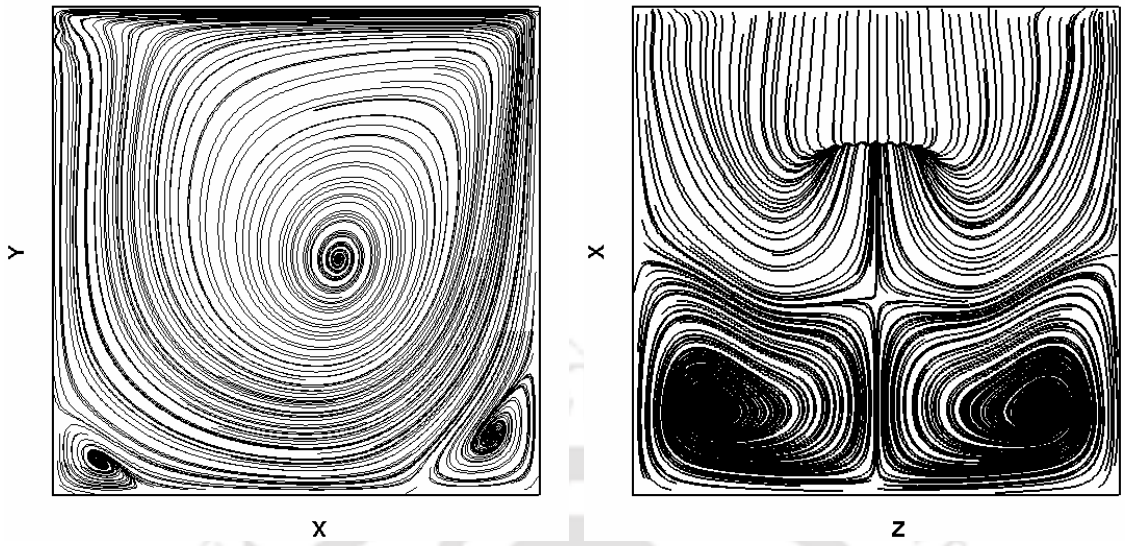

(a) $z = 0.5$ (b) $y = 0.5$

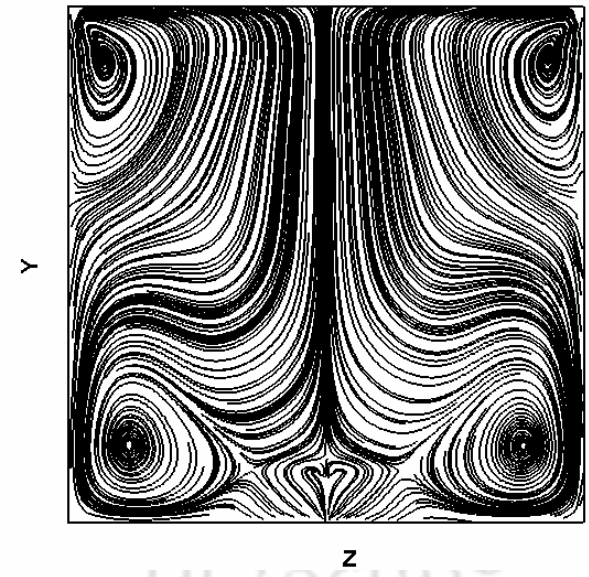

(c) $x = 0.5$

Figure 6.8: Streamtraces on three mid-planes for $Re = 1000$.

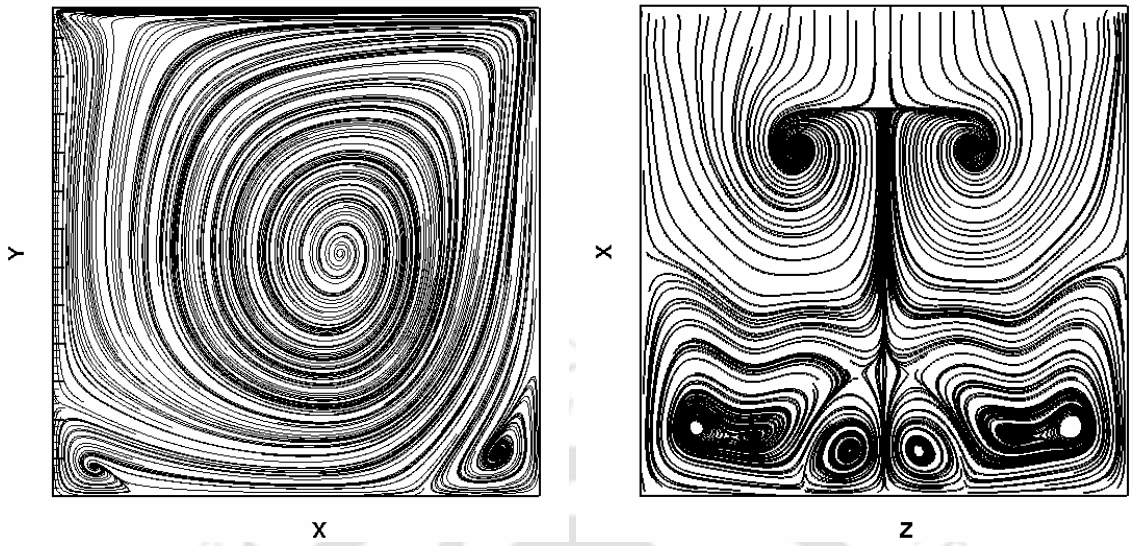

(a) $z = 0.5$ (b) $y = 0.5$

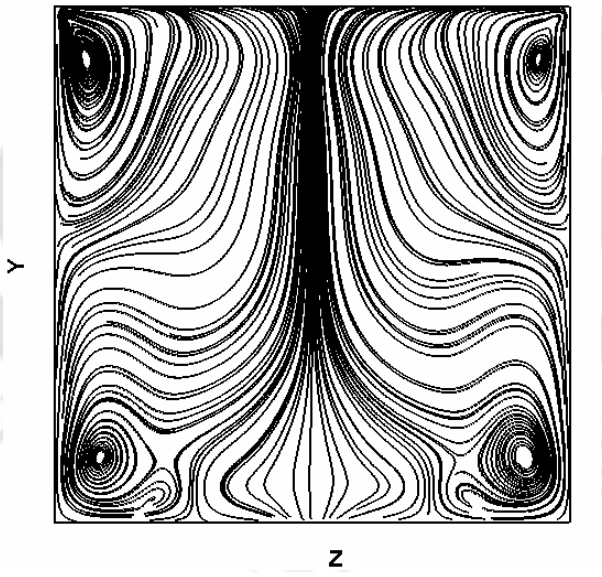

(c) $x = 0.5$

Figure 6.9: Streamtraces on three mid-planes for $Re = 2000$.

However, at low *Re,* the cubic cavity flow patterns in the symmetry plane are similar to those of a square cavity case. As the Reynolds number increases the dissimilarity between 2D and 3D symmetry plane patterns increases. Also with the increase in Reynolds number the primary vortex core in the symmetry plane shows a tendency to move towards the geometric centre; however, this tendency is not as prominent as in the case of the square cavity. Compared with the square cavity, the secondary corner vortices at the bottom are seen to form at a higher Reynolds number at the mid-span of the cubic cavity. Figure 6.8 shows clearly visible secondary vortices at both the left and right bottom corners at Re = 1000; however at Re = 400 (Figure 6.7) unlike the square cavity flow, the bottom left corner secondary vortex has not yet developed.

Figures 6.6 (b) - 6.9 (b) show the projection of the streamtraces on a plane parallel to the moving plane at y = 0.5. Though a central axis of symmetry exists at all Reynolds number, the pattern is seen to become more and more complex as Reynolds number increases. Figures 6.6 (c) - 6.9 (c) show the projection of the streamtraces on the plane normal to the direction of motion at x = 0.5. At Re = 100 (Figure 6.6 (c)) no Taylor-Görtler-type vortex is seen. At Re = 400 (Figure 6.7 (c)) a pair of Taylor-Görtler-Like vortices is seen to develop at the bottom corners. At Re = 1000 (Figure 6.8 (c)) another pair of Taylor-Görtler-Like vortices is seen to appear at the top corners and the pair of vortices at the bottom corners is seen to grow in size. At Re = 2000 (Figure 6.9 (c)) both the pairs of Taylor-Görtler-Like vortices are now prominent. The endwalls thus play a significant role in making the flow three-dimensional as the Reynolds number increases.

6.3.2. Test Problem 2 - Single lid-driven Prism cavity flow

The prism cavity configuration is the three-dimensional analogue of the two-dimensional deep cavity flow. The geometry of the three-dimensional single lid-driven prism cavity flow is shown in Figure 6.10. The cavity has a depth-to-width aspect ratio of unity and a height to width aspect ratio of 2.0. In this section, the *D3Q19* model is used to do the LBM computation.

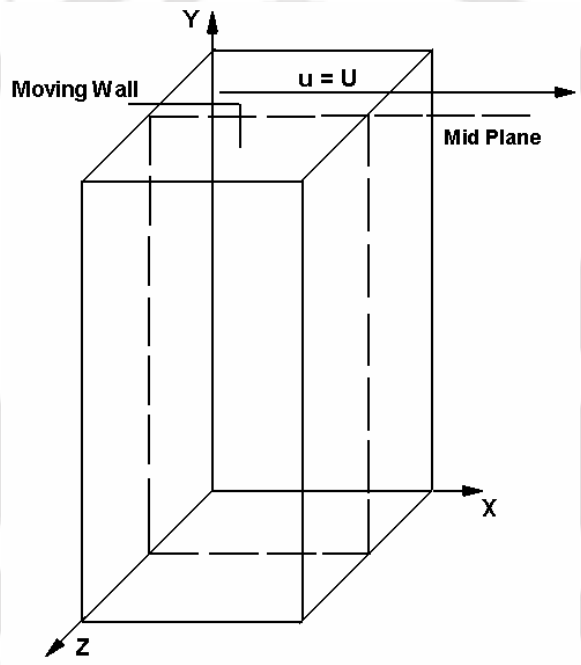

Figure 6.10: Geometry of the three-dimensional single lid-driven prism cavity flow.

The boundary conditions for the prism cavity are

$$\begin{aligned} &u = v = w = 0 \ \text{ at } \ x = 0 \text{ and } \ x = 1 \\ &u = U \ \text{ and } \ v = w = 0 \ \text{ at } \ y = 2 \\ &u = v = w = 0 \ \text{ at } \ y = 0 \\ &u = v = w = 0 \ \text{ at } \ z = 0 \text{ and } \ z = 1. \end{aligned} \tag{6.2}$$

Figures 6.11-6.13 show the centreline velocity profiles obtained for an aspect ratio of 2.0 for both the three-dimensional mid-span and two-dimensional cases. All the computations have been carried out on a 47×47×94 lattice arrangement. The two-dimensional results obtained by the *D2Q9* model (129×129) are included in Figures 6.11-6.13 to show the 3D effect. A satisfactory agreement is found between calculated velocity profiles and those reported in the 3D computations of Cortes and Miller [102]. It is seen that, for the low Reynolds number simulations the centreline velocity profiles are almost identical. At $Re \geq 400$, the two centreline velocity profiles are very different from each other. It may be recalled that similar deviation is observed for the case of cubic and square cavities. Overall, the three-dimensional boundary layer effect can be clearly observed from Figures 6.11-6.13.

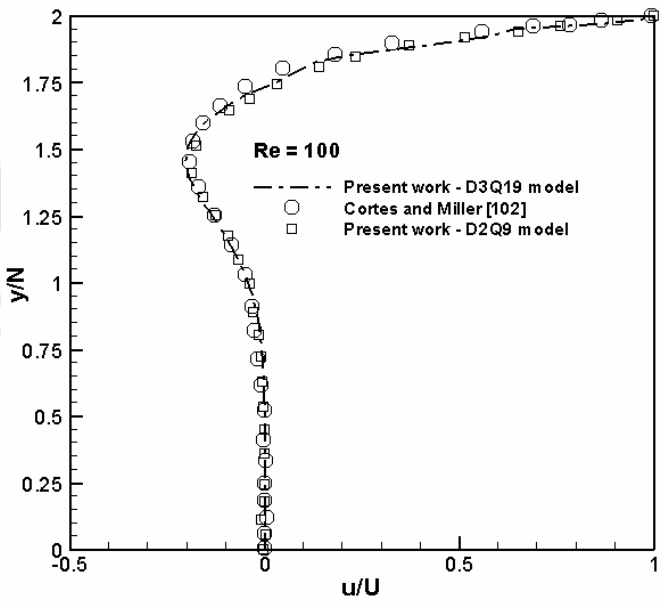

Figure 6.11: Comparison of the centreline velocity profiles from a prism cavity (mid-span) and a 2D deep cavity with an aspect ratio of 2.0 at Re = 100.

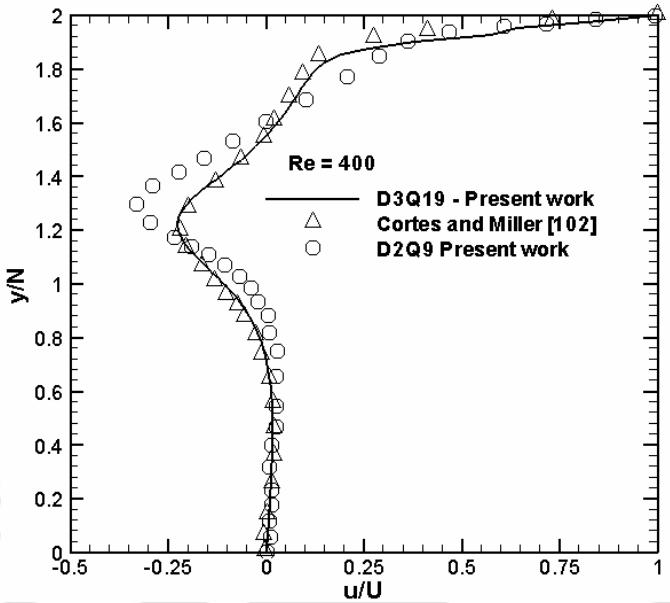

Figure 6.12: Comparison of the centreline velocity profiles from a prism cavity (mid-span) and a 2D deep cavity with an aspect ratio of 2.0 at *Re* = 400.

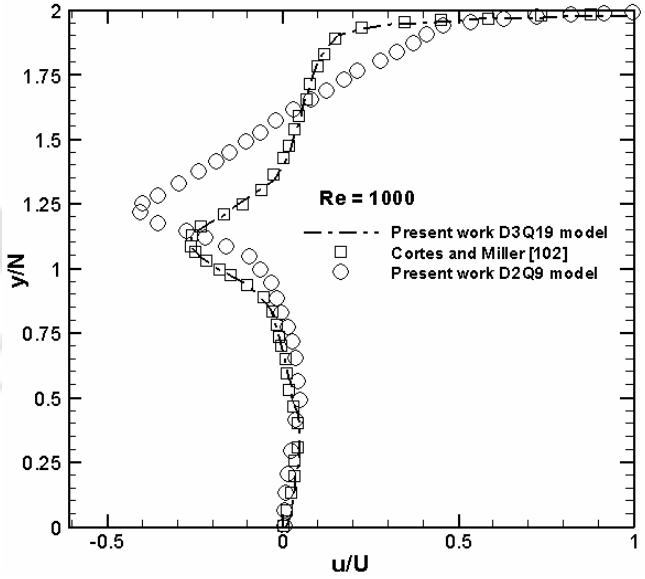

Figure 6.13: Comparison of the centreline velocity profiles from a prism cavity (mid-span) and a 2D deep cavity with an aspect ratio of 2.0 at *Re* = 1000.

6.3.3. Test Problem 3- Two-sided non-facing lid-driven cubic cavity flow

The majority of the available three-dimensional results deal with lid-driven cubic and prism cavities only. Moreover for three-dimensional two-sided lid-driven cubical cavity problem extensive literature is not available. Recently, Beya and Lili [107] extended the simulation of 2D two-sided non-facing lid-driven square cavity reported by Wahba [76] to three-dimensions (3D-TSNFL). The 3D TSNFL driven cavity computation of [107] revealed the existence of a critical Reynolds number of 1073 for the two-dimensional analogue. Beyond this critical Reynolds number steady solutions, though exists, is not unique. Here 3D-TSNFL driven cubic cavity problem is investigated for *Re* = 500, at which the solution is unique, using Lattice Boltzmann Method.

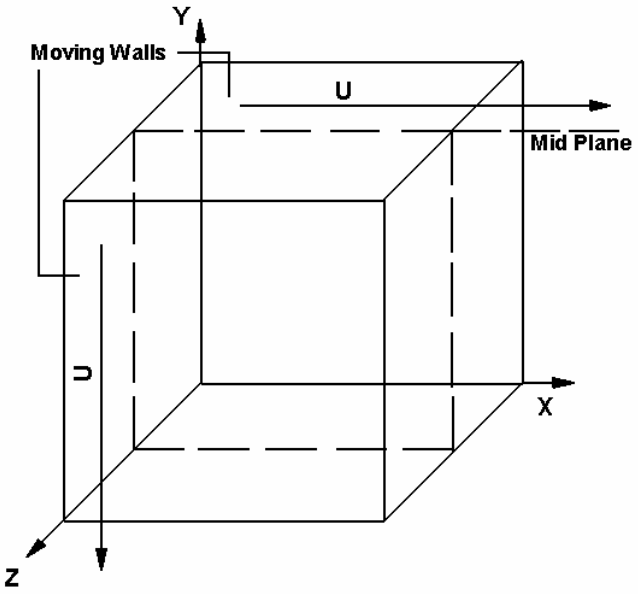

Figure 6.14: Geometry of the three-dimensional two-sided lid-driven cubic cavity flow.

Figure 6.14 shows the geometry of a three-dimensional two-sided non-facing lid-driven cubic cavity flow. The top wall of the cavity is moving towards right while the left

vertical wall is moving downwards with constant velocity U. The cubic cavity is filled with a Newtonian fluid with constant viscosity and density. Figure 6.15 shows the projected streamtraces at $z = 0.5$ (mid-span) of the cavity. The *D3Q19* model is used to do the LBM computation on a 67×67×67 lattice arrangement. As a result of the specified wall motion, at mid-span (Figure 6.15) a pair of primary and another pair of secondary vortices, symmetrical about the diagonal passing through the common trailing edge point of the moving walls, is formed. Our streamtraces agree well with those reported by Beya and Lili [107]. It is seen that the three-dimensional TSNFL driven cavity mid-span result bears some resemblance with similar result of the two-dimensional TSNFL flow reported in chapter 5 (section 5.3.2).

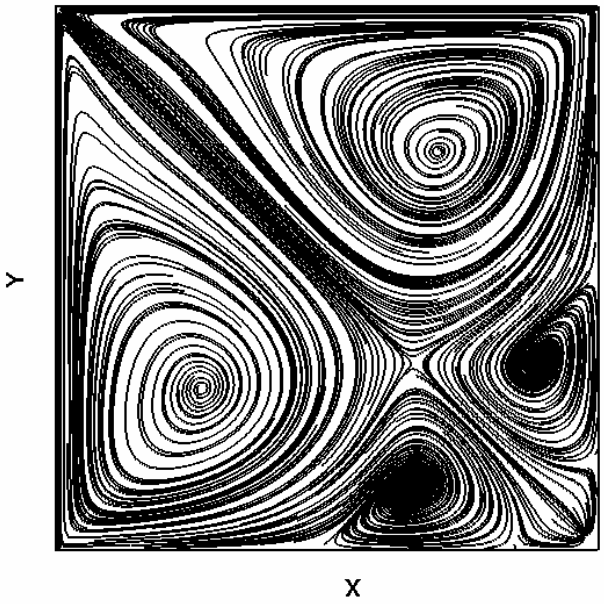

Figure 6.15: Streamtraces on plane $z = 0.5$ at $Re = 500$ for the 3D two-sided non-facing lid-driven cubic cavity flow.

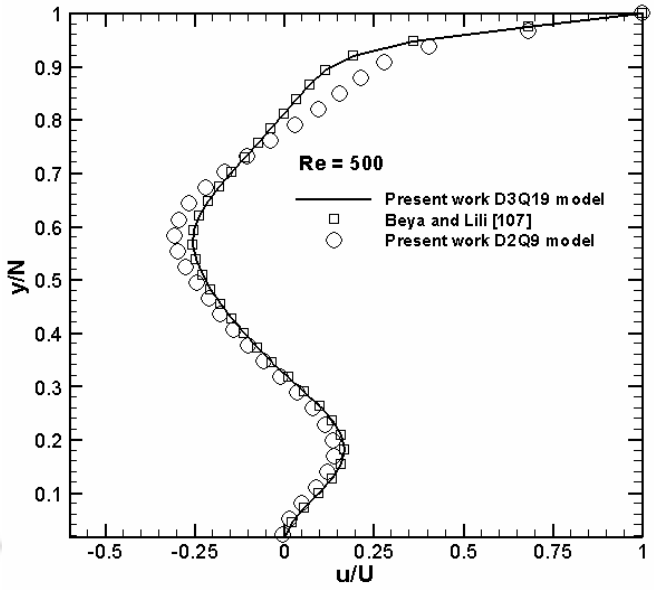

Figure 6.16: Comparison of centreline *u*-velocity profile of the 3-D TSNFL (mid-span) and 2-D TSNFL at *Re* = 500.

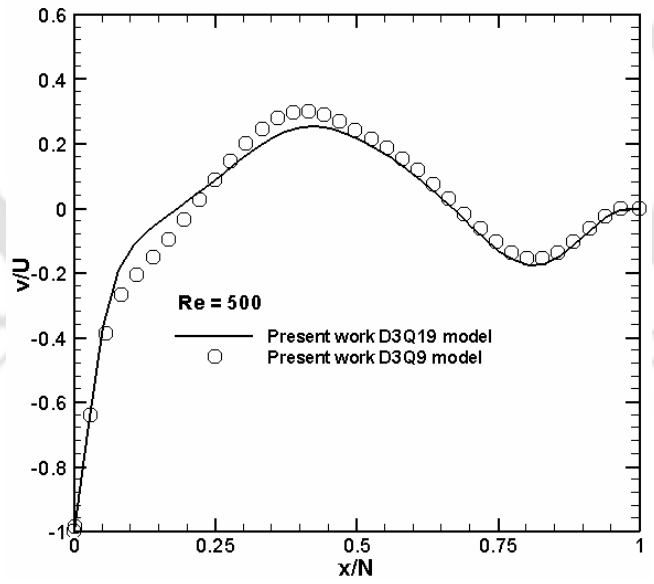

Figure 6.17: Comparison of centreline *v*-velocity profile of the 3-D TSNFL (mid-span) and 2-D TSNFL at *Re* = 500.

Figures 6.16 and 6.17 show the variations of centreline u-velocity in the vertical direction and v-velocity in the horizontal direction at $z = 0.5$ for $Re = 500$. The u-velocity profile compares very well that given by Beya and Lili [107]. Also shown in the same figures are the 2D velocity profiles obtained by using the *D2Q9* lattice model to study the end-wall effect. The noticeable discrepancy between the 2D and 3D profiles points out that even at a relatively low $Re = 500$, the endwalls have significant influence on the flow field.

6.4. Conclusion

Computational results for three three-dimensional flow problems for a wide range of Reynolds numbers with various types of wall motion using three 3-D LBM models like *D3Q15*, *D3Q19* and *D3Q27* are presented in this chapter. The three-dimensional LBM results are compared with two-dimensional LBM results in the central plane and the discrepancy demonstrates the effect of three-dimensionality of the flow fields. The *D3Q19* model is seems to be the most useful of the three 3D lattice models from the point of view of accuracy and computational time as it is more accurate than *D3Q15* and less time-consuming than *D3Q27*. Overall the computations are carried out for low to high Reynolds number and they are validated by comparison with established results wherever possible. It is thus demonstrated that the lattice Boltzmann method could be an accurate and alternative numerical method for solving the Navier-Stokes equations for three-dimensional problems.

Chapter 7

Simulation of Incompressible Thermal Flows

7.1. Introduction

In the past few decades, the problem of buoyancy driven square cavity with adiabatic top and bottom walls and differentially heated vertical walls has been the topic of extensive study [42-49, 57, 108-116]. Along with the lid-driven cavity problem, it has become one of the popular means for testing and validating numerical algorithms and computer codes. This problem is also attractive because of its importance in technological processes such as nuclear reactor insulation, ventilation of rooms, solar energy collection and many others [110]. Two features of this square cavity problem are: (i) its simple geometry with no singularity except at the corners and (ii) the availability of experimental and numerical data on this problem.

A large number of investigations have been carried out for natural convection in two-dimensional enclosures only. Peng *et al.* [46] simulated natural convection in a square cavity using a simplified thermal model of Internal Energy Density Distribution Function (IEDDF) approach. Dixit and Babu [49] have carried out natural convection in a square cavity for a wide range of Rayleigh numbers by LBM. De Vahl Davis [108] presented the reliable solutions for various Rayleigh numbers of a square cavity by finite difference method. Kalita *et al.* [110] computed solutions of the square cavity flow with a fourth-

order-accurate higher-order scheme. In order to simulate practical situations, natural convection in three-dimensional flow calculations is highly desirable. Limited number of reliable numerical results for steady state three-dimensional natural convection in the cubic cavity flows has been obtained in the past several years. Peng *et al.* [57] extended the solutions by IEDDF model to the three-dimensional cubic cavity flows in the range of Rayleigh numbers 10^3 to 10^5. Numerical simulations for natural convection in a cubic cavity have also been reported using numerical schemes based on a pseudocompressibility approach [115], the finite difference method [116], the pseudo-spectral Chebyshev approach [117], etc. This chapter is concerned with the application of the thermal Lattice Boltzmann model to compute incompressible two- and three-dimensional flows in cavities.

7.2. Overview of Thermal Lattice Boltzmann Method (TLBM)

Simulation of incompressible thermal flows is one of the challenging issues in Lattice Boltzmann Method (LBM) research. In general, the thermal LBM models fall into three main categories, namely, the passive-scalar, the multi-speed approach and the internal energy density distribution function (IEDDF) approach. The IEDDF approach proposed by He *et al.* [44] shows greater stability. The proper discretization of the continuous Boltzmann equation in temporal and spatial and particle velocity spaces affords a solution procedure for isothermal flow equation. Similarly an LBE thermal model can be developed by discretizing the continuous evolution equation for the internal energy density distribution. This IEDDF model is numerically more stable, and it can incorporate viscous heat dissipation and compression work done by the pressure [49].

Two convection test cases are namely, the laminar flow in a differentially heated square cavity and a cubic cavity are numerically analyzed through LBM. The Internal Energy Density Distribution Function (IEDDF) approach with two three-dimensional particle velocity models, namely, the *D3Q15* and *D3Q19* models and a two-dimensional model, namely, the nine-velocity model (*D2Q9*) have been used. The boundary condition used are stable and of good accuracy. To lend credibility to the thermal-lattice-Boltzmann-model square cavity results they are further compared with those obtained from a finite difference based code developed for this purpose.

The present chapter is arranged in five sections. Section 7.2 discusses with the overview of thermal Lattice Boltzmann Method; Section 7.3-7.5 deals with the governing equations, problems description, non-dimensional parameters and boundary conditions; section 7.6 includes the two- and three-dimensional results and discussion and finally, in section 7.7 concluding remarks are made.

7.3. Internal Energy Density Distribution Function (IEDDF) Model

For the incompressible thermal flows, He *et al.* [44] proposed IEDDF model, the relevant equations for which are

$$\frac{\partial f_i}{\partial t} + \left(\boldsymbol{c_i}.\nabla\right) f_i = -\frac{1}{\tau_v}\left(f_i - f_i^{eq}\right) + F \tag{7.1}$$

$$\frac{\partial g_i}{\partial t} + \left(\boldsymbol{c_i}.\nabla\right) g_i = -\frac{1}{\tau_c}\left(g_i - g_i^{eq}\right) \tag{7.2}$$

where F is an external force term. After suitable discretization, the governing equations for the internal energy density distribution function (IEDDF) model become [49]

$$f_i(\mathbf{x}+\boldsymbol{c_i}\Delta t,t+\Delta t)-f_i(\mathbf{x},t)=-\frac{1}{\tau_v}\left(f_i(\mathbf{x},t)-f_i^{eq}(\mathbf{x},t)\right)+F_i \tag{7.3}$$

$$g_i(\mathbf{x}+\boldsymbol{c_i}\Delta t,t+\Delta t)-g_i(\mathbf{x},t)=-\frac{1}{\tau_c}\left(g_i(\mathbf{x},t)-g_i^{eq}(\mathbf{x},t)\right) \tag{7.4}$$

where $f_i(\mathbf{x},t)$ is the density distribution function, $f_i^{eq}(\mathbf{x},t)$ is the equilibrium density distribution function, $g_i(\mathbf{x},t)$ is the internal energy distribution function and $g_i^{eq}(\mathbf{x},t)$ is the equilibrium internal energy distribution function at $\mathbf{x},t$. These are two relaxation times in thermal LBM model; τ_v is the relaxation time for the density distribution function and τ_c is the relaxation time for the internal energy distribution function. The equilibrium distribution function for the density $f_i^{eq}(\mathbf{x},t)$ can be written as [49]

$$f_i^{eq}=w_i\rho\left[1+\frac{3\left(\boldsymbol{c_i}.\boldsymbol{u}\right)}{c^2}+\frac{9\left(\boldsymbol{c_i}.\boldsymbol{u}\right)^2}{2c^2}-\frac{3\boldsymbol{u}^2}{2c^2}\right] \qquad i=0,1,2\ldots,N \tag{7.5}$$

where the weights w_i are as given by [49] in chapter 2. For the *D2Q9* model the equilibrium internal energy distribution function can be written as [49]

$$\begin{aligned}
g_0^{eq} &= -\frac{2\rho e}{3}\frac{\boldsymbol{u}^2}{2c^2}\\
g_{1,2,3,4}^{eq} &= \frac{\rho e}{9}\left[\frac{3}{2}+\frac{3\left(\boldsymbol{c_i}.\boldsymbol{u}\right)}{2c^2}+\frac{9\left(\boldsymbol{c_i}.\boldsymbol{u}\right)^2}{2c^4}-\frac{3\boldsymbol{u}^2}{2c^2}\right]\\
g_{5,6,7,8}^{eq} &= \frac{\rho e}{36}\left[3+\frac{6\left(\boldsymbol{c_i}.\boldsymbol{u}\right)}{c^2}+\frac{9\left(\boldsymbol{c_i}.\boldsymbol{u}\right)^2}{2c^4}-\frac{3\boldsymbol{u}^2}{2c^2}\right]
\end{aligned} \tag{7.6}$$

For the *D2Q9* model density relaxation parameter τ_v is related to the kinematic viscosity υ by

$$\upsilon = \left(\tau_v - \frac{1}{2} \right) c_s^2 \Delta t \tag{7.7}$$

and the internal energy relaxation parameter τ_c is related to the thermal diffusivity α by

$$\alpha = \frac{2}{3}\left(\tau_c - \frac{1}{2} \right) \Delta t \tag{7.8}$$

where c_s is the lattice speed of sound equal to 1/3.

For the *D3Q15* model the equilibrium internal energy distribution function can be written as [57]

$$\begin{aligned} g_0^{eq} &= -\frac{\rho e}{3}\frac{\boldsymbol{u}^2}{c^2} \\ g_{1-6}^{eq} &= \frac{\rho e}{9}\left[1 + \frac{\left(\boldsymbol{c_i}.\boldsymbol{u}\right)}{c^2} + \frac{9\left(\boldsymbol{c_i}.\boldsymbol{u}\right)^2}{2c^4} - \frac{3\boldsymbol{u}^2}{2c^2} \right] \\ g_{7-14}^{eq} &= \frac{\rho e}{72}\left[3 + 7\frac{\left(\boldsymbol{c_i}.\boldsymbol{u}\right)}{c^2} + \frac{9\left(\boldsymbol{c_i}.\boldsymbol{u}\right)^2}{2c^4} - \frac{3\boldsymbol{u}^2}{2c^2} \right] \end{aligned} \tag{7.9}$$

For the *D3Q19* model the equilibrium internal energy distribution function can be written as [57]

$$\begin{aligned} g_0^{eq} &= -\frac{\rho e}{2}\frac{\boldsymbol{u}^2}{c^2} \\ g_{1-6}^{eq} &= \frac{\rho e}{18}\left[1 + \frac{\left(\boldsymbol{c_i}.\boldsymbol{u}\right)}{c^2} + \frac{9\left(\boldsymbol{c_i}.\boldsymbol{u}\right)^2}{2c^4} - \frac{3\boldsymbol{u}^2}{2c^2} \right] \\ g_{7-18}^{eq} &= \frac{\rho e}{36}\left[2 + 4\frac{\left(\boldsymbol{c_i}.\boldsymbol{u}\right)}{c^2} + \frac{9\left(\boldsymbol{c_i}.\boldsymbol{u}\right)^2}{2c^4} - \frac{3\boldsymbol{u}^2}{2c^2} \right] \end{aligned} \tag{7.10}$$

For the above three-dimensional *D3Q15* and *D3Q19* models density relaxation parameter τ_v is related to the kinematic viscosity υ by

$$\upsilon = \frac{2\tau_v - 1}{6} \tag{7.11}$$

The internal energy relaxation parameter τ_c is related to the thermal diffusivity α for both models by

$$\alpha = \frac{5}{9}\left(\tau_c - \frac{1}{2}\right)\Delta t \tag{7.12}$$

Then the macroscopic density, velocity and temperature are calculated by

$$\begin{aligned} \rho &= \sum_{i=0}^{N} f_i , \\ \rho \boldsymbol{u} &= \sum_{i=0}^{N} f_i \boldsymbol{c_i} , \\ \rho e &= \sum_{i=0}^{N} g_i . \end{aligned} \tag{7.13}$$

where the internal energy, e, for two-dimensional flows is given by $e = RT$ and for three-dimensional flows is given by $e = 3RT/2$. Here R is the gas constant and temperature of the fluid is described by the internal energy e. The macroscopic density and velocity field are simulated using the density distribution function and the macroscopic temperature is simulated using the internal energy distribution function. Equation (7.3) can recover the mass and momentum equations, while Equation (7.4) can recover the energy equation at the macroscopic level through the Chapman-Enskog expansion [57].

7.4. Problem Description

7.4.1. Case I - Thermally Driven Square Cavity

The problem considered here is the two-dimensional incompressible steady state flow of air, considered a Boussinesq fluid of Prandtl number (Pr) 0.71 in an upright square cavity

of side L. Figure 7.1 shows the geometry and coordinate system of the square cavity. The vertical walls are both isothermal; the left wall at temperature T_H is hotter than the right wall at temperature T_C. The horizontal walls are both insulated. Natural convection starts owing to the temperature difference between the left and right walls. Body forces are present in the form of gravitational force that acts in the negative *y*-direction.

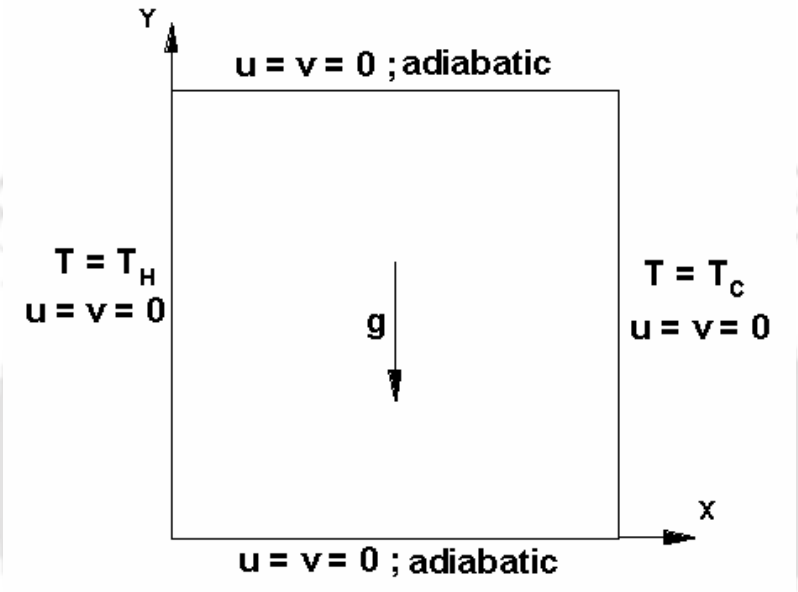

Figure 7.1: Geometry and boundary conditions of the square enclosure.

7.4.2. Case II - Thermally Driven Cubic Cavity

The cubic cavity has an aspect ratio of unity and is filled with the working fluid of air for which the Prandtl number (Pr) is fixed at 0.71. Figure 7.2 shows the geometry and coordinate system of the cubic enclosure. No-slip boundary conditions are imposed on all the faces of the cube. The left and right vertical walls are considered to be isothermal but at different temperatures of T_H and T_C respectively. The remaining four walls are taken as adiabatic walls. The buoyancy force due to gravity acts in the negative *y*-direction.

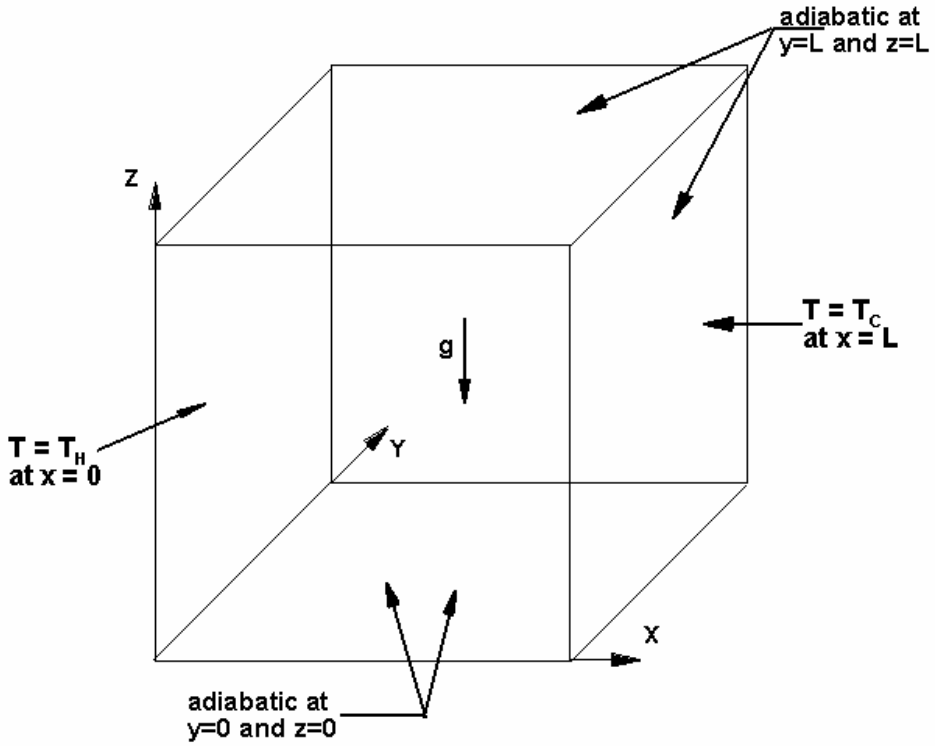

Figure 7.2: Geometry and boundary conditions of the cubic enclosure.

7.4.3. Buoyancy Force and Non-Dimensional Parameters

Natural convection problem can be characterized by two dimensionless parameters namely, the Rayleigh number Ra and the Prandtl number Pr

$$Ra = \frac{g\beta\Delta T L^3}{\upsilon\alpha}$$
$$Pr = \frac{\upsilon}{\alpha} \qquad (7.14)$$

with g the acceleration due to gravity, β the coefficient of thermal expansion, ΔT the temperature difference between the two vertical walls and L the side of the cavity. In the simulation, the external force term corresponding to the buoyancy force is

$$F_i = \frac{\boldsymbol{G}.(\boldsymbol{c_i} - \boldsymbol{u})}{RT} f_i^{eq} \qquad (7.15)$$

The Boussinesq approximation is applied to the buoyancy force term

$$\rho \boldsymbol{G} = \rho \beta g (T - T_m) \hat{\boldsymbol{j}} \tag{7.16}$$

where T_m is the mean temperature of the fluid, $\hat{\boldsymbol{j}}$ is the vertical direction opposite to that of gravity. To ensure that the code is working properly in the near incompressible regime, the Mach number is set to be equal to 0.1. The Mach number is given as $Ma = u/c_s$, where u is the characteristic velocity ($u = \sqrt{\beta g \Delta T L}$) and c_S is the lattice speed of sound equal to 1/3. This relation is used to calculate the value of β. Then kinematic viscosity υ and thermal diffusivity α are determined from the two non-dimensional parameters *Ra* and *Pr*. Then the two relaxation times τ_v and τ_c are obtained using kinematic viscosity υ and thermal diffusivity α. Nusselt number is the most important dimensionless number in describing the convective heat transport. The local heat flux in the $x-$direction $q_x(x, y)$ is equal to $uT - \alpha \frac{\partial T}{\partial x}$. The average Nusselt number on the boundary for square cavity is given by [46]

$$\overline{Nu} = \int_0^1 \left. \frac{\partial T(x, y)}{\partial x} \right|_{x=0, \text{ or } x=1} dy \tag{7.17}$$

7.4.4. Boundary Conditions

It is known that no-slip velocity conditions are imposed on the rigid walls of the cavity. For the square cavity problem, fixed temperature (Dirichlet condition) is applied on the vertical walls, whereas the horizontal walls are perfectly insulated (Neumann condition).

The bounce-back rule of the non-equilibrium distribution function is used for the density distribution function [44].

$$f_{\sigma}^{iso} = f_{\sigma^1}^{iso} \tag{7.18}$$

where σ and σ^1 indicate opposite directions. For the temperature distribution function, second-order finite difference approximation is used (discussed in chapter 2, section 2.5.3). The method used to find the temperature is also found to be numerically stable. For all LBM simulations, the initial velocity is zero at all lattice nodes and the temperature distributes linearly from the left wall to right wall.

7.5. Finite Difference (FD) Stream Function-Vorticity Based Solver

The stream function-vorticity $(\psi - \omega)$ formulation was used in the present work to validate our 2D thermal-LBM-model results. The non-dimensional governing equations are given by

$$\begin{aligned} u\frac{\partial \omega}{\partial x} + v\frac{\partial \omega}{\partial y} &= Pr\nabla^2\omega + RaPr\frac{\partial T}{\partial x} \\ \nabla^2\psi &= -\omega \\ u\frac{\partial T}{\partial x} + v\frac{\partial T}{\partial y} &= \nabla^2 T \end{aligned} \tag{7.19}$$

where *Ra* and *Pr* are dimensionless parameters mentioned earlier. The FDM solution methodology is as described in chapter 3.

7.6. Results and Discussion

This section describes the results obtained for the two- and three-dimensional natural convection flows by the IEDDF thermal model. First, the results of the square cavity computations for a fluid of $Pr = 0.71$ with *Ra* ranging from a moderate to a high laminar

regime (Ra = 10^3 to 10^6) are presented through tables and graphs. Figure 7.3 shows the square cavity streamlines, isotherms and vorticity contours computed by IEDDF approach using *D2Q9* model for Ra = 10^3. At Ra = 10^3, streamlines are those of a single vortex, with its centre in the centre of the domain. Figures 7.4-7.6 show the same for Ra = 10^4, 10^5 and 10^6 respectively. As the Rayleigh number increases from 10^3 to 10^4 the vortex core takes an elliptic shape and the effect of convection is more pronounced in the isotherms. Temperature gradients are now sharper near the vertical walls, but diminish in the centre. At Ra = 10^5 (Figure 7.5) the vortex core is further elongated and breaks into two vortices and the longer axis of the oval-shaped core, which joins the two smaller vortices is seen to turn in the direction of the convection current. At Ra = 10^6 these two smaller vortices are seen to move towards the top-left and bottom-right corners so that the line joining them turns further in the direction of the circulation generated. From Figures 7.3-7.6, on the vertical walls boundary layer thickness is seen to progressively decrease as Ra increases. These results show that the heat transfer changes from conduction dominated to convection dominated as Rayleigh number increases. For the range of Rayleigh numbers considered here, there is generally a centro-symmetry of velocity, vorticity and temperature distribution. As mentioned earlier these LBM results are now substantiated by comparison with the results obtained by the FDM code. Figures 7.7-7.10 show the streamlines, isotherms and vorticity contours in the square cavity computed through the finite difference method (FDM) for the same Rayleigh numbers. Very close resemblance of the streamlines, isotherm patterns and vorticity contours of the LBM and FDM results lends credibility to the present LBM results computed through the IEDDF approach.

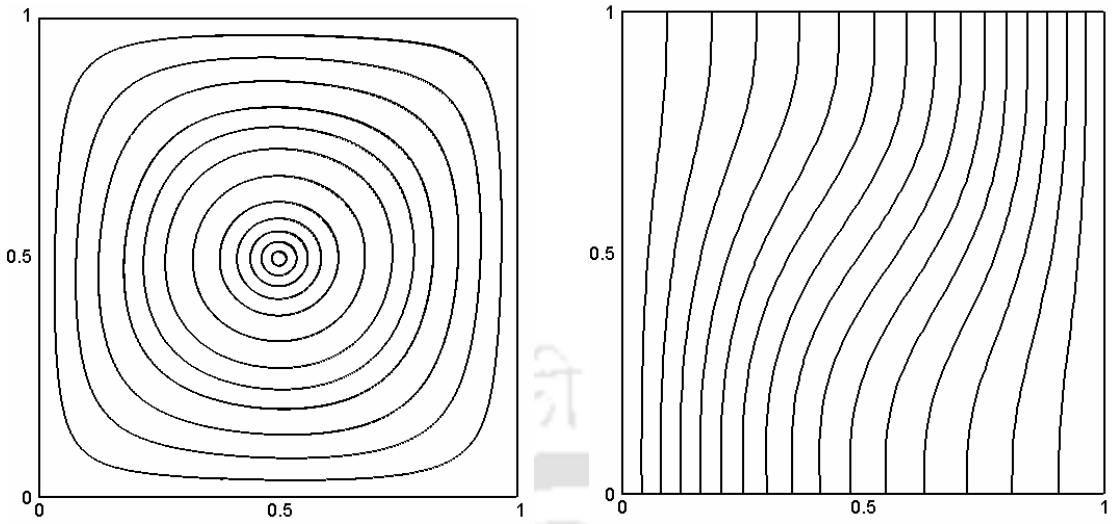

(a) (b)

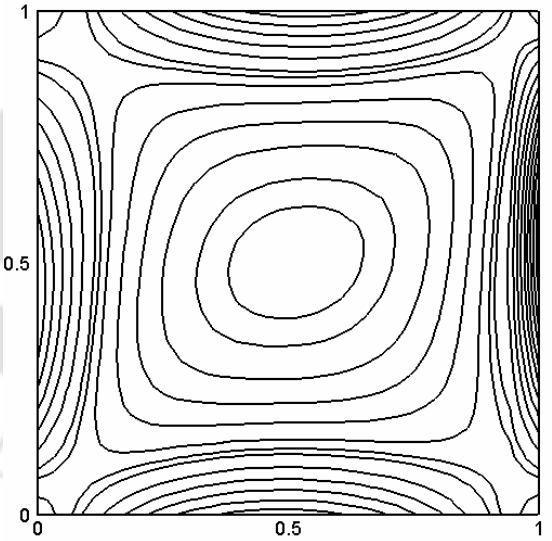

(c)

Figure 7.3: $Ra = 10^3$, Model: *D2Q9*, lattice size: 129 × 129: (a) streamlines (b) isotherms (c) vorticity contours for the thermally driven square cavity flow.

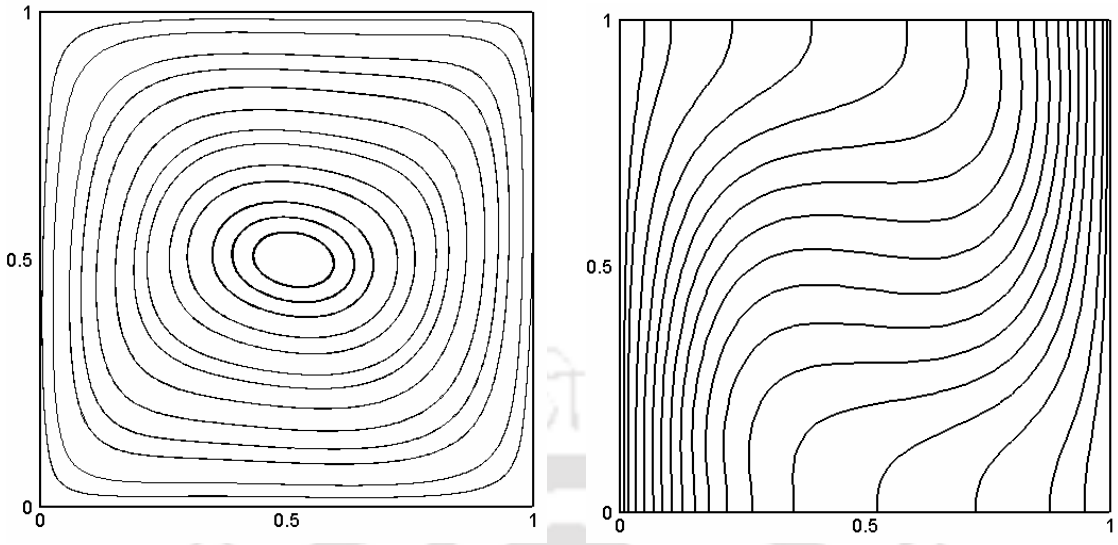

(a) (b)

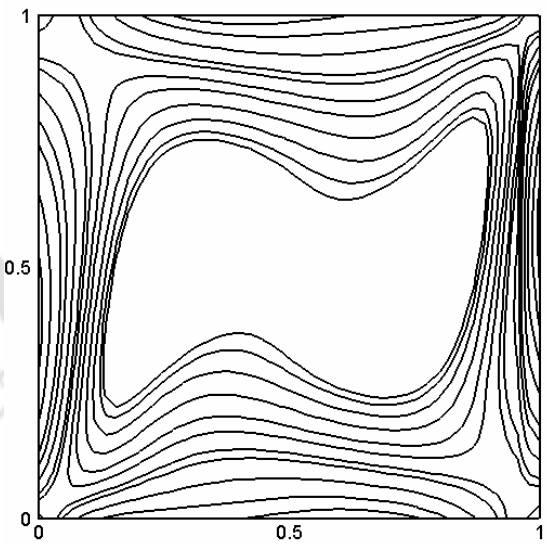

(c)

Figure 7.4: $Ra = 10^4$, Model: *D2Q9*, lattice size: 161 × 161: (a) streamlines (b) isotherms (c) vorticity contours for the thermally driven square cavity flow.

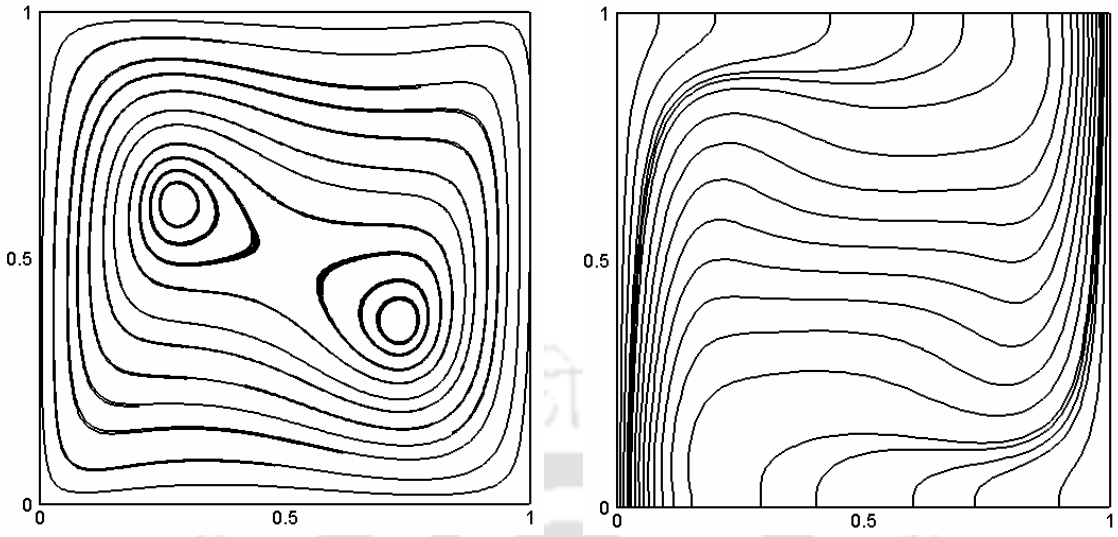

(a) (b)

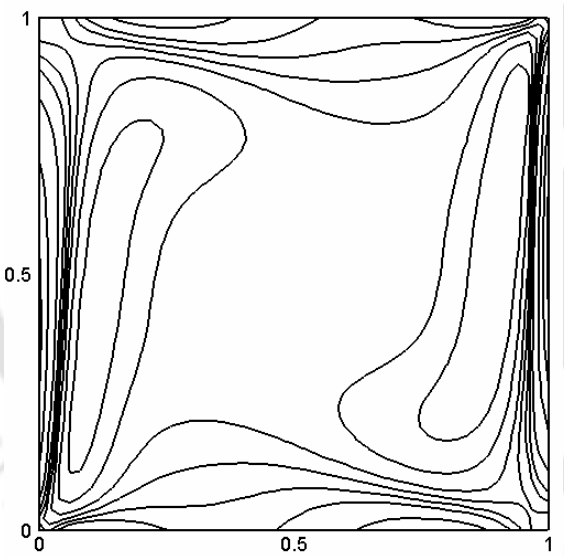

(c)

Figure 7.5: $Ra = 10^5$, Model: *D2Q9*, lattice size: 191 × 191: (a) streamlines (b) isotherms (c) vorticity contours for the thermally driven square cavity flow.

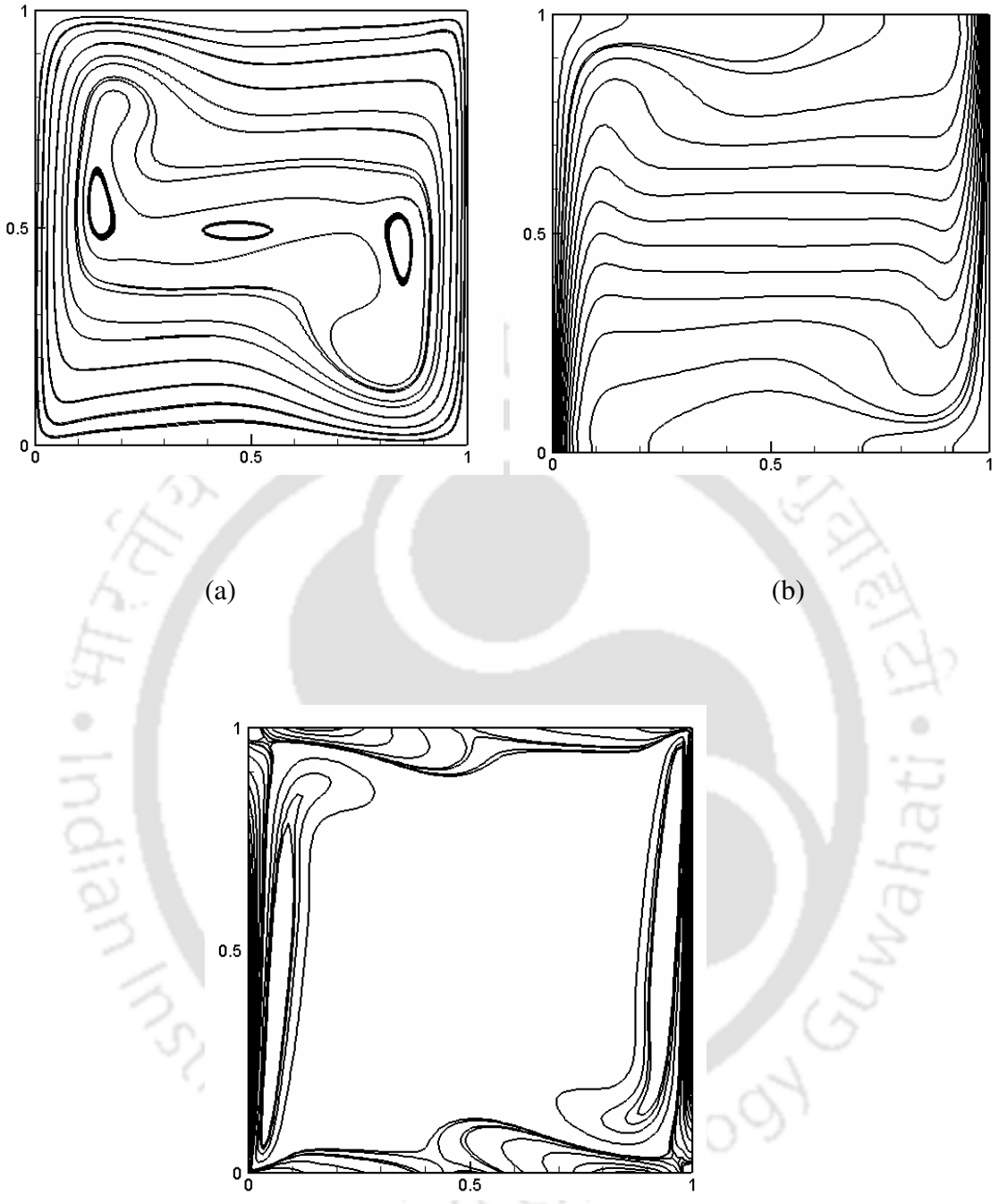

Figure 7.6: $Ra = 10^6$, Model: *D2Q9*, lattice size: 221 × 221: (a) streamlines (b) isotherms (c) vorticity contours for the thermally driven square cavity flow.

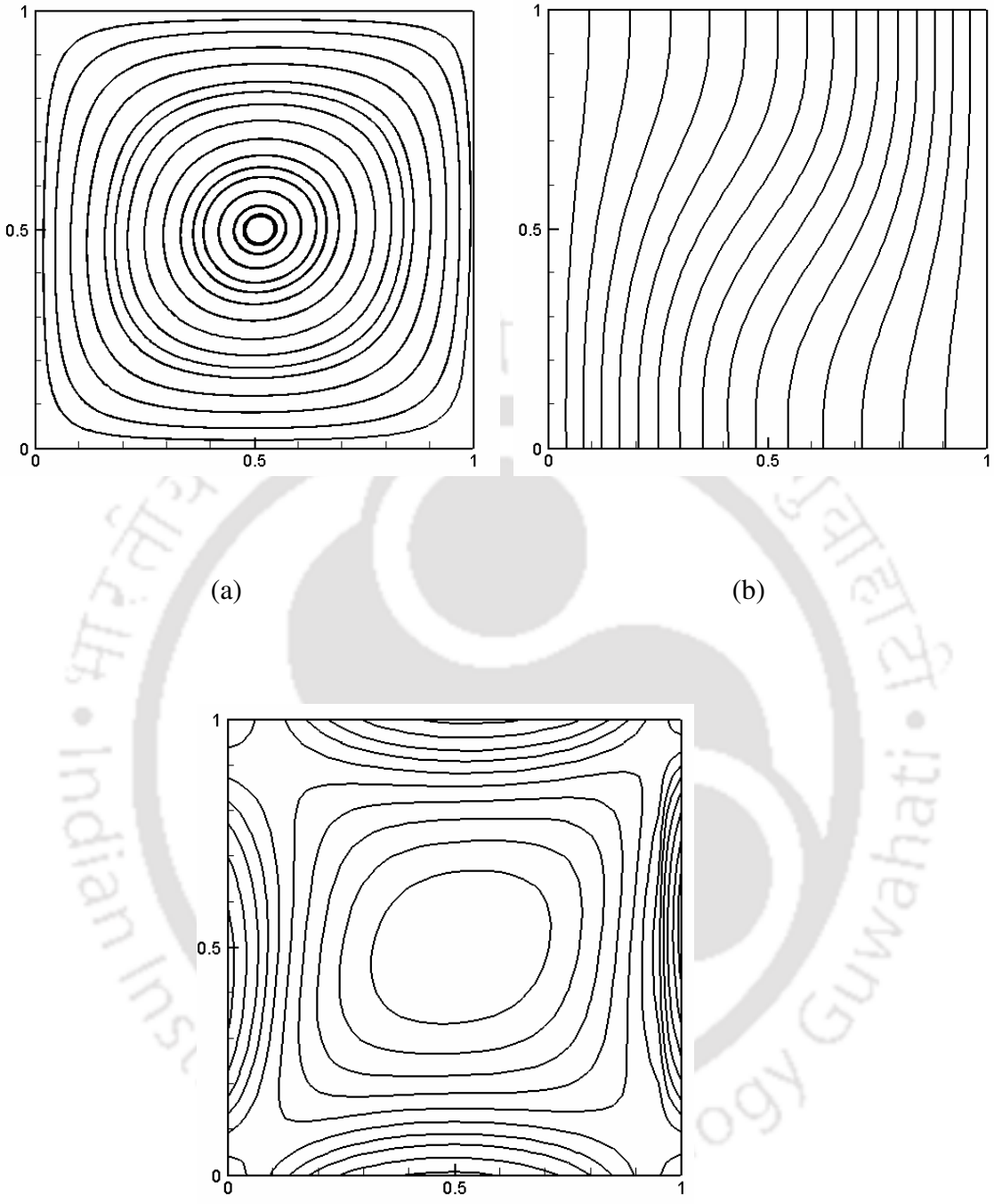

Figure 7.7: $Ra = 10^3$, Grid size: 129 × 129: (a) streamlines (b) isotherms (c) vorticity contours obtained by FDM for the thermally driven square cavity flow.

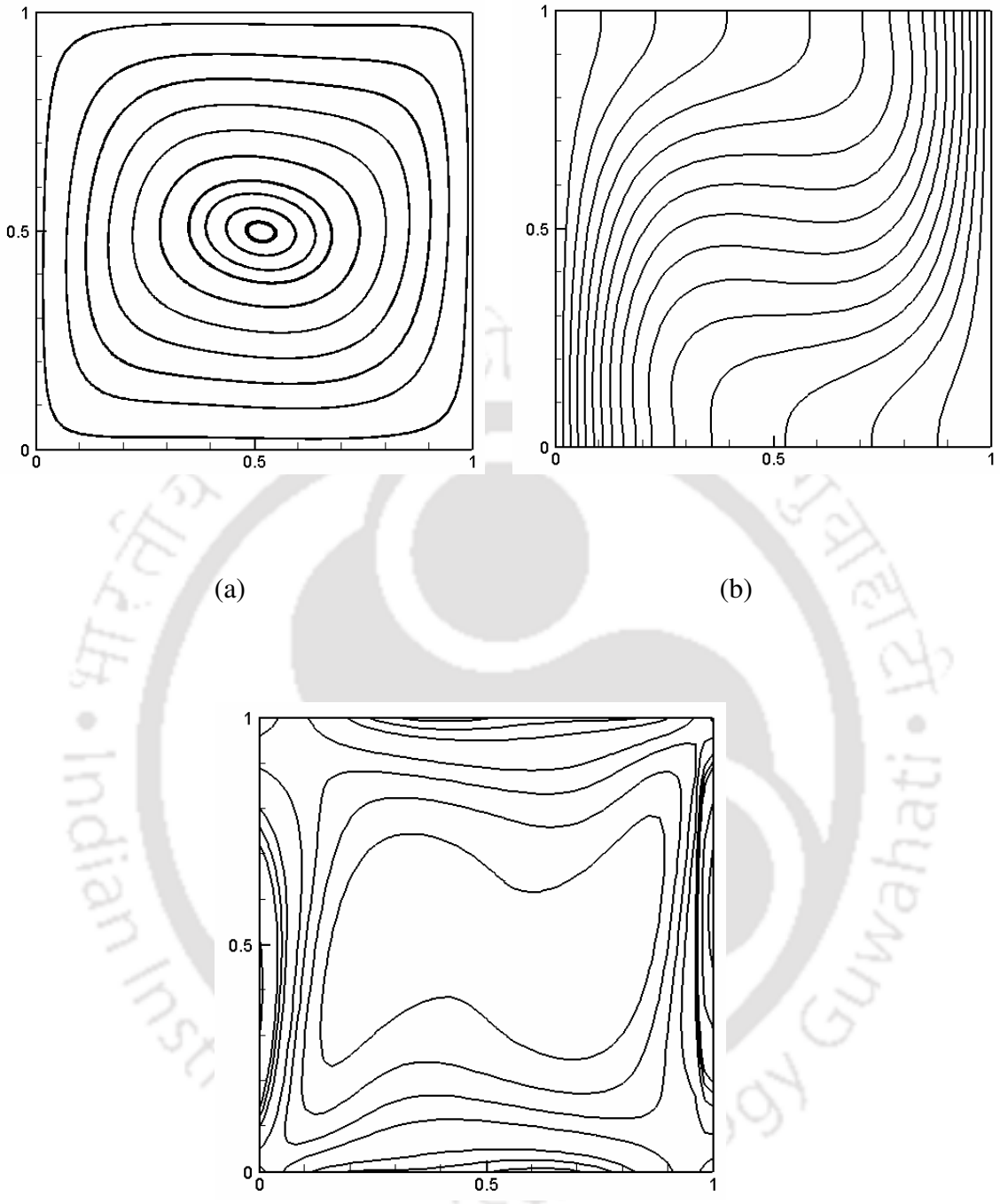

Figure 7.8: $Ra = 10^4$, Grid size: 161 × 161: (a) streamlines (b) isotherms (c) vorticity contours obtained by FDM for the thermally driven square cavity flow.

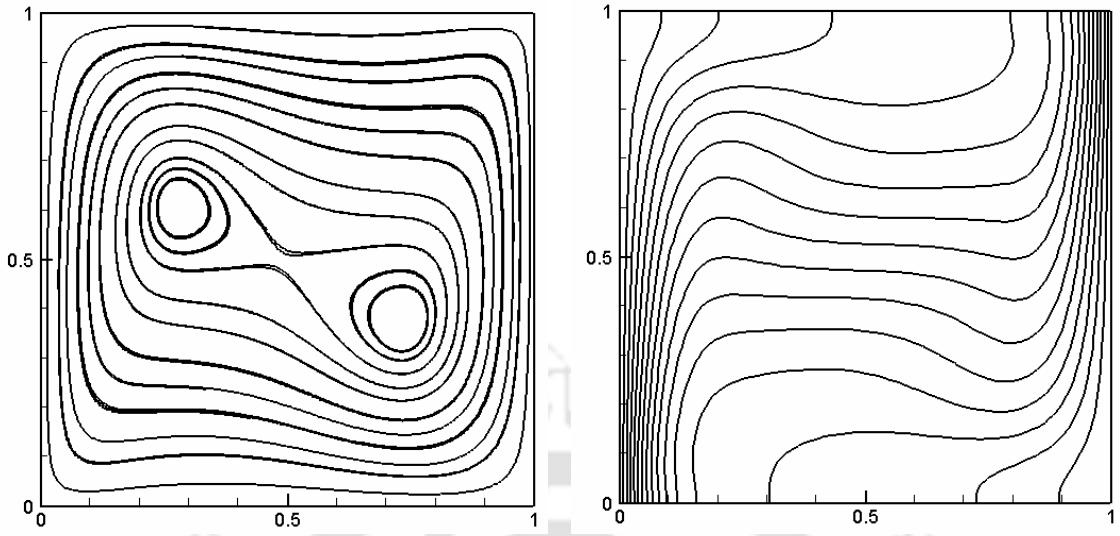

(a) (b)

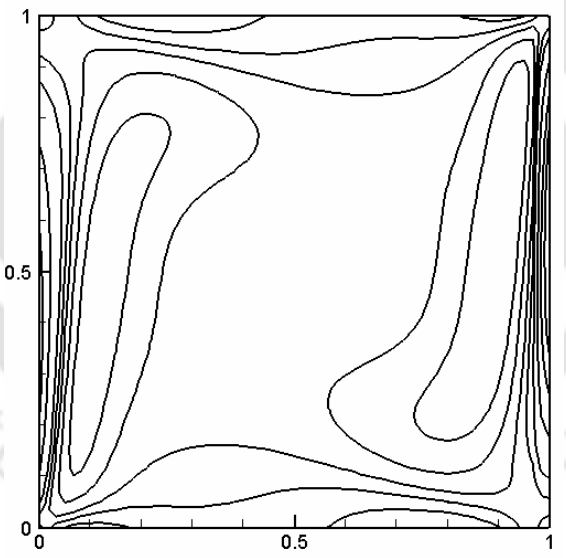

(c)

Figure 7.9: $Ra = 10^5$, Grid size: 191 × 191: (a) streamlines (b) isotherms (c) vorticity contours obtained by FDM for the thermally driven square cavity flow.

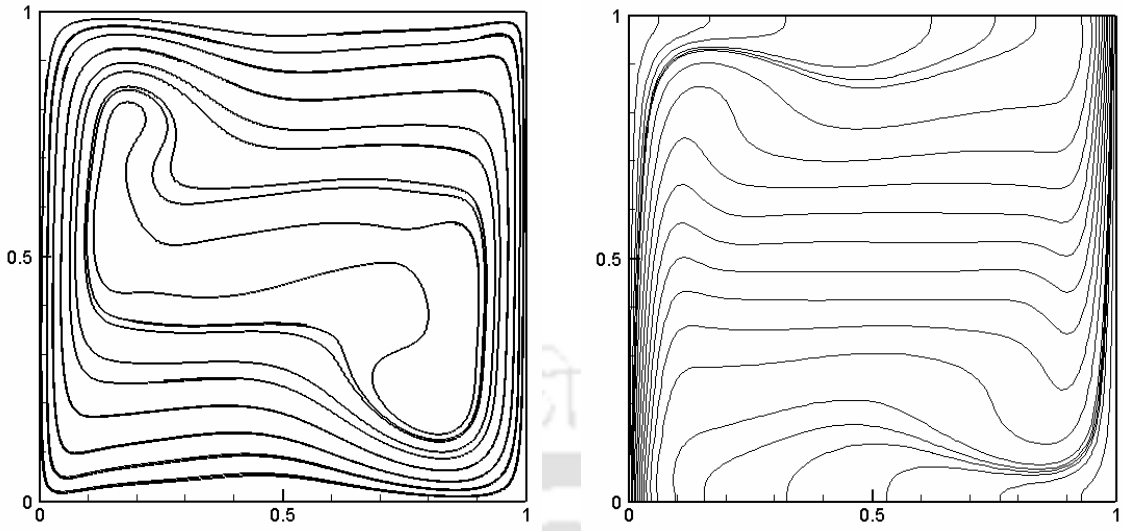

(a) (b)

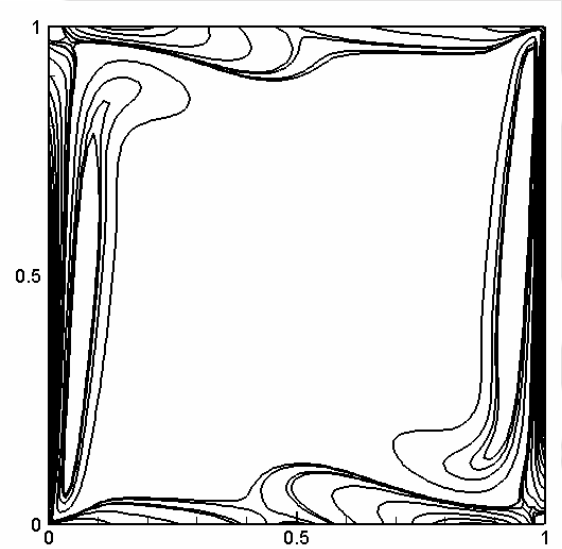

(c)

Figure 7.10: $Ra = 10^6$, Grid size: 221 × 221: (a) streamlines (b) isotherms (c) vorticity contours obtained by FDM for the thermally driven square cavity flow.

It is known that De Vahl Davis [108] presented reliable solutions for various Rayleigh numbers for a square cavity by FDM. He obtained his results using Forward Time Centered Space (FTCS) scheme of second-order spatial accuracy in conjunction with Richardson extrapolation; similarly Chenoweth and Paolucci [109] used a second-order accurate method followed by three point Richardson extrapolation and claimed their results to be sixth-order accurate. The streamlines and isotherms also display very close resemblance with these results and similar results presented by Peng *et al*. [46], Shu *et al.* [48], Dixit and babu [49], De Vahl Davis [108], Kalita *et al.* [110], and other investigators [111, 112].

Table 7.1: Effect of lattice size on the thermally-driven square cavity results for $Ra = 10^3$.

Lattice Size	$U_{\max}$	$V_{\max}$	Nu_0	$Nu_{1/2}$
67 × 67	3.642	3.672	1.115	1.119
129 × 129	3.646	3.689	1.117	1.118
161 × 161	3.651	3.682	1.118	1.118

Table 7.1 shows the numerical results of the maximum horizontal velocity $U_{\max}$ on the vertical centreline of the cavity, the maximum vertical velocity $V_{\max}$ on the horizontal centreline of the cavity, the average Nusselt number Nu_0 at the hot wall and the average Nusselt number $Nu_{1/2}$ along the vertical centreline. The effect of lattice size on the square cavity results for $Ra = 10^3$ is clearly visible from Table 7.1 and the results for the lattice size of 161 × 161 can be considered acceptable.

Table 7.2: Effect of lattice size on the thermally-driven square cavity results for $Ra = 10^4$.

Lattice Size	U_{max}	V_{max}	Nu_0	$Nu_{1/2}$
129 × 129	16.321	19.508	2.221	2.253
161 × 161	16.289	19.621	2.241	2.246
201 × 201	16.256	19.605	2.243	2.245

Table 7.3: Effect of lattice size on the thermally-driven square cavity results for $Ra = 10^5$.

Lattice Size	U_{max}	V_{max}	Nu_0	$Nu_{1/2}$
161 × 161	36.289	66.542	4.348	4.507
191 × 191	35.526	68.071	4.489	4.520
221 × 221	34.675	68.572	4.516	4.521

Table 7.4: Effect of lattice size on the thermally-driven square cavity results for $Ra = 10^6$.

Lattice Size	U_{max}	V_{max}	Nu_0	$Nu_{1/2}$
191 × 191	63.987	215.798	7.787	8.417
221 × 221	65.635	214.189	8.489	8.810
257 × 257	65.594	218.572	8.516	8.821

Table 7.2 - 7.4 present the effect of lattice size on the results for $Ra = 10^4$, 10^5 and 10^6. From Tables 7.1- 7.4 we can observe that as the Rayleigh number increases average Nusselt number on the boundary increases. Through the present study, the lattice sizes of 129×129 for $Ra = 10^3$, 161×161 for $Ra = 10^4$, 191×191 for $Ra = 10^5$ and 221×221 for

$Ra = 10^6$ are found to be sufficient for engineering purposes. The comparison of average Nusselt number ($\overline{Nu}$) on the boundary for the square cavity for different works is shown in Table 7.5. It can be seen that our numerical results computed through the thermal Lattice Boltzmann Method and Finite Difference Method agree quite well with those obtained by the other investigators.

Table 7.5: Comparison of square cavity average Nusselt number ($\overline{Nu}$) on the boundary for different works for the thermally-driven square cavity flow.

Ra	10^3	10^4	10^5	10^6
De Vahl Davis [108]	1.118	2.243	4.519	8.800
Chenoweth and Paolucci [109]	1.118	2.244	4.520	8.822
Kalita *et al.* [110]	1.118	2.245	4.522	8.829
Ball and Kuo [111]	1.118	2.244	4.522	8.825
Ho and Lin [112]	1.118	2.248	4.528	8.824
Present TLBM	1.118	2.245	4.521	8.821
Present FDM	1.118	2.244	4.520	8.819

It is also seen from Table 7.5 that in the high Rayleigh number cases the average Nusselt number on the boundary obtained by the thermal LBM is slightly smaller than that of existing continuum-based results. The same trend was observed in the simulation of the thermal square and cubic cavity flows by some LBM works [46-49]. This is probably due to the fact that the macroscopic equations of the LBM are equivalent to the Navier-Stokes equations only up to the second-order of the macroscopic flow velocity [47].

Most of the existing results for the thermally-driven cavity are for the square cavity flow only. We now use the *D3Q15* and *D3Q19* LBM models to compute the three-dimensional flow in a thermally-driven cubic cavity. Figures 7.11 - 7.13 show the *D3Q19* model natural convection results in a cubic cavity at Rayleigh numbers of $Ra = 10^3$, 10^4 and 10^5 at the plane $z = 0.5$. From the figures it is observed that at the mid-plane the thickness of the boundary layer near the isothermal walls decreases with the increase in Rayleigh number. For the *D3Q19* model, a lattice size independence study is conducted for $Ra = 10^3$ and $Ra = 10^4$. Table 7.6 gives the results of this study for four different lattice arrangements. It indicates that the accuracy of the numerical predictions of the flow and thermal characteristics increases consistently with the lattice size refinement and the results for the 81 × 81 × 81 case appears to be acceptable. Average Nusselt number on the boundary for the cubic cavity obtained with *D3Q15* and *D3Q19* models are tabulated in Table 7.7. We observe that the value of the average Nusselt number on the boundary given by the supposedly more accurate *D3Q19* model is higher than that given by the *D3Q15* model for the all the three Rayleigh numbers.

Table 7.6: Effect of Lattice size (*D3Q19*) on the thermally-driven cubic cavity average Nusselt Number on the boundary for $Ra = 10^3$ and $Ra = 10^4$.

$Ra = 10^3$		$Ra = 10^4$	
Lattice Size	Average Nusselt Number on the boundary	Lattice Size	Average Nusselt Number on the boundary
41 × 41 × 41	1.0920	51 × 51 × 51	2.2291
55 × 55 × 55	1.0950	55 × 55 × 55	2.2299
67 × 67 × 67	1.0967	67 × 67 × 67	2.2314
81 × 81 × 81	1.0971	81 × 81 × 81	2.2319

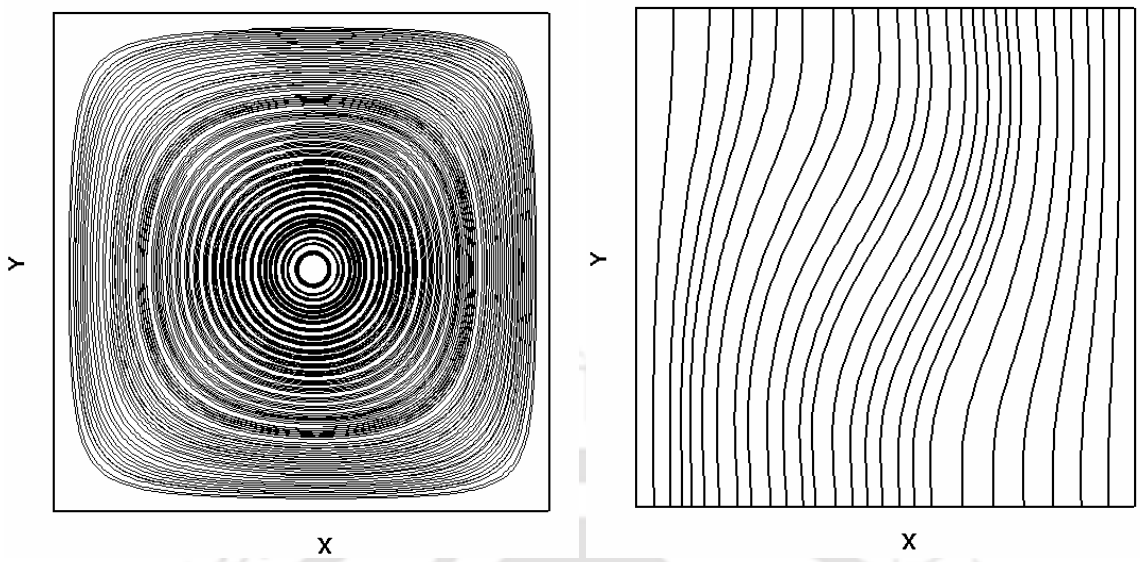

(a) (b)

Figure 7.11: $Ra = 10^3$, Model: *D3Q19*, lattice size: 67 × 67 × 67: (a) streamtraces (b) isotherms for the thermally driven cubic cavity flow at $z = 0.5$.

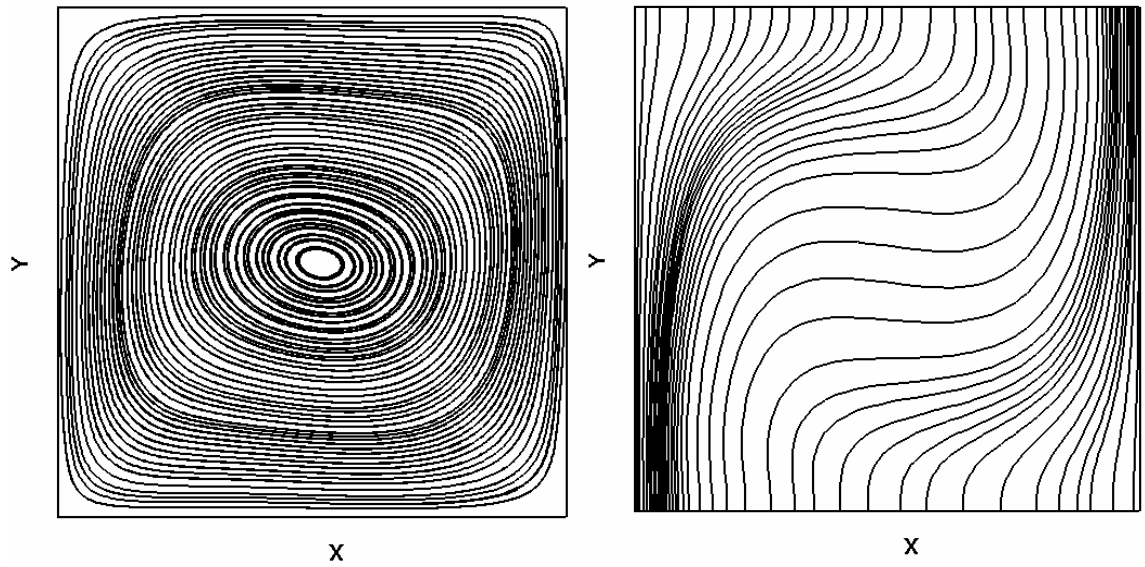

(a) (b)

Figure 7.12: $Ra = 10^4$, Model: *D3Q19*, lattice size: 67 × 67 × 67: (a) streamtraces (b) isotherms for the thermally driven cubic cavity flow at $z = 0.5$.

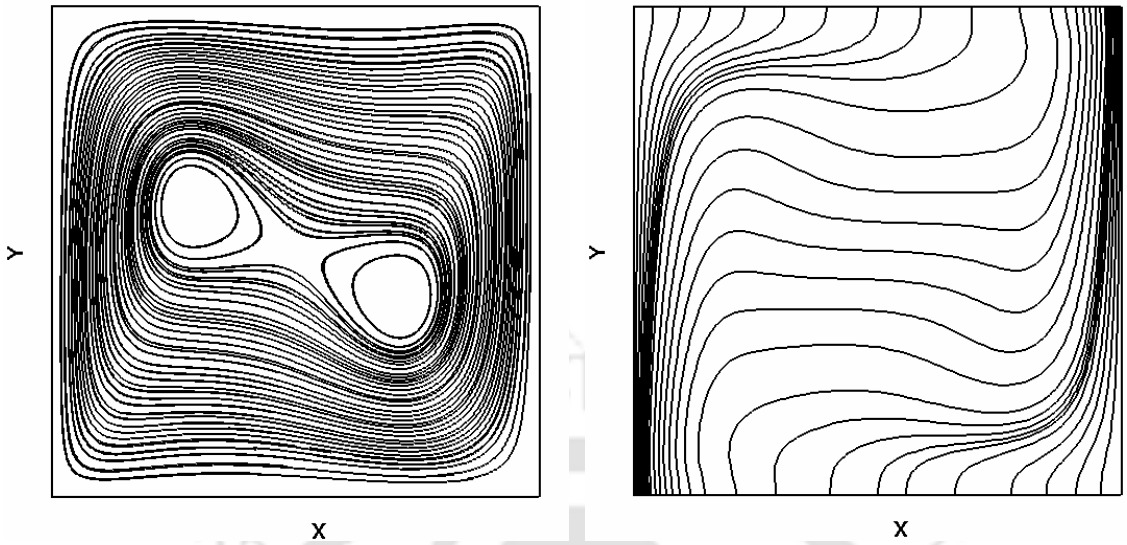

(a) (b)

Figure 7.13: $Ra = 10^5$, Model: *D3Q19*, lattice size: 81 × 81 × 81: (a) streamtraces (b) isotherms for the thermally driven cubic cavity flow at $z = 0.5$.

Table 7.7: Comparison of cubic cavity average Nusselt numbers on the boundary for *D3Q15* and *D3Q19* models.

Rayleigh Number	10^3		10^4		10^5	
Lattice Size	67 × 67 × 67	67 × 67 × 67	67 × 67 × 67	67 × 67 × 67	81 × 81 × 81	81 × 81 × 81
Lattice Model	*D3Q15*	*D3Q19*	*D3Q15*	*D3Q19*	*D3Q15*	*D3Q19*
Average Nusselt Number on the boundary	1.0920	1.0967	2.2303	2.2314	4.326	4.429

Table 7.7 shows that the average Nusselt numbers on the boundary obtained by the *D3Q19* and *D3Q15* models are almost identical at all Rayleigh numbers. It may be

recalled that, the *D3Q19* model seems to be the most useful of the three 3D lattice models from the point of view of accuracy and numerical stability as it is more accurate than *D3Q15* model. The velocity profiles of the *u*- component on the vertical centreline and the *v*- component on the horizontal centreline on the plane $z = 0.5$ (mid-span) at $Ra = 10^3$, 10^4 and 10^5 are shown in Figures 7.14-7.16. To plot 3D centreline velocity profiles, the *D3Q19* model is used in the present section. Also shown in the same figures are the 2D velocity profiles obtained by using the *D2Q9* model and FDM to study the three-dimensional effect. It is seen that the peak values of the horizontal and vertical velocities increase owing to the intensified convective activities with the increase in Rayleigh number. Steep rise in the normal gradient of the *v*-velocity with the Rayleigh number (Figures 7.14 (b) – 7.16 (b)) on the hot and cold walls also indicates increased convective activity at higher values of the Rayleigh number.

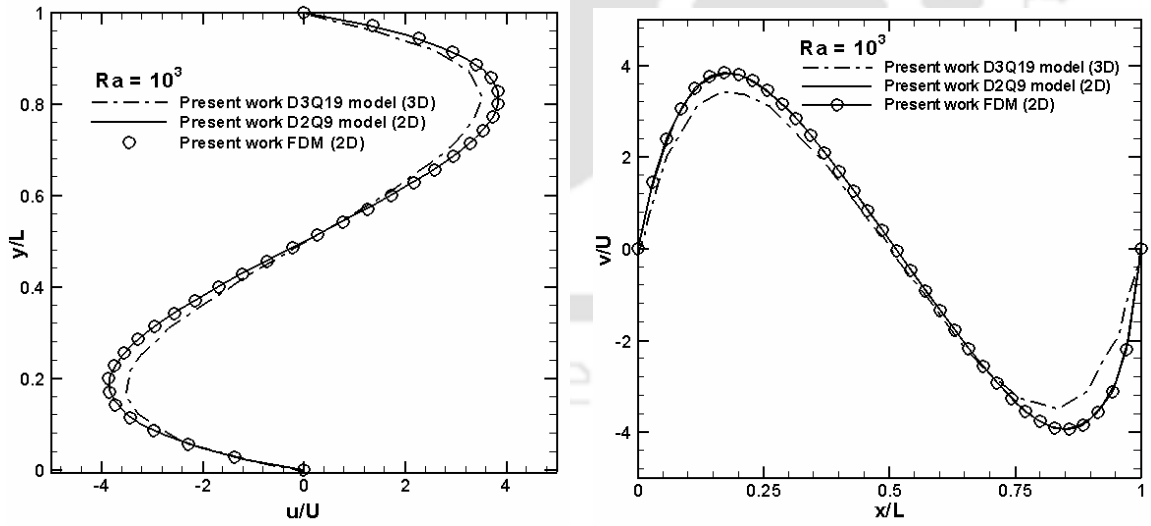

(a) Centreline *u*- velocity (b) Centreline *v*- velocity

Figure 7.14: Comparison of centreline velocities of cubic (mid-span) and square cavity at $Ra = 10^3$.

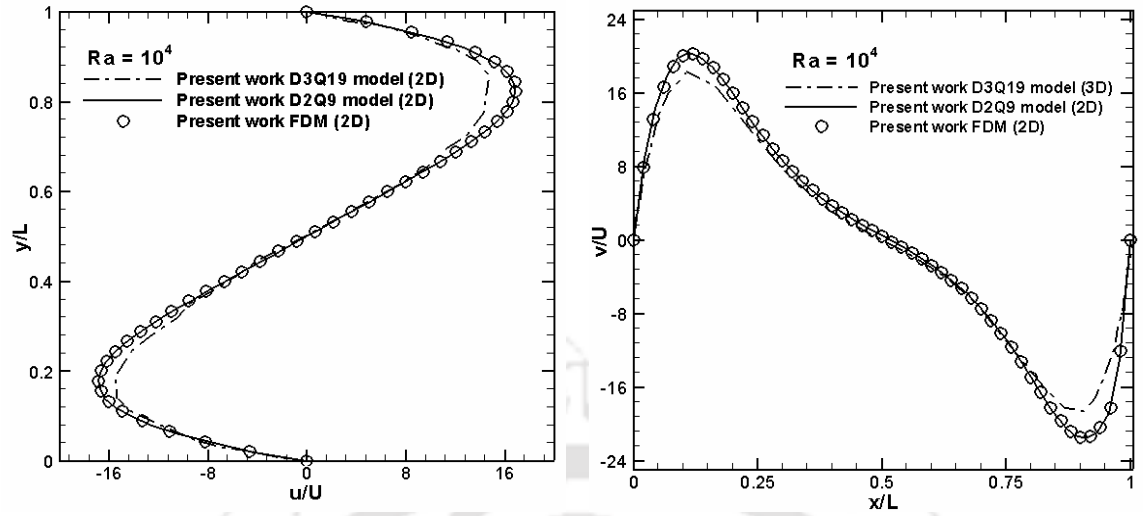

(a) Centreline *u*- velocity (b) Centreline *v*- velocity

Figure 7.15: Comparison of centreline velocities of cubic (mid-span) and square cavity at $Ra = 10^4$.

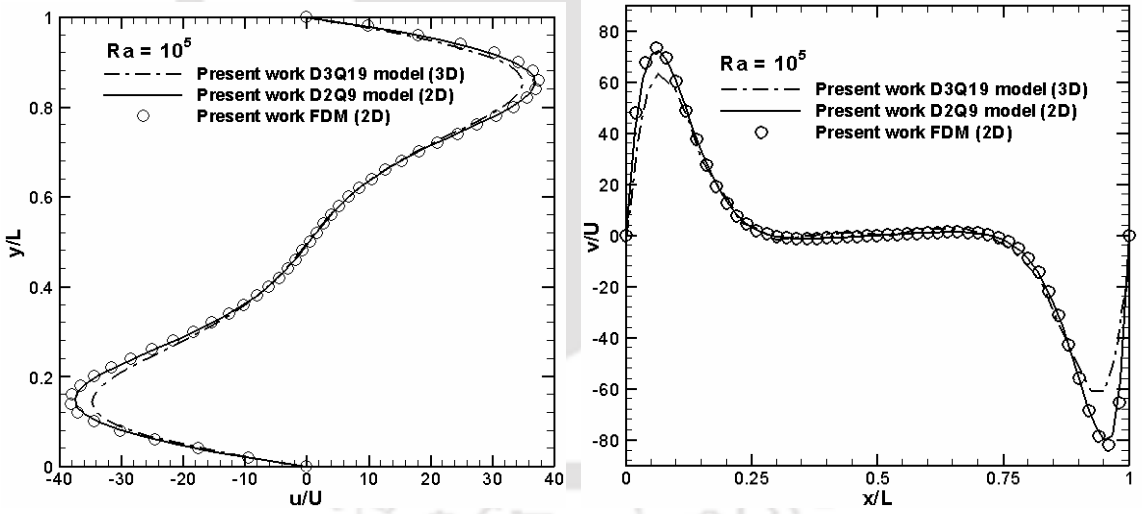

(a) Centreline *u*- velocity (b) Centreline *v*- velocity

Figure 7.16: Comparison of centreline velocities of cubic (mid-span) and square cavity at $Ra = 10^5$.

From Figures 7.14 (b) – 7.16 (b) we can also observe the end-wall effect by comparing the velocity profiles of the 2D cavity and those of the 3D cavity at the mid-span. It may

be noted that the convective current produced by differential heating is not as strong as the one produced by lid movement of the lid-driven cavity (chapter 3), for which reason there is a large overlap of the 2D and 3D profiles at mid-span especially in the central part of the plane, significant difference is observed only in the regions where the peak values of u and v are there. The velocity profiles in Figures 7.14 – 7.16 also indicate the accuracy of the present computations. Close match of the *D2Q9* LBM results and 2D FDM results show the accuracy of the 2D LBM results. This shows that the present IEDDF approach of LBM together with the chosen boundary conditions have the ability to accurately compute the flow in a 2D differentially heated cavity. Since the same approach is used to compute the flow in the 3D cavity and utmost care has been taken to carry out the computations, the presented velocity profiles in the symmetry plane enjoys good accuracy. The comparison between the 2D and 3D velocity profiles, which is not seen in literature, therefore throws new light into the end-wall effect of the thermally-driven cavity flow.

7.7. Conclusion

Computational results for both two- and three-dimensional thermal LBE models in the natural convection flow domain of a square and cubic cavity at different Rayleigh numbers are presented. The close agreement of the present square cavity LBM results with the IEDDF model and those available in literature for various Rayleigh numbers shows that LBM has the potential of being competitive with classical techniques like finite difference and finite volume even for free convection flows. Close comparison of the 2D velocity profiles with those given by the FDM method adds further credibility to

the 2D results. Reasons are also given for the accuracy of the velocity profiles in the symmetry plane of the cubic cavity. Comparison between the square cavity profiles and those in the symmetry plane of the cubic cavity throws light on the 3D effect at mid-span. The relative ease with which the computer code can be developed adds to the attractiveness of the method. The present code with suitable modification can be used to compute similar two- and three-dimensional flows with convective heat transfer to explore the range of applicability of the IEDDF approach. Overall, besides opening up new possibilities, the present IEDDF method may be considered as an efficient one for computation of flow for these physical configurations.

Chapter 8

Simulation of Gaseous Microflows

8.1. Introduction

In the past few years there has been significant progress in the development of Micro-electro-mechanical systems (MEMS) and Nano-electro-mechanical systems (NEMS) at the application and as well as at the simulation levels [68-73, 118-134]. It has motivated and necessitated the study of flows in micro-scale geometries such as micro-couette, micro lid-driven cavity and micro-channel. Both experimental and computational efforts have been undertaken to understand the specific features of the microscale flows. It is known that, the laws of fluid motion for microfluidic systems are different from those that of large scale (macro) systems in terms of forces and surface effects.

The study of gaseous flow in these micro and nano-devices has been an interesting and active topic of research in recent days. Because of obvious difficulties associated with testing and validating these micro-devices experimentally, numerical analysis is an alternative choice for investigating the flow inside the micro-scale geometries. It is also necessary to understand and employ the physical laws governing the flow in these small-scale devices to design the devices effectively. Micro-devices have attracted increasing attention due to their applications in various of fields, such as DNA analysis, cell separation, cell manipulation, biological and chemical analysis, inkjet printing, thermal

management of electronic devices [118, 119]. Flows through microchannels are the most common configuration in all of the biomedical applications [120]. Micro lid-driven cavity is also a common example of a microfluidic system. Cavities, steps and cut-outs occur frequently in many engineering designs [121]. The micro lid-driven cavity flows are quite simple in geometry but they display almost all micro-fluid mechanical phenomena. Shear driven gaseous flows such as micro-couette flows are commonly encountered in several MEMS-based applications, ranging from micro-motors, micro-accelerometers, comb mechanisms to the flying slider heads in computer hard drives [122]. This chapter is concerned with application of the Lattice Boltzmann Method (LBM) to compute gaseous flows in micro-geometries.

8.1.1. Microfluidic Concepts

Traditional numerical simulations relying on continuum approach and the Navier-Stokes equations break down at higher values of the Knudsen number *Kn* which equals the ratio of the mean free path of the gas molecules λ to the characteristic length L of the flow system. In the micro-scale geometries *Kn* is generally high and the Navier-Stokes equation loses validity. Figure 8.1 describes different regimes of gaseous flow depending on the Knudsen number (*Kn*). It is generally accepted that the Navier-Stokes equations with no-slip boundary conditions are only appropriate when $Kn < 0.001$. The gas flow for $0.001 < Kn < 0.1$ is termed slip regime and $0.1 < Kn < 10$ is termed transition regime. For $Kn > 10$ the system can be considered as a free molecular flow. In the above regimes, it is known that as the Knudsen number increases the non-continuum effects such as slip flow and non-equilibrium (or) rarefaction effects emerge.

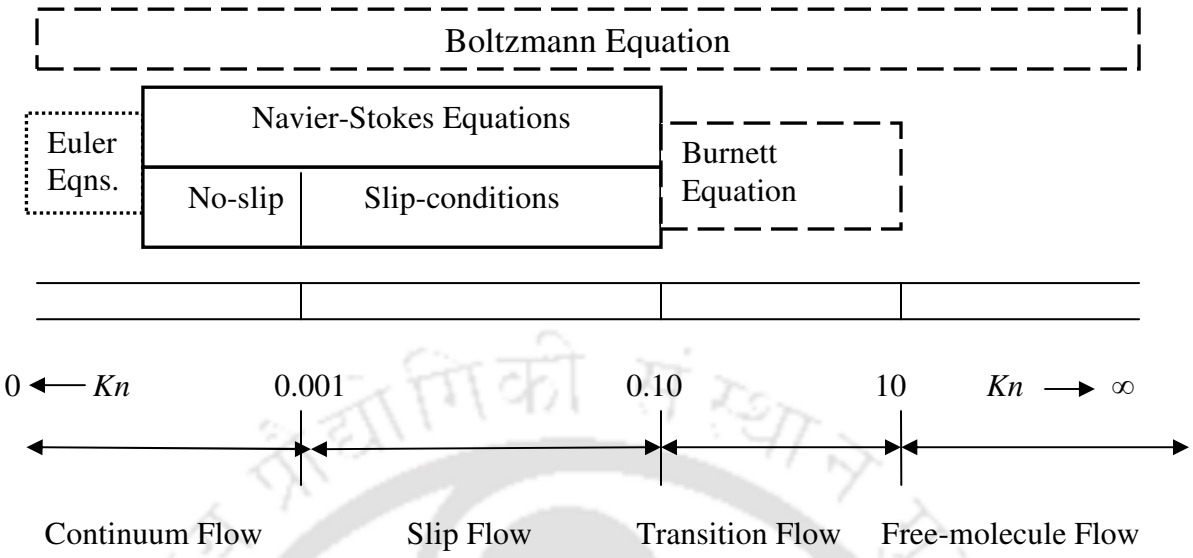

Figure 8.1: Different regimes of gaseous flow based on Knudsen number [118].

The surface tension forces and electrostatics play no role at all in the study of macro-scales but are enormously important in the study of microfluidics. The mean free path of molecules at normal temperature and pressure is approximately 70 nm. The Reynolds number, which characterizes the presence of turbulent flow, is extremely low and thus the flow will remain laminar in microflows. The Knudsen number is used to measure the degree of rarefaction in the microflows. Particle based methods such as Molecular Dynamics (MD) and the Direct Simulation Monte Carlo (DSMC) made some progress in simulation of micro-geometries. However, the computational cost of these methods is usually very large.

In the past few years, Lattice Boltzmann Method (LBM) emerged as an alternative and computationally efficient method to study the rarefied gaseous flows [68-73]. It is quite distinctive from molecular dynamics method (MD) on the one hand and the methods based on the discretization of partial differential equations (finite difference method,

finite volume method, finite element method, spectral method) on the other. Raabe [119] has written a review paper on LBM for micro and nano-scale fluid dynamics in materials science and engineering. In particular, LBM is now being applied to micro-flows in the slip and low-transition regimes. The choice of using LBM for microflow simulation is a good one owing to the fact that it is based on the Boltzmann equation which is valid for the whole range of the Knudsen number. Lattice Boltzmann Methods have earlier been used extensively to simulate incompressible fluid flows with no-slip boundary conditions; but application of LBM to compute gaseous microflows is still an emerging area with some unanswered questions. In this chapter, LBM is applied to simulate the pressure driven microchannel flows, micro-couette flows and micro-lid-driven cavity flows. Simulation of microflow not only requires an appropriate method, it also requires suitable boundary conditions to provide a well-posed problem and unique solution. Three slip boundary conditions, namely, diffuse scattering boundary condition, specular reflection and a combination of bounce-back and specular reflection is used here to predict the flow fields.

The main objective of this chapter is to demonstrate that LBM can be used for flow simulation beyond the continuum regime and that LBM approach could be a valuable alternative approach besides other particle based schemes such as MD and DSMC. Another objective is to examine the effect of varying the Knudsen number, boundary conditions and Tangential Momentum Accommodation Coefficients (TMAC). This chapter is organized in four sections. In Section 8.1, we delineate some of the distinctive and demarcating fundamental aspects of gaseous micro-scale flows. Section 8.2 discusses some aspects of the LBM including the governing equation and implementational issues.

Section 8.3 describes the results and discussions. Finally in Section 8.4 concluding remarks are made.

8.2. LBM Numerical Simulation

The Lattice Boltzmann equation (LBE) which can be linked to the Boltzmann equation in kinetic theory is formulated as [129]

$$f_i(\mathbf{x}+c_i\Delta t, t+\Delta t)-f_i(\mathbf{x}, t) = -\frac{1}{\tau}\left(f_i(\mathbf{x}, t)-f_i^{(0)}(\mathbf{x}, t)\right) \tag{8.1}$$

Here, f_i is the set of discrete populations representing the probability of finding a particle at position **x** at time t moving along the direction identified by the discrete particle velocity c_i, i is the number of links at each point and τ is the time relaxation parameter. In an incompressible fluid flow the relaxation time is relates with viscosity based on the continuum assumption. It is known that the reference length in microflows is very small, and the continuum assumption may not be valid. Another issue is that there are velocity slip and temperature jump in microflows. On the microscale, the standard no-slip boundary condition used in hydrodynamics has to be replaced by a slip boundary condition. Therefore, the bounce-back scheme used in the conventional LBM cannot be applied. To simulate microscopic gaseous flows LBM relates the relaxation time τ to the Knudsen number from the kinetic theory. Lim *et al.* [129] related τ with Knudsen number Kn

$$\tau = Kn\,(N_y - 1) \tag{8.2}$$

where N_y is the number of lattice nodes in y-direction. The macroscopic quantities such as density ρ and momentum density $\rho\boldsymbol{u}$ are defined as velocity moments of the distribution function f_i as follows:

$$\rho = \sum_{i=0}^{N} f_i ,$$
$$\rho \boldsymbol{u} = \sum_{i=0}^{N} f_i \boldsymbol{c_i} \quad . \tag{8.3}$$

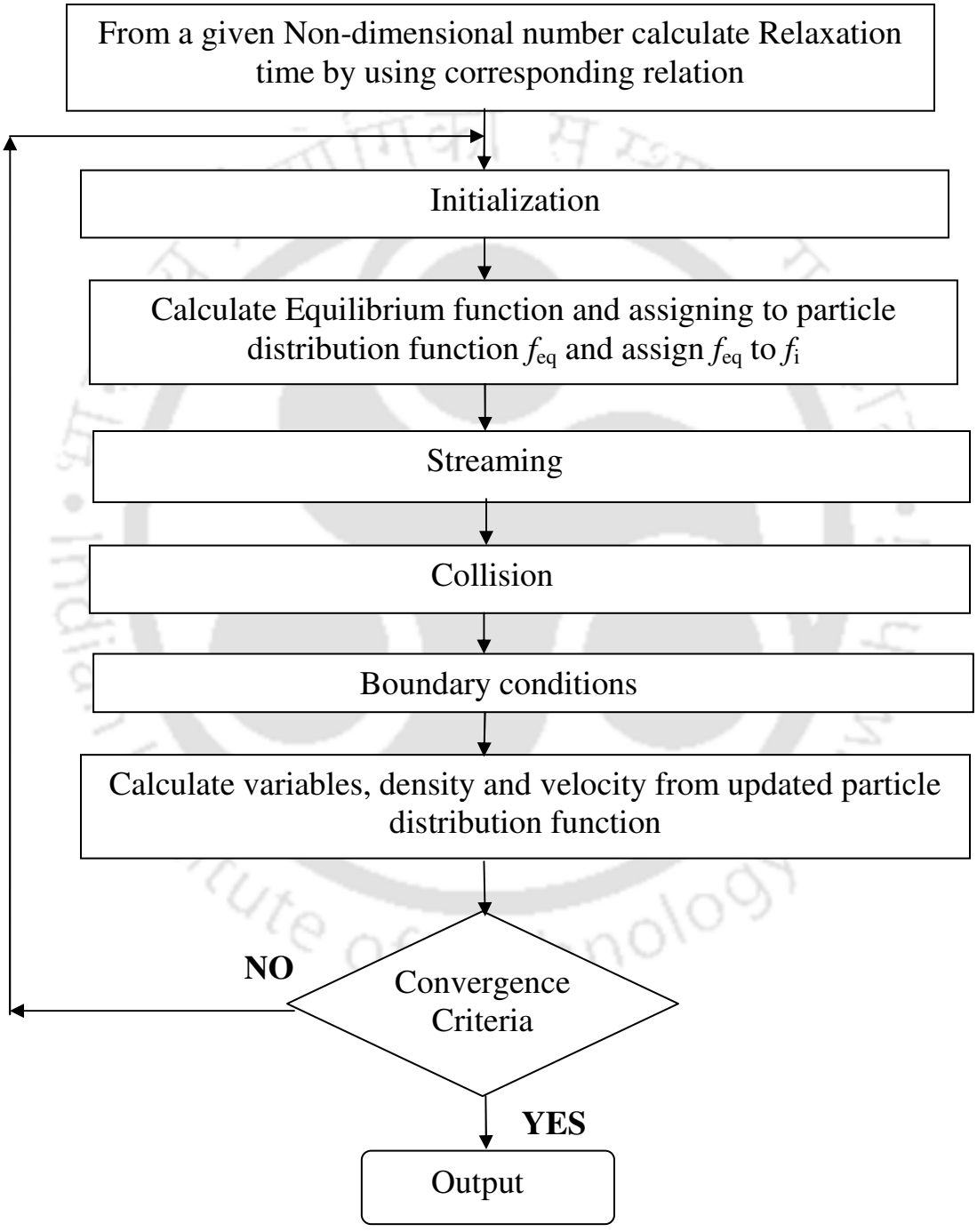

Figure 8.2: Flow-chart for LBM microflow simulation.

8.3. Results and Discussion

In this chapter Lattice Boltzmann Method computation in three micro-geometries, namely, the micro-couette flow, the microchannel flow and the micro lid-driven cavity flow with various aspect ratios are carried out. The general algorithm for LBM microflow simulation is shown in Figure 8.2. A lattice node resolution study was carried out using three lattice sizes composed of 250×250, 300×300 and 350×350 nodes. The numerical results were equivalent for the 300×300 and 350×350 lattice nodes. Therefore 300×300 lattice size was considered in all simulations in the micro-couette flow and micro lid-driven cavity flow.

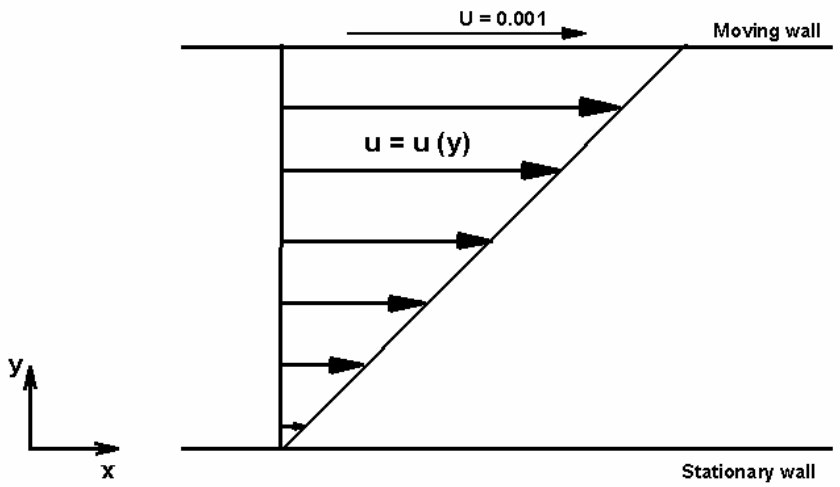

Figure 8.3: Geometry and boundary conditions of a micro-couette flow.

8.3.1. Micro-couette flow

The micro-couette flow problem is one of the simplest benchmark problems in rarefied gas dynamics. The geometry of the micro-couette flow is shown in Figure 8.3. In this problem the flow is confined between two parallel plates, the upper plate moves with a constant velocity U and the lower plate is stationary. It is known that micro-couette flow is shear-driven and the pressure does not change in the streamwise direction. The flow

field between the two plates is generated exclusively by the shear stress exerted on the fluid by the moving upper plate, resulting in a velocity profile across the flow $u = u(y)$, as sketched in Figure 8.3. Periodic boundary conditions are applied in the inlet and outlet. Combination of bounce-back and specular reflection boundary condition (BSBC) (discussed in Chapter 2) is used in the stationary wall. Initially the x- direction velocity is assumed to be uniform through out the channel except at the upper plate where the velocity is $U = 0.001$ and y- velocity is taken as 0. Density used during simulation is 1.0. At moving (upper) wall particle distribution functions are updated by the equilibrium distribution function.

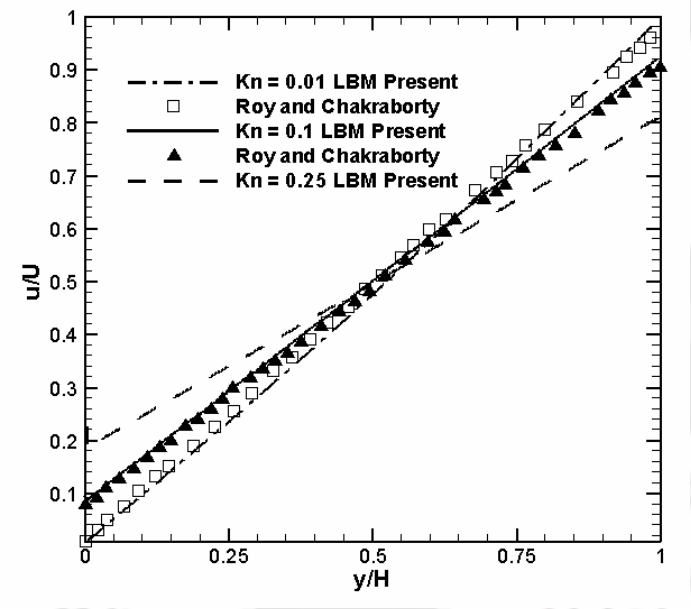

Figure 8.4: Micro-couette velocity profile for different *Kn.*

Figure 8.4 depicts the velocity profiles of gaseous flow between two plates for different Knudsen numbers (Kn = 0.01, 0.1 and 0.25). The predicted LBM results agree well with existing results of Roy and Chakraborty [122]. It is seen that as the Knudsen number increases, slip velocity at the lower wall increases, but the velocity profile remains linear and 'symmetric'.

8.3.2. Pressure-Driven Microchannel Flow

Next, Lattice Boltzmann Method with *D2Q9* model is used to simulate the two-dimensional microchannel flow. The flow is driven by pressure gradient in the main stream direction. The geometry of the microchannel with a flow profile is shown in Figure 8.5. Initially the *x*-direction velocity is assumed to be uniform through out the channel and *y*-velocity is taken as zero. Density is fixed at a value of 1.0 at inlet. It is assumed to vary linearly from inlet to outlet, while remaining constant at each section. Density is fixed at a value of 1.0/PR (PR indicates Pressure ratio) at outlet. All the unknown distribution functions at inlet and outlet are updated by equilibrium distribution functions after finding velocities at inlet and outlet.

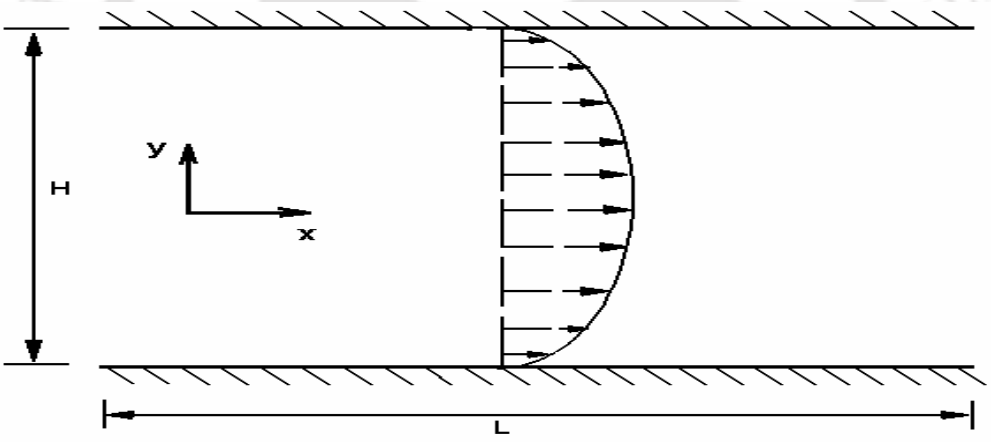

Figure 8.5: Geometry of micro-channel with a flow profile.

First, the developed LBM code is used to compute the microchannel flow at a low Knudsen number. The flow with pressure ratio PR = 2.02 and the Knudsen number of 0.053 is studied. Figure 8.6 shows the normalized pressure deviation from the linear pressure distribution $P^* = \left(P - P_{lin}\right)/P_{out}$ along the microchannel. Established experimental results of Pong *et al.* [125], analytical results of Arkilic *et al.* [126] and LBM results of Niu *et al.* [73] exist for the same problem and these works are used for

establishing the credibility of the present LBM code. The pressure distribution result that takes the TMAC $\sigma = 0.7$ (see chapter 2, section 2.5.4) are in reasonable agreement with the experimental and analytical data [125, 126]. Chen *et al.* [127] indicated that gas flow in microchannels may involve three factors such as compressibility, rarefaction (slip on the surface) and surface roughness effects. That the first two effects are considered in the present work will be shown by our pressure and velocity profile results. The effect of TMAC on the velocity profile at $Kn = 0.053$ is also studied and the results are depicted in Figure 8.7. As TMAC decreases, slip at the wall increases and the maximum velocity at the centre of the channel decreases.

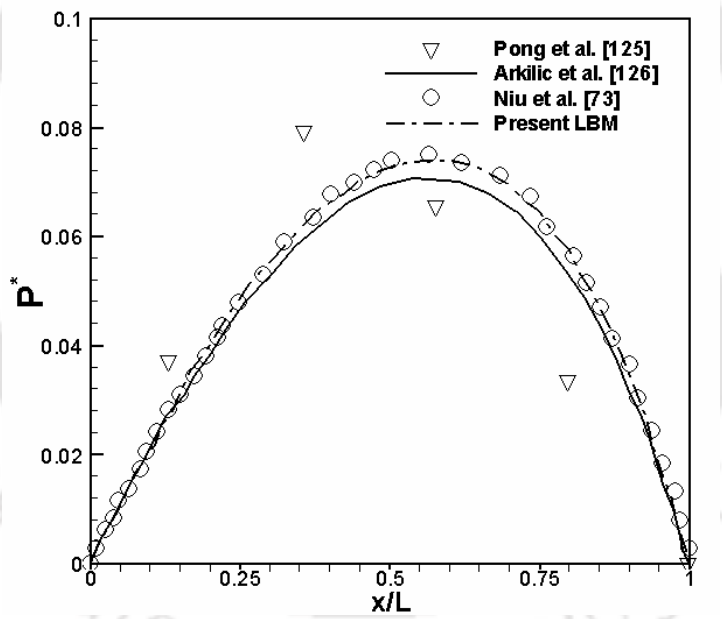

Figure 8.6: Normalized pressure deviation from the linear pressure distribution (Kn = 0.053, PR = 2.02, $\sigma = 0.7$).

Next the effect of pressure ratio for the same Knudsen number is studied. Pong *et al.* [126] experimentally investigated the pressure distributions for different Knudsen numbers along the channel, and concluded that they are nonlinear in microchannel flows.

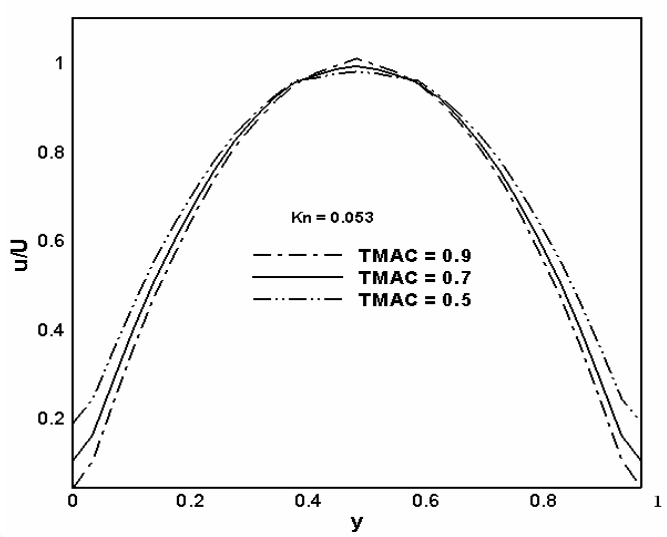

Figure 8.7: The effect of TMAC on the velocity profile $Kn = 0.053$.

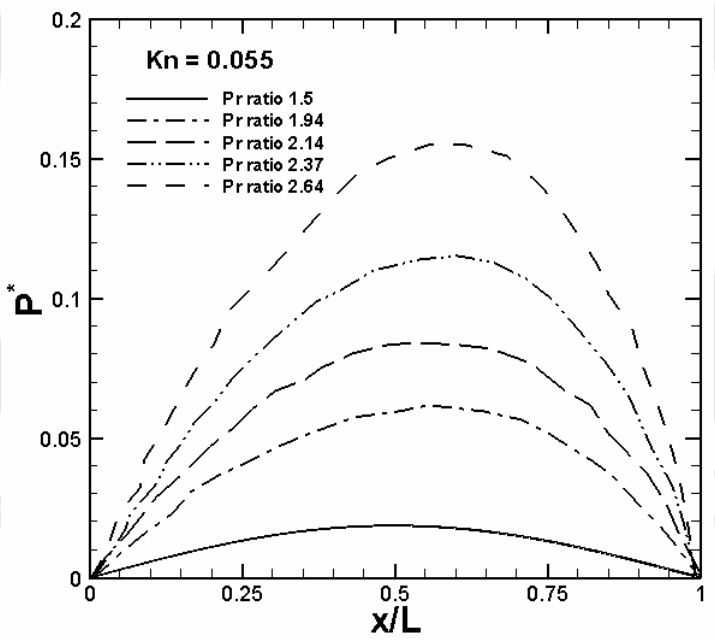

Figure 8.8: Pressure along the channel for $Kn = 0.055$.

Figure 8.8 shows the nonlinear pressure variation $P^* = \left(P - P_{lin}\right)/P_{out}$ for different pressure ratios with $Kn = 0.055$ and $\sigma = 0.7$. Here P_{lin} is the pressure linearly interpolated between the inlet and outlet pressure and P_{out} is the pressure at the exit of

the channel. As seen from Figure 8.8, when the pressure ratio is small the pressure distribution is almost linear. As the pressure ratio increases the pressure distribution become nonlinear due to the compressibility effects. Also seen is the fact that pressure variation peaks shift towards the channel exit as pressure ratio increases. The effect of increasing the Knudsen number is observed. Figure 8.9 shows the nonlinear pressure variation for different Knudsen numbers for a pressure ratio of 2.0 and $\sigma = 0.7$. The nonlinearity of the pressure distribution as observed here can be ascribed [125] to the fact that compressibility and rarefaction effects, which are not equal, makes the pressure variation take a different path compared with that for the continuum flow. The results of the present study in this section reveal many interesting features of microchannel flows. It may be concluded that the present study produces results that are in conformity with earlier numerical and experimental observations [73, 125-127, 129, 131].

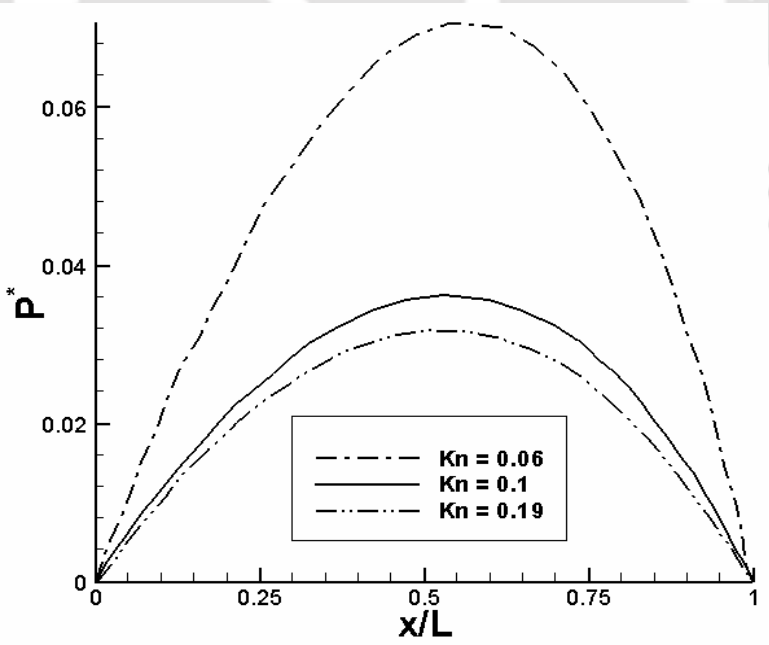

Figure 8.9: Pressure along the channel for various *Kn* at $\frac{P_{in}}{P_{out}} = 2.0$.

8.3.3. Micro lid-driven cavity flow

Lattice Boltzmann Method is now used to investigate the micro-lid-driven cavity flow. The geometry of the micro-lid-driven-square-cavity flow is shown in Figure 8.10. Here, the upper wall moves with a constant velocity from the left to right and the other three walls are stationary. First, LBM is used to compute the micro-lid-driven cavity flow in a square cavity on a 300×300 lattice arrangement. The equilibrium distribution function is then assigned to the particle distribution function at the surface of the moving wall. From our study of the microchannel we observe that a TMAC of $\sigma = 0.7$ produces results that are in good agreement with analytical, experimental and numerical results. That is why on the stationary walls we use a combination of specular and bounce-back boundary condition using a TMAC of $\sigma = 0.7$.

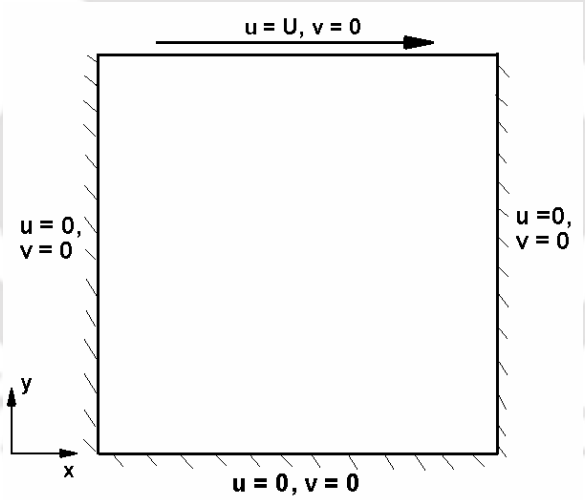

Figure 8.10: Geometry of the micro-lid-driven square-cavity flow.

Figures 8.11 (a) - 8.14 (a) show the streamline patterns at *Kn* = 0.01, 0.05, 0.1 and 0.135 respectively. With the increase in Knudsen number a slight downward movement of the vortex centre is perceived; however, no horizontal shift of the vortex centre is observed. Our streamline pattern results agree well with those of Mizzi *et al.* [121], Darbandi *et al.*

[123], Ansumali *et al.* [133] and Jiang *et al.* [134]. Figures 8.11 (b) - 8.14 (b) show the pressure contours at Kn = 0.01, 0.05, 0.1 and 0.135 respectively. These results agree well with the LBM results of Tang *et al.* [70], Ansumali *et al.* [133] and the DSMC results of Jiang *et al.* [134]. However, agreement with Ansumali *et al.* [133] is better. The reason behind the small difference between the LBM simulation and DSMC result of pressure contours is that the strong singularity at the corner points in the micro cavity affects a larger and larger region as Knudsen number increases. Figures 8.15 and 8.16 show for various Knudsen numbers, the x-velocity (u) profile along the vertical centreline and the y-velocity (v) profile along a horizontal centreline passing through the geometric centre of the cavity. These figures represent the effect of Knudsen number on the velocity profiles and on the velocity-slip condition at the boundary. The values of u at the top and bottom walls (Figure 8.15) and the values of v at the left and right walls (Figure 8.16) clearly show that slip is nonzero, as the flow is not in the continuum regime. The effect of slip is most pronounced at the moving top wall where at the lowest value of Kn = 0.01 slip is almost zero and the fluid velocity is almost equal to the lid-velocity so that u is close to 1; for the highest value of Kn = 0.135, slip is expectedly maximum and u is about 0.5. From Figure 8.15 one can also observe that the maximum leftward x-velocity is obtained for the lowest Kn = 0.01. Figure 8.16 shows that the maximum downward (near the right wall) and maximum upward (near the left wall) y-velocity is obtained once again for the lowest Kn = 0.01. This is along expected lines as at the lowest Knudsen number the ability of the top wall to drive the flow is at its highest and it generates the highest clockwise circulation.

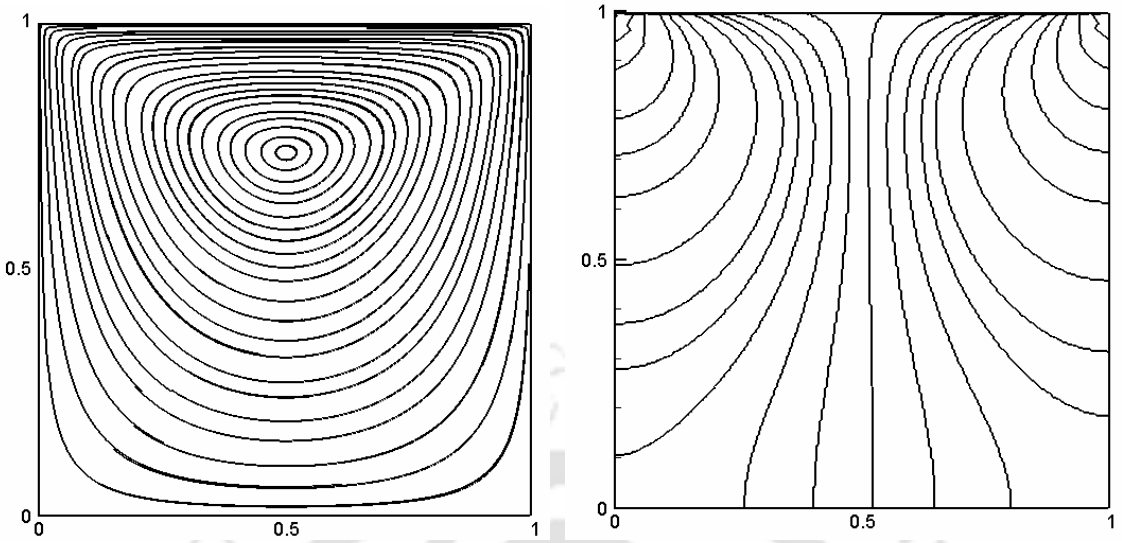

(a) (b)

Figure 8.11: (a) streamline patterns, (b) pressure contours of micro lid-driven square-cavity flow at $Kn = 0.01$ on a 300×300 lattice arrangement.

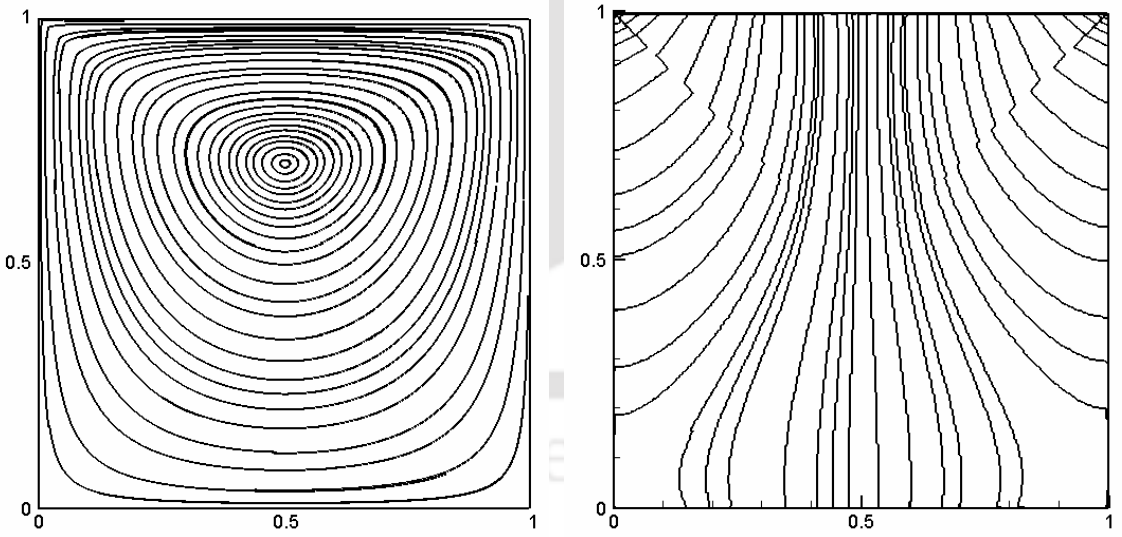

(a) (b)

Figure 8.12: (a) streamline patterns, (b) pressure contours of micro lid-driven square-cavity flow at $Kn = 0.05$ on a 300×300 lattice arrangement.

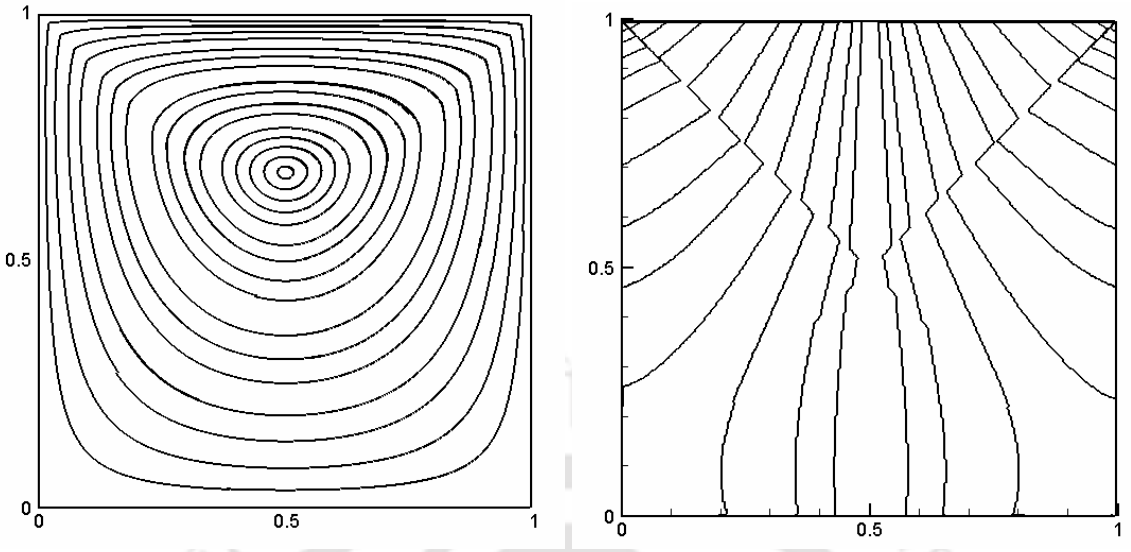

(a) (b)

Figure 8.13: (a) streamline patterns, (b) pressure contours of micro lid-driven square-cavity flow at $Kn = 0.10$ on a 300×300 lattice arrangement.

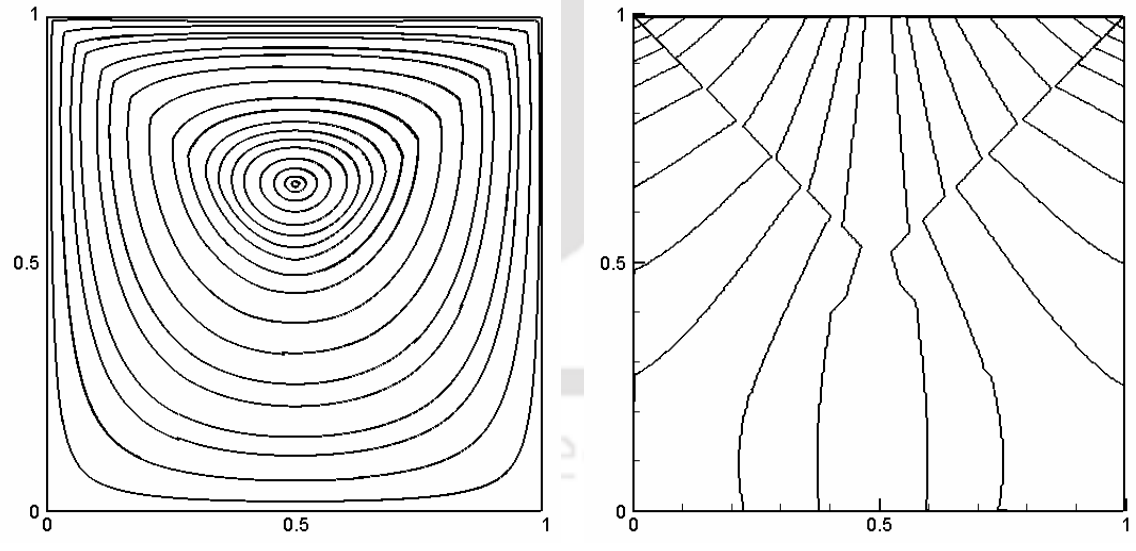

(a) (b)

Figure 8.14: (a) streamline patterns, (b) pressure contours of micro lid-driven square-cavity flow at $Kn = 0.135$ on a 300×300 lattice arrangement.

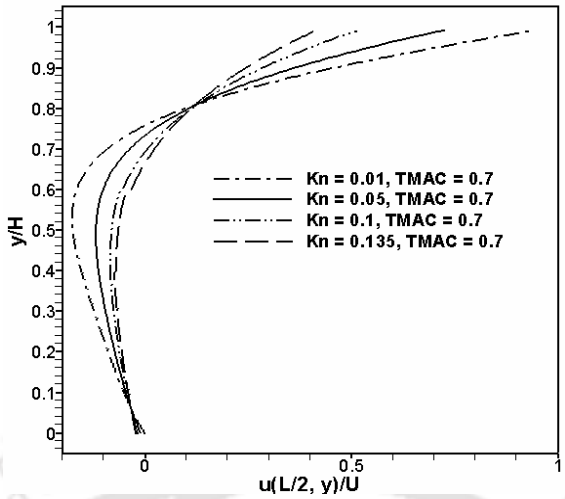

Figure 8.15: *u*-velocity profile along the vertical centreline of the micro-lid-driven square-cavity for different Knudsen numbers.

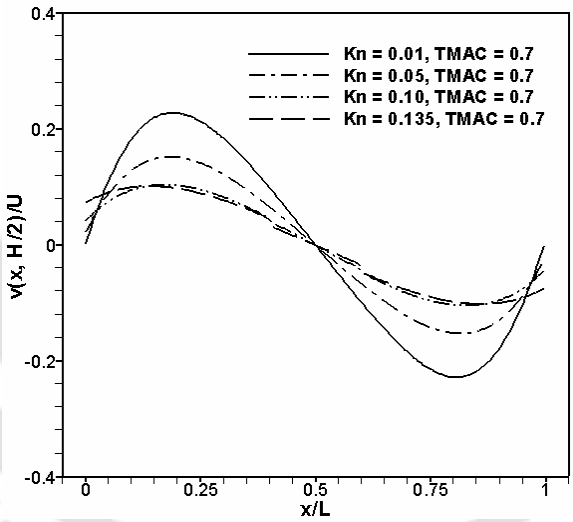

Figure 8.16: *v*-velocity profile along the vertical centreline of the micro-lid-driven square-cavity for different Knudsen numbers.

Figure 8.17 depicts the velocity profiles in the micro-lid-driven square-cavity flow for *Kn* = 0.05 with different boundary conditions, namely, BSBC ($\sigma = 0.7$), SBC and DSBC (described in chapter 2) on the stationary walls. It is seen that BSBC and SBC velocity profile results are similar and DSBC result shows some deviation from these two slip

boundary conditions. The reason may be that the DSBC result is a slip boundary condition derived from gas-surface interaction law of the kinetic theory.

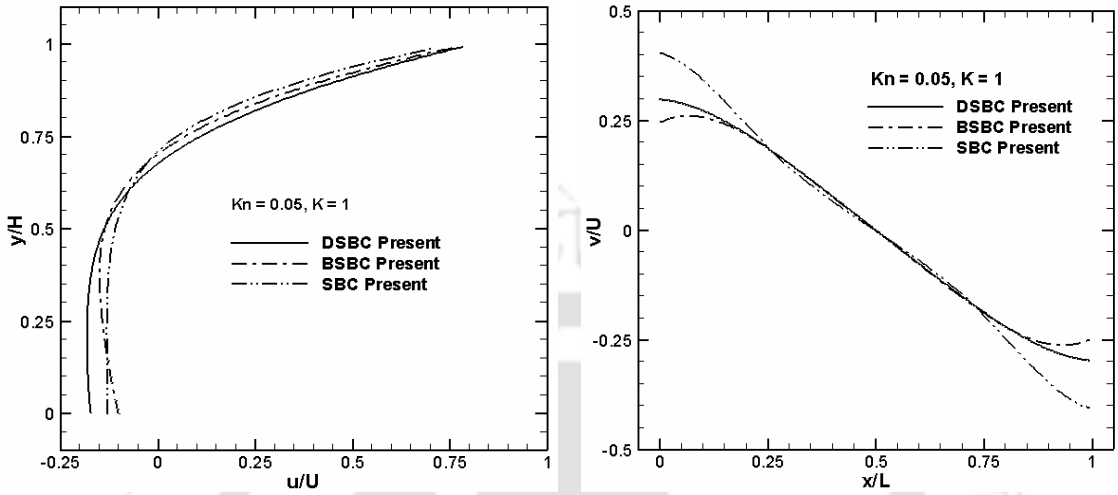

Figure 8.17: (a) *u*-velocity profile along the vertical centreline (b) *v*-velocity profile along the horizontal centreline for the micro-lid-driven square-cavity flow at $Kn = 0.05$ with the BSBC, SBC and DSBC boundary conditions. Lattice size: 300×300.

Figure 8.18 depicts the streamline patterns for micro lid-driven cavity flow at $Kn = 0.01$ with aspect ratios $K = 0.5$, 2 and 5. For aspect ratio $K = 0.5$ there is only one primary vortex and for $K = 2$ and 5 secondary vortices appear under the top one. It is seen that as the aspect ratio K of the micro lid-driven cavity increases, counter-rotating vortices appear in the bottom of the cavity. It is also seen that, the flow is almost symmetric with respect to the vertical centreline. Figure 8.19 depicts the streamline patterns for micro lid-driven cavity flow at $Kn = 0.1$ (high-slip regime) with aspect ratios $K = 0.5$ and 2. Here is seen that even at $K = 2$ there is only one vortex. Thus the present study reveals the fact that multiple vortices may be absent even at higher cavity-aspect ratios if the Knudsen number is relatively high.

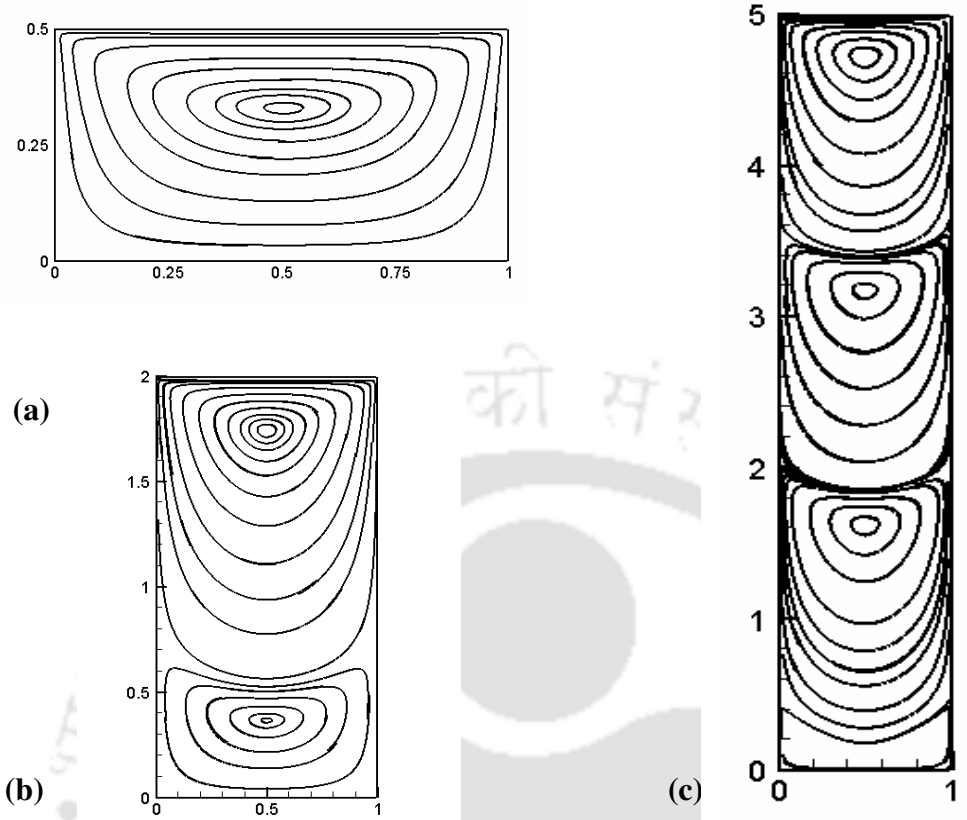

Figure 8.18: Streamline patterns for the micro-lid-driven cavity flow with aspect ratios K = 0.5, 2 and 5 at Kn = 0.01.

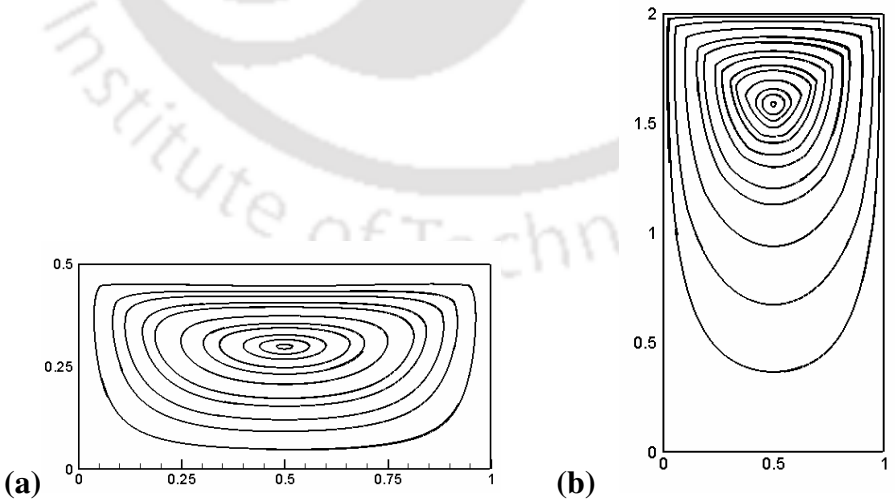

Figure 8.19: Streamline patterns for the micro-lid-driven cavity flow with aspect ratios K = 0.5 and 2 at Kn = 0.1.

Another point is that a central primary vortex appears in the cavity in all examined aspect ratios. For all Knudsen numbers the present streamline patterns agree well with those reported by Darbandi *et al.* [123].

8.4. Conclusion

The application of the LBM to compute rarefied gaseous flows is presented in this chapter. For the first geometry, namely, micro-couette flow some numerical and theoretical results exist, which are reproduced with the LBM. This knowledge is then utilized when applying the LBM to compute flows in the second geometry, namely, a two-dimensional micro-channel flow. As good care has been taken to include appropriate measures in the computational method, these results enjoy good credibility. Variation of slip with Knudsen number is then studied in some details through the computation of flow in the micro-cavity. It is seen that all the flow features captured are in keeping with the physics of the problem. The Knudsen numbers explored in this work range from the slip to the threshold of the transition regime. Then the effect of Knudsen number with different boundary conditions is studied through the computation of flow in the micro-cavity with various aspect ratios. Results are presented for Knudsen numbers within the slip and the threshold of the transition regime where the onsets of non-equilibrium effects are usually observed. Good agreement is found in predicting the general features of the velocity flow filed and recirculating flow. To sum up, the present study reveals many interesting features of micro-couette, microchannel and micro lid-driven cavity flows and demonstrates the capability of the LBM to capture this features. It can be concluded that the present LBM, as an alternative to the particle based methods such as MD and DSMC, holds very good promise in gaseous microflows.

Chapter 9

Concluding Remarks and Scope for Future Work

9.1. Concluding Remarks

This chapter is concerned with summing up of the thesis highlighting the major achievements. The Lattice Boltzmann Method has made a substantial progress since the early nineteen nineties till today, especially in the computation of incompressible isothermal and thermal flows. As already mentioned the method is based on a simplified kinetic model using discrete particle velocities that exploit the fact that the collective behaviour of the molecules does not strongly depend on the dynamics of the individual molecules. Since its inception many attempts have been made to apply the method to attack those fluid-flow problems that were earlier the traditional bastions of the continuum-based methods like the finite difference, finite volume and finite element so as to establish it as a credible alternative to these methods. The present thesis belongs to this body of works that attempt to extend the application of Lattice Boltzmann Method to new situations and new problems. The thesis also studies some common problems to make new observations. Throughout the thesis qualitative and quantitative aspects of the results are systematically analyzed with the help of a large number of figures and tables.

Development of several LBM codes based on the 'C' programming language for various 2D, 3D, isothermal and thermal fluid flow problems is an integral part of the present work. Several LBM boundary conditions proposed in the literature are incorporated in the codes so as to obtain accurate solutions. If there are noticeable differences between the results given by various boundary conditions, they are given side by side to throw light on their merits and demerits. Though majority of the codes are applied to rectangular 2D and 3D geometries, one code is written for the flow around a circular cylinder to demonstrate that LBM has the ability to produce accurate results for flows involving curved geometries as well. To give credibility to the LBM results for hitherto unexplored flow configurations though comparison exercises, an accurate 2D FDM code based on ADI technique is also developed to compute flows in cavities. The accuracy of the results produced by this code is systematically established before using it as a means for comparison. While carrying out LBM computation of isothermal flows in the single li-driven square, shallow and deep cavities, the effect of aspect ratio and Reynolds number on the size, shape, centre-position and number of vortices are brought out in a systematic way. It is also shown through capturing a quaternary corner vortex (not reported earlier through LBM) by using a finer lattice arrangement that LBM shows the ability to resolve smaller scales the same way grid-refinement enhances this ability in FDM, FVM and FEM. It is also demonstrated that LBM-SRT method, though simpler to apply, has its share of drawbacks especially in the neighbourhood of the singular points in the cavity at higher Reynolds numbers when it fails to give smooth nonoscillatory contours. LBM-MRT method is seen to remove these spurious oscillations.

In the shape of two-sided lid-driven square cavity, a new test problem is proposed. The problem involves both 'parallel' and 'antiparallel' motion of two facing walls of a square cavity. For the parallel motion of the walls, LBM is shown to capture a 'free-shear' layer midway between the moving plates. It is also shown that for the `antiparallel' wall motion, the near-trailing-edge corner vortices form at a much lower Reynolds number in this flow compared with the single-lid-driven square-cavity flow. Several figures and tables serve as qualitative and quantitative means for comparison. To give further credibility to these grid-independent results, they are shown to compare very well with those given by a highly accurate FDM code. Consequently, the flow configuration and results, like those of the single lid-driven cavity flow, may be used for validating the algorithm for computing steady flows governed by the two-dimensional incompressible Navier-Stokes equations. Also given briefly are the results of a deep cavity for both parallel and antiparallel motion of the walls.

So far various works have demonstrated the ability of continuum-based approaches to capture multiple steady-flow solutions exhibited by some nonlinear situations. However, it was not known whether the simplified kinetic model of LBM has in it the requisite mechanism to capture multiple steady solutions, which are specifically nonlinear phenomena. The present work on the two-sided and four-sided square cavity flow and also two-sided rectangular lid-driven cavity flow demonstrates that LBM has the innate ability to compute multiple steady-flow situations. However, the strategy used to capture these multiple solutions has to be necessarily different from the ones used in continuum-based methods. This strategy is described in the relevant chapter of the thesis. It may further be noted that the traditional mathematical concept of well-posedness does not

apply here and for the first time the ability and accuracy of the Lattice Boltzmann Method to obtain solutions to this peculiar class of problems is demonstrated. With this added ability it can be concluded that LBM, as an alternative to the continuum-based methods, holds very good promise in computational fluid dynamics.

Three-dimensional LBM computations are carried out for the flow in the single- and two-sided cubic cavity and the single-sided prism cavity using *D3Q15, D3Q19* and *D3Q27* lattice models. *D3Q19* model appears to be the most useful of the three 3D lattice models from the point of view of accuracy and computational time as it is more accurate than *D3Q15* and less time-consuming compared with *D3Q27*. For these computations various results in the symmetry plane are compared with the corresponding 2D results to demonstrate that with the increase in Reynolds number, expectedly, the end walls exert increasingly strong influence resulting in increased discrepancy between the 2D and 3D results.

LBM computations are also carried out for the thermally-driven square and cubic cavity flows using the IEDDF approach for various Rayleigh numbers showing that LBM has the potential of being competitive with classical techniques like FDM or FVM even for free-convection flows. For the cubic cavity, the present work is one of the few instances of LBM being used to compute the thermally-driven flow. The comparison of the 2D and 3D velocity profiles in the symmetry plane, not seen in literature, throws new light into the end-wall effect of the thermally-driven cavity flow. It is found that the convective current generated by differential heating is not as strong as the one produced by lid movement in the lid-driven cavity, for which reason, unlike in the lid-driven cavity flow,

in the thermally-driven cavity flow there is a large overlap of the 2D and 3D velocity profiles at the symmetry plane especially in the central part.

As seen earlier LBM computations are also carried out for the gaseous flows in various micro-geometries. In these computations boundary conditions play an important role as there is a partial slip flow at the solid walls. Different boundary conditions are experimented with and how parameters like the TMAC can be carefully chosen to obtain reliable results are shown. The present study reveals many interesting features of micro-couette, micro-channel (pressure-driven) and micro-lid-driven cavity flows, and demonstrates the capability of LBM to capture those features. The Lattice Boltzmann Method appears to be a convenient method of computing microflows as it has the innate advantage of being a simplified kinetic method so that it can be applied even in those situations where the continuum hypothesis breaks down.

The main concern of the thesis is LBM computation of various isothermal and thermal incompressible *steady* flows. In keeping with this theme, LBM computations are also carried out for the flow around a circular cylinder mainly at low Reynolds numbers when the flow is steady and symmetric. The present LBM results appear to be highly accurate as they give drag coefficients closer to the experimental data compared with other numerical works. To demonstrate the ability of the present code, and hence LBM, to compute time-varying flows, instantaneous streamline and vorticity plots are also given for a higher Reynolds number at which the symmetry breaks and the flow becomes time-periodic. However, in keeping with the central theme of steady flows, detailed analysis of these plots are not carried out.

All the results reported in the thesis are independent of lattice arrangements and wherever possible they are substantiated through a carefully carried out comparison exercise with established results. Wherever results for new flow configurations are presented, extreme care has been taken to establish their credibility. Though all the computed flows fall in the laminar regime, difficult flow configurations exemplified by large values of the Reynolds and Rayleigh numbers are also solved. The work lives true to its original aim in that (i) LBM is used to propose a new test problem, (ii) LBM is shown to give extremely accurate results in some situations and have the ability to produce multiple-steady solutions and (iii) LBM is used to solve a variety of fluid-flow and heat-transfer problems in the micro and macro regimes of flow, thus demonstrating that it has already established itself as an important alternative solution procedure in computational fluid dynamics.

9.2. Limitations and Range of Applicability

The treatment of flow turbulence arises as a key issue. It is known that, an application of the original LBM equations, directly to turbulent flow [139] requires the use of too fine lattice resolutions, leading to too large problem sizes. Thus, the employment of a "turbulence model" becomes necessary, as it is the case in the Navier-Stokes equations based formulation. Within this context, two-equation turbulence models have already been used [140-141] in conjunction with LBM, which correspond to an unsteady RANS (Reynolds Averaged Numerical Simulation) type of description. A Large Eddy Simulation (LES) [142] like formulation based on the definition of a subgrid-scale

viscosity may be found to offer a more natural approach for the intrinsically unsteady methodology of LBM, and is also widely used for computing turbulent flows.

9.2. Scope for Future Works

This dissertation has been an attempt to develop and expand the field of application of Lattice Boltzmann Method particularly for incompressible viscous flows and gaseous microflows; but the potential still remains to explore many more areas and break new grounds. The following are some of the probable works that could be taken up in future:

- LBM can be used for detailed numerical analysis of problems like the flow over a circular, square and elliptical cylinder for transient flows.
- Most of the LBM-MRT models are used to solve two-dimensional problems. Only a few attempts with LBM-MRT models have been made to solve real three-dimensional problems. Therefore, there is a huge possibility to develop and implement LBM-MRT models to solve three-dimensional complex problems.
- In this dissertation we have carried out the computations of two-sided and four-sided lid-driven square cavity, and two-sided rectangular cavity flows by LBM-SRT model to obtain multiple steady solutions. A similar study with LBM-MRT method can be an interesting and important area of research.
- Application of LBM to compute microflows is still an emerging area with some unanswered questions. For example, while computing flows in micro driven cavities with LBM-SRT method, handling the corner singularities appears to be a difficult task. Resolving this problem may be another goal for research.

- As has already been seen, LBM has made deep inroads into the computation of incompressible flows. However, it is still in its infancy so far as computation of compressible flows with large temperature gradients is concerned. This is a challenging and almost virgin area that requires LBM assault.

References

[1] S. Succi, The Lattice Boltzmann Method for Fluid Dynamics and Beyond, Oxford University Press, 2001.

[2] Y. Sone, Kinetic Theory and Fluid Dynamics, Birkhauser, Boston, 2002.

[3] T.J. Chung, Computational Fluid Dynamics, Cambridge University Press, Cambridge, 2002.

[4] Q. Chang, D. Alexander and J. Iwan, Application of Lattice Boltzmann Method, VDM Verlag, 2008.

[5] S. Chen and G.D. Doolen, Lattice Boltzmann method for fluid flows, *Annual Review of Fluid Mechanics*, **30**, 282-300, 1998.

[6] X. He and L.S. Luo, A priori derivation of the lattice Boltzmann equation, *Physical Review E*, **55,** R6333-R6336, 1997.

[7] X. He and L.S. Luo, Theory of the lattice Boltzmann method: From the Boltzmann equation to the lattice Boltzmann equation, *Physical Review E*, **56**, 6811-6817, 1997.

[8] D.O. Martinez, S. Chen and W. Matthaeus, Lattice Boltzmann magnetohydrodynamics, *Physical Review E*, **47**, R2249-R2252, 1994.

[9] K. Gunstensen, D.H. Rothman, S. Zaleski and G. Zanetti, Lattice Boltzmann model of immiscible fluids, *Physical Review A*, **43**, 4320-4327, 1991.

[10] D. Grunau, S. Chen and K. Eggart, A lattice Boltzmann model for multi-phase fluid flows, *Physics of Fluids A*, **5**, 2557-2562, 1993.

[11] C.H-Taw and L.J-Yuh, Numerical analysis of hyperbolic heat conduction, *International Journal of Heat and Mass Transfer*, **36** (11), 2891-2898, 1993.

[12] J.R. Ho, C.P. Kuo, W.S. Jiaung and C.J. Twu, Lattice Boltzmann scheme for hyperbolic heat conduction equation, *Numerical Heat transfer, Part B,* **41**, 591-607, 2002.

[13] S.C. Mishra, B. Mondal, T. Kush, B.S.R. Krishna, Solving transient heat conduction problems on uniform and non-uniform lattices using the lattice Boltzmann method, *International Communications in Heat and Mass Transfer*, **36**, 322-328, 2009.

[14] J. Bernsdrof, G. Brenner and F. Durst, Numerical analysis of the pressure drop in porous media flow with lattice Boltzmann (BGK) automata, *Comp. Phys. Communications*, **129**, 233-246, 2000.

[15] S. Chen, Z. Wang, X. Shan and G.D. Doolen, Lattice Boltzmann computational fluid dynamics in three dimensions, *Journal of Statistical Physics*, **68**, 379-400, 2000.

[16] J. Hardy, Y. Pomeau and O. de Pazzis, Time evolution of a two-dimensional classical lattice system, *Physical Review Letters*, **31**, 276-279, 1973.

[17] U. Frisch, B. Hasslacher and Y. Pomeau, Lattice-gas automata for the Navier-Stokes equations, *Physical Review Letters*, **56**, 1505-1508, 1986.

[18] G. McNamara and G. Zanetti, Use of a Boltzmann equation to simulate lattice-gas automata, *Physical Review Letters*, **61**, 2332, 1988.

[19] F. Higuera and J. Jimenez, Boltzmann approach to lattice gas Simulations, *Europhysics Letters*, **9** (7), 663-668, 1989.

[20] P.L. Bhatnagar, E.P. Gross and M. Krook, A model for collision Processes in gases. I. Small amplitude processes in charged and neutral one-component systems, *Physical Review*, **94**, 511-525, 1954.

[21] J.M.V.A. Koelman, A simple lattice Boltzmann scheme for Navier-Stokes fluid flow, *Europhysics Letters*, **15** (6), 603-607, 1991.

[22] S. Chen, H. Chen, Martinez and Matthaeus, Lattice Boltzmann model for simulation of magnetohydrodynamics, *Physical Review Letters*, **67** (27), 3776-3780, 1991.

[23] Y.H. Qian, D. d'Humieres and P. Lallamand, Lattice BGK models for Navier-Stokes equation, *Europhysics Letters*, **17** (6), 479-484, 1992.

[24] H. Chen, S. Chen and W.H. Matthaeus, Recovery of the Navier-Stokes equation using a lattice-gas Boltzmann method, *Physical Review A*, **45** (8), R5339-5342, 1992.

[25] P.N. Shankar and M.D. Deshpande, Fluid mechanics in the driven cavity, *Annual Review of Fluid Mechanics*, **32**, 93-136, 2000.

[26] W. Miller, Flow in the driven cavity calculated by the lattice Boltzmann method, *Physical Review E*, **51**, 3659-3669, 1995.

[27] S. Hou, Q. Zou, S. Chen, G. Doolen and A. C. Cogley, Simulation of cavity Flow by the lattice Boltzmann method, *Journal of Computational Physics*, **118**, 329-347, 1995.

[28] B. Shi, N. He, N. Wang and Z. Guo, Lattice Boltzmann simulations of fluid flows, *Springer-Verlag Berlin-Heidelberg*, **24**, 322-332, 2003.

[29] S. De, K. Nagendra and K.N. Lakshmisha, Simulation of laminar flow in a three-dimensional lid-driven cavity by lattice Boltzmann method, *International Journal of Numerical Methods for Heat & Fluid Flow,* **19** (6), 790-815, 2009.

[30] D.V. Patil, K.N. Lakshmisha, Finite volume TVD formulation of lattice Boltzmann simulation on unstructured mesh, *Journal of Computational Physics*, **228**, 5262-5279, 2009.

[31] C. Shu, X.D. Niu and Y. T. Chew, Taylor series expansion and least squares-based lattice Boltzmann method: two-dimensional formulation and its applications, *Physical Review E*, **65**, 0367081-036708-13, 2002.

[32] M. Cheng and K.C. Hung, Vortex structure of steady flow in a rectangular cavity, *Computers & Fluids*, **35** (10), 1046-1062, 2006.

[33] D.V. Patil, K.N. Lakshmisha and B.Rogg, Lattice Boltzmann simulation of lid-driven flow in deep cavities, *Computers & Fluids*, **35**, 1116-1125, 2006.

[34] D.R. Noble, S. Chen, J.G. Georgiadis and R.O. Buckius, A consistent hydrodynamic boundary condition for the lattice Boltzmann method, *Physics of Fluids*, **7** (1), 203-209, 1995.

[35] T. Inamuro, M. Yoshino and F. Ogino, A non-slip boundary condition for lattice Boltzmann method, *Physics of Fluids*, **7** (12), 2928-2930, 1995.

[36] R.S. Maier, R.S. Bernard and D.W. Grunau, Boundary conditions for the lattice Boltzmann method, *Physics of Fluids*, **8** (7), 1788-1801, 1996.

[37] Q. Zou and X. He, On pressure and velocity boundary conditions for the lattice Boltzmann BGK model, *Physics of Fluids*, **9**, 1591-1598, 1997.

[38] O. Filippova and D. Hanel, Grid refinement for lattice-BGK models, *Journal of Computational Physics,* **147**, 219-228, 1998.

[39] R. Mei, L.S. Luo and W. Shyy, An accurate curved boundary treatment in the lattice Boltzmann method, *Journal of Computational Physics*, **155**, 307-330, 1999.

[40] M. Bouzidi, M. Firdaouss and P. Lallamand, Momentum transfer of a lattice Boltzmann fluid with boundaries, *Physics of Fluids*, 13, 3452-3459, 2001.

[41] D. Yu, R. Mei, W. Shyy, A unified boundary treatment in lattice Boltzmann method, Newyork: *American Institute of Aeronautics and Astronautics*, 2003-0953, 2003.

[42] G. McNamara, A.L. Garcia and B.J. Alder, Stabilization of thermal lattice Boltzmann models, *Journal of Statistical Physics*, **91**, 395-408, 1995.

[43] J.G.M. Eggels and J.A. Somers, Numerical simulation of free convective flow using the lattice Boltzmann scheme, *International Journal of Heat and Fluid Flow*, **16**, 357-364, 1995.

[44] X. He, S. Chen and G.D. Doolen, A novel thermal model for the lattice Boltzmann method in incompressible limit, *Journal of Computational Physics*, **146**, 282 – 300, 1998.

[45] X. Shan, Simulation of Rayleigh-Benard convection using a lattice Boltzmann method, *Physical Review E*, **55**, 2780-2788, 1997.

[46] Y. Peng, C. Shu and Y.T. Chew, Simplified thermal lattice Boltzmann model for incompressible thermal flows, *Physical Review E*, **68**, 026701-8, 2003.

[47] J. Onishi, Y. Chen and H. Ohashi, Lattice Boltzmann Simulation of Natural Convection in a Square Cavity, *JSME Int. Journal Series B*, **44** (1), 53-62, 2001.

[48] C. Shu, Y. Peng and Y.T. Chew, Simulation of natural convection in a square cavity by Taylor series expansion and least squares based lattice Boltzmann method, *International Journal of Modern Physics C*, **13** (10), 1399-1414, 2002.

[49] H.N. Dixit and V. Babu, Simulation of high Rayleigh number natural convection in a square cavity using the lattice Boltzmann method, *International Journal of Heat and Mass Transfer*, **49**, 727 – 739, 2006.

[50] J. Tolke, M. Krafczyk and E. Rank, A multigrid-solver for the discrete Boltzmann equation, *Journal of Statistical Physics,* 117 (2), 573-591, 2002.

[51] D.J. Mavriplis, Multigrid solution of the steady-state lattice Boltzmann equation, *Computers & Fluids,* **35**, 793-804, 2006.

[52] X. He, L.S. Luo and M. Dembo, Some progress in lattice Boltzmann method. Part I. Non-uniform mesh grids, *Journal of Computational Physics*, **129**, 357 – 363, 1996.

[53] F. Kuznik, J. Vareilles, G. Rusaouen and G. Krauss, A double-population lattice Boltzmann method with non-uniform mesh for the simulation of natural convection in a square cavity, *International Journal of Heat and Fluid Flow*, **28**, 862-870, 2007.

[54] D. Yu, R. Mei, L.S. Luo and W. Shyy, Viscous flow computations with the method of lattice Boltzmann equation, *Progress in Aerospace Sciences,* **39**, 329-367, 2003.

[55] R. Mei, W. Shyy, D. Yu and L. S. Luo, Lattice Boltzmann method for 3-D Flows with curved boundary, *Journal of Computational Physics,* **161**, 680-699, 2000.

[56] C. Shu, X.D. Niu and Y. T. Chew, Taylor series expansion and least squares-based lattice Boltzmann method: three-dimensional formulation and its applications, *International Journal of Modern Physics C*, **14**, 925-944, 2003.

[57] Y. Peng, C. Shu and Y.T. Chew, A 3D incompressible thermal lattice Boltzmann model and application to simulate natural convection in a cubic cavity, *Journal of Computational Physics*, **193**, 260 – 274, 2003.

[58] F. J. Alexander, H.D. Chen and S.Y. Cheu, Lattice-Boltzmann model for compressible fluids, *Physical Review A*, **46**, 1967-1970, 1992.

[59] Y.H. Qian and S.A. Orzsag, Lattice BGK model for the Navier-Stokes Equation: Nonlinear deviation in compressible regimes, *Europhysics Letters*, **21** (3), 255-259, 1993.

[60] C. Sun, Lattice Boltzmann models for high speed flows, *Physical Review E*, **58**, 7283-7287, 1997.

[61] C. Sun, Simulation of compressible flows with strong shocks by an adaptive lattice Boltzmann model, *Journal of Computational Physics*, **115**, 107 – 120, 2000.

[62] H. Yu and K. Zhao, Lattice Boltzmann method for compressible flows with high Mach numbers, *Physical Review E*, **61** (4), 3867-3870, 2000.

[63] M. Yoshino, Y. Matsuda and C. Shao, Comparison of accuracy and efficiency between the Lattice Boltzmann method and the finite difference Method in viscous/thermal fluid flows, *International Journal of Computational Fluid Dynamics*, **18**, 333 – 345, 2004.

[64] M. Breuer, J. Bernsdorf, T. Zeiser and F. Durst, Accurate computations of the laminar flow past a square cylinder based on two different methods: lattice-Boltzmann and finite-volume, *International Journal of Heat and Fluid Flow,* 21, 186-196, 2000.

[65] S. Geller, M. Krafczyk, J. Tolke, S. Turek and J. Hron, Benchmark computations based on lattice-Boltzmann, finite element and finite volume methods for laminar flows, *Computers & Fluids*, **35**, 888-897, 2006.

[66] D.O. Martinez, W.H. Matthaeus and S. Chen, Comparison of spectral method and Lattice Boltzmann simulations of two-dimensional hydrodynamics, *Physics of Fluids*, **6**, 1285-1298, 1994.

[67] X. He, G.D. Doolen and T. Clark, Comparison of the Lattice Boltzmann method and the artificial compressibility method for Navier-Stokes equations, *Journal of Computational Physics*, **179**, 439 – 451, 2002.

[68] X. Nie, G.D. Doolen, and S. Chen, Lattice-Boltzmann Simulations of Fluid Flows in MEMS, *Journal of Statistical Physics*, **107**, 279-289, 2002.

[69] G. H. Tang, W. Q. Tao, and Y. L. He, Lattice Boltzmann method for simulating gas flow in microchannels, *International Journal of Modern Physics C,* **15**, 335-347, 2004.

[70] G. H. Tang, W. Q. Tao, and Y. L. He, Lattice Boltzmann method for gaseous microflows using kinetic theory boundary conditions, *Physics of Fluids,* **17**, 058101, 2005.

[71] Y. H. Zhang, R. S. Qin, Y. H. Sun, R. W. Barber, and D. R. Emerson, Gas Flow in Microchannels - A Lattice Boltzmann Method Approach, *Journal of Statistical Physics*, **121**, 257-267, 2005.

[72] E. Shirani and S. Jafari, Application of LBM in Simulation of Flow in Simple Micro-Geometries and Micro Porous Media, *African Physical Review*, **1**, 0003, 2007.

[73] X. D. Niu, C. Shu, and Y. T. Chew, Numerical Simulation of Isothermal Micro Flows by Lattice Boltzmann Method and theoretical analysis of the Diffuse scattering boundary condition, *International Journal of Modern Physics C*, **16**, 1927–1941, 2005.

[74] C.K. Aidun, N.G. Triantafillooulos and J.D. Benson, Global stability of a lid-driven cavity with through flow: flow visualization studies, *Physics of Fluids A*, **3**, 2081-2091, 1991.

[75] S. Albensoeder, H.C. Kuhlmann, H.J. Rath, Multiplicity of steady two-dimensional flows in two-sided lid-driven cavities, *Theoretical Computational Fluid Dynamics*, **14**, 223-241, 2001.

[76] E.M. Wabha, Multiplicity of states for two-sided and four-sided lid-driven cavity flows, *Computers and Fluids*, **38**, 247-253, 2009.

[77] C. Cercignani, The Boltzmann equation and its application, Springer, New York, 1988.

[78] P. Lallemand and L.S. Luo, Theory of the lattice Boltzmann method: dispersion, dissipation, isotropy, Galilean invariance, and stability, *Physical Review E*, **61**, 6546-6562, 2000.

[79] D. d'Humieres, 1992, Generalized lattice Boltzmann equation, in rarefied gas dynamics: theory and simulations, *Progress in Astronautics and Aeronautics,* Vol. 159, edited by B.D. Shizgal and D.P. Weaver, AIAA, D.C. Washington, pp: **450-458.**

[80] J.-S. Wu and Y.-L. Shao, Simulation of lid-driven cavity flows by parallel lattice Boltzmann method using multi-relaxation-time scheme, *International Journal of Numerical Methods in Fluids*, **46**, 921–937, 2004.

[81] O.R. Burggraf, Analytical and numerical studies of the structure of steady separated flows, *Journal of Fluid Mechanics*, **24**, 113-151, 1966.

[82] F. Pan and A. Acrivos, Steady flows in rectangular cavities, *Journal of Fluid Mechanics*, **28**, 643-655, 1967.

[83] U. Ghia, K. N. Ghia and C. T. Shin, High-Re solutions for incompressible flow using the Navier-Stokes equations and a multigrid method, *Journal of Computational Physics,* **48**, 387-411, 1983.

[84] M.M. Gupta and J.C. Kalita, A new paradigm for solving Navier-Stokes equations: streamfunction-velocity formulation, *Journal of Computational Physics*, **207**, 52-68, 2005.

[85] C-H. Bruneau and M. Sadd, The 2D lid-driven cavity problem revisited, *Computers & Fluids,* **35**, 326-348, 2006.

[86] C-H. Bruneau and C. Jouron, An efficient scheme for solving steady incompressible Navier-Stokes equations, *Journal of Computational Physics*, **89**, 389-413, 1990.

[87] X. He and G. Doolen, Lattice Boltzmann method on curvilinear coordinates system: flow around a circular cylinder, *Journal of Computational Physics*, **134** (2), 306–315, 1997.

[88] D. J. Tritton, Experiments on the flow past a circular cylinder at low Reynolds numbers, *Journal of Fluid Mechanics,* **6**, 547, 1959.

[89] S. C. R. Dennis and G. Chang, Numerical solutions for steady flow past a circular cylinder at Reynolds number up to 100, *Journal of Fluid Mechanics,* **42**, 471, 1970.

[90] D. Calhoun, A cartesian grid method for solving the two-dimensional streamfunction-vorticity equations in irregular regions, *Journal of Computational Physics*, **176,** 231–275, 2002.

[91] C.H. Blohm and H.C. Kuhlmann, The two-sided lid-driven cavity: experiments on stationary and time-dependent flows, *Journal of Fluid Mechanics*, **450**, 67-95, 2002.

[92] H.C. Kuhlmann, M. Wanschura and H.J. Rath, Flow in two-sided lid-driven cavities:non-uniqueness, instability, and cellular structures, *Journal of Fluid Mechanics*, **336**, 267-299, 1997.

[93] H.C. Kuhlmann, M. Wanschura and H.J. Rath, Elliptic instability in two-sided lid-driven cavity flow, *European Journal of Mech. B/Fluids*, **17**, 561-569, 1998.

[94] S. Albensoeder and H.C. Kuhlmann, Linear stability of rectangular cavity flows driven by anti-parallel motion of two-facing walls, *Journal of Fluid Mechanics,* **458**, 153-180, 2002.

[95] J.C. Kalita, A.K. Dass and D.C. Dalal, A transformation-free HOC scheme for steady convection-diffusion on nonuniform grid, *International Journal for Numerical Methods in Engineering*, **38**, 3497-3521, 2004.

[96] N. Kumar, J.C. Kalita and A.K. Dass. HOC computation of Two-Sided Lid-Driven Cavity Flow. in *2006 Proceedings of the Int. Conference on Computational Mechanics and Simulation, ICCMS 2006*, IIT Guwahati, India, 2006.

[97] D.W. Peaceman and H.H. Rathford, The Numerical solution of parabolic and elliptic differential equations, *Journal of the Society for Industrial and Applied Mathematics*, **3,** 28-41, 1955.

[98] W.-J. Luo and R.-J. Yang, Multiple fluid flow and heat transfer solutions in a two-sided lid-driven cavity, *International Journal of Heat and Mass Transfer*, **50**, 2394-2405, 2007.

[99] Y.G. Lai, C.L. Lin and J. Huang, Accuracy and efficiency study of a lattice Boltzmann method for steady-state flow simulations, *Numerical Heat Transfer, Part B*, **39**, 21-43, 2001.

[100] S. Albensoeder and H.C. Kuhlmann, Accurate three-dimensional lid-driven cavity flow, *Journal of Computational Physics*, **206**, 536-558, 2005.

[101] J.R. Koseff, and R.L. Street, Visualization studies of a shear driven three-dimensional recirculating flow, *Journal of Fluids Engineering*, **106**, 21-33, 1984.

[102] A.B. Cortes and J.D. Miller, Numerical Experiments with the Lid driven cavity problem, *Computers & Fluids,* **23** (8), 1005-1027, 1994.

[103] T.W.H. Shew and S.F. Tsai, Flow topology in a steady three-dimensional lid-driven cavity, *Computers & Fluids*, **31**, 911-934, 2002.

[104] H.C. Ku, R.S. Hirsh and T.D. Taylor, A Pseudospectral method for solution of the three dimensional incompressible Navier-Stokes equations, *Journal of Computational Physics*, **70**, 439-462, 1987.

[105] C. Shu, L. Wang, and Y. T. Chew, Numerical computation of three-dimensional incompressible Navier-Stokes equations in primitive variable form by DQ method, *International Journal of Numerical Methods in Fluids*, **43**, 345–368, 2003.

[106] R. Iwatsu, J.M. Hyun and K.Kuwahara, Analyses of three-dimensional flow calculationsin a driven cavity, *Fluid Dynamics Research*, **6**, 91-102, 1990.

[107] B.B. Beya and T. Lili, Three-dimensional incompressible flow in a two-sided non-facing lid-driven cubical cavity*, C.R. Mecanique*, **336,** 863-872, 2008.

[108] G. De Vahl Davis, Natural convection of air in a square cavity: a bench mark solution, *International Journal of Numerical Methods in Fluids*, **3**, 249–264, 1983.

[109] D.R. Chenoweth and S. Paolucci, Natural convection in an enclosed vertical air layer with large horizontal temperature differences, *Journal of Fluid Mechanics*, **169**, 173-210, 1986.

[110] J. C. Kalita, D.C. Dalal and Anoop K. Dass, Fully compact higher-order computation of steady-state natural convection in a square cavity, *Physical Review E*, **64**, 066703, 2001.

[111] K.S. Ball and D.C. Kuo, Spectral simulation of thermal convection using a vorticity-velocity formulation, *Journal of Heat Transfer*, **2**, 313-320, 1994.

[112] C.J. Ho and F.H. Lin, Simulation of natural convection in a vertical enclosure by using a new incompressible flow formulation- pseudo vorticity-velocity formulation, *Numerical Heat Transfer, Part A*, **31**, 881-896, 1997.

[113] F. Alexanders, S. Chen and J. Sterling, Lattice-Boltzmann thermo- hydrodynamics, *Physical Review E*, **47**, R2249-R2252, 1993.

[114] G. Barrios, R. Rechtman, J. Rojas and R. Tovar, The lattice Boltzmann equation for natural convection in a two-dimensional cavity with a partially heated wall, *Journal of Fluid Mechanics*, **522**, 91-100, 2005.

[115] J.C. Mandal, L. Agrawal and A.G. Marathe, Computation of incompressible flows with natural convection using pseudocompressibility approach, *Journal of Thermophysics*, **14** (4), 606-612, 2000.

[116] T. Fusegi, J.M. Hyun, H. Kuwahara and B. Farouk, A numerical study of three-dimensional natural convection in a differentially heated cubical enclosure, *International Journal of Heat and Mass Transfer*, **34** (6), 1543-1557, 1991.

[117] E. Tric, G. Labrosse and M. Betrouni, A first incursion into the 3D structure of natural convection of air in a differentially heated cubic cavity from accurate numerical solutions, *International Journal of Heat and Mass Transfer*, **43**, 4043-4056, 2000.

[118] M. Gad-el-Hak, The fluid mechanics of microdevices-The Freeman Scholar Lecture, *Journal of Fluids Engineering*, **121**, 6-33, 1999.

[119] D. Raabe, Overview of the lattice Boltzmann method for nano- and microscale fluid dynamics in materials science and engineering, *Modelling and Simulation in Materials Science and Engineering*, **12** (6), R13-R46, 2004.

[120] A. A. Rostami, A. S. Mujumdar and N. Saniei, Flow and heat transfer for gas flowing in microchannels: A review, *Heat and Mass Transfer*, **38**, 359–367, 2002.

[121] S. Mizzi, D.R. Emerson, S.K. Stefanov, R.W. Barber and J.M. Reese, Effects of rarefaction on cavity flow in the slip regime, *Journal of Computational and Theoretical Nanoscience*, **4** (4), 817-822, 2007.

[122] S. Roy and S. Chakraborty, Near wall effects in micro scale couette flow and heat transfer in the Maxwell-slip regimes, *Microfluid Nanofluid*, **3**, 437-449, 2007.

[123] M. Darbandi, Y. Daghighi, S. Vakilipour and G.E. Schneider, Microflow in lid-driven microcavity with variour aspect ratios, *AIAA Aerospace Science Meeting and Exhibit,* 1285, 2008.

[124] S. Naris and D. Valougeorgis, The driven cavity flow over the whole range of the Knudsen number, *Physics of Fluids*, **17** (9), 097106, 2005.

[125] K-C. Pong, C-M. Ho, J. Liu and Y-C. Tai, Non-linear pressure distribution in uniform microchannels, *ASME winter annual meeting, FED*, **197**, 51-56, 1994.

[126] E.B. Arkilic, M.A. Schmidt and K.S. Breuer, Gaseous slip flow in long microchannels, *Journal of Microelctromechanical systems*, **6**, 167-178, 1997.

[127] C.S. Chen, S.M. Lee and J.D. Sheu, Numerical analysis of gas flow in microchannels, *Numerical Heat Transfer Part A,* **33**, 749-762, 1998.

[128] A. Beskok, G.E. Karniadakis and W. Trimmer, Rarefaction and compressibility effects in gas microflows, *Transaction of the ASME*, **118**, 448–456, 1996.

[129] C.Y. Lim, C. Shu, X.D. Niu and Y.T. Chew, Application of the lattice Boltzmann method to simulate microchannel flows, *Physics of Fluids,* **14**, 2209–2308, 2002.

[130] E.B. Arkilic, K.S. Breuer and M.A. Schmidt, Mass flow and tangential momentum accommodation in silicon micromachined channels, *Journal of Fluid Mechanics*, **437**, 29-43, 2001.

[131] F.B. Bao and J.Z. Lin, Burnett simulations of gas flow in microchannels, *Fluid Dynamics Research*, **40**, 679-694, 2008.

[132] X. D. Niu, C. Shu, and Y. T. Chew, Lattice Boltzmann BGK model for simulation of micro flows, *Euro Physics Letters*, **67**, 600-606, 2004.

[133] S. Ansumali, C.E. Frouzakis, I.V. Karlin and I.G. Kevrekidis, Exploring hydrodynamic closures for the lid-driven micro-cavity, *http://arxiv.org/abs/cond-mat/0502018,* 2005.

[134] J.Z. Jiang, J. Fan, C. Shen, Statistical simulation of micro-cavity flows, in *23rd Int. Symposium on Rarefied Gas Dynamics*, 784-780*,* 2003.

[135] J.E. Broadwell, Study of rarefied shear flow by the discrete velocity method, *Journal of Fluid Mechanics*, **19** (3), 401-414, 1964.

[136] T. Inamuro, A lattice kinetic scheme for incompressible viscous flows with heat transfer, *Phil. Trans. R. Soc. Lond. A*, **360**, 477-484, 2002.

[137] Y. Peng, C. Shu, Y.T. Chew and H.W. Zheng, New lattice kinetic schemes for incompressible viscous flows, *International Journal of Modern Physics C*, **15** (9), 1197-1213, 2004.

[138] Y. Peng, C. Shu and Y.T. Chew, Lattice kinetic schemes for incompressible viscous thermal flows on arbitrary meshes, *Physical Review E*, **69,** 01673-1, 2004.

[139] H. Xu, Y.H. Qian and W.Q. Tao, Revisiting two-dimensional turbulence by lattice Boltzmann method, *Progress in Computational Fluid Dynamics,* **9,** 133-140, 2009.

[140] C. Teixeira, Incorporating turbulence models into the lattice Boltzmann equations, *International Journal of Modern Physics C*, **9**, 1159-1175, 1999.

[141] A. Keating, J. Beedy and R. Shock, Lattice Boltzmann simulations of the DLR-F4, DLR-F6 and variants, *AIAA*, 2008-74, 2008.

[142] P. Sagaut, *Large Eddy Simulation for Incompressible flows*, 2nd Edition, Springer, Berlin, 2002.

Appendix A

Theory of the Lattice Boltzmann Method

A.1. Derivation of the Lattice Boltzmann Equation from the Boltzmann Equation

The Boltzmann Equation with single-relaxation-time approximation can be written as [7]

$$\frac{\partial f}{\partial t} + \boldsymbol{c}.\nabla f = -\frac{1}{\lambda}(f - g) \tag{A.1}$$

where, $f \equiv f(\boldsymbol{x},\boldsymbol{c},t)$ is the single particle distribution function and g is the Boltzmann-Maxwellian distribution function.

Equation (A.1) can be rewritten in the form of ordinary differential equation

$$\frac{df}{dt} + \frac{1}{\lambda} f = \frac{1}{\lambda} g \tag{A.2}$$

where $\frac{d}{dt} = \frac{\partial}{\partial t} + \boldsymbol{c}.\nabla$

For the following equation

$$\frac{dy}{dx} + Py = Q \tag{A.3}$$

we may write

$$\frac{dy}{dx} e^{\int Pdx} + Py\, e^{\int Pdx} = Q\, e^{\int Pdx} \tag{A.4}$$

$$\frac{d}{dx}\left(y\ e^{\int Pdx} \right) = Q\ e^{\int Pdx} \tag{A.5}$$

Compare Equations (A.2) and (A.3)

$$x = t\,; \qquad y = f\,; \qquad P = \frac{1}{\lambda}\ ; \qquad Q = \frac{1}{\lambda}\, g\,;$$

From Equation (A.5) $$\frac{d}{dt}\left(f\ e^{\int \frac{1}{\lambda} dt} \right) = \frac{1}{\lambda}\, g\, e^{\int \frac{1}{\lambda} dt} \tag{A.6}$$

Equation (A.6) can be integrated over a time step δ_t

$$\int_0^{\delta_t} d\left(f\ e^{\int \frac{dt}{\lambda}} \right) = \int_0^{\delta_t} \left(\frac{1}{\lambda}\ g\ e^{\int \frac{dt}{\lambda}} \right) dt \tag{A.7}$$

$$f\left(\boldsymbol{x}+\boldsymbol{c}\delta_t,\ \boldsymbol{c},\ t+\delta_t\right)\ e^{\delta_t/\lambda} - f\left(\boldsymbol{x},\ \boldsymbol{c},\ t\right)\ e^{0} = \frac{1}{\lambda} \int_0^{\delta_t} e^{t^1/\lambda}\ g\left(\boldsymbol{x}+\boldsymbol{c}t^1,\ \boldsymbol{c},\ t+t^1\right) dt^1 \tag{A.8}$$

$$f\left(\boldsymbol{x}+\boldsymbol{c}\delta_t,\ \boldsymbol{c},\ t+\delta_t\right) = e^{-\delta_t/\lambda} \frac{1}{\lambda} \int_0^{\delta_t} g\left(\boldsymbol{x}+\boldsymbol{c}t^1,\ \boldsymbol{c},\ t+t^1\right) dt^1\ e^{t^1/\lambda} + e^{-\delta_t/\lambda} f\left(\boldsymbol{x},\ \boldsymbol{c},\ t\right) \tag{A.9}$$

Assuming that δ_t is small enough and g is smooth enough locally, linear interpolation gives

$$g\left(\boldsymbol{x}+\boldsymbol{c}t^1,\ \boldsymbol{c},\ t+t^1\right) = \mathrm{g}\left(\boldsymbol{x},\boldsymbol{c},t\right) - \frac{t^1}{\delta_t}\ \mathrm{g}\left(\boldsymbol{x},\boldsymbol{c},t\right) + \frac{t^1}{\delta_t}\ \mathrm{g}\left(x+\boldsymbol{c}\delta_t,\ \boldsymbol{c},\ t+\delta_t\right) + o\left(\delta_t^2\right),\quad 0 \le t' \le \delta_t$$

$$\Rightarrow\ g\left(\boldsymbol{x}+\boldsymbol{c}t^1,\ \boldsymbol{c},\ t+t^1\right) = \left(1-\frac{t^1}{\delta_t}\right) \mathrm{g}\left(\boldsymbol{x},\boldsymbol{c},t\right) + \frac{t^1}{\delta_t}\ \mathrm{g}\left(\boldsymbol{x}+\boldsymbol{c}\delta_t,\ \boldsymbol{c},\ t+\delta_t\right) \tag{A.10}$$

With this approximation Equation (A.9) becomes

$$\begin{aligned} f\left(\boldsymbol{x}+\boldsymbol{c}\delta_t,\ \boldsymbol{c},\ t+\delta_t\right)\ - f\left(\boldsymbol{x},\ \boldsymbol{c},\ t\right) &= \frac{1}{\lambda}\ e^{-\delta_t/\lambda} \int_0^{\delta_t} e^{t^1/\lambda} \left(1-\frac{t^1}{\delta_t}\right) g\left(\boldsymbol{x},\boldsymbol{c},t\right) dt^1 \\ + \frac{1}{\lambda}\ e^{-\delta_t/\lambda} \int_0^{\delta_t} e^{t^1/\lambda} \frac{t^1}{\delta_t}\ g\left(\boldsymbol{x}+\boldsymbol{c}\Delta t^1,\ \boldsymbol{c},\ t+t^1\right) dt^1 &+ e^{-\delta_t/\lambda} f\left(\boldsymbol{x},\ \boldsymbol{c},\ t\right) - f\left(\boldsymbol{x},\ \boldsymbol{c},\ t\right) \end{aligned} \tag{A.11}$$

$$f\left(\boldsymbol{x}+\boldsymbol{c}\delta_t,\ \boldsymbol{c},\ t+\delta_t\right)\ - f\left(\boldsymbol{x},\ \boldsymbol{c},\ t\right) = \left[\mathrm{e}^{-\delta_t/\lambda} - 1\right] f\left(\boldsymbol{x},\ \boldsymbol{c},\ t\right) + \frac{1}{\lambda}\ e^{-\delta_t/\lambda} \int_0^{\delta_t} e^{t^1/\lambda}\ \mathrm{g}\left(\boldsymbol{x},\boldsymbol{c},t\right) dt^1$$

$$- \frac{1}{\lambda}\ e^{-\delta_t/\lambda} \int_0^{\delta_t} e^{t^1/\lambda} \frac{t^1}{\delta_t}\ \mathrm{g}\left(\boldsymbol{x},\ \boldsymbol{c},\ t\right) dt^1 + \frac{1}{\lambda}\ e^{-\delta_t/\lambda} \int_0^{\delta_t} e^{t^1/\lambda}\ \frac{t^1}{\delta_t}\ g\left(\boldsymbol{x}+\boldsymbol{c}\delta_t,\ \boldsymbol{c},\ t+\delta_t\right)\ dt^1 \tag{A.12}$$

In the right hand side (R.H.S.) of the above equation

Ist Item: $\left[e^{-\delta_t/\lambda} - 1\right] f\left(\boldsymbol{x},\ \boldsymbol{c},\ t\right)$; IInd Item: $\frac{1}{\lambda}\ e^{-\delta_t/\lambda} \int_0^{\delta_t} e^{t^1/\lambda}\ g\left(\boldsymbol{x},\boldsymbol{c},t\right) dt^1$

IIIrd Item: $- \frac{1}{\lambda}\ e^{-\delta_t/\lambda} \int_0^{\delta_t} e^{t^1/\lambda} \frac{t^1}{\delta_t}\ \mathrm{g}\left(\boldsymbol{x},\ \boldsymbol{c},\ t\right) dt^1$

IVth Item: $\frac{1}{\lambda}\ e^{-\delta_t/\lambda} \int_0^{\delta_t} e^{t^1/\lambda}\ \frac{t^1}{\delta_t}\ g\left(\boldsymbol{x}+\boldsymbol{c}\delta_t,\ \boldsymbol{c},\ t+\delta_t\right)\ dt^1$

Evaluation of the frequently occurring term

$$\int_0^{\delta_t} e^{t^1/\lambda}\, t^1\, dt^1 \tag{A.13}$$

We know that (integration by parts)

$$\int_a^b f_1 f_2\, dx = f_1 \int_a^b f_2\, dx - \int_a^b \left[\frac{d}{dx}(f_1) \times \int f_2\, dx \right] dx \tag{A.14}$$

$$\int_0^{\delta_t} t^1\, e^{t^1/\lambda}\, dt^1 = t^1 \int_0^{\delta_t} e^{t^1/\lambda}\, dt^1 - \int_0^{\delta_t} \left[\frac{d}{dt^1}(t^1) \times \int e^{t^1/\lambda}\, dt^1 \right] dt^1$$

$$\int_0^{\delta_t} t^1\, e^{t^1/\lambda}\, dt^1 = \lambda \left[t^1 e^{t^1/\lambda} \right]_0^{\delta_t} - \int_0^{\delta_t} \left(1 \times \lambda \left[e^{t^1/\lambda} \right] \right) dt^1$$

$$= \lambda\, \delta_t e^{\delta_t/\lambda} - \lambda \left[\frac{e^{t^1/\lambda}}{1/\lambda} \right]_0^{\delta_t}$$

$$= \lambda\, \delta_t e^{\delta_t/\lambda} - \lambda^2 e^{\delta_t/\lambda} + \lambda^2 \tag{A.15}$$

Coming back to the right hand side of Equation (A.12), we now have

I[st] term:
$$\left[e^{-\delta_t/\lambda} - 1 \right] f(x, \boldsymbol{c}, t) \tag{A.16}$$

II[nd] term:
$$\frac{1}{\lambda}\, e^{-\delta_t/\lambda} \int_0^{\delta_t} e^{t^1/\lambda}\, g(\boldsymbol{x}, \mathbf{c}, t)\, dt^1$$

$$\Rightarrow \frac{1}{\lambda}\, e^{-\delta_t/\lambda} g(\boldsymbol{x}, \mathbf{c}, t) \int_0^{\delta_t} e^{t^1/\lambda} dt^1 \quad \Rightarrow \frac{1}{\lambda}\, e^{-\delta_t/\lambda} g(\boldsymbol{x}, \mathbf{c}, t) \left[\frac{e^{t^1/\lambda}}{1/\lambda} \right]_0^{\delta_t}$$

$$\Rightarrow \frac{1}{\lambda}\, e^{-\delta_t/\lambda} g(\boldsymbol{x}, \mathbf{c}, t) \lambda \left[e^{\delta_t/\lambda} - 1 \right] \quad \Rightarrow e^{-\delta_t/\lambda} g(\boldsymbol{x}, \mathbf{c}, t) \left[e^{\delta_t/\lambda} - 1 \right]$$

$$\Rightarrow g(\boldsymbol{x}, \mathbf{c}, t) \left[e^{-\delta_t/\lambda} . e^{\delta_t/\lambda} - e^{-\delta_t/\lambda} \right] \quad \Rightarrow -g(\boldsymbol{x}, \boldsymbol{c}, t) \left[e^{-\delta_t/\lambda} - 1 \right] \tag{A.17}$$

III[rd] Term:

$$-\frac{1}{\lambda}\, e^{-\delta_t/\lambda} \int_0^{\delta_t} e^{t^1/\lambda} \frac{t^1}{\delta_t}\, g(\boldsymbol{x}, \boldsymbol{c}, t)\, dt^1$$

$$\Rightarrow \quad -\frac{1}{\lambda}\, e^{-\delta_t/\lambda}\, \frac{g(\boldsymbol{x},\, \mathbf{c},\, t)}{\delta_t} \int_0^{\delta_t} e^{t^1/\lambda} t^1 \, dt^1$$

$$\Rightarrow \quad -\frac{1}{\lambda}\, e^{-\delta_t/\lambda}\, \frac{g(\boldsymbol{x},\, \mathbf{c},\, t)}{\delta_t} \left[\lambda\delta_t e^{\delta_t/\lambda} - \lambda^2 e^{\delta_t/\lambda} + \lambda^2\right]$$

$$\Rightarrow \quad -e^{-\delta_t/\lambda}\, \frac{g(\boldsymbol{x},\, \boldsymbol{c},\, t)}{\delta_t} \left[\delta_t e^{\delta_t/\lambda} - \lambda e^{\delta_t/\lambda} + \lambda\right]$$

$$\Rightarrow \quad -e^{-\delta_t/\lambda}\, \frac{g(\boldsymbol{x},\, \boldsymbol{c},\, t)}{\delta_t} \left[\delta_t e^{\delta_t/\lambda} - \lambda e^{\delta_t/\lambda} + \lambda\right]$$

$$\Rightarrow \quad -g(\boldsymbol{x},\, \boldsymbol{c},\, t)\, \frac{e^{-\delta_t/\lambda}}{\delta_t} \left[\delta_t e^{\delta_t/\lambda} - \lambda e^{\delta_t/\lambda} + \lambda\right] \quad \Rightarrow \quad -g(\boldsymbol{x},\, \boldsymbol{c},\, t) \left[1 - \frac{\lambda}{\delta_t} + \lambda \frac{e^{-\delta_t/\lambda}}{\delta_t}\right]$$

$$\Rightarrow \quad -g(\boldsymbol{x},\, \boldsymbol{c},\, t) \left[1 + \frac{\lambda}{\delta_t}(e^{-\delta_t/\lambda} - 1)\right] \tag{A.18}$$

IVth Term:

$$\frac{1}{\lambda}\, e^{-\delta_t/\lambda} \int_0^{\delta_t} e^{t^1/\lambda}\, \frac{t^1}{\delta_t}\, g(\boldsymbol{x} + \mathbf{c}\delta_t,\, \mathbf{c},\, t + \delta_t)\, dt^1$$

$$\Rightarrow \quad \frac{1}{\lambda}\, e^{-\delta_t/\lambda}\, \frac{g(\boldsymbol{x} + \boldsymbol{c}\delta_t,\, \boldsymbol{c},\, t + \delta_t)}{\delta_t} \int_0^{\delta_t} e^{t^1/\lambda}\, t^1\, dt^1$$

$$\Rightarrow \quad \frac{1}{\lambda}\, e^{-\delta_t/\lambda}\, \frac{g(\boldsymbol{x} + \boldsymbol{c}\delta_t,\, \boldsymbol{c},\, t + \delta_t)}{\delta_t} \left[\lambda\delta_t e^{\delta_t/\lambda} - \lambda^2 e^{\delta_t/\lambda} + \lambda^2\right]$$

$$\Rightarrow \quad e^{-\delta_t/\lambda}\, \frac{g(\boldsymbol{x} + \boldsymbol{c}\delta_t,\, \boldsymbol{c},\, t + \delta_t)}{\delta_t} \left[\delta_t e^{\delta_t/\lambda} - \lambda e^{\delta_t/\lambda} + \lambda\right]$$

$$\Rightarrow g(\boldsymbol{x} + \boldsymbol{c}\delta_t,\, \boldsymbol{c},\, t + \delta_t)\, \frac{e^{-\delta_t/\lambda}}{\delta_t} \left[\delta_t e^{\delta_t/\lambda} - \lambda e^{\delta_t/\lambda} + \lambda\right]$$

$$\Rightarrow g(\boldsymbol{x} + \boldsymbol{c}\delta_t,\, \boldsymbol{c},\, t + \delta_t) \left[1 - \frac{\lambda}{\delta_t} + \lambda \frac{e^{-\delta_t/\lambda}}{\delta_t}\right]$$

$$\Rightarrow g(\boldsymbol{x} + \boldsymbol{c}\delta_t,\, \boldsymbol{c},\, t + \delta_t) \left[1 + \frac{\lambda}{\delta_t}(e^{-\delta_t/\lambda} - 1)\right] \tag{A.19}$$

Substituting Equations (A.16-A.19) into Equation (A.12) we get

$$f\left(\boldsymbol{x}+\boldsymbol{c}\delta_t,\ \boldsymbol{c},t+\delta_t\right)\ -f\left(\boldsymbol{x},\ \boldsymbol{c},t\right)=\left(e^{-\delta_t/\lambda}-1\right)f\left(\boldsymbol{x},\ \boldsymbol{c},t\right)-\left(e^{-\delta_t/\lambda}-1\right)g\left(\boldsymbol{x},\boldsymbol{c},t\right)$$

$$-g\left(\boldsymbol{x},\ \boldsymbol{c},t\right)\left[1+\frac{\lambda}{\delta_t}(e^{-\delta_t/\lambda}-1)\right]+g\left(\boldsymbol{x}+\boldsymbol{c}\delta_t,\ \boldsymbol{c},t+\delta_t\right)\left[1+\frac{\lambda}{\delta_t}(e^{-\delta_t/\lambda}-1)\right] \tag{A.20}$$

$$f\left(\mathbf{x}+\boldsymbol{c}\delta_t,\ \boldsymbol{c},t+\delta_t\right)\ -f\left(\mathbf{x},\ \boldsymbol{c},t\right)=\left(e^{-\delta_t/\lambda}-1\right)\left[f\left(\mathbf{x},\ \boldsymbol{c},\mathrm{t}\right)-\mathrm{g}\left(\mathbf{x},\mathbf{c},t\right)\right]$$

$$+\left[1+\frac{\lambda}{\delta_t}(e^{-\delta_t/\lambda}-1)\right]\left[g\left(\mathbf{x}+\boldsymbol{c}\delta_t,\ \boldsymbol{c},t+\delta_t\right)-\mathrm{g}\left(\mathbf{x},\ \boldsymbol{c},t\right)\right] \tag{A.21}$$

We know that

$$e^{-x}=1-x+\frac{x^2}{2!}-\frac{x^3}{3!}+\ldots;\qquad e^{-x}-1=-x+\frac{x^2}{2!}-\frac{x^3}{3!}+\ldots$$

$$e^{-\delta_t/\lambda}-1=-\frac{\delta_t}{\lambda}+\frac{\delta_t^2}{2\lambda^2}+\ldots\ ;$$

Neglecting the higher order terms $e^{-\delta_t/\lambda}-1=-\frac{\delta_t}{\lambda}$

In Equation (A.21) we may write

$$\left[1+\frac{\lambda}{\delta_t}(\mathrm{e}^{-\delta_t/\lambda}-1)\right]=\left[1+\frac{\lambda}{\delta_t}(-\frac{-\delta_t}{\lambda})\right]=0 \tag{A.22}$$

We now introduce the non-dimensional relaxation time $\tau\equiv\frac{\lambda}{\delta_t}$

So that in Equation (A.21)

$$e^{-\delta_t/\lambda}-1=-\frac{\delta_t}{\lambda}=-\frac{1}{\tau}\ ; \tag{A.23}$$

Substituting Equation (A.22) and (A.23) into Equation (A.21) we may now write

$$f\left(\mathbf{x}+\boldsymbol{c}\delta_t,\boldsymbol{c},t+\delta_t\right)\ -f\left(\mathbf{x},\ \boldsymbol{c},t\right)=-\frac{1}{\tau}\left[f\left(\mathbf{x},\ \boldsymbol{c},t\right)-\mathrm{g}\left(\mathbf{x},\ \boldsymbol{c},t\right)\right]$$
$$+0\ \times\left[g\left(\mathbf{x}+\boldsymbol{c}\delta_t,\ \boldsymbol{c},t+\delta_t\right)-g\left(\mathbf{x},\ \boldsymbol{c},t\right)\right] \tag{A.24}$$

The discretized Boltzmann Equation then becomes

$$f\left(\mathbf{x}+\boldsymbol{c}\delta_t,\ \boldsymbol{c},t+\delta_t\right)\ -f\left(\mathbf{x},\ \boldsymbol{c},t\right)=-\frac{1}{\tau}\left[f\left(\mathbf{x},\ \boldsymbol{c},t\right)-g\left(\mathbf{x},\boldsymbol{c},t\right)\right] \tag{A.25}$$

The lattice Boltzmann equation is derived from the discretized Boltzmann equation (A.25) by using discrete particle velocities and directions.

A.2 Equilibrium Distribution Function in the Low Mach number Limit

The Boltzmann Equation with LBGK or single-relaxation-time approximation can be written as [7]

$$\frac{df}{dt} + \frac{1}{\lambda} f = \frac{1}{\lambda} g \ ; \tag{A.26}$$

Where $f \equiv f(\boldsymbol{x},\boldsymbol{c},t)$ is the single particle distribution function, $\boldsymbol{c}$ is is the particle velocity, λ is the relaxation time due to collision and g is the Boltzmann-Maxwellian distribution function

$$\mathrm{g} = \frac{\rho}{(2\pi RT)^{D/2}} \exp\left(-\frac{(\boldsymbol{c}-\boldsymbol{u})^2}{2RT}\right) \tag{A.27}$$

Where R is the ideal gas constant, D is the dimension of the space and $\rho, \boldsymbol{u}, T$ are the macroscopic density of mass, velocity and temperature respectively. The macroscopic variables are the moments of the distribution function f with the microscopic velocity $\boldsymbol{c}$:

$$\rho = \int f \ d\boldsymbol{c} = \int g \ d\boldsymbol{c} \tag{A.28}$$

$$\rho\boldsymbol{u} = \int \boldsymbol{c} f \ d\boldsymbol{c} = \int \boldsymbol{c} g \ d\boldsymbol{c} \tag{A.29}$$

$$\rho\varepsilon = \frac{1}{2}\int (\boldsymbol{c}-\boldsymbol{u})^2 f \ d\boldsymbol{c} = \frac{1}{2}\int (\boldsymbol{c}-\boldsymbol{u})^2 \ g \ d\boldsymbol{c} \tag{A.30}$$

The energy can also be in terms of temperature T

$$\varepsilon = \frac{D_o}{2} RT = \frac{D_o}{2} N_A k_B T \tag{A.31}$$

where D_0, N_A, k_B are the number of degrees of freedom of a particle, Avagardo's number and the Boltzmann constant respectively. In Equations (A.28) - (A.30) the Chapman Enskog analysis has been applied

$$\int h(\boldsymbol{c}) f(\boldsymbol{x},\boldsymbol{c},t) \ d\boldsymbol{c} = \int h(\boldsymbol{c}) \ g(\boldsymbol{x},\boldsymbol{c},t) \ d\boldsymbol{c} \tag{A.32}$$

where $h(\boldsymbol{c})$, a linear combination of collisional invariants (conserved quantities), is

$$h(\boldsymbol{c}) = A + \boldsymbol{B}.\boldsymbol{c} + C\,\boldsymbol{c}.\boldsymbol{c} \tag{A.33}$$

In the above equation A, C are arbitrary constants, and $\boldsymbol{B}$ is an arbitrary constant vector. With appropriate discretization, integration in momentum space can be approximated by quadrature upto a certain degree of accuracy, that is,

$$\int \psi(\boldsymbol{c}) \ \mathrm{g}(\boldsymbol{x},\boldsymbol{c},t) \ d\boldsymbol{c} = \sum_i w_i \ \psi(\boldsymbol{c}_i) g(\boldsymbol{x},\boldsymbol{c}_i,t) \tag{A.34}$$

where $\psi(\boldsymbol{c})$ is a polynomial in $\boldsymbol{c}$ and w_i and $\boldsymbol{c}_i$ are the weights and the discrete velocities of the quadrature respectively. The hydrodynamic moments of Equations (A.28) - (A.30) can be computed by

$$\rho = \sum_i f_i = \sum_i g_i \tag{A.35}$$

$$\rho \boldsymbol{u} = \sum_i \boldsymbol{c}_i f_i = \sum_i \boldsymbol{c}_i g_i \tag{A.36}$$

$$\rho\varepsilon = \frac{1}{2}\sum_i (\boldsymbol{c}_i - \boldsymbol{u})^2 f_i = \frac{1}{2}\sum_i (\boldsymbol{c}_i - \boldsymbol{u})^2 g_i \tag{A.37}$$

where $f_i \equiv f_i(\boldsymbol{x},t) \equiv w_i f(\boldsymbol{x},\boldsymbol{c},t)$, $g_i \equiv g_i(\boldsymbol{x},t) \equiv w_i g(\boldsymbol{x},\boldsymbol{c},t)$.

From Equation (A.27) $\mathrm{g} = \dfrac{\rho}{(2\pi RT)^{D/2}} \exp\left(-\dfrac{(\boldsymbol{c}-\boldsymbol{u})^2}{2RT}\right)$

$$g = \frac{\rho}{(2\pi RT)^{D/2}} exp\left(-\frac{\boldsymbol{c}^2}{2RT}\right) exp\left(\frac{\boldsymbol{c}.\boldsymbol{u}}{RT} - \frac{\boldsymbol{u}^2}{2RT}\right) \tag{A.38}$$

We know that $e^x = 1 + \mathrm{x} + \dfrac{x^2}{2!} + \dfrac{x^3}{3!} + \ldots\ldots\ldots\ldots$

$$exp\left(\frac{\boldsymbol{c}.\boldsymbol{u}}{RT} - \frac{\boldsymbol{u}^2}{2RT}\right) = 1 + \frac{\boldsymbol{c}.\boldsymbol{u}}{RT} - \frac{\boldsymbol{u}^2}{2RT} + \frac{\dfrac{(\boldsymbol{c}.\boldsymbol{u})^2}{(RT)^2} + \dfrac{\boldsymbol{u}^4}{4(RT)^2} - \dfrac{2\boldsymbol{c}.\boldsymbol{u}}{RT}\times\dfrac{\boldsymbol{u}^2}{2RT}}{2!} + \ldots \tag{A.39}$$

$f^{(eq)}$ (form of g to be used in LBM) only retains the terms upto $O(\boldsymbol{u}^2)$ so that for low velocity (and Mach number) we can write in Equation (A.38)

$$exp\left(\frac{\boldsymbol{c}.\boldsymbol{u}}{RT} - \frac{\boldsymbol{u}^2}{2RT}\right) = 1 + \frac{\boldsymbol{c}.\boldsymbol{u}}{RT} - \frac{\boldsymbol{u}^2}{2RT} + \frac{(\boldsymbol{c}.\boldsymbol{u})^2}{2(RT)^2} \tag{A.40}$$

so that

$$f^{(eq)} = \frac{\rho}{(2\pi RT)^{D/2}} exp\left(-\frac{\boldsymbol{c}^2}{2RT}\right) \times \left(1 + \frac{\boldsymbol{c}.\boldsymbol{u}}{RT} - \frac{\boldsymbol{u}^2}{2RT} + \frac{(\boldsymbol{c}.\boldsymbol{u})^2}{2(RT)^2}\right) \tag{A.41}$$

The equilibrium distribution given by Equation (A.41) is known as Low Mach Number Approximation (LMNA). The hydrodynamic moments of this equation is equivalent to evaluating the following integral in general

$$I = \int \psi(\boldsymbol{c}) f^{(\mathrm{eq})} d\boldsymbol{c} = \frac{\rho}{(2\pi RT)^{D/2}} \int \psi(\boldsymbol{c})\, exp\left(-\frac{\boldsymbol{c}^2}{2RT}\right) \times \left(1 + \frac{\boldsymbol{c}.\boldsymbol{u}}{RT} - \frac{\boldsymbol{u}^2}{2RT} + \frac{(\boldsymbol{c}.\boldsymbol{u})^2}{2(RT)^2}\right) d\boldsymbol{c} \tag{A.42}$$

A.3. Discretization of Phase Space Using Two-Dimensional Nine-Velocity Square Lattice Model

Figure A.1 shows the two-dimensional nine-velocity square lattice model with discrete velocities.

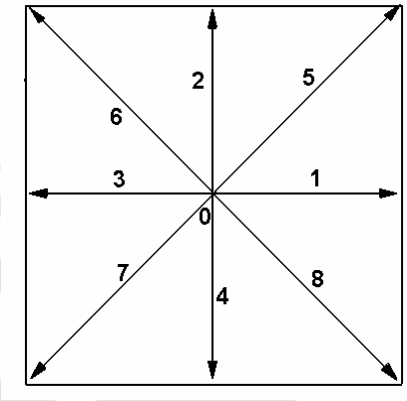

Figure A.1: Two-Dimensional nine-velocity square lattice model.

The three abscissas (ς_j^m) and the corresponding weights (w_j) used in the numerical integration are given by

$$\varsigma_1 = -\sqrt{3/2} \qquad \varsigma_2 = 0 \qquad \varsigma_3 = \sqrt{3/2} \tag{A.43}$$

$$w_1 = \sqrt{\pi/6} \qquad w_2 = 2\sqrt{\pi/3} \qquad w_3 = \sqrt{\pi/6} \tag{A.44}$$

It may be noted that

$$w_\alpha = \frac{w_i w_j}{\pi} \tag{A.45}$$

Therefore, nine (9) combinations w_α will come

$$\frac{w_1 w_1}{\pi} = \frac{w_1^2}{\pi} = \frac{1}{36}\ ; \qquad \frac{w_1 w_2}{\pi} = \frac{1}{9}; \qquad \frac{w_1 w_3}{\pi} = \frac{1}{36}; \qquad \frac{w_2 w_1}{\pi} = \frac{1}{9}; \qquad \frac{w_2 w_2}{\pi} = \frac{4}{9};$$

$$\frac{w_2 w_3}{\pi} = \frac{1}{9}; \qquad \frac{w_3 w_1}{\pi} = \frac{1}{36}; \qquad \frac{w_3 w_2}{\pi} = \frac{1}{9}; \qquad \frac{w_3 w_3}{\pi} = \frac{1}{36}.$$

It can be shown that the integral of the moment in Equation (A.42) boils down to

$$I = \int \psi(\boldsymbol{c})\, f^{(\mathrm{eq})}\, d\boldsymbol{c} = \frac{\rho}{\pi} \sum_{i,j=1}^{3} w_i w_j\ \psi(\boldsymbol{c}_{i,j}) \left(1 + \frac{\boldsymbol{c}.\boldsymbol{u}}{RT} + \frac{(\boldsymbol{c}.\boldsymbol{u})^2}{2(RT)^2} - \frac{\boldsymbol{u}^2}{2RT}\right) \tag{A.46}$$

$$f_{i,j}^{(eq)} = \frac{w_i w_j}{\pi}\rho\left\{1+\frac{(\boldsymbol{c}_{i,j}.\boldsymbol{u})}{RT}+\frac{(\boldsymbol{c}_{i,j}.\boldsymbol{u})^2}{2(RT)^2}-\frac{\boldsymbol{u}^2}{2RT}\right\} \tag{A.47}$$

We know that, $RT = c_s^2 = \frac{c^2}{3}; \sqrt{RT} = \frac{c}{\sqrt{3}}; \sqrt{2RT} = c\sqrt{\frac{2}{3}};$ $\qquad \boldsymbol{c}_{i,j} = \sqrt{2RT}\,(\zeta_i, \zeta_j)$

$$f_{i=1,j=1}^{(eq)} = \frac{w_1 w_1}{\pi}\rho\left\{1+\frac{\left[\sqrt{2RT}\,(\zeta_1,\zeta_1).\boldsymbol{u}\right]}{RT}+\frac{\left[\sqrt{2RT}\,(\zeta_1,\zeta_1).\boldsymbol{u}\right]^2}{2(RT)^2}-\frac{\boldsymbol{u}^2}{2RT}\right\} \tag{A.48}$$

$\zeta_1 = -\sqrt{\frac{3}{2}}; \zeta_2 = 0; \zeta_3 = \sqrt{\frac{3}{2}}; \frac{w_1^2}{\pi} = \frac{1}{36};$ The above Equation (A.48) becomes

$$f_{i=1,j=1}^{(eq)} = \frac{1}{36}\rho\left\{1+\frac{\left[c\sqrt{\frac{2}{3}}(-\sqrt{\frac{3}{2}},-\sqrt{\frac{3}{2}}).\boldsymbol{u}\right]}{RT}+\frac{\left[c\sqrt{\frac{2}{3}}(-\sqrt{\frac{3}{2}},-\sqrt{\frac{3}{2}}).\boldsymbol{u}\right]^2}{2(RT)^2}-\frac{\boldsymbol{u}^2}{2RT}\right\} \tag{A.49}$$

$$f_{i=1,j=1}^{(eq)} = \frac{1}{36}\rho\left\{1+\frac{[(-1,-1)c.\boldsymbol{u}]}{RT}+\frac{[(-1,-1)c.\boldsymbol{u}]^2}{2(RT)^2}-\frac{\boldsymbol{u}^2}{2RT}\right\}$$

$$RT = \frac{c^2}{3}; \qquad f_{i=1,j=1}^{(eq)} = \frac{1}{36}\rho\left\{1+\frac{3[(-1,-1)c.\boldsymbol{u}]}{c^2}+\frac{9[(-1,-1)c.\boldsymbol{u}]^2}{2c^4}-\frac{3}{2}\frac{\boldsymbol{u}^2}{c^2}\right\} \tag{A.50}$$

Similarly we can derive other particle directions.

$$f_{1,2}^{(eq)} = \frac{1}{9}\rho\left\{1+\frac{3[(-1,0)c.\boldsymbol{u}]}{c^2}+\frac{9[(-1,0)c.\boldsymbol{u}]^2}{2c^4}-\frac{3}{2}\frac{\boldsymbol{u}^2}{c^2}\right\}; \quad f_{1,3}^{(eq)} = \frac{1}{36}\rho\left\{1+\frac{3[(-1,1)c.\boldsymbol{u}]}{c^2}+\frac{9[(-1,1)c.\boldsymbol{u}]^2}{2c^4}-\frac{3}{2}\frac{\boldsymbol{u}^2}{c^2}\right\}$$

$$f_{2,1}^{(eq)} = \frac{1}{9}\rho\left\{1+\frac{3[(0,-1)c.\boldsymbol{u}]}{c^2}+\frac{9[(0,-1)c.\boldsymbol{u}]^2}{2c^4}-\frac{3}{2}\frac{\boldsymbol{u}^2}{c^2}\right\}; \quad f_{2,2}^{(eq)} = \frac{4}{9}\rho\left\{1+\frac{3[(0,0)c.\boldsymbol{u}]}{c^2}+\frac{9[(0,0)c.\boldsymbol{u}]^2}{2c^4}-\frac{3}{2}\frac{\boldsymbol{u}^2}{c^2}\right\}$$

$$f_{2,3}^{(eq)} = \frac{1}{9}\rho\left\{1+\frac{3[(0,1)c.\boldsymbol{u}]}{c^2}+\frac{9[(0,1)c.\boldsymbol{u}]^2}{2c^4}-\frac{3}{2}\frac{\boldsymbol{u}^2}{c^2}\right\}; \quad f_{3,1}^{(eq)} = \frac{1}{36}\rho\left\{1+\frac{3[(1,-1)c.\boldsymbol{u}]}{c^2}+\frac{9[(1,-1)c.\boldsymbol{u}]^2}{2c^4}-\frac{3}{2}\frac{\boldsymbol{u}^2}{c^2}\right\}$$

$$f_{3,2}^{(eq)} = \frac{1}{9}\rho\left\{1+\frac{3[(1,0)c.\boldsymbol{u}]}{c^2}+\frac{9[(1,0)c.\boldsymbol{u}]^2}{2c^4}-\frac{3}{2}\frac{\boldsymbol{u}^2}{c^2}\right\}; \quad f_{3,3}^{(eq)} = \frac{1}{36}\rho\left\{1+\frac{3[(1,1)c.\boldsymbol{u}]}{c^2}+\frac{9[(1,1)c.\boldsymbol{u}]^2}{2c^4}-\frac{3}{2}\frac{\boldsymbol{u}^2}{c^2}\right\}$$

$w_0 = \frac{4}{9} \Rightarrow i = j = 2 \Rightarrow (0,0) \Rightarrow \alpha = 0;$ $\qquad w_1 = \frac{1}{9} \Rightarrow i = 3, j = 2 \Rightarrow (1,0) \Rightarrow \alpha = 1;$

$w_2 = \frac{1}{9} \Rightarrow i = 2, j = 3 \Rightarrow (0,1) \Rightarrow \alpha = 2;$ $\qquad w_3 = \frac{1}{9} \Rightarrow i = 1, j = 2 \Rightarrow (-1,0) \Rightarrow \alpha = 3;$

$w_4 = \frac{1}{9} \Rightarrow i = 2, j = 1 \Rightarrow (0,-1) \Rightarrow \alpha = 4;$ $\qquad w_5 = \frac{1}{36} \Rightarrow i = 3, j = 3 \Rightarrow (1,1) \Rightarrow \alpha = 5;$

$w_6 = \frac{1}{36} \Rightarrow i = 1,\ j = 3 \Rightarrow (-1,1) \Rightarrow \alpha = 6$; $w_7 = \frac{1}{36} \Rightarrow i = 1,\ j = 1 \Rightarrow (-1,-1) \Rightarrow \alpha = 7$;

$w_8 = \frac{1}{36} \Rightarrow i = 3,\ j = 1 \Rightarrow (1,-1) \Rightarrow \alpha = 8$

The Equilibrium distribution function of the nine-velocity square lattice model

$$f_i^{(eq)} = w_i \rho \left\{ 1 + \frac{3[\boldsymbol{c}_i.\boldsymbol{u}]}{c^2} + \frac{9[\boldsymbol{c}_i.\boldsymbol{u}]^2}{2c^4} - \frac{3}{2}\frac{\boldsymbol{u}^2}{c^2} \right\} \tag{A.51}$$

where

$\boldsymbol{c}_i = (0,0) \Rightarrow i = 0$; $\boldsymbol{c}_i = (\cos\theta_i, \sin\theta_i)c \Rightarrow \theta_i = \frac{(i-1)\pi}{2} \Rightarrow i = 1,2,3,4$;

$\boldsymbol{c}_i = \sqrt{2}(\cos\theta_i, \sin\theta_i)C \Rightarrow \theta_i = \frac{(i-5)\pi}{2} + \frac{\pi}{4} \Rightarrow i = 5,6,7,8$.

Appendix B

A Lattice Kinetic Scheme for Incompressible Viscous Flows

B.1. Introduction

A two-dimensional lattice kinetic scheme on the uniform lattice arrangement was recently proposed by Inamuro [136], based on the standard lattice Boltzmann method (LBM). In this scheme, we can implement the same standard LBM boundary conditions and it can save computer memory [137, 138]. The derivative term is dropped out and the difficulty of the relatively large viscosity is eased by controlling the time step Δt or speed of sound Cs. To validate this new lattice kinetic scheme, the numerical simulations of the two-dimensional square driven cavity flow at Reynolds numbers from 100 to 1000 are carried out.

B.2. Standard Lattice Boltzmann Method

The lattice BGK model (LBGK) with single-relaxation-time, which is a commonly used Lattice Boltzmann Method is given by [99]

$$f_i\left(\mathbf{x}+\boldsymbol{c}_i\Delta t, t+\Delta t\right)-f_i\left(\mathbf{x},t\right)=-\frac{1}{\tau}\left[f_i\left(\mathbf{x},t\right)-f_i^{eq}\left(\mathbf{x},t\right)\right] \qquad i=0,1....,N \tag{B.1}$$

The equilibrium distribution functions $f_i^{eq}\left(\mathbf{x},t\right)$ can be expressed in the form [99]

$$f_i^{(eq)}=\rho w_i\left[1+3\left(\boldsymbol{c}_i.\boldsymbol{u}\right)+4.5\left(\boldsymbol{c}_i.\boldsymbol{u}\right)^2-1.5(\boldsymbol{u}.\boldsymbol{u})\right] \tag{B.2}$$

The macroscopic quantities such as density ρ and momentum density $\rho\boldsymbol{u}$ are defined in terms of the particle distribution function f_i as follows:

$$\rho = \sum_{i=0}^{N} f_i, \tag{B.3}$$

$$\rho\,\boldsymbol{u} = \sum_{i=0}^{N} f_i\boldsymbol{c}_i. \tag{B.4}$$

The relaxation time τ is related to the kinematic viscosity υ by

$$\upsilon = \frac{2\tau - 1}{6} \tag{B.5}$$

B.3. Lattcie Kinetic Scheme

If the dimensionless relaxation time τ in Equation (B.1) is set to unity, we obtain [136]

$$f_i\left(\mathbf{x} + \boldsymbol{c}_i \Delta t, t + \Delta t\right) = f_i^{eq}\left(\mathbf{x}, t\right) \tag{B.6}$$

The macroscopic quantities such as density ρ and momentum density $\rho \boldsymbol{u}$ are defined in terms of the particle distribution function f_i as follows:

$$\rho = \sum_{i=0}^{N} f_i, \tag{B.7}$$

$$\rho \boldsymbol{u} = \sum_{i=0}^{N} f_i \boldsymbol{c}_i. \tag{B.8}$$

The relaxation time τ is related to the kinematic viscosity υ by

$$\upsilon = \frac{1}{6}\Delta t \tag{B.9}$$

The equilibrium distribution functions $f_i^{eq}\left(\mathbf{x}, t\right)$ can be expressed in the form as [136]

$$f_i^{(eq)} = \rho w_i \left[1 + 3c_{i\gamma}\boldsymbol{u}_\gamma + \frac{9}{2} c_{i\gamma}c_{i\delta}\boldsymbol{u}_\gamma\boldsymbol{u}_\delta - \frac{9}{2}\boldsymbol{u}_\gamma\boldsymbol{u}_\gamma + A\Delta x\left(\frac{\partial \boldsymbol{u}_\delta}{\partial x_\gamma} + \frac{\partial \boldsymbol{u}_\gamma}{\partial x_\delta}\right)c_{i\gamma}c_{i\delta}\right] \tag{B.10}$$

where $\gamma, \delta = x, y$ represent Cartesian coordinates (the summation convention is used), and A is a constant parameter of $O(1)$, which determines the fluid viscosity as described below. The parameter A may be regarded as a relaxation parameter of the stress tensor in the generalized lattice Boltzmann equation. The main advantage of this method is less memory because Equation (B.6) has fewer terms than Equation (B.1). In order to verify the accuracy of the lattice kinetic scheme, lid-driven square cavity flows are simulated and the results are compared with existing results.

B.4. Cavity Flow Simulation

The two-dimensional nine-velocity (*D2Q9*) lattice model is used in the present work. In Figure B.1 streamlines for the lid driven square cavity at various Reynolds numbers are shown. The bounce-back scheme is used in these simulations to copy the velocity no-slip condition on the walls. A lid-velocity of U = 0.1 has been considered in this work. Numerical simulations were carried out using the Lattice kinetic scheme for Re = 100, 400 and 1000. It is seen that the lattice kinetic scheme with 161×161 lattices can capture

most of the physical variables satisfactorily. The lattice kinetic scheme results, however, are computationally more efficient. Figure B.2 shows the velocity profiles for u-velocity along the vertical centreline and v-velocity along the horizontal centreline of the cavity. It is observed that the agreement between our results and those of Ghia *et al.* [83] is excellent.

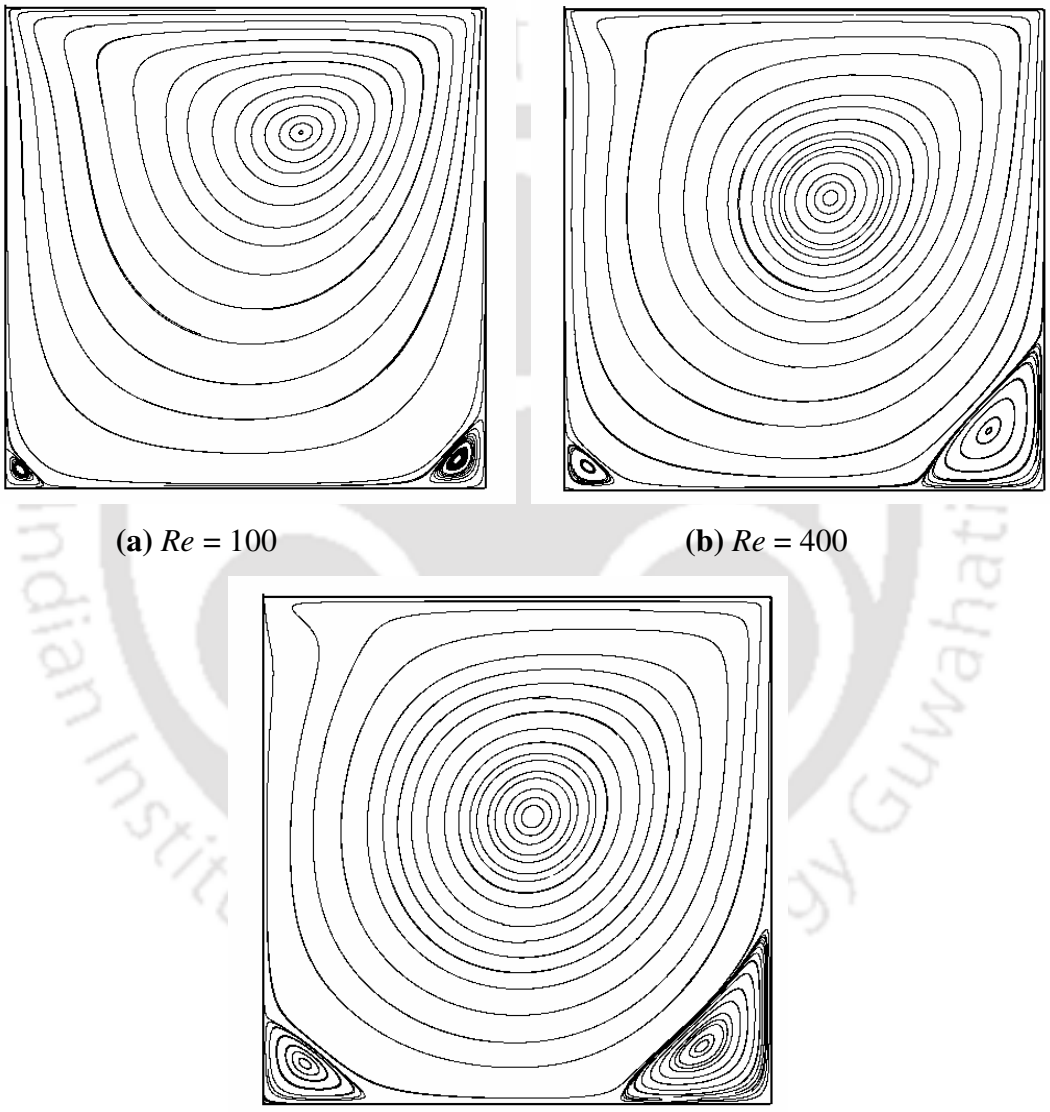

(a) Re = 100 **(b)** Re = 400

(c) Re = 1000

Figure B.1: Streamline pattern for (a) Re = 100 (b) Re = 400 (c) Re = 1000 by lattice kinetic scheme on a 129× 129 lattice.

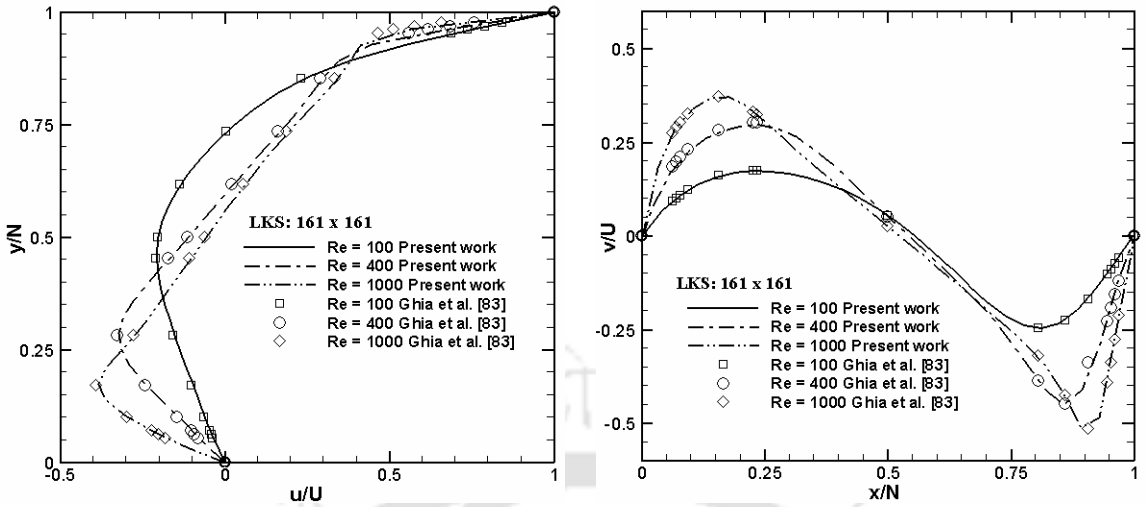

(a) (b)

Figure B.2: Computed profiles of u-velocity along the vertical centreline and v-velocity along the horizontal centreline of the cavity at various Reynolds numbers.

B.5. Conclusion

A recent lattice kinetic scheme proposed by Inamuro, which is based on the standard lattice Boltzmann method, is validated in this section. It is concluded that, this needs less memory than the standard lattice Boltzmann method. Also, preliminary calculations show that the present lattice kinetic scheme is also stable like the standard LBM at low Reynolds numbers.

Appendix C

LBM for 1D and 2D Heat-Conduction Problems

C.1. Introduction

The application of LBM to heat transfer problems received less attention than the field of fluid flow problems. Over the years, numerical schemes for the heat conduction are based mostly on continuum-based methods. Therefore in this section, the LBM is used to solve heat conduction problems in one- and two-dimensional geometries just for instructional purpose. The governing lattice Boltzmann equation with BGK approximation can be written as [12]

$$f_i\left(\mathbf{x}+\boldsymbol{c}_i\Delta t, t+\Delta t\right)-f_i\left(\mathbf{x},t\right)=-\frac{\Delta t}{\tau}\left[f_i\left(\mathbf{x},t\right)-f_i^{eq}\left(\mathbf{x},t\right)\right]\quad i=0,1....,N \tag{C.1}$$

where $f_i(\mathbf{x},t)$ and $f_i^{(eq)}(\mathbf{x},t)$ are the particle and equilibrium distribution functions at $(\mathbf{x},t)$, $\boldsymbol{c}_i$ is the particle velocity along the i^{th} direction and τ is the relaxation time parameter. The relaxation time τ for the one-dimensional models can be written as [13]

$$\tau = \frac{3\alpha}{\left|\boldsymbol{c}_i^{\,2}\right|}+\frac{\Delta t}{2} \tag{C.2}$$

The equilibrium distribution function can be written as

$$f_i^{eq}(\mathbf{x},t) = w_i T(\mathbf{x},t) \tag{C.3}$$

Figure C.1 shows the *D1Q2 and D1Q3* lattice models. The particle velocities and their corresponding weights for different lattice models are shown in Table C.1. It is known that $C = \Delta x/\Delta t$ and weights satisfy the relation $\sum_{i=1}^{N} w_i = 1$. The macroscopic temperature is obtained as

$$T = \sum_{i=0}^{N} f_i(\mathbf{x},t) = \sum_{i=0}^{N} f_i^{eq}(\mathbf{x},t) \tag{C.4}$$

Some details of the heat transfer simulations by LBM can be found in [11-13]. The solution procedure of the LBM at each time step comprise the streaming and collision steps, application of boundary conditions, calculation of particle distribution function followed by calculation of macroscopic variables.

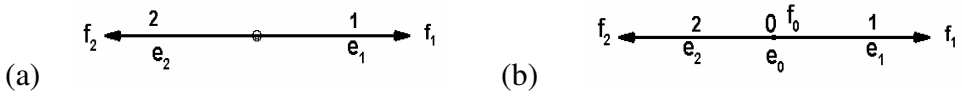

Figure C.1: One-Dimensional lattice models (a) *D1Q2* and (b) *D1Q3*.

Table C.1: Important parameters of different lattice models.

Lattice Model	Particle velocity ($\boldsymbol{c}_i$)	Weights (w_i)
D1Q2	$c_1 = C$, $c_2 = -C$	$w_1 = 1/2$, $w_2 = 1/2$
D1Q3	$c_0 = 0$, $c_1 = C$, $c_2 = -C$	$w_0 = 1/2$, $w_1 = 1/4$, $w_2 = 1/4$
D1Q5	$c_0 = 0$, $c_{1,2} = \pm C$, $c_{3,4} = \pm 2C$	$w_0 = 6/12$, $w_{1,2} = 2/12$, $w_{3,4} = 1/12$
D2Q9	$c_0 = (0,0)$, $c_{1,2} = (\pm 1,0).C$, $c_{3,4} = (0, \pm 1).C$, $c_{5\text{-}8} = (\pm 1, \pm 1).C$	$w_0 = 4/9$, $w_{1,2} = 1/9$, $w_{3,4} = 1/36$

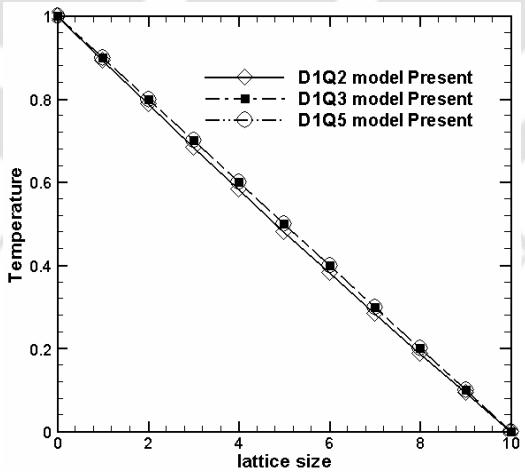

Figure C.2: One-Dimensional temperature distribution obtained by the LBM.

Case I: In the one-dimensional heat conduction problem, the left and right side temperatures are known. The left and right sides are maintained at 1.0 and 0. Figure C.2

shows the temperature distributions by the LBM for 1-D geometry. It is seen that *D1Q3* and *D1Q5* models give highly accurate results that exactly matches each other. The results given by *D1Q2* model, however, is seen to be deficient.

Case II: A 2-D square geometry with all boundaries of known temperatures is now considered. The bottom side is maintained at a temperature of 1.0 and the other three sides are maintained at a temperature of 0.

$$T_L = T_R = T_T = 0.0; T_B = 1 \qquad \text{(C.5)}$$

The *D2Q9* model is used to find the temperature distribution through LBM. Figure C.3 shows the isotherms computed by the LBM. The results are well-known and it exhibits no surprises, thereby confirming the fact that our LBM computation yields quantitatively accurate results.

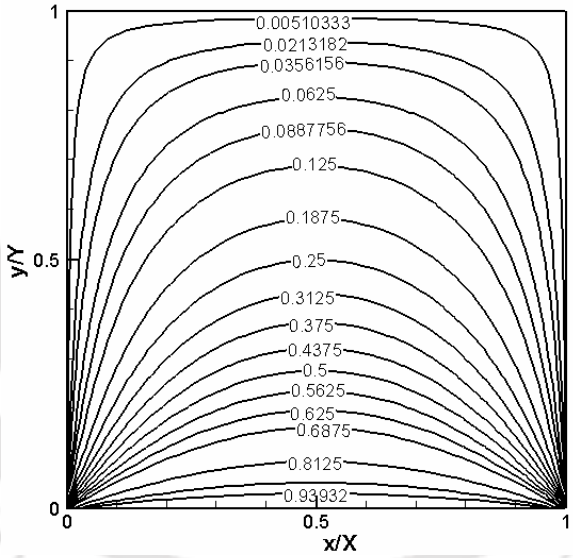

Figure C.3: Two-Dimensional temperature distribution by the LBM.

C.2. Conclusion

The lattice Boltzmann method is used to solve simple heat conduction problems in one- and two-dimensional geometries. The *D1Q3* model is seen to give accurate results compared with *D1Q2* and is less expensive compared with *D1Q5* model. The *D2Q9* model is also seen to give accurate results for the two-dimensional temperature distribution. Simplicity of the method appears to be a notable merit.

Appendix D

Some Formulational Details of 2D LBM with *D2Q9* Lattice for the Lid-Driven Cavity Problem

D.1. Nondimensionalization

Here we intend to give some useful information that will help one relate some of the frequently appearing variables with a physical system, namely, the lid-driven cavity. In the cavity, *i* indicates the lattice node in the *x*-direction and *j* indicates the lattice node in the *y*-direction.

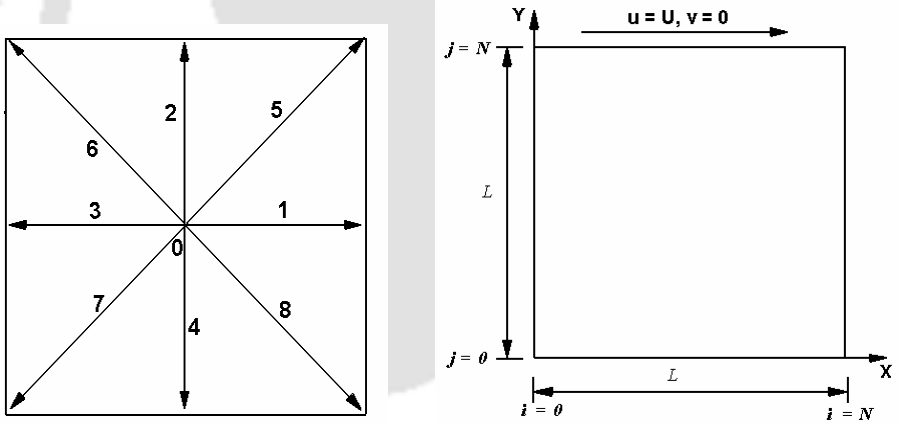

Figure D.1(a): Two-Dimensional nine-velocity square lattice model and (b) 2D lid-driven square cavity

First we attempt to give some idea about the non-dimensionalization. Here 'starred' quantities indicate nondimensional variables. For the sake of brevity, the symbols appearing in the Figures D.1(a) and (b) will be used directly without explaining what they are, as these figures already appear in the main body of the thesis. The nondimensional fluid velocity vector, position vector, time and kinematic viscosity are given by

$$\boldsymbol{u}^* = \frac{\boldsymbol{u}}{\Delta x/\Delta t}, \quad \boldsymbol{x}^* = \frac{\boldsymbol{x}}{\Delta x}, \quad t^* = \frac{t}{\Delta t}, \quad \upsilon^* = \frac{\upsilon}{(\Delta x)^2/\Delta t} \tag{D.1}$$

where $\boldsymbol{u}$ is the fluid velocity, $\Delta x = \Delta y = \frac{L}{N}$ is the lattice spacing, Δt is the characteristic time-step and υ the kinematic viscosity of the fluid. For the square cavity the side length L serves as the characteristic length scale x_{ref}. Some other nondimensional variables are as follows:

$$f_k^* = \frac{f_k}{\rho_{ref}}, \quad \rho^* = \frac{\rho}{\rho_{ref}}, \quad \tau^* = \frac{\tau}{\Delta t} \tag{D.2}$$

where f_k is the nonequilibrium distribution function for the k^{th} particle velocity (k = 0,1,…8 for *D2Q9* lattice), ρ is the local mass density and τ is the single-relaxation time scale. The Reynolds number for the flow is

$$Re = \frac{u_{ref} x_{ref}}{\upsilon_{ref}} \tag{D.3}$$

Now the discrete Boltzmann equation with BGK approximation reads

$$\frac{\partial f_k^*}{\partial t} + \boldsymbol{c}_k^* . \nabla f_k^* = - \frac{1}{\tau^*} \left(f_k^* - f_k^{(eq)*} \right) \tag{D.4}$$

The single-relaxation time scale τ^* is given by (see Ref. [33])

$$\tau^* = \frac{6\upsilon^* + 1}{2} = \frac{1}{2} + 3\upsilon^* \tag{D.5}$$

Now $\upsilon^* = \dfrac{\upsilon_{ref}}{(\Delta x)^2/\Delta t} = \dfrac{u_{ref} x_{ref}/Re}{(\Delta x)^2/\Delta t} = \dfrac{1}{Re} \dfrac{u_{ref} x_{ref} \Delta t}{(\Delta x)^2}$

From the last two relations we may now write

$$\tau^* = \frac{1}{2} + \frac{3}{Re} \frac{u_{ref} x_{ref} \Delta t}{(\Delta x)^2} \tag{D.6}$$

Now for the sake of elegance we drop 'star' with the understanding that in course of what follows the variables are nondimensional. The discrete Boltzmann equation, when discretized over a lattice model (say *D2Q9*), gives the nondomensional lattice Boltzmann equation

$$f_k(\mathbf{x}+\boldsymbol{c_k}\Delta t, t+\Delta t) - f_k(\mathbf{x},t) = -\frac{1}{\tau}\left(f_k(\mathbf{x},t) - f_k^{(eq)}(\mathbf{x},t) \right) \tag{D.7}$$

As we have seen in Appendix A, the local and instantaneous mass and momentum density can now be written as

$$\rho(\mathbf{x},t) = \sum_{k=0}^{8} f_k^{(eq)}(\mathbf{x},t), \tag{D.8}$$

$$\rho \boldsymbol{u}(\mathbf{x},t) = \sum_{k=0}^{8} f_k^{(eq)}(\mathbf{x},t)\, \boldsymbol{c_k} \tag{D.9}$$

For the D2Q9 model, the equilibrium velocity distribution is

$$f_k^{(eq)} = \rho w_k \left[1 + 3(\boldsymbol{c_k}.\boldsymbol{u}) + \frac{9}{2}(\boldsymbol{c_k}.\boldsymbol{u})^2 - \frac{3}{2}(\boldsymbol{u}.\boldsymbol{u}) \right] \tag{D.10}$$

where $w_0 = 4/9,\ w_1 = w_2 = w_3 = w_4 = 1/9$ and $w_5 = w_6 = w_7 = w_8 = 1/36.$ The pressure is given by $p = \rho\, c_s^2$ and the nondimensional speed of sound by $c_s = 1/\sqrt{3}$.

It may be noted that in LBM it is a standard practice to keep u_{ref} low so that the compressible limit (for which the LBM model is valid) is not exceeded. For the computation of cavity flow for a certain Reynolds number by LBM, lid velocity $u_{ref} = \boldsymbol{U}$ may be changed within the incompressible Mach number limit. The relation for τ^* developed above shows that for the same Reynolds number, altering the value of the lid velocity $\boldsymbol{U}$ results in the change of value of the relaxation time, which determines the rate of approach to equilibrium with every collision.